Aeroelastic Optimization of MW Wind Turbines

Risø-R-Report

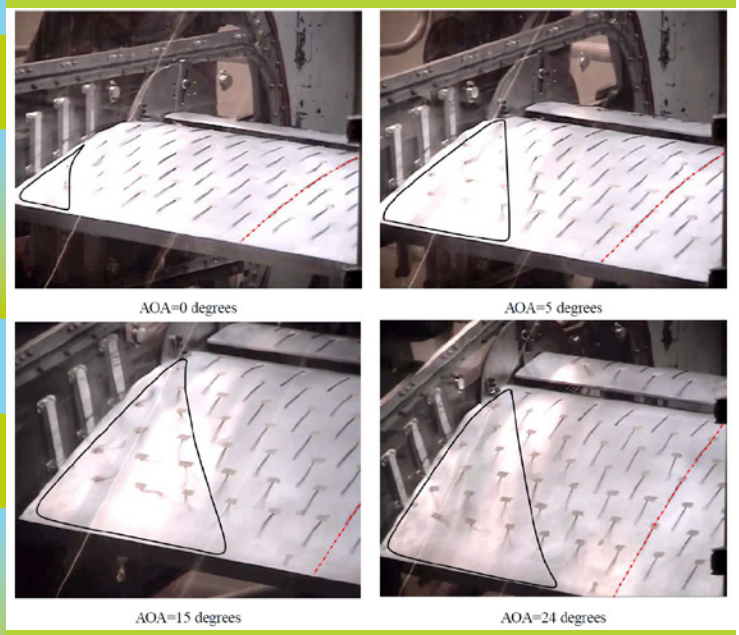

Edited by Morten Hartvig Hansen and Frederik Zahle
Risø-R-1803(EN)
December 2011

Risø DTU
National Laboratory for Sustainable Energy

Author: Edited by Morten Hartvig Hansen and Frederik Zahle
Title: Aeroelastic Optimization of MW Wind Turbines
Department: Aeroelastic Design – DTU Wind Energy, Risø Campus

Risø–R–1803(EN)
December 2011

Abstract: This report contains the results from the Energy Development and Demonstration Project "Aeroelastic Optimization of MW wind turbine" (AeroOpt). The project has had the following five Work Packages:

1. **Geometric non-linear, anisotropic beam element for HAWC2**
2. **Closed-loop eigenvalue analysis of controlled wind turbines**
3. **Resonant wave excitation of lateral tower bending modes**
4. **Development of next generation aerodynamic design tools**
5. **Advanced design and verification of airfoils**

The purposes of these Work Packages are briefly described in the Preface and a summary of the results are given in Section 2. Thereafter, the results from each Work Package are described in eight subsequent chapters.

ISBN 978-87-550-3962-9

Contract no.:
EUDP-64009-0002

Group's own reg. no.:
1110073-00

Sponsorship:
Danish Energy Authorities

Cover:
Wool tufts flow visualization of slatted airfoil in the LM wind tunnel.

Pages: 143

Information Service Department
Ris National Laboratory for
Sustainable Energy
Technical University of Denmark
P.O.Box 49
DK-4000 Roskilde
Denmark
Telephone +45 4677 4005
bibl@risoe.dtu.dk
Fax +45 4677 4013
www.risoe.dtu.dk

Contents

1 Preface

This report contains the results of the EUDP funded project “Aeroelastic Optimization of MW Wind Turbines” (AeroOpt) that has been running from April 2009 to October 2011 in partnership between the Aeroelastic Design Programme in the Wind Energy Division of Risø DTU and the Fluid Mechanics Section of the Department of Mechanical Engineering (MEK) at DTU. The project also included four industrial partners Siemens Wind Power A/S, Vestas Wind Systems A/S, DONG Energy A/S, and LM Wind Power A/S, which have contributed with inputs on the applicability of the research and with relevant questions and suggestions to the work at two Aeroelastic Workshops both with over 30 external participants and two Steering Committee meetings by the key academic and industrial persons.

The main goal of this project was to ensure the continuous development and improvement of the aeroelastic design complex and hereby contribute to a direct optimization to the industrial development in general. At Risø DTU and DTU MEK the aeroelastic design complex has been developed and demonstrated in cooperation with the industry in different areas such as; Computational Fluid Dynamics (CFD), aeroelasticity, aerodynamics, structural dynamics, stability, airfoil and rotor optimization, design optimization and controls. These research areas have been developed partly through a series of EFP-funded projects called ”Aeroelastic Research Programme” started in 1997, and have contributed to aid the industry analyze and develop their turbines. Continued development with focus on implementation of the tools is needed to achieve an effective exploitation of the complete aeroelastic design complex and to extend the high competence level in both Danish research institutes and Danish wind turbine industry in a dynamic interaction. The highest prioritized research areas and associated tool development have been condensed into five Work Packages of this project:

1 **Geometric non-linear, anisotropic beam element for HAWC2**
The purpose of this work has been to develop two new types of elements; an anisotropic one that can handle the anisotropic material properties of composite structures important for accurate modeling of blades, and a nonlinear one that can be used for modeling of mooring lines and other cables and chains without bending stiffness. The results of these works are described in details in Sections 3 and 4.

2 **Closed-loop eigenvalue analysis of controlled wind turbines**
The purpose of this work has been to develop and demonstrate the possibilities of closed-loop aero-servo-elastic eigenvalue analysis for the design and tuning of wind turbine controllers, and for an extended stability analysis of wind turbines under operation. The results of this work are described in details in Section 5.

3 **Resonant wave excitation of lateral tower bending modes**
The purpose of this work has been to estimate and develop methods for prediction of the total aero-hydro-elastic modal damping of the lateral tower bending mode, which in simulations is known to be excited in resonance with wave loads. Accurate predictions of the total lateral tower mode are important for accurate predictions of the resonant response that may determine the design loads. The results of this work are described in details in Section 6.

4 **Development of next generation aerodynamic design tools**
The purpose of this work has been to develop improved sub-models that can be directly implemented into existing BEM based design codes in industry based on the results of the recent large scale experiment DANAERO, and a completely new aerodynamic model for performance and load predictions based on a coupling of a vortex line method for rotor blade aerodynamics with 2-D and quasi 3-D viscous-inviscid interaction models. The results of this work are described in details in Section 7.

5 Advanced design and verification of airfoils

The purpose of this work has been twofold: 1) Design and verification of airfoils with thicknesses from 30 % to 50 % of the chord length for use on the inner part of wind turbine rotors with a focus on high aerodynamic efficiency, high roughness insensitivity and high maximum lift and 2) Design and verification of an airfoil with thicknesses around 15 % of the chord length, with the objective of high aerodynamic efficiency, high roughness insensitivity, insensitivity to transition point positions due to inflow turbulence and low noise emission. The results of these works are described in details in Sections 8, 9 and 10.

Besides the full description of the results in the subsequent sections, many results of the project have been published in journals and proceedings:

- Hansen, M. H. (2011), "Aeroelastic properties of backward swept blades", In *Proceedings of the 49th AIAA Aerospace Sciences Meeting Including the New Horizons Forum and Aerospace Exposition*, 4 - 7 January 2011, Orlando, Florida.
- Hansen, M.O.L., Madsen, H.Aa., 2011, "Review paper on wind turbine aerodynamics", *Journal of Fluids Engineering*, vol.133(11), pp. 114001.
- Kallesøe, B. S. and Hansen, A. M. (2011), "Dynamic mooring line modeling in hydro-aeroelastic wind turbine simulations", In *Proceedings of the 21st International Offshore and Polar Engineering Conference*, Maui, Hawaii, p. 375-382, 2011.
- Kim, T., Branner, K., and Hansen, A. M. (2011), "Developing Anisotropic Beam Element for Design Composite Wind Turbine Blades", In *Proceedings of the 18th International Conference on Composite Material*, Jeju, Korea, 21-26 August, 2011.
- Kim, T., Branner, K., and Hansen, A. M. (2011), "Anisotropic Beam Element for Modeling of the Wind Turbine Blades," In *Proceedings of the European Wind Energy Association Conference 2011*, Brussels, Belgium, 14-17 March, 2011.
- Kim, T., Buhl, T., and Bak, C. (2010), "Development of Wind Turbine Blade Optimization Tool for Enhancing the Performance," In *Proceedings of the The Science of making Torque from Wind 2010*, Crete, Greece, 28-30 June, 2010.
- Kim, T., Bak, C., and Buhl, T. (2011), "Optimization of the Wind Turbine Rotor to Enhance the Performance," In *Proceedings of the 52nd AIAA/ASME/ASCE/AHS/ASC Structural Dynamics and Materials Conference*, Denver, Colorado, 4-7 April, 2011.
- Madsen, H. Aa., Bak, C., Paulsen, U. S., Gaunaa, M., Sørensen, N. N., Fuglsang, P., Romblad, J., Olsen, N. A., Enevoldsen, P., Laursen, J. and Jensen, L. (2010), "The DAN-AERO MW Experiments". In *Proceedings of the 48th AIAA Aerospace Sciences Meeting Including the New Horizons Forum and Aerospace Exposition*, 4 - 7 January 2010, Orlando, Florida.
- Sørensen, J.N. (2011), "Aerodynamic aspects of wind energy conversion", Annual Review of Fluid Mechanics, vol. 43, pp. 427-448.
- Sørensen, J.N. (2011), "Instability of helical tip vortices", Journal of Fluid Mechanics, vol. 682, pp. 1-4.
- Yang, H., Shen, W.Z., Sørensen, J.N. and Zhu, W.J. (2011), "Extraction of airfoil data using PIV and pressure measurements", Wind Energy, vol. 14, issue 4, pp. 539-556.
- Zhu, W.J., Shen, W.Z. and Sørensen, J.N. (2011), "High-order numerical simulations of flow-induced noise". Int. Journal for Numerical Methods in Fluids, vol. 66, issue 1, pp. 17-37.
- Zahle, F., Gaunaa, M., Sørensen, N. N., and Bak, C. (2012), "Design and Wind Tunnel Testing of a Thick, Multi-Element High-Lift Airfoil", Submitted for the Annual European Wind Energy Association Conference 2012

The presentations from the two Aeroelastic Workshops have been published in the following reports (available from www.vindenergi.dtu.dk):

- Hansen, M. H. (Editor), "Presentations from the Aeroelastic Workshop - latest results from AeroOpt", *Risø-R-1769(EN)*, February 2011, Roskilde.
- Hansen, M. H. (Editor), "Presentations from the Aeroelastic Workshop 2 - latest results from AeroOpt", *Risø-R-1796(EN)*, October 2011, Roskilde.

2 Summary

Here is a short summary of the results from each milestone:

1 Geometric non-linear, anisotropic beam element for HAWC2
A new beam element has been developed to model the anisotropic structures produced by layered materials based on a cross-sectional stiffness matrix provided by a pre-processor e.g. BECAS, or VABS. The element is validated with known test cases for both static and dynamic responses. Another nonlinear bar element has been implemented to model mooring structures. The bottom contact is handled by a set of springs and dampers in each node with varying properties dependent on its distance to the bottom. Individual line systems are connected by use of a series of constraints.

2 Closed-loop eigenvalue analysis of controlled wind turbines
A linear aero-servo-elastic state-space model of a wind turbine operating at a given operating point defined by constant wind speed, rotor speed and pitch angle has been developed for open- and closed-loop aero-servo-elastic eigenvalue and frequency-domain analysis. The applications of this tool called HAWCStab2 are: closed-loop stability analysis, controller tuning based on poles placement and frequency response design, and derivation of linear first-principle reduced order models for model-based controllers. Examples of the two former applications are given in this report.

3 Resonant wave excitation of lateral tower bending modes
The aerodynamic damping of lateral tower vibrations have been estimated by 3D CFD and unsteady BEM models. A good comparison between the two models with very different complexity supports the continuous use of unsteady BEM for aerodynamic modeling of wind turbine dynamics. Generator torque control has furthermore been used to add active damping to the lateral tower vibrations reducing the tower fatigue load by 40 % with the cost of only 10 % increase in drivetrain fatigue load. Yaw slip can also be used to damp out excessive lateral tower vibrations if the distance from the yaw axis to the center of gravity of the nacelle-rotor structure is sufficiently large.

4 Development of next generation aerodynamic design tools
A viscous-inviscid model for predicting the aerodynamic behavior of airfoils subject to steady and unsteady motions has been developed. The inviscid part is modeled using a panel method whereas the viscous part is modeled using the integral form of the laminar and turbulent boundary layer equations, including a quasi-3D approach to include rotational effects. A design and optimization code based on a lifting line method coupled with a Lagrange multiplier approach has been presented. The circulation distribution which minimizes the induced loss is found, and the blade geometry is consequently derived using 2-D airfoil data.

5 Advanced design and verification of airfoils
The validation of the predictive capability of EllipSys2D for flatback airfoils indicated that the drag can be captured for these airfoils. In all 2D cases, the steady state results are closer to the measured lift than the unsteady results. CFD can be used to compare the quality of different flatback designs. The investigation of using slats to improve the performance of this airfoils concluded that lift coefficients of above 3.0 can be achieved for a 40 % flatback airfoil fitted with a 30 % chord leading edge slat with a stall angle of approximately 24 deg. The multi-element airfoil design was validated in an extensive wind tunnel campaign and comparisons between the experimental results and computations showed good agreement.

3 Anisotropic beam element

Author: Taeseong Kim

This chapter deals with the development of anisotropic beam element. It is shown that a typical wind turbine blade has very small couplings, but that these can be introduced by adding angled unidirectional layers [1]. However, aeroelastic codes in the wind energy field, such as HAWC2, use the classical beam model. Therefore such codes cannot be used to investigate the coupling effects of anisotropic materials.

The main aims of the present chapter are to develop a new beam element for the anisotropic structures, to implement the beam element into HAWC2, and to investigate a structural coupling effect.

3.1 Methods

Finite Element Analysis (FEA) is considered to compute a new beam element. Fig. 3.1 shows a sketch of the coordinate system of the considered beam element.

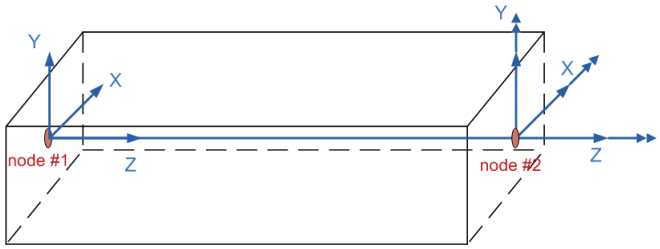

Figure 3.1. A sketch of the coordinate system

In order to compute element stiffness and mass matrix, the elastic energy and the kinetic energy of the beam are considered. Eq. 3.1 and Eq. 3.2 show the final form of the elastic and the kinetic energy of the beam element. More detailed expressions of the equations are addressed in [2].

$$\begin{aligned} U &= \frac{1}{2}\int_0^L \varepsilon^T S \varepsilon dz \\ &= \frac{1}{2} d^T {N_\alpha}^T \left[\int_0^L B^T S B dz\right] N_\alpha d \\ &= \frac{1}{2} d^T K d \end{aligned} \tag{3.1}$$

$$\begin{aligned} T &= \frac{1}{2}\int_0^L \dot{r}^T E \dot{r} dz \\ &= \frac{1}{2} \dot{d}^T {N_\alpha}^T \left[\int_0^L N^T E N dz\right] N_\alpha \dot{d} \\ &= \frac{1}{2} \dot{d}^T M \dot{d} \end{aligned} \tag{3.2}$$

where U is the elastic energy, ε is the generalized strains, superscript T is transpose, S is the cross-sectional stiffness matrix, d is nodal degrees of freedom, N is the polynomial matrix, B is the strain-displacement matrix, K is the element stiffness matrix, $\dot{r}$ is the velocity of the body, E is the cross-sectional mass matrix, and M is the element mass matrix.

3.2 Results

Three different cases are investigated to validate the new beam element model. The effect of using an anisotropic material is studied as well. Fig. 3.2 shows a sketch of the considered cases.

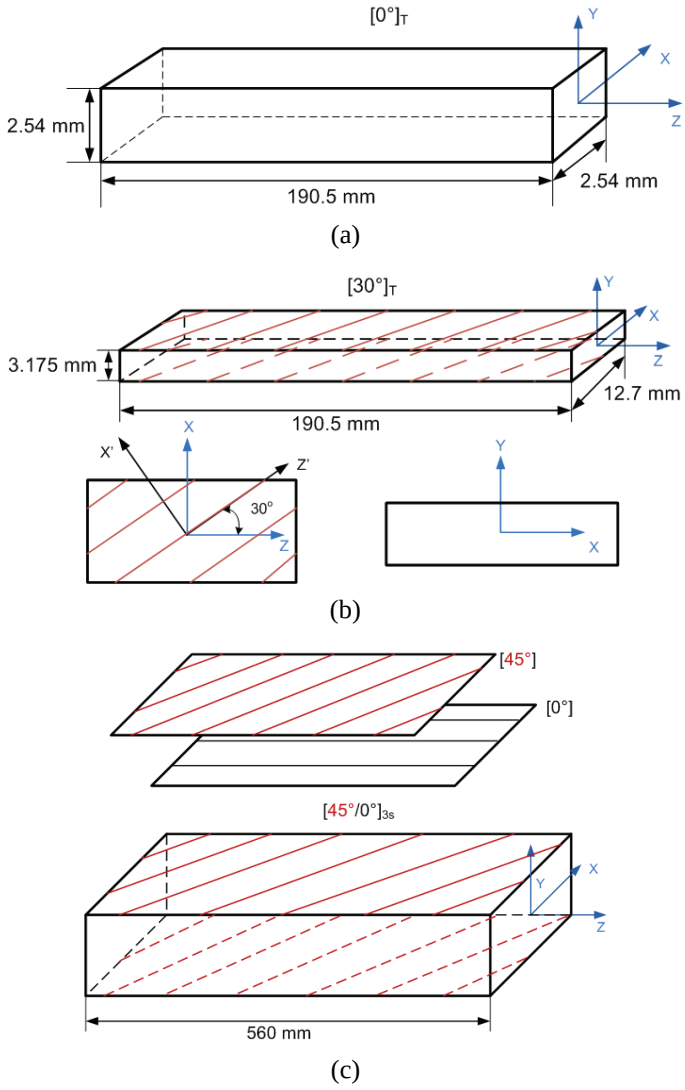

Figure 3.2. A sketch of considered cases. (a) Case1: $[0^\circ]_T$ layup with arbitrary isotropic material, (b) Case 2: $[30^\circ]_T$ layup with Graphite/Epoxy, (c) Case 3: $[45^\circ/0^\circ]_{3S}$ layup with Graphite/Epoxy

Table. 3.1 shows the detailed structural properties and cross-sectional stiffness matrix for the first example. For Case 2 and Case 3, only sectional stiffness information is displayed in Table. 3.2. More detailed information about the material properties and geometries is addressed in [3] and [4]. Case 1 is used for validating whether the new beam model is correctly implemented into HAWC2 or not. The other two cases are used for the comparisons between new HAWC2 computation with anisotropic material and the other existing results obtained from [3] and [4].

Table 3.1. Structural properties of Case 1 [5]

Material	Arbitrary material
E_{11}, E_{22}, E_{33}	100 *Pa*
G_{12},G_{13},G_{23}	41.667 *Pa*
ν_{12},ν_{13},ν_{23}	0.2
ρ	$1 kg/m^3$
Width	0.1 *m*
Height	0.1 *m*
Length	7.5 *m*
Sectional stiffness of Case 1	
S_{11}, S_{22}	$3.4899 \times 10^{-1}(N)$
S_{33}	$1(N)$
S_{44}, S_{55}	$8.3384 \times 10^{-4}(Nm^2)$
S_{66}	$5.9084 \times 10^{-4}(Nm^2)$

Table 3.2. Sectional stiffness of Cases 2 and 3

Stiffness of Case 2 [3]		Stiffness of Case 3 [4]	
S_{11}	$4.4702400 \times 10^5(N)$	S_{11}	$4.1673312 \times 10^5(N)$
S_{13}	$5.6667520 \times 10^5(N)$	S_{13}	$-2.070544 \times 10^5(N)$
S_{22}	$3.8404032 \times 10^4(N)$	S_{22}	$3.0237504 \times 10^4(N)$
S_{33}	$1.5861568 \times 10^6(N)$	S_{33}	$3.6099968 \times 10^6(N)$
S_{44}	$0.1313736 \times 10^1(Nm^2)$	S_{44}	$5.314632 \times 10^{-1}(Nm^2)$
S_{46}	$-9.225995 \times 10^{-1}(Nm^2)$	S_{46}	$9.894628 \times 10^{-2}(Nm^2)$
S_{55}	$1.1656606 \times 10^1(Nm^2)$	S_{55}	$2.634072 \times 10^2(Nm^2)$
S_{66}	$0.1454637 \times 10^1(Nm^2)$	S_{66}	$3.584220 \times 10^{-1}(Nm^2)$

3.2.1 Eigenvalue analysis

Eigenvalue analysis is performed for the three different cases. Table. 3.3 shows the natural frequency comparisons of Case 1 between the new beam element before being implemented in HAWC2 and after implementation, respectively. They are completely identical because they are using same shape functions and same number of elements. From this result, it may be concluded that the new beam element is successfully implemented into HAWC2.

Table. 3.4 shows the natural frequency comparisons between the other existing results and a HAWC2 computation. The HAWC2 result shows good agreement with [3] and [4], respectively.

Small discrepancies in Cases 2 and 3 of Table. 3.4 might occur due to converting the units from English to SI units and using different shape functions.

It is clear to see that flapwise bending-torsion, (S_{46}), and axial-edgewise deflections, (S_{13}), are coupled on the structure of Cases 2 and 3 from Table. 3.2. The coupling effects on the structure can be captured through the mode shape analyses. Fig. 3.3 shows the first 6 mode shapes of Case 2. From the mode 1, 3, 4, and 6 it is shown that the flap related modes (u_y and θ_x) are coupled with the torsion related mode (θ_z). Fig. 3.4 shows the first 6 mode shapes of Case 3. It is observed by mode 1, 2, 3, 5, and 6 that the flap related modes are also coupled with the torsion related mode.

From the above results of natural frequencies and mode shapes the new beam model can capture the physical behaviors of structural coupled characteristics.

An additional eigenvalue analysis is performed with Cases 2 and 3 in order to investigate physi-

Table 3.3. Natural frequency comparison of Case 1

Mode	New beam element only [Hz]	HAWC2 [Hz]
1	2.87262×10^{-3}	2.87262×10^{-3}
2	2.87262×10^{-3}	2.87262×10^{-3}
3	1.80466×10^{-2}	1.80466×10^{-2}
4	1.80466×10^{-2}	1.80466×10^{-2}
5	5.09409×10^{-2}	5.09409×10^{-2}
6	5.09409×10^{-2}	5.09409×10^{-2}

Table 3.4. Natural frequency comparison of Cases 2 and 3

Case 2			Case 3		
Mode	HAWC2 [Hz]	Ref.[3][Hz]	Mode	HAWC2 [Hz]	Ref.[4][Hz]
1 (flap-torsion)	52.5	52.6	1 (flap-torsion)	4.66	4.66
2 (edge)	209.7	209.8	2 (flap-torsion)	29.18	29.60
3 (flap-torsion)	326.1	326.3	3 (flap-torsion)	81.57	84.89
4 (flap-torsion)	899.3	899.8	4 (edge)	105.99	N/A
5 (edge)	1284.2	1284.9	5 (flap-torsion)	113.35	113.43
6 (flap-torsion)	1660.9	1661.3	6 (flap-torsion)	159.52	N/A

cal differences between isotropic and anisotropic structures by using the old version (i.e. before implementing the new beam model) and the new version (i.e. after implementing the new beam model) of HAWC2. In order to produce an isotropic structure case, the off-diagonal terms from the anisotropic structural property are removed, which does not offer equivalent conditions. However, these comparisons may be helpful for understanding the physical importance of the off-diagonal terms.

Table. 3.5 shows the natural frequency differences between the isotropic and the anisotropic

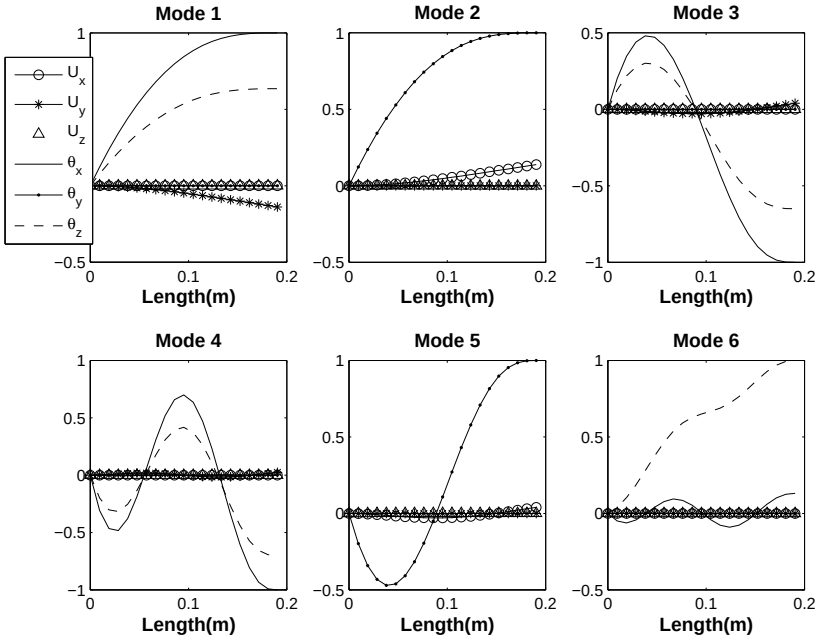

Figure 3.3. First 6 mode shapes of Case 2 with anisotropic properties

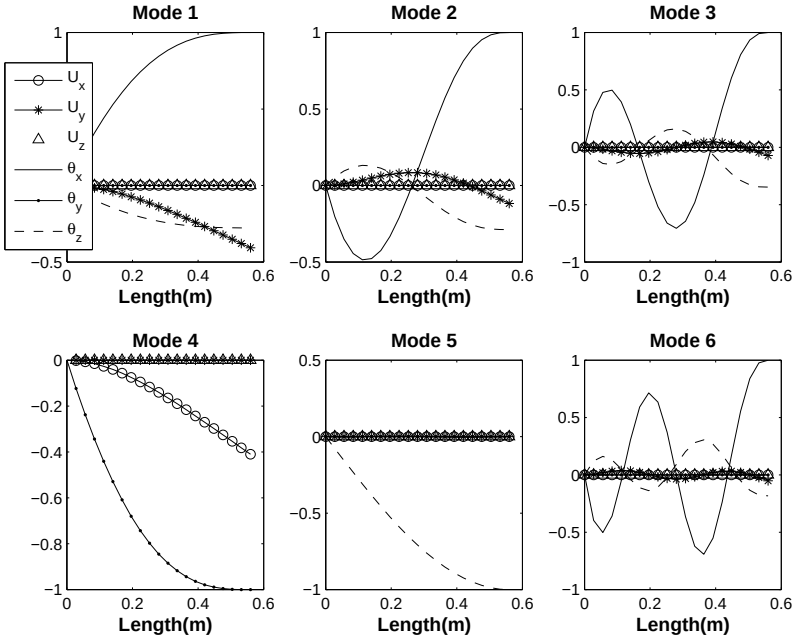

Figure 3.4. First 6 mode shapes of Case 3 with anisotropic properties

model of Cases 2 and 3. It is obvious that the obtained natural frequencies from isotropic model are overpredicted as compared with anisotropic's one. It is because the isotropic model does not have the abilities to capture the coupling effects.

Table 3.5. Natural frequency comparison of Cases 2 and 3

HAWC2 simulation of Case 2			
Mode	Anisotropic [Hz]	Mode	Isotropic [Hz]
1 (FT)	52.5	1 (F)	70.5
2 (E)	209.7	2 (E)	210.0
3 (FT)	326.1	3 (F)	436.1
4 (FT)	899.3	4 (F)	1196.6
5 (E)	1284.2	5 (E)	1296.5
6 (FT)	1660.9	6 (F)	1675.0
HAWC2 simulation of Case 3			
Mode	Anisotropic [Hz]	Mode	Isotropic [Hz]
1 (FT)	4.66	1 (F)	4.78
2 (FT)	29.18	2 (F)	29.97
3 (FT)	81.57	3 (F)	83.81
4 (E)	105.99	4 (E)	106.01
5 (FT)	113.35	5 (T)	113.34
6 (FT)	159.52	6 (F)	163.95

In Table. 3.5, FT is flap-torsion mode, E is edge mode, F is flap mode, and T is torsion mode. Fig. 3.5 and Fig. 3.6 show the mode shapes of Cases 2 and 3 with an isotropic structure, respectively. As expected no coupled modes are observed.

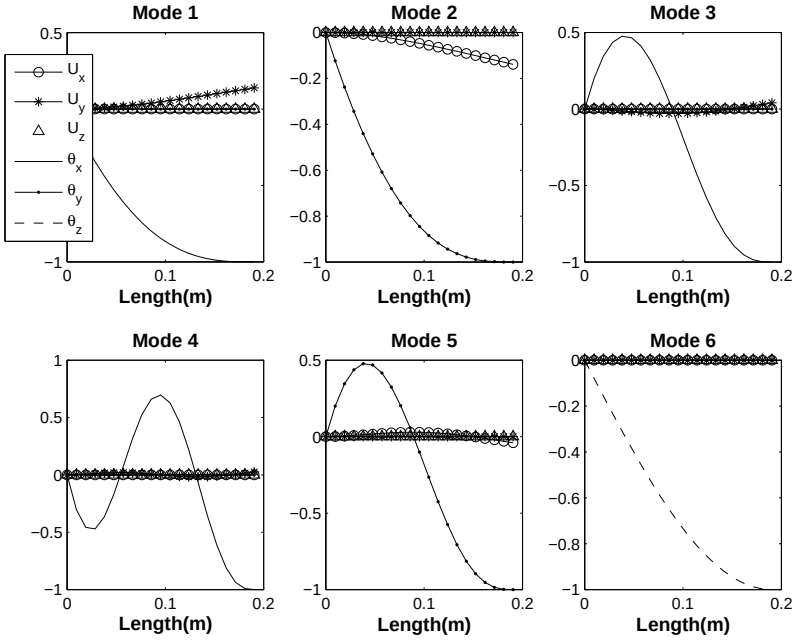

Figure 3.5. First 6 mode shapes of Case 2 with isotropic properties

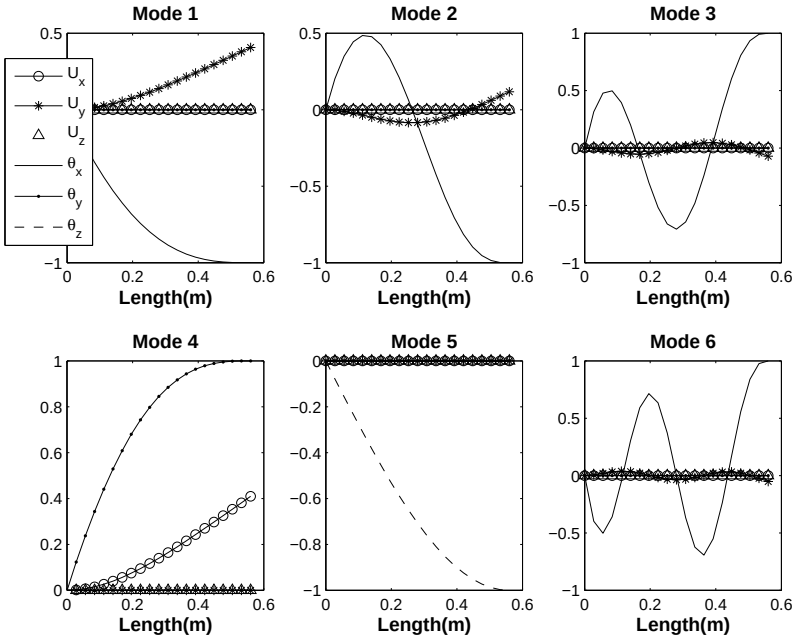

Figure 3.6. First 6 mode shapes of Case 3 with isotropic properties

3.2.2 Static analysis

A static analysis is performed with Cases 2 and 3. A cantilevered graphite-epoxy beam is considered. Fig. 3.7 shows a sketch of the cantilevered beam with static load and torsional moment. For the Case 2, $4.45N$ static load is applied. For the Case 3, $0.113Nm$ static torsional moment is applied.

The static deflections and rotations of Case 2 are presented in Fig. 3.8. In the figure, the dashed line and solid line represent anisotropic and isotropic results, respectively. As we have already

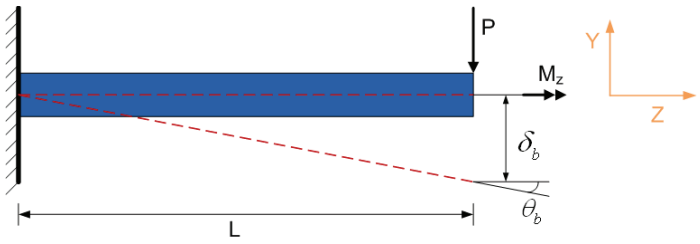

Figure 3.7. A sketch of the cantilevered graphite-epoxy beam

shown, flapwise bending-torsion and axial-edgewise deflection are coupled on the structure. Therefore, when the static load is applied to the flapwise direction not only additional flapwise deflection but also additional flapwise bending which also results in torsion is produced. From the results, the expected characteristics are observed with the new beam element while the isotropic model cannot capture the effects.

Fig. 3.9 shows a comparison of the static deflections and rotations of Case 3. This case has the same couplings as Case 2. Therefore, when the torsion is applied to the structure, not only additional torsion but also additional flapwise bending which also results in flapwise deflection should be captured. From the results the new beam element captures the expected physical behavior correctly while the isotropic model does not.

As we have investigated above there are differences between isotropic and anisotropic results from natural frequencies, mode shapes, static deflections, and static rotations. They are important parameters when designing wind turbines. In that sense, the anisotropic behavior should be included in the relevant aeroelastic numerical tool if the blades have structural couplings.

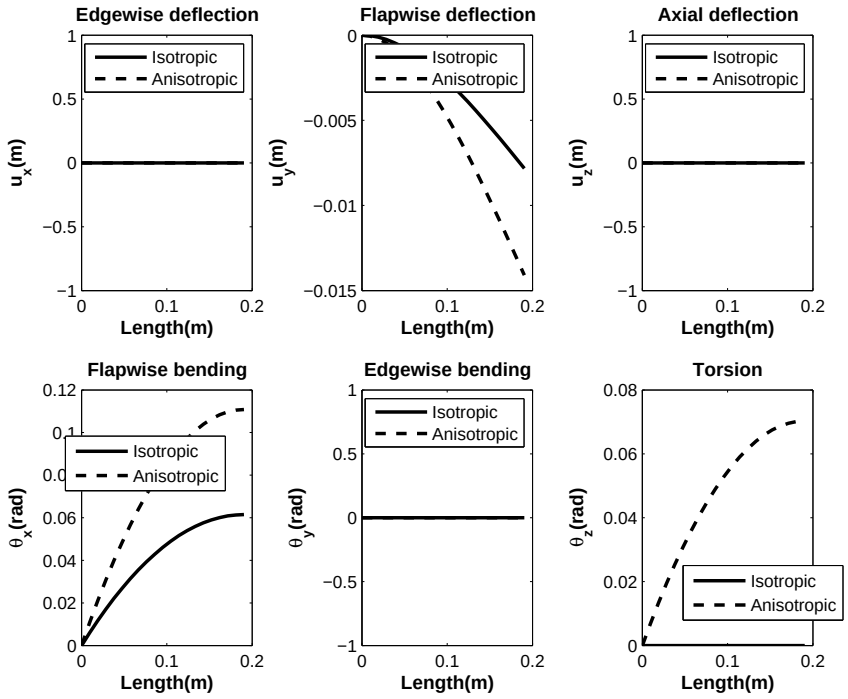

Figure 3.8. Differences of the displacements and rotations between anisotropic and isotropic properties for Case 2

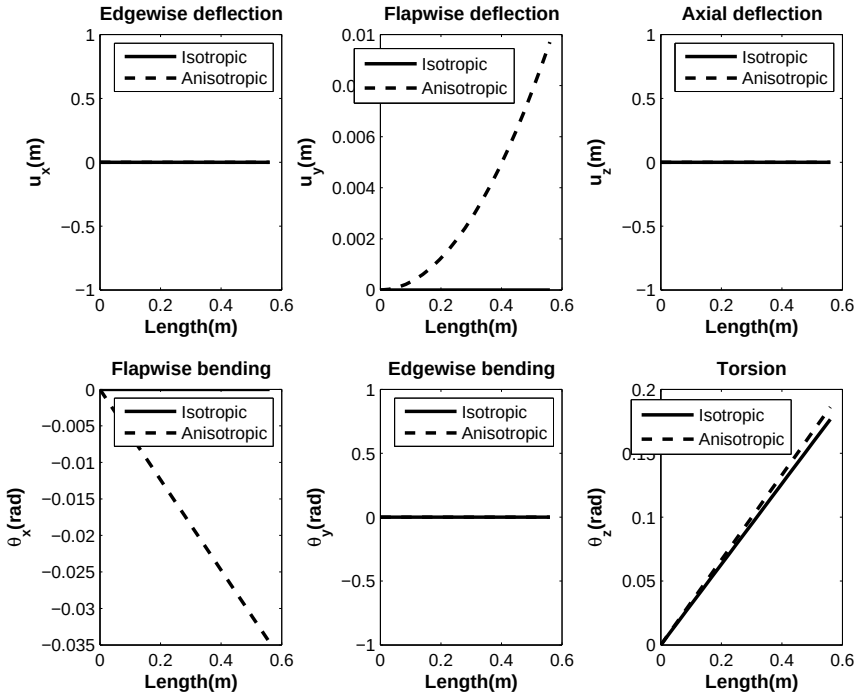

Figure 3.9. Differences of the displacements and rotations between anisotropic and isotropic properties for Case 3

3.2.3 A parametric study for a blade bending-torsion coupling effect

In this section a blade bending-torsion coupling effect is examined in order to investigate a load reduction potential by considering the structural couplings. For this study, the NREL 5MW Reference Wind Turbine (RWT) is considered [6]. To produce the 6 by 6 cross sectional stiffness matrix the same values used for the old version of HAWC2 are applied. Eq. 3.3 shows how the new cross sectional values for the new beam element are obtained with the existing sectional data.

$$S_{11} = k_x GA, \quad S_{22} = k_y GA, \quad S_{33} = EA, \quad S_{44} = EI_x, \quad S_{55} = EI_y, \quad S_{66} = GJ \tag{3.3}$$

where k_x and k_y represent shear factor for x and y direction, G and E represent shear and elastic modulus, A represents cross sectional area, I_x, I_y, and J represent area moment of inertia with respect to x- and y- axis, and torsional stiffness constant, respectively.
Table. 3.6 shows the natural frequency comparison of 5MW RWT using the old version (i.e. before implementing the new beam model) and the new version (i.e. after implementing the new beam model) of HAWC2. All frequencies obtained show good agreement.
Structural couplings are arbitrarily assigned based on Eq. 3.4 [7]. This equation shows that diagonal stiffness terms are kept its own values while coupling effects (off-diagonal terms) are assigned. In this study only a blade flapwise bending-torsion coupling is considered.

$$S = \begin{bmatrix} S_{11} & 0 & 0 & 0 & 0 & 0 \\ 0 & S_{22} & 0 & 0 & 0 & 0 \\ 0 & 0 & S_{33} & 0 & 0 & 0 \\ 0 & 0 & 0 & S_{44} & 0 & S_{BT} \\ 0 & 0 & 0 & 0 & S_{55} & 0 \\ 0 & 0 & 0 & S_{BT} & 0 & S_{66} \end{bmatrix} \tag{3.4}$$

where S_{BT} illustrates the coupling term represented as

$$S_{BT} = \alpha\sqrt{EI_x \times GJ}, \qquad -1 < \alpha < 1 \tag{3.5}$$

Table 3.6. 5MW RWT Natural frequency comparison

Whole turbine natural frequency			Blade natural frequency		
Mode	Old version	New version	Mode	Old version	New version
1	$2.99499E-01$	$2.99489E-01$	1	$6.42915E-01$	$6.42126E-01$
2	$3.01766E-01$	$3.01745E-01$	2	$9.70733E-01$	$9.70323E-01$
3	$5.88521E-01$	$5.88366E-01$	3	$1.74780E+00$	$1.74320E+00$
4	$6.10445E-01$	$6.09750E-01$	4	$2.81604E+00$	$2.81413E+00$
5	$6.36840E-01$	$6.36079E-01$	5	$3.52602E+00$	$3.52027E+00$
6	$6.67130E-01$	$6.66403E-01$	6	$4.74572E+00$	$4.74129E+00$
7	$9.66966E-01$	$9.66564E-01$	7	$5.41973E+00$	$5.41629E+00$
8	$9.78581E-01$	$9.78093E-01$	8	$6.62254E+00$	$6.61381E+00$
9	$1.58169E+00$	$1.57891E+00$	9	$7.41935E+00$	$7.42257E+00$
10	$1.69090E+00$	$1.68696E+00$	10	$8.24123E+00$	$8.21291E+00$

The amount of couplings is assigned by α. A bending-torsion coupling that is 1m flapwise bending deflection (toward tower) resulting in approximately 0.3deg twist (toward feather) at the blade tip is considered: $\alpha = -0.05$. Fig. 3.10 shows the static deflections and rotations of considered example.

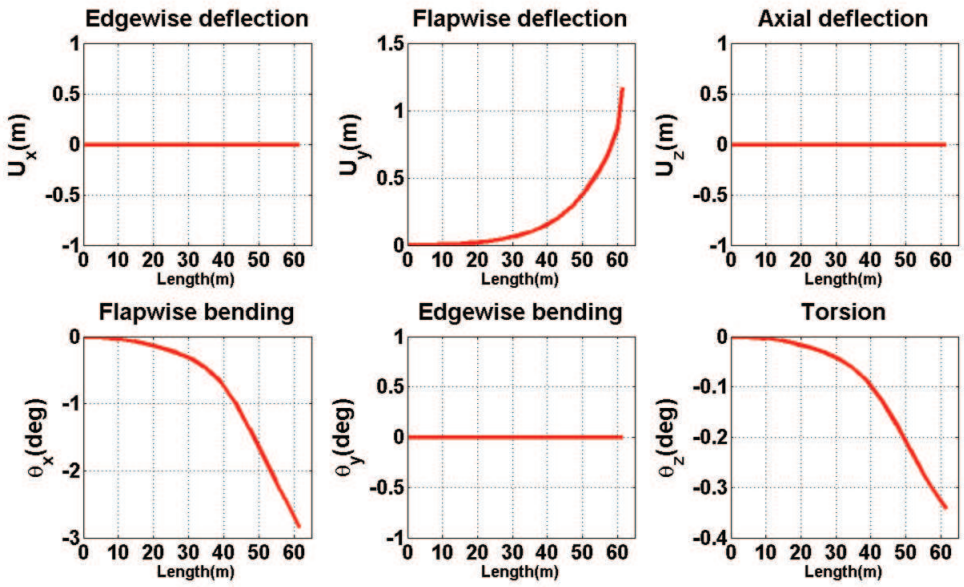

Figure 3.10. The static deflections and rotations of the coupled beam when $\alpha = -0.05$

A single wind speed case, 7 m/s, is considered with 22% turbulence intensity. Fig. 3.11 shows the blade equivalent fatigue loads and maximum blade tip deflection. The blade flapwise, edgewise, and torsional equivalent fatigue loads, and the blade maximum tip deflection are reduced up to approximately 2.5%, 0.5%, 10%, and 8%, respectively without losing mechanical power production (Fig. 3.12).

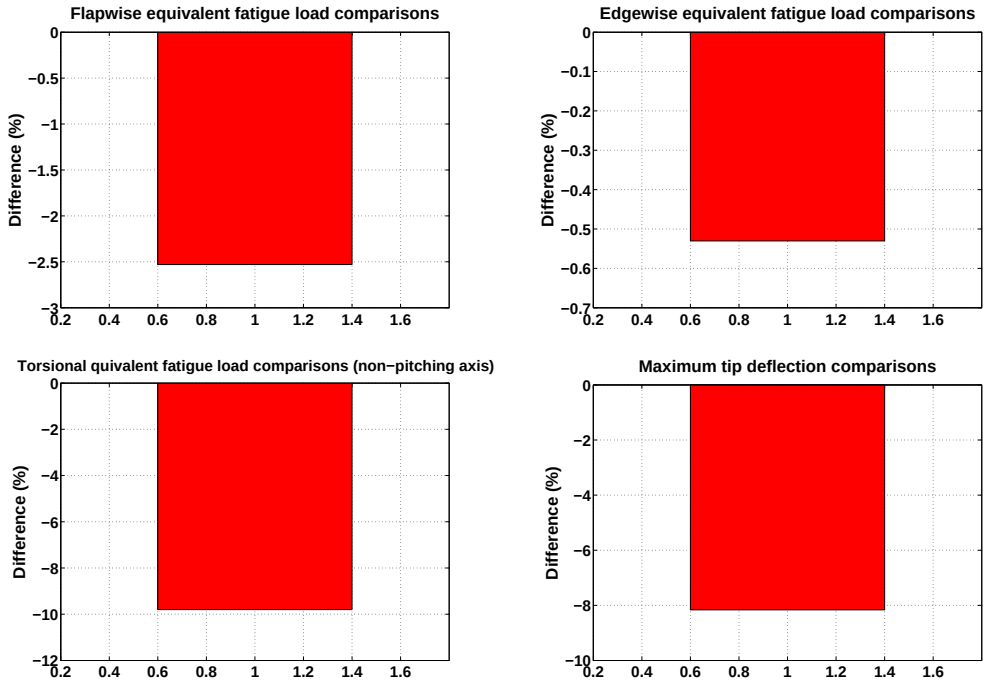

Figure 3.11. Equivalent fatigue loads and maximum tip deflection when $\alpha = -0.05$

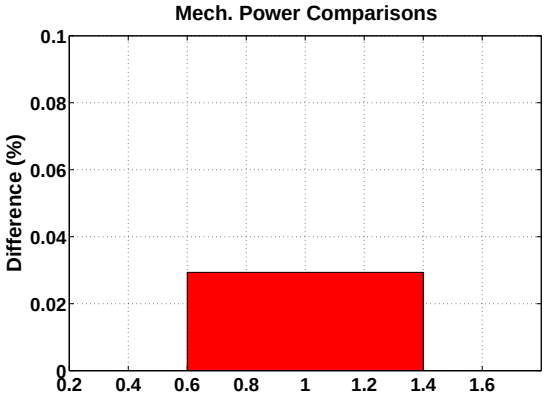

Figure 3.12. Mechanical power when $\alpha = -0.05$

3.3 Conclusion

In this chapter a new beam element, which is able to consider the anisotropic behaviors, is developed and implemented into HAWC2. Validations for the beam model are performed with 3 different cases. The eigenvalue and the static analyses are performed. From the results the anisotropic characteristics show different behaviors compared to the isotropic ones. A parametric study to investigate a structural coupling has been performed with the 5MW RWT. Only a blade flapwise bending-torsion coupling is considered. When the structural coupling which produces 0.3deg twist at the blade tip toward feather for a 1m flapwise tip deflection towards the tower is considered the blade flapwise, edgewise, and torsional root equivalent fatigue loads are reduced up to 2.5%, 0.5%, and 10% respectively. Also, blade tip clearance is improved approximately 8% without power reduction. This results show a potential to improve turbine performance by considering a small amount of structural coupling on the structure. This additional effect may be used for developing new types of blades such as blades with less pitch

control.

References

[1] M. Luczak, S. Manzato, B. Peeters, K. Branner, P. Berring, and M. Kahsin. Dynamic investigation of twist-bend coupling in a wind turbine blade. *Journal of Theoretical and Applied Mechanics*, 49(3), 2011.

[2] T. Kim, K. Branner, and A. M. Hansen. Developing anisotropic beam element for design of composite wind turbine blades. In *18th International Conference on Composite Materials*, Korea, Aug. 21-26 2011.

[3] W. Yu. Efficient high-fidelity simulation of multi-body systems with composite dimensionally reducible components. *Journal of the American Helicopter Society*, 52(1):49–57, 2007.

[4] D.H. Hodges, A.R. Atilgan, M.V. Fulton, and L.W. Rehfield. Free-vibration anaysis of composite beams. *Journal of the American Helicopter Society*, 36(3):36–47, 1991.

[5] J. P. Blasques and B. Lazarov. *A Cross Section Analysis Tool for Anisotropic and Inhomogeneous Sections of Arbitrary Geometry*. Risø-R-1785 (EN), 2011.

[6] J. Jonkman, S. Butterfield, W. Musial, and G. Scott. Definition of a 5-MW reference wind turbine for offshore system development. Technical report, NREL, 2009.

[7] D.W. Lobitz and P.S. Veers. Aeroelastic behaviors of twist-coupled hawt blades. In *In ASME/AIAA Wind Energy Symposium*, Reno, NV, 1998.

4 Detailed and reduced models of dynamic mooring system

Author: Anders M. Hansen and Bjarne S. Kallesøe

4.1 Introduction

The first part of this chapter deals with the effect of different levels of details in mooring line model on wind turbine loads in hydro-aero-elastic simulations of floating wind turbines. In wind turbine load simulations, it is common to use a quasi-static approach in mooring line models. In this work, a dynamic mooring line model is developed and coupled to a state of the art hydro-aero-elastic wind turbine simulation code. The effect of the dynamic mooring line modeling on the wind turbine loads are analyzed and compared to results from a quasi-static modeling approach. It is found that the dynamic mooring line model doesn't affect the blade extreme or fatigue loads, nor does it affect the tower extreme loads, but the tower bottom bending equivalent load is reduced by 5-20 % in some load cases and the equivalent lifetime load is reduced by 5-10 %. The reductions indicate that the dynamics off the mooring system is significant and should be included in the simulation model of the floating wind turbine to get the right design loads.

The second part of this chapter describes a method that can be used to derive an equivalent model as a set of first order ODEs which captures the dynamics of mooring systems.

4.2 Detailed model

The offshore wind turbine development has focused on bottom fixed concepts, but since the shallow water sites are limited and many countries only have deep waters, an increasing interest has been towards floating wind turbine concepts. For instance Statoil has launched the worlds first full scale floating turbine HYWIND off the coastline of Norway [1]. Floating turbines are complex and relatively flexible structures, where all subcomponents depend on each other. For instance, the turbine loads depend on the motion of the floating platform, and the platform motion depends on the aerodynamic loading and control of the turbine. The mooring system is an integrated component for the overall dynamic response of the full wind turbine structure. Compared to other offshore installations, such as oil rigs, the low profit from wind turbines combined with a low risk (small human and environmental threat), floating turbines will be designed in a low cost framework and with smaller safety factors, all leading to more flexible and dynamic structures.

In floating wind turbine simulations, it is common to used quasi-static mooring line models [2]. This work will look into the validity of a quasi-static mooring line model approach and analyze if more complex mooring line models will affect the wind turbine loads.

The comprehensive state of the art hydro-aero-elastic time simulation code for wind turbines HAWC2 [3] is extended with a dynamic mooring line model. HAWC2 is an aeroelastic code for computing loads for onshore, bottom mounted and floating offshore wind turbines. The code is based on a multi-body formulation, where each body is a linear beam. The wave loading on the offshore turbine is computed by Morison formula. The code has been used for load computations of several floating turbines, e.g. the HYWIND turbine, but the mooring forces has been based on quasi-static lookup tables.

The developed dynamic mooring line model is based on a cable element with hydrodynamic drag, added mass, and buoyancy forces and a nonlinear spring stiffness modelling the bottom contact. The quasi-static response of the mooring model is validated against the code MIMOSA from MARINTEK showing good agreement.

The dynamic mooring line model in HAWC2 enables a fully coupled analysis of the influence of different mooring line models on wind turbine loads. The setup is used to analyse the effect of mooring models on a floating turbine of the spar buoy type (HYWIND type). It is found that the dynamic mooring line modeling doesn't affect the blade extreme or fatigue loads, nor does it affect the tower extreme loads, but the tower bottom bending equivalent load is reduced by 5-20 % in some load cases and the equivalent lifetime load is reduced by 5-10 %.

4.2.1 Wind Turbine Modeling

The hydro-aero-elastic simulations are based on the HAWC2 code. The HAWC2 code is intended for calculating wind turbine response in time domain [4].

The structural part of the code is based on a multi-body formulation as described in [5] using the floating frame of reference method. In this formulation, the wind turbine main structures are subdivided into a number of bodies where each body is an assembly of Timoshenko beam elements. The bodies representing the mechanical parts of the turbine are connected by joints also referred to as constraints. The constraints are formulated as algebraic equations that impose limitations on the bodies' motion. The structural model is general, but in its simplest form a turbine is modeled using one body for the tower, one for the nacelle and one for each blade. The capability of modeling floating turbines is inherent in the general multi-body formulation, which does not need to have the modeled structure attached to the global frame.

The aerodynamic part of the code is based on the blade element momentum theory, but extended from the classic approach to handle dynamic inflow, dynamic stall, skew inflow, shear effects on the induction and effects from large deflections. The dynamic stall model is a modified Beddoes-Leishmann model that includes the effects of shed vorticity from the trailing edge (Theodorsen theory), as well as the effects of stall separation lag caused by an instationary trailing edge separation point [6].

The stochastic wind is generated outside the HAWC2 code. The turbulence generator is the Mann model [7], which is a full 3D correlated turbulence flow field. Tower shadow effects are also a part of the wind module, as it changes the wind conditions locally near the tower.

The hydrodynamic loads are based on the, within offshore technology well-known, Morisons equation. The wave kinematics are not calculated within the HAWC2 code but provided externally through a defined DLL (Dynamic Link Library) interface, where the present open source DLL includes regular and irregular Airy waves.

Buoyancy loads are based on axial dynamic pressures inserted as concentrated forces on end nodes and distributed forces over conical sections. A perpendicular force contribution is distributed on angled elements and a restoring moment is distributed on conical sections.

The wind turbine controllers are implemented in external DLL's and coupled to the code by a defined DLL interface.

The HAWC2 code is a state of the art hydro-aero-elastic code and has been used for simulating loads on a variety of wind turbines and wind turbine concepts. The code has participated in the code-to-code comparison project OC3 [8] with very good results.

The wind turbine used in this work is a conventional MW size upwind variable speed pitch regulated turbine. The turbine is controlled by Risø's baseline PID controller [4]. The controller is modified as discussed in Larsen et al. [4] to handle the inherent controller instability of pitch regulated floating turbines.

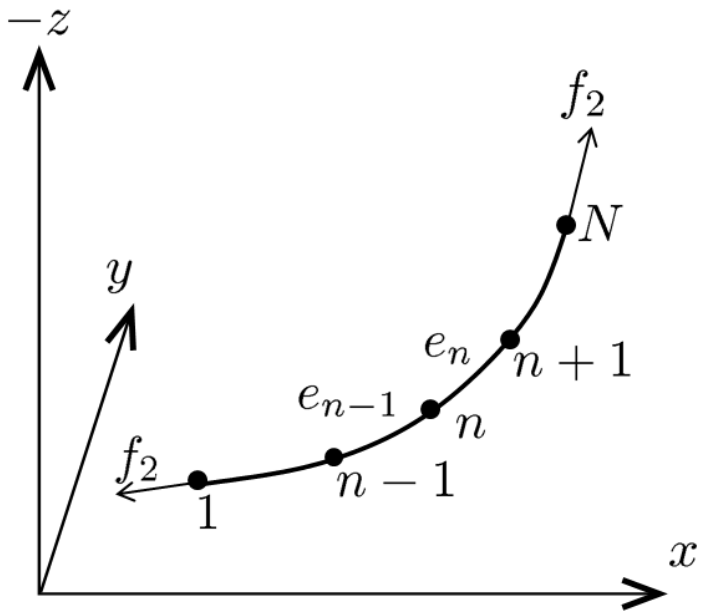

Figure 4.1. One section of the flexible mooring line with uniform properties divided into N equal sized elements.

4.2.2 Mooring Line Modeling

Quasi-Static Modeling Approach
The quasi-static mooring line model in HAWC2 is based on pre-computed results from the MIMOSA code by MARINTEK. The quasi-static mooring line stiffness characteristics are tabulated as positions of the float versus restoring forces from the mooring system. HAWC2 uses these data for looking up the force from the mooring system that should be applied in each time step depending on the turbine position.

Dynamic Modeling Approach
The flexible mooring line is model by a general cable element formulation, similar to e.g. [9].

Figure 4.1 shows one section of the flexible line divided into N equal sized elements. The length of one loaded element is given by

$$L_n = \sqrt{(x_{n-1}-x_n)^2 + (y_{n-1}-y_n)^2 + (z_{n-1}-z_n)^2} \tag{4.1}$$

and the Green strain measure can then be found by

$$\varepsilon_G = \frac{L_n^2 - L_{n,0}^2}{2L_{n,0}^2} \tag{4.2}$$

where L_0 is the length of the unloaded element. Having this strain in the element the longitudinal force in the element can be found by

$$f = EA\varepsilon_G \tag{4.3}$$

where E is Young's modulus and A is the cross section area. The element stiffness matrix can then be formulated as

$$K_e = f/L_n \begin{bmatrix} 1 & 0 & 0 & -1 & 0 & 0 \\ 0 & 1 & 0 & 0 & -1 & 0 \\ 0 & 0 & 1 & 0 & 0 & -1 \\ -1 & 0 & 0 & 1 & 0 & 0 \\ 0 & -1 & 0 & 0 & 1 & 0 \\ 0 & 0 & -1 & 0 & 0 & 1 \end{bmatrix} \tag{4.4}$$

which is nonlinear since $K_e = K_e(\mathbf{x}_{n-1}, \mathbf{x}_n)$ where $\mathbf{x}_n = [x_n, y_x, z_n]^T$. Inserting this element stiffness matrix in the equations of motion

$$K_e \begin{bmatrix} \mathbf{x}_n \\ \mathbf{x}_{n+1} \end{bmatrix} = \begin{bmatrix} -f\delta \\ f\delta \end{bmatrix}, \quad \delta = \begin{bmatrix} \frac{x_{n+1}-x_n}{L_n} \\ \frac{y_{n+1}-y_n}{L_n} \\ \frac{z_{n+1}-z_n}{L_n} \end{bmatrix} \tag{4.5}$$

so it is seen that it gives the line force projected onto the (x,y,z)-directions.

The equations of motion for one line segment becomes

$$\mathbf{M}\ddot{\mathbf{x}}(t) + \mathbf{K}(\mathbf{x})\mathbf{x}(t) - \mathbf{F}_{gravity} - \mathbf{F}_{buoyancy} - \mathbf{F}_{drag}(\mathbf{x}, \dot{\mathbf{x}}) = \mathbf{f} \tag{4.6}$$

where the mass matrix $\mathbf{M}$ is constant in time and given by integrating the distributed mass of each element. The stiffness matrix $\mathbf{K}(\mathbf{x})$ is a collection of the element stiffness matrices (4.5) and depends on the deflection and orientation of the element. The gravity force $\mathbf{F}_{gravity}$ and buoyancy force $\mathbf{F}_{buoyancy}$ are both computed initially and applied in the downwards and upwards directions, respectively. A perpendicular and a longitudinal linear viscous drag force ($\mathbf{F}_{drag}(\mathbf{x}, \dot{\mathbf{x}})$) is applied to the element. The drag forces are based on drag coefficients multiplied by the perpendicular and longitudinal speed of the element, respectively, and projected onto the (x,y,z)-directions. The drag force depends both on the element velocity and orientation. There are no wave loading on the elements, but since the mooring is connected to the main structure at 54 m depth on the particular turbine model, the wave loading is assumed not to be important.

The bottom contact is modeled by a vertical non-liner stiffness applied to each node

$$f_z = \begin{cases} 0 & \text{if } z > z_0 \\ K\left((z-z_0)^2 + (z-z_0)\right) & \text{if } z \leq z_0 \end{cases} \tag{4.7}$$

where f_z is the vertical reaction force from the sea bottom, z is the vertical position of the node, z_0 is the sea bottom, and K is a sea bottom stiffness.

This element formulation only holds for cables with uniform properties, so each section of different cable type (chain, synthetic rope etc.) is modeled as a separate body and connected by ball joint constraint[1] in HAWC2's multi-body formulation.

Point masses are implemented with both linear and quadratic viscous damping terms to model clump masses and drag buoys.

As an example of using the model, a mooring system consisting of an anchor, a chain section and a fiber rope section will be modeled by one body with the chain properties and one body with the fiber rope properties. The chain body will be connected by a ball joint constrain to the anchor and the fibre rope body in its first and last node, respectively, and the fiber rope body will be connected to the main structure by a ball joint constrain at its last node. The anchor is assumed to be fixed in space.

4.2.3 The mooring system

The mooring system consists of three catenary lines with a concentrated mass on each of the lines for additional stiffness. The mooring system is similar to the one used in the OC3 project[8]. The mooring system has two delta lines splitting each catenary line into two connection points on the float. In the quasi-static modeling framework, these delta lines are neglected and the main line is extended and connected directly to the float[2]. In the dynamic modeling frame work, the delta line configuration is straight forward to include, and two model versions are constructed; one where the main line is extended and connected to the tower resembling the quasi-static model (M1) and one where the delta lines are included in the model resembling the true mooring system (M2). The quasi-static mooring line characteristic from the MIMOSA

[1] A ball joint constraint fixes two nodes relative to each other in translations but they a free in relative rotations.

[2] This simplified model is the modeling approach used in the OC3 project among other studies of floating turbine.

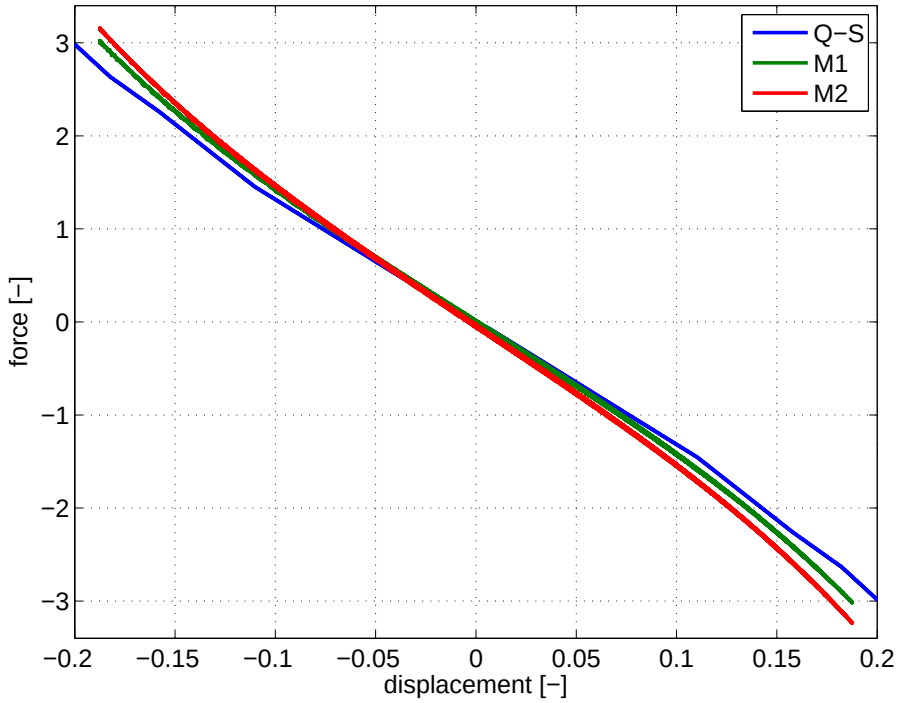

Figure 4.2. Results for the mooring system at very slow oscillations ($T_p = 400$ s) compared to quasi-static results from MIMOSA. The restoring force and displacement are normalized by the rated aerodynamic thrust and rotor diameter of the particular turbine.

program has only been available for the simplified model, so the delta line configuration (M2) cannot be compared directly to quasi-static results.

The line segment modeling the two delta lines in the M1 model is given the mass and drag properties as the sum of mass and drag coefficients from the two delta lines in the M2 model. The mooring line properties are taken from a mooring system of a test turbine, and is therefore confidential.

4.2.4 Mooring Line Response

In this section, the dynamic mooring system model is validated against quasi-static results, showing good results. Furthermore, the effect of including the dynamic model is shown and discussed. All results in this section are based on measuring the horizontal mooring force for prescribed harmonic oscillating motion of the mooring-turbine connection point.

Figure (4.2) shows force response to slow motion of the two dynamic mooring line models compared to the quasi-static results from MIMOSA. The restoring force and displacement is normalized by the rated aerodynamic thrust and rotor diameter of the particular turbine. All models are seen to agree very well. Furthermore, it is seen that to balance the rated aerodynamic thrust from the turbine the float will be pushed around 0.1 rotor diameters down wind. Figure (4.3) shows the restoring force for a higher oscillation frequency. The drag forces in the dynamic models (M1 and M2) are seen to open the loop and introduce some hysteresis in the oscillations.

The yaw stiffness are different for the two model versions (M1 and M2) where the delta lines of the M2 model increase the quasi-static yaw stiffness considerably (Figure (4.4)). Notice that the curve for M2 at high angles are parallel to the M1 single line model because the delta lines collapse into one line at these high angles.

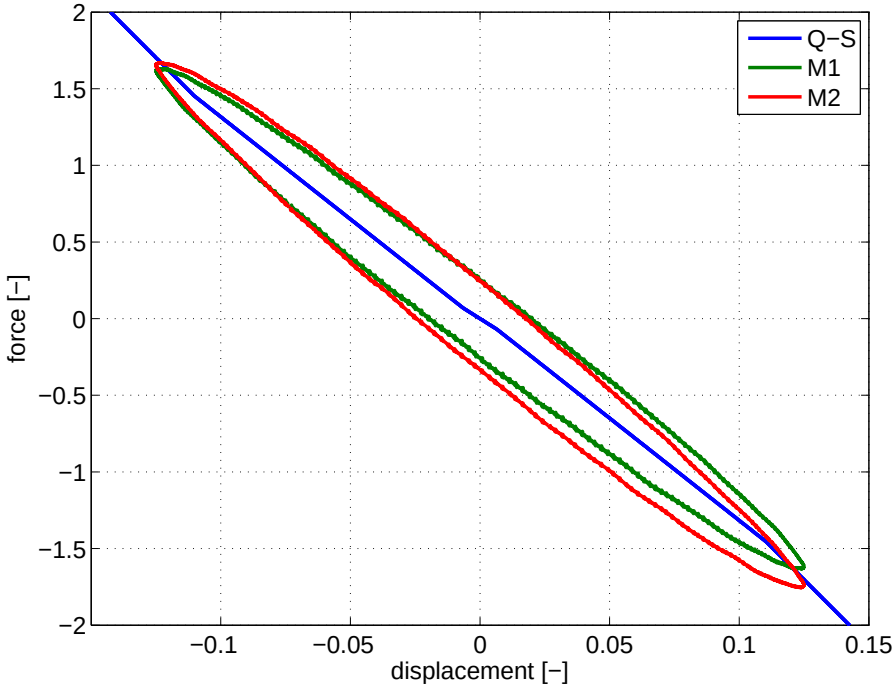

Figure 4.3. Results for the mooring system at $T_p = 50$ s oscillations compared to quasi-static results from MIMOSA. The loops follows an anticlockwise direction. The mooring restoring force is normalized by the rated aerodynamic thrust for the particular turbine and the displacement by the rotor diameter.

Ws	[m/s]	5	7	9	11	13
Ti	[-]	0.2244	0.1860	0.1647	0.1511	0.1417
H_s	[m]	1.94	2.26	2.65	3.11	3.61
T_p	[s]	3.82	3.98	4.20	4.49	4.85
time	[h]	22460	26068	25102	23340	18958
Ws	[m/s]	15	17	19	21	23
Ti	[-]	0.1348	0.1295	0.1254	0.1220	0.1192
H_s	[m]	4.14	4.70	5.25	5.79	6.31
T_p	[s]	5.26	5.73	6.24	6.77	7.30
time	[h]	14123	9708	6182	3657	2014

Table 4.1. Wind speed, turbulence intensity, significant wave hight, wave period and the number of hours at the wind speed in the life time for the load cases used in the hydro-aero-elastic simulations.

4.2.5 Hydro-aero-elastic response

This section deals with the effect of the different mooring model complexity on the turbine loads. The full mooring system is applied to a floating wind turbine in hydro-aero-elastic simulations at different operational conditions. Table 4.1 shows the load cases used in this work. The wave fields are irregular and based on Jonswap spectrum with the significant wave height and period given in table 4.1. The wind and wave directions are assumed to coincide. Each load case is simulated six times with different realizations of wind and wave fields. Each simulation is 1200 seconds of which the first 300 seconds is discarded to remove initial transients leaving 15 minuets for analysis. The same six wind and wave fields for each wind speed are used for each model, such that results can be compared directly.

To analyze the extreme loads the maximum value for the five sensors (Flapwise and edgewise blade root bending, and longitudinal and lateral tower bottom bending[3] and yaw moments)

[3]Flapwise and edgewise blade motion is out of and in rotor plan motion, respectively. Tower longitudinal and lateral motion is in the wind direction and perpendicular to the wind direction, respectively.

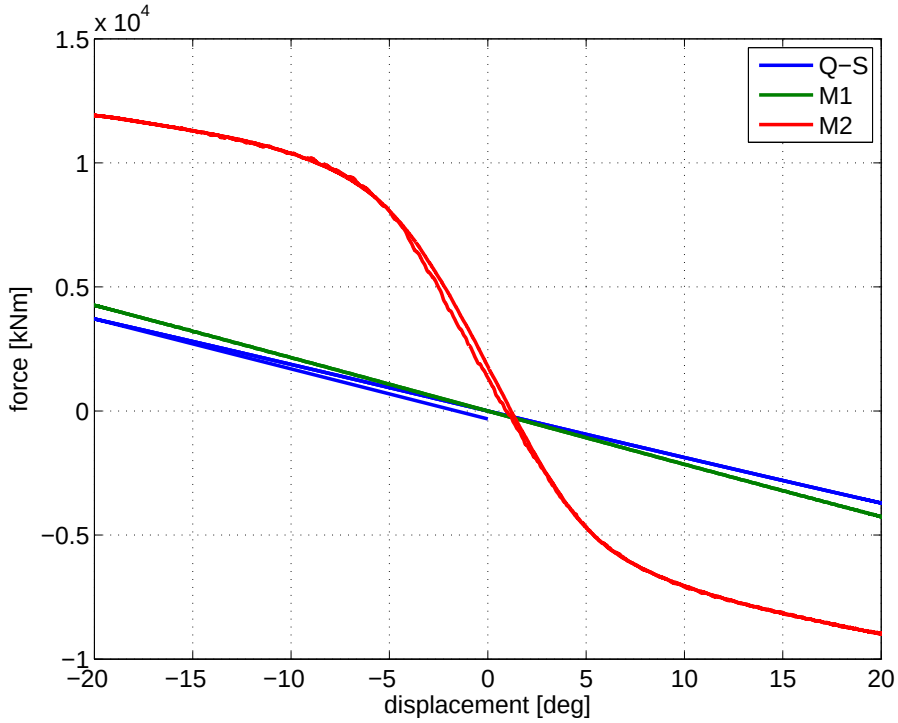

Figure 4.4. Results for the full mooring system at $T_p = 200$ s yaw oscillating with 20 deg amplitude compared to quasi-static results from MIMOSA.

are extracted from each simulation. All results from each wind speed are normalized with respect to the corresponding results from the quasi-static model. The mean value for the different wind and wave realizations, for each wind speed and each model, are computed alongside the standard deviation between the different realizations. Figure 4.5 and 4.6 shows these relative extreme loads and standard deviations for blade root bending moments and tower bottom bending moments, respectively. For the blade loads, longitudinal tower and yaw loads, the variations between models are seen to be less than the variation between the different wind and wave realizations with the same model, so the mooring model does not affect these loads. The lateral tower bending loads decrease for the M2 model (dynamic mooring line with delta lines), but the lateral bending moment is two to four times smaller than the longitudinal, so the decrease in extreme lateral tower bending does not affect the over all tower load, since it is the longitudinal load that is design given. The reason for the decrease in the extreme lateral tower loads for the M2 model, is that the delta lines increases the yaw stiffness, and therefore the down wind component contributing to the lateral tower loads is less, resulting in reduced lateral tower bending loads.

The effect of the mooring line modeling on the turbine fatigue loads is measured by computing the equivalent load for the same sensors as used in the extreme load analysis above. The equivalent load are computed for each time series and the mean and standard deviations for each load cases and model are computed and normalized with respect to the quasi-static results. Figure 4.7 and 4.8 shows these relative equivalent loads and standard deviations for blade root bending moments and tower bottom bending moments, respectively. The blade fatigue loads are not affected by the mooring line modeling. The longitudinal tower bottom equivalent bending moment is seen to be reduced by around 10 % for the low wind speeds and the lateral tower bottom equivalent bending moment is reduced by around 20 % for intermediate wind speeds.

To evaluate what these changes in equivalent loads account for in the turbines lifetime, the lifetime equivalent loads are computed based on the number of operating hours given in Table 4.1. Table 4.2 shows the lifetime equivalent loads normalized by the value of the loads for the quasi-static model. It is seen that the longitudinal and lateral tower load are reduced by around

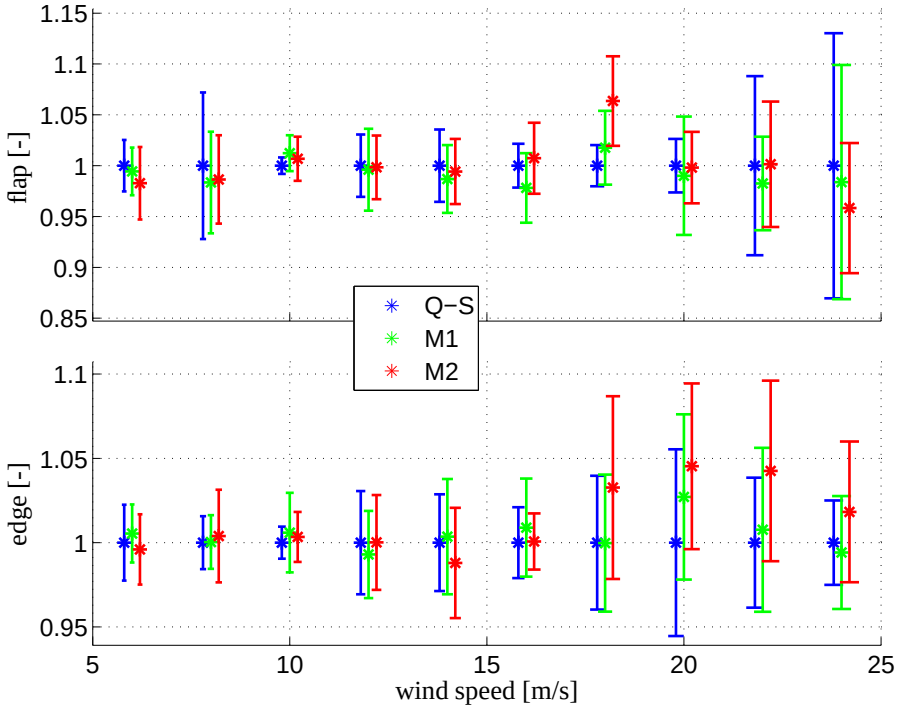

Figure 4.5. Blade extreme loads; top and bottom plots show extreme flapwise and edgewise blade root bending moments, respectively. For each wind speed and each model six simulations with different realization of wind and wave filed are conducted. All results are normalized by the quasi-static results at the given wind speed. The figure shows the mean value of the six different simulations with each model and the standard deviation between the simulations.

model	blade		tower		
	flap	edge	long.	late.	yaw
Q-S	1	1	1	1	1
M1	0.97	1.0	0.95	0.89	0.99
M2	0.97	1.0	0.94	0.83	0.99

Table 4.2. Lifetime equivalent load relative to the quasi-static results.

5 % and 10 %, respectively, while all other loads stays almost constant.

4.3 Reduced model

The number of DOFs for an entire mooring system is large compared to the rest of the wind turbine model. It is therefore desirable to reduce the number of DOFs and only retain a minimum number of DOFs necessary to describe the dynamic response of the mooring system of interest, i.e. in the frequency range of interest. Such a procedure has been developed and tested and the procedure is described next.

In brief, the procedure uses the simulated response from simulations of the full mooring system in HAWC2 to identify a reduced set of 1st order ODEs which can then be imported by other software models, e.g. HAWCStab2, HAWC2 itself, or others. The steps in the procedure are as follows:

- Simulate the response of the system to obtain a set of simultaneous inputs and outputs. In the present example, the movement of the interface node is prescribed and the reaction force in the same node is captured from the simulation.

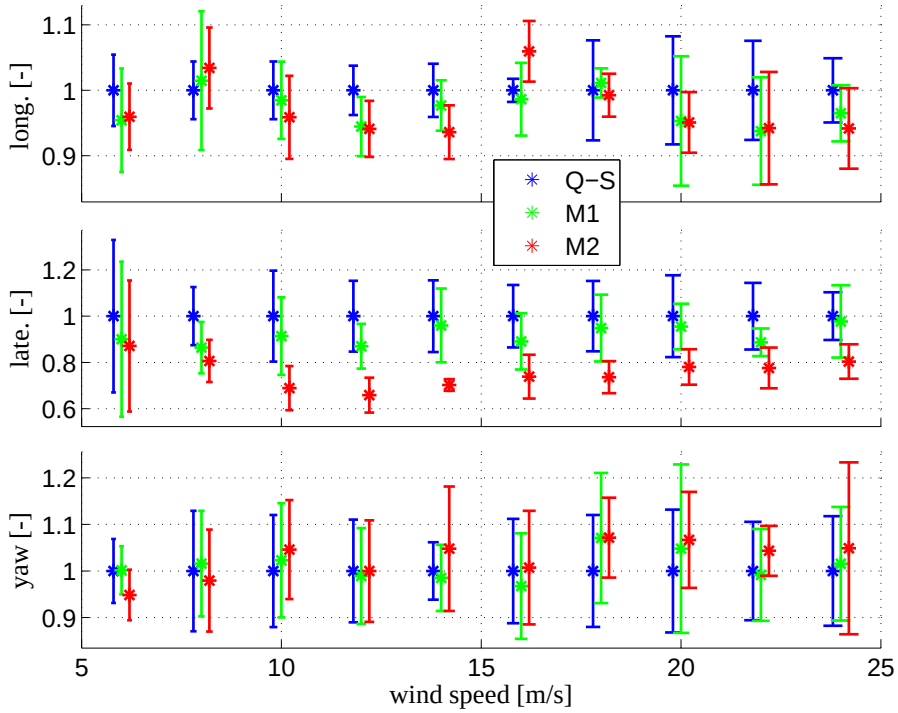

Figure 4.6. Tower extreme loads; from the top the plots show longitudinal, lateral and yaw tower bottom extreme bending moments, respectively. For each wind speed and each model six simulations with different realization of wind and wave filed are conducted. All results are normalized by the quasi-static results at the given wind speed. The figure shows the mean value of the six different simulations with each model and the standard deviation between the simulations.

- A linear state-space model is identified based on the simulated input/output by using an identification routine in MATLAB (*n4sid* or *pem*)
- The identified state-space model (which is in discrete time format) is transformed into a continuous time state-space model.
- A modal reduction of the full continuous time state-space model is made. Here the frequency limit where the resulting model is valid is chosen.
- Finally, a state variable transformation is made which firstly introduces the output state variables as direct state variables in the ODEs, and secondly makes the final ODEs work conjugate to the input/output definition.

Through the rest of this section an example is shown which demonstrates each step in the procedure. The chosen example focuses on a realistic mooring system for a floating wind turbine, and the aim is to derive a simplified dynamic model describing the relation between force and displacement of the interface point between mooring system and floating foundation.

The first step of the procedure is to obtain a time series of interrelated force and displacement. The full mooring system is modelled in HAWC2 and the interface point is forced to move in such a way that the frequency spectrum of the displacement have sufficient contents in the frequency range of interest. In the present case the displacement signal is derived by filtering random noise through a second order low pass filter. The resulting time series of interrelated force and displacement at the interface is shown in Figure (4.9). Note that in this (qualitative) example the force and displacement have been normalised by their maximum values.

The transfer function between displacement and force can de estimated directly from the time series in Figure (4.9), see Figure (4.10) titled ”Raw data”. The upper plot in Figure (4.10) shows

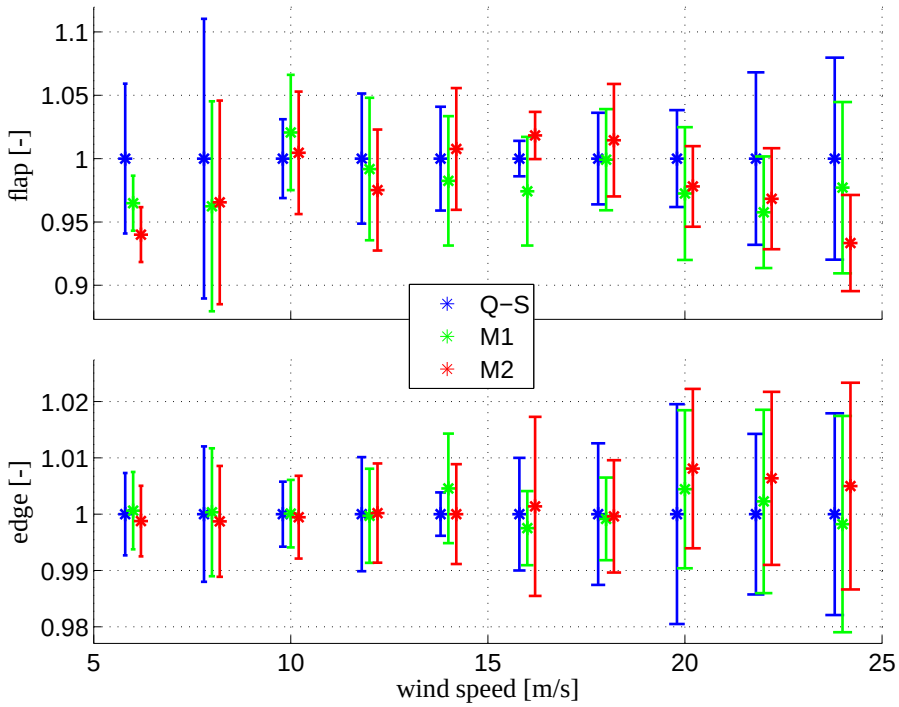

Figure 4.7. Blade fatigue loads; top and bottom plot show flapwise and edgewise blade root equivalent bending moments, respectively. For each wind speed and each model six simulations with different realization of wind and wave filed are conducted. All results are normalized by the quasi-static results at the given wind speed. The figure shows the mean value of the six different simulations with each model and the standard deviation between the simulations.

the amplitude of the transfer function and the lower plot shows the phase. The remaining graphs other then the ”Raw data” graph are results from the individual steps in the reduction procedure and they will be referenced below. The frequency scale has been normalised by the sampling frequency that was used in the simulation, however, it is emphasized that the shown frequency range covers the frequencies which we are normally interested in for load calculations.

It is seen from the shape of the transfer function that the mooring system behaves dynamically in the frequency range coinciding with that of the wind turbine, and thus indicates that it is important not to treat the mooring system as quasi-static in load simulations of floating wind turbines. The transfer function corresponding to a quasi-static mooring system model would appear in Figure (4.10) (top plot) as a horizontal line crossing the y-axis in the same location as the dynamic transfer function, and the phase (bottom plot) would be zero at all frequencies.

The next step of the method is to identify a linear state-space system which is able to describe the response. This is done by use of the MATLAB toolbox methods *n4sid* or *pem*. The result of this step is a system like the one in Eq. (4.8) with a certain system order. The transfer function associated with the identified state-space system is shown as the second graph titled ”Discrete model” in Figure (4.10). For the present example, the chosen model order was 60 which is quite high compared to the order which MATLAB chose by default. This order was chosen based of the correlation between the transfer function of the raw input relations and the identified model.

$$\begin{aligned} \mathbf{x}_{n+1} &= \mathbf{A}_D\mathbf{x}_n + \mathbf{B}_D\mathbf{u}_n \\ \mathbf{y}_n &= \mathbf{C}_D\mathbf{x}_n \end{aligned} \tag{4.8}$$

In the next step, the identified discrete state-space is transformed into a continuous state-space model like the one in Eq. (4.9) by use of the built-in MATLAB method *d2c*. The transfer

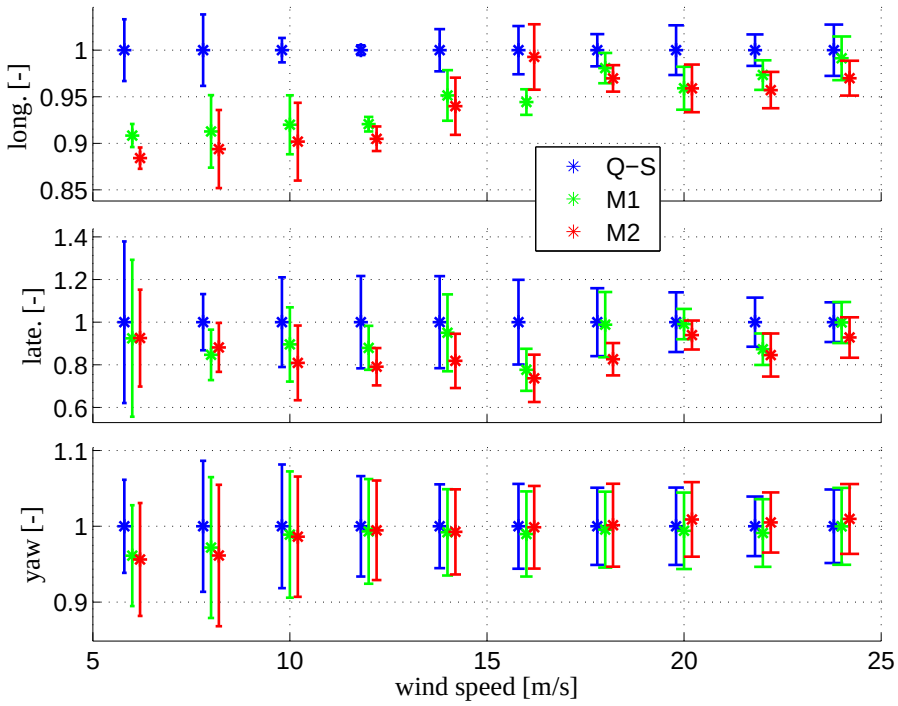

Figure 4.8. Tower fatigue loads; from the top the plots show longitudinal, lateral and yaw tower bottom equivalent bending moments, respectively. For each wind speed and each model six simulations with different realization of wind and wave filed are conducted. All results are normalized by the quasi-static results at the given wind speed. The figure shows the mean value of the six different simulations with each model and the standard deviation between the simulations.

function for the associated continuous state-space model is shown as the third graph titled "Continuous model" in Figure (4.10). The correlation with the preceding transfer functions is good for low frequency, but it starts to deviate with increasing frequency. This has to do with the way the the force input is assumed to vary between time steps for the *d2c* method, and it emphasizes the need for small time steps in the sampling of time series dependent on which frequency range the reduced model has to be valid within. It seems that sampling frequency (one divided by simulation time step) should be at least 10 times the upper frequency of interest for the reduction model, meaning that if the reduction model should be valid up to say 5 Hz then the sampling frequency should be at least 50 Hz (time step of 0.02s).[4]

$$\begin{aligned} \dot{\mathbf{x}} &= \mathbf{A}\mathbf{x} + \mathbf{B}\mathbf{u} \\ \mathbf{y} &= \mathbf{C}\mathbf{x} \end{aligned} \tag{4.9}$$

The system order of the continuous time model is the same as the original discrete model, and this order is reduced further in the next step by a modal reduction. The state vector $\mathbf{x}$ is expanded by a limited number of eigenvectors of $\mathbf{A}$ - exactly those eigenvectors that have eigenvalues in the frequency range of interest. [5]. The complex eigenmodes used in the expansion is chosen (and ordered) by the permutation matrix, $\mathbf{P}$. The ordering of the picked eigenmodes is such that the resulting expansion matrix, $\mathbf{G_s} = \mathbf{GP}$ is divided into two complex conjugates column blocks. The state vector $\mathbf{x}$ then becomes

$$\mathbf{x} = \mathbf{GPq} = \mathbf{G_s q} = \begin{bmatrix} \gamma_s & \overline{\gamma_s} \end{bmatrix} \mathbf{q} \tag{4.10}$$

[4] Alternatively, reduction of the discrete model by keeping only the eigenvectors corresponding to low frequency can be done before the conversion into a continuous time model.

[5] If real eigenvalues exist the corresponding eigenvector can be included directly as extra columns in $\mathbf{T}$ in Eq. (4.12)

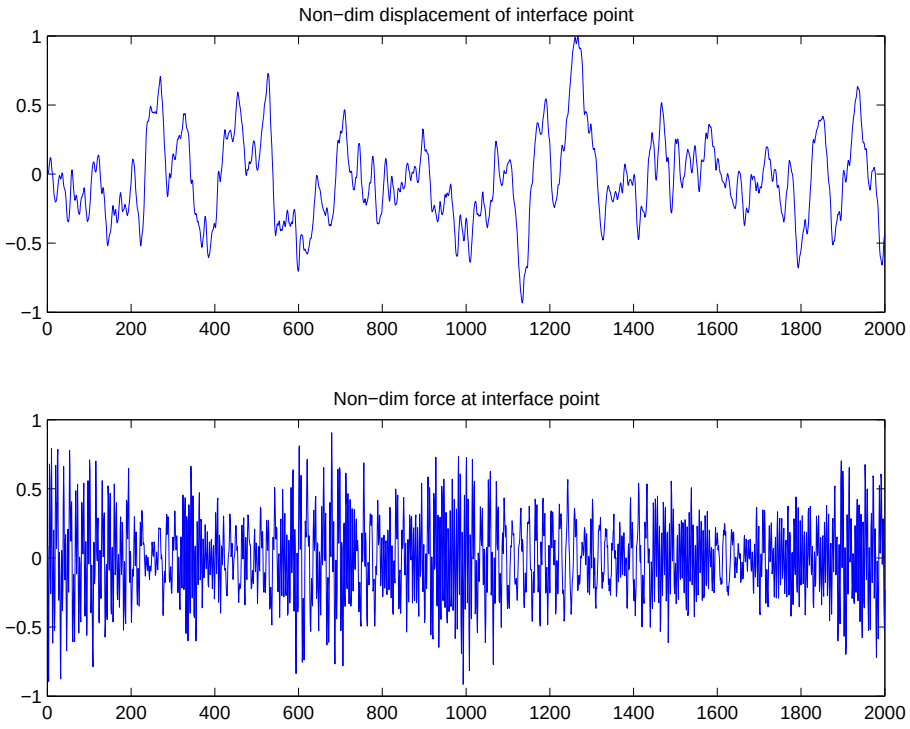

Figure 4.9. Displacement (top) and force (bottom) of mooting system simulated by HAWC2 used as input/output relation for system id.

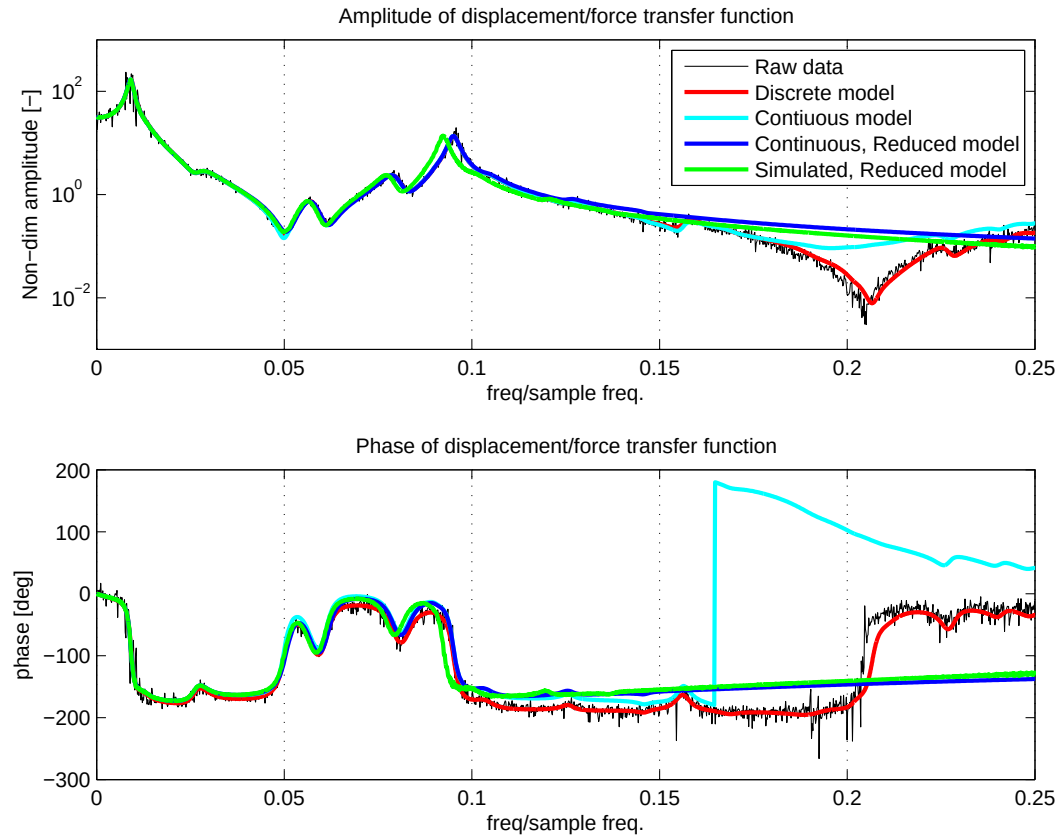

Figure 4.10. Transfer function between displacement and force for the various steps in the reduction procedure. Upper plot is amplitude and lower plot is phase.

where $\overline{()}$ means the complex conjugate of $()$. Since $\mathbf{x}$ is a real vector and $\mathbf{G}$ is a complex matrix, then $\mathbf{q}$ is also complex. This is undesirable because the final reduced set of equations will then also be complex. To avoid this, a transformation of $\mathbf{q}$ into a new set of state variables, $\mathbf{q_s}$, is made.

$$\mathbf{q} = \begin{bmatrix} \mathbf{I} & j\mathbf{I} \\ \mathbf{I} & -j\mathbf{I} \end{bmatrix} \mathbf{q_s} \overset{(\mathbf{I_s})}{=} \mathbf{I_s q_s} \tag{4.11}$$

where $j = \sqrt{-1}$ and $\mathbf{I}$ is the identity matrix. By inserting (4.11) into (4.10) the final transformation and reduction matrix, $\mathbf{T}$, is found,

$$\mathbf{x} = \begin{bmatrix} \gamma_s & \overline{\gamma_s} \end{bmatrix} \begin{bmatrix} \mathbf{I} & j\mathbf{I} \\ \mathbf{I} & -j\mathbf{I} \end{bmatrix} \mathbf{q_s} = \begin{bmatrix} \gamma_s + \overline{\gamma_s} & j(\gamma_s - \overline{\gamma_s}) \end{bmatrix} \mathbf{q_s} \overset{(\mathbf{T})}{=} \mathbf{T q_s} \tag{4.12}$$

Note that $\mathbf{T}$ is composed of the real and imaginary parts of γ_s and is therefore a real matrix. The pseudo inverse of $\mathbf{T}$ become $\mathbf{T}^{-1} = {\mathbf{I_s}}^{-1}\mathbf{P}^T\mathbf{G}^{-1}$, and by inserting (4.12) into (4.9) and pre-multiplication by $\mathbf{T}^{-1}$ the reduced set of EOMs become

$$\dot{\mathbf{q_s}} = \mathbf{T}^{-1}\mathbf{A}\mathbf{T}\mathbf{q_s} + \mathbf{T}^{-1}\mathbf{B}\mathbf{u} \overset{(\mathbf{A_s},\ \mathbf{B_s})}{=} \mathbf{A_s q_s} + \mathbf{B_s u} \tag{4.13}$$

$$\mathbf{y} = \mathbf{C}\mathbf{T}\mathbf{q_s} \overset{(\mathbf{C_s})}{=} \mathbf{C_s q_s} \tag{4.14}$$

The reduced system matrix $\mathbf{A_s}$ has the form

$$\mathbf{A_s} = \begin{bmatrix} Re(\lambda_s) & -Im(\lambda_s) \\ Im(\lambda_s) & Re(\lambda_s) \end{bmatrix} \tag{4.15}$$

where $Re()$ and $Im()$ means the real and the imaginary part of the argument, respectively, and λ_s is the diagonal matrix containing the eigenvalues corresponding to the eigenvectors γ_s.

Generally, any similarity transformation of the state variables are allowed - such transformations do not alter the system behavior related to the input/output and this property is exploited in the final step. The final step in the procedure introduces the output state variables, $\mathbf{y}$, as direct state variables in the ODEs, and makes the final ODEs work conjugate to the input/output definition by two successive state variable transformations. Both the input matrix, $\mathbf{B_s}$, and the output matrix $\mathbf{C_s}$ enter into these transformations.

The first transformation is defined via the transformation matrix $\mathbf{T_1}$ (this is the transformation which makes the final ODEs work conjugate to the input/output definition)

$$\mathbf{T_1} = \begin{bmatrix} \mathbf{B_s} & | & \mathbf{0} \\ & & \mathbf{I} \end{bmatrix} = \begin{bmatrix} \mathbf{B_s^1} & \mathbf{0} \\ \mathbf{B_s^2} & \mathbf{I} \end{bmatrix} \tag{4.16}$$

where $\mathbf{B_s^1}$ is the upper quadratic matrix of $\mathbf{B_s}$ and $\mathbf{B_s^2}$ is the remaining lower part.

The second transformation is defined via the transformation matrix $\mathbf{T_2}$ (this is the transformation which makes $\mathbf{y}$ the (upper) part of the final state variables)

$$\mathbf{T_2} = \begin{bmatrix} (\mathbf{C_s B_s})^{-1} & -(\mathbf{C_s B_s})^{-1}\mathbf{C_s^2} \\ \mathbf{0} & \mathbf{I} \end{bmatrix} \tag{4.17}$$

and thus

$$\mathbf{T_2}^{-1} = \begin{bmatrix} (\mathbf{C_s B_s}) & \mathbf{C_s^2} \\ \mathbf{0} & \mathbf{I} \end{bmatrix} \tag{4.18}$$

where $\mathbf{C_s^2}$ the right sub matrix of $\mathbf{C_s} = \begin{bmatrix} \mathbf{C_s^1}\ \mathbf{C_s^2} \end{bmatrix}$ and $\mathbf{C_s^1}$ is quadratic.

By substitution of $\mathbf{q_s} \overset{(\mathbf{q_f})}{=} \mathbf{T_1 T_2 q_f}$ into (4.13) and (4.14) and post-multiplication by ${\mathbf{T_1}}^{-1}$, we arrive at the final set of ODEs

$$\mathbf{T_2}\dot{\mathbf{q}}_\mathbf{f} = {\mathbf{T_1}}^{-1}\mathbf{A_s T_1 T_2 q_f} + {\mathbf{T_1}}^{-1}\mathbf{B_s u} \tag{4.19}$$

$$\mathbf{y} = \mathbf{C_s T_1 T_2 q_f} \tag{4.20}$$

Doing the matrix multiplications which defines the new input matrix and the new output matrix reveals the idea of the two transformation, namely that the input matrix, $\mathbf{T_1}^{-1}\mathbf{B_s} = \begin{bmatrix} \mathbf{I} \\ \mathbf{0} \end{bmatrix}$, and similarly for the new output matrix, $\mathbf{C_s T_1 T_2} = \begin{bmatrix} \mathbf{I} & \mathbf{0} \end{bmatrix}$. It is seen from the structure of this new output matrix that the output state is now actually contained directly as the upper part of the variables which means that we can discard all of Eq. (4.20). So, the final ODEs can be written as

$$\mathbf{D_f}\dot{\mathbf{q}}_\mathbf{f} - \mathbf{A_f q_f} = \begin{Bmatrix} \mathbf{u} \\ \mathbf{0} \end{Bmatrix} \tag{4.21}$$

where

$$\mathbf{D_f} = \mathbf{T_2} \tag{4.22}$$

$$\mathbf{A_f} = \mathbf{T_1}^{-1}\mathbf{A_s T_1 T_2} \tag{4.23}$$

$$\mathbf{q_f} = \begin{Bmatrix} \mathbf{y} \\ \vdots \end{Bmatrix} \tag{4.24}$$

remembering the location of $\mathbf{y}$ inside $\mathbf{q_f}$. The transfer function of the final model is shown in Figure (4.10) titled "Continuous, Reduced model". The final model has 26 DOFs which is a bit more than expected considering how the transfer function looks. Still it is indeed an acceptable size to include elsewhere (e.g. in HAWCStab2) considering the information about the dynamic behaviour the model provides.

Finally, a time simulation of the model ODEs using the original force input in Figure (4.9) was made. The transfer function between input/output was estimated by the built-in function *tfestimate*, and the result is shown in Figure (4.10) titled "Simulated, Reduced model". The correlation with the other results are good at low frequencies. For higher frequencies the peaks in the spectrum are seen to shift towards lower frequency. This is due to the frequency shift which is inherent in the Newmark time integration method. Since the Newmark time integration scheme is also used inside HAWC2, it means that the same frequency shift is already present in the time series on which all the results above are based. This fact once more emphasizes the significance of choosing a sufficiently low time step in the simulations dependent on the upper frequency of interest.

4.4 Conclusion

The development of floating wind turbines is a challenge for the conventional design tools. In wind turbine load simulations mooring systems are normally modeled as quasi-static nonlinear springs with the same stiffness characteristic as the mooring system. In this work a dynamic mooring line model is developed and implemented in a comprehensive state of the art aeroelastic wind turbine simulation tool. The new simulation tool is used to analyze the effect of different mooring line model complexities on wind turbine loads.

It is found that both extreme and fatigue loads on the blades are unaffected by the different mooring line models. The lateral tower extreme load is reduced by the most comprehensive mooring models (M2), but the extreme lateral tower load is not a design driving tower load. The fatigue of both the lateral and longitudinal tower modes are reduced, and these reductions can lead to tower cost reductions.

The results in this work indicate that the mooring system has an effect on the tower loads, but for the wind turbine loads it seems to be conservative to use the quasi-static modeling approach.

Finally, a general method which can be used to extract a reduced, linear model of the mooring system or other systems was described. The method converts a simulated response of the full mooring system into a set of first order ODEs which can be used to include the dynamics of the

mooring system in other applications, e.g. for modal analysis. The result of using the method shows the significance of using sufficiently small time steps in the simulated input/output which is used as basis for the method.

References

[1] M. O. E. Vera Ingunn. Floating turbine captures wind energy in deep water enviroment. *Welding Journal (Miami, Fla)*, 89(5):54–58, 2010.

[2] J. Jonkman. Dynamics of offshore floating wind turbines model development and verification. *Wind Energy*, 12(5):459–492, 2009.

[3] T. J. Larsen and A. M. Hansen. How 2 HAWC2, the user's manual. Risø-r-1597(ver. 3-7)(en), RisøNational Laboratory, 2009.

[4] T. J. Larsen and T. D. Hanson. A method to avoid negative damped low frequent tower vibrations for a floating, pitch controlled wind turbine. *Journal of Physics: Conference Series*, 75(1):012073–1–11, 2007.

[5] A. A. Shabana. *Dynamics of Multibody Systems*. Cambridge University Press, University of Illinois at Chicago, 2nd edition, 1998.

[6] M. H. Hansen, M. Gaunaa, and H. A. Madsen. A Beddoes-Leishman type dynamic stall model in state-space and indicial formulation. Technical Report Risø -R-1354(EN), Risø National Laboratory, (available from www.risoe.dk), August 2004.

[7] J. Mann. Wind field simulation. *Probabilistic Engineering Mechanics*, 13(4):269–282, 1998.

[8] P. Passon, M. Kuhn, S. Butterfield, J. Jonkman, T. Camp, and T. J. Larsen. Oc3-benchmark exercise of aero-elastic offshore wind turbine codes. *Journal of Physics: Conference Series*, 75(1):012071, 2007.

[9] P. B. Bergan, E. Mollestad, and N. Sandsmark. Non-linear static and dynamic response analysis for floating offshore structures. *Engineering Computations (Swansea, Wales)*, 2(1):13–20, 1985.

[10] T. Belytschko, W. K. Liu, and B. Moran. *Nonlinear Finite Elements for Continua and Structures*. John Wiley & Sons Ltd., 2000.

5 Closed-loop aero-servo-elastic analysis

Author: Morten Hartvig Hansen

New possibilities of closed-loop aero-servo-elastic eigenvalue and frequency-domain analyses of wind turbines based on the recent code HAWCStab2 are described in this section. Open-loop aeroelastic eigenvalue analyses based on linear aeroelastic models of wind turbines have led to new knowledge about the aeroelastic stability boundaries of wind turbines [1]. Additions of linear models of actuators and controllers to the linear aeroelastic models enable the new possibilities: closed-loop aero-servo-elastic stability analysis, controller tuning based on pole placement and frequency response design, and derivation of linear first-principle reduced order models for model-based controllers. This section contains first an overall description of the linear aero-servo-elastic model of HAWCStab2, and then examples of closed-loop aero-servo-elastic analyses of a combined collective and cyclic pitch controller, showing some of the new possibilities.

5.1 Linear aero-servo-elastic model

The structure of a three-bladed wind turbine is described in HAWCStab2 by articulated Timoshenko beam elements in a co-rotational finite element formulation [2]. The turbine is divided into three main substructures: a ground fixed structure (tower and nacelle-tower connection), an axis-symmetric structure rotating at a constant mean speed (drivetrain and main shaft), and a three-bladed isotropic rotor structure (hub and rotor blades). The aerodynamic forces are modeled by the Blade Element Momentum (BEM) method coupled with a modified four-state Beddoes-Leishman model of 2D unsteady aerodynamics in each aerodynamic calculation point along the blades. There is currently no model of dynamic inflow effects implemented in HAWCStab2; the plan is to implement the dynamic inflow model of HAWC2.

The nonlinear equations of motion are derived from Lagrange's equations with the generalized forces due to the non-conservative aerodynamic forces derived from the principle of virtual work [3]. Analytical linearization and transformation into multi-blade coordinates using the Coleman transformation (see e.g. [1] or [4]) render the following linear time-invariant aeroelastic equations of motion:

$$\mathbf{M}\ddot{\mathbf{z}}_s + (\mathbf{C}_d + \mathbf{G} + \mathbf{C}_a)\dot{\mathbf{z}}_s + (\mathbf{K} + \mathbf{K}_a)\mathbf{z}_s + \mathbf{A}_f\mathbf{z}_a = \mathbf{B}_q\mathbf{q} + \mathbf{B}_{vs}\mathbf{v} \tag{5.1a}$$

$$\dot{\mathbf{z}}_a + \mathbf{A}_d\mathbf{z}_a + \mathbf{C}_s\dot{\mathbf{z}}_s + \mathbf{K}_s\mathbf{z}_s = \mathbf{B}_{va}\mathbf{v} \tag{5.1b}$$

where $\mathbf{z}_s$ and $\mathbf{z}_a$ contain the structural displacement states and aerodynamic states, respectively, noting that the states on the rotor are given in multi-blade coordinates. The matrices of the structural equation (5.1a) are the mass matrix $\mathbf{M}$, the structural damping matrix $\mathbf{C}_d$ given by a spectral damping model [5], the gyroscopic matrix $\mathbf{G}$, the aerodynamic damping matrix $\mathbf{C}_a$, the elastic and centrifugal stiffness matrix $\mathbf{K}$, the aerodynamic stiffness matrix $\mathbf{K}_a$, and a coupling matrix $\mathbf{A}_f$ containing the forces on the structure due to variations of the aerodynamic states. The right hand side of the structural equation contains the input matrix $\mathbf{B}_q$ from variations in pitch and generator bearing torques $\mathbf{q}$, and the input matrix $\mathbf{B}_{vs}$ from variations in wind field $\mathbf{v}$. The matrices of the aerodynamic equation (5.1b) are the system matrix $\mathbf{A}_d$, the feedback matrices $\mathbf{C}_s$ and $\mathbf{K}_s$ from the structural velocities and deflections, and a similar wind input matrix $\mathbf{B}_{va}$ on the right hand side. Using the Coleman transformation, the wind field vector $\mathbf{v}$ consists of variations of the mean wind and two linear wind shears $\mathbf{v} = \{v_m\ v_v\ v_h\}^T$, where v_v and v_h are the variations of linear vertical and horizontal shears, respectively. Similar, the variations of the pitch bearing torques in the vector $\mathbf{q}$ are described by a torque $q_{\theta_{\text{col}}}$ describing simultaneous pitch actuation on all three blades and by two cyclic torques $q_{\theta_{\cos}}$ and $q_{\theta_{\sin}}$ describing 1P azimuthal actuation of the blades. In HAWCStab2, the azimuth angle is zero for the blade pointing down, thus the cosine and sine cyclic pitch actuation correspond to tilt and yaw excitation (for rigid blades as discussed later), respectively.

The linear aero-servo-elastic equations (5.1) can be set up for any operational point given by the mean wind speed, pitch angle, and rotor speed. The linearization is performed assuming small vibrations about the steady state obtained by solving the nonlinear equations of equilibrium between the internal elastic and centrifugal forces (including nonlinear geometric stiffness) and the external aerodynamic forces. This steady nonlinear deflection state of the rotor blades is stationary because the incoming wind is assumed to be uniform and perpendicular to the rotor (neglecting e.g. wind shear, tower shadow, turbulence, and static and elastic rotor tilt), and the gravity is neglected.

Closed-loop aero-servo-elastic equations

To close the loop, the aeroelastic equations of motion (5.1) are first rewritten into first order state-space form as

$$\dot{\mathbf{x}} = \mathbf{A}\mathbf{x} + \mathbf{B}\mathbf{u} + \mathbf{B}_v\mathbf{v} \tag{5.2a}$$

$$\mathbf{y} = \mathbf{C}\mathbf{x} + \mathbf{D}\mathbf{u} + \mathbf{D}_v\mathbf{v} \tag{5.2b}$$

where the state vector is $\mathbf{x} = \{\mathbf{z}_a\ \mathbf{z}_s\ \dot{\mathbf{z}}_s\}^T$, the input vector is $\mathbf{u} = \mathbf{q}$, and the system matrix $\mathbf{A}$ can be derived as

$$\mathbf{A} = \begin{bmatrix} \mathbf{A}_d & \mathbf{K}_s & \mathbf{C}_s \\ \mathbf{0} & \mathbf{0} & \mathbf{I} \\ -\mathbf{M}^{-1}\mathbf{A}_f & -\mathbf{M}^{-1}(\mathbf{K}+\mathbf{K}_a) & -\mathbf{M}^{-1}(\mathbf{C}+\mathbf{G}+\mathbf{C}_a) \end{bmatrix} \tag{5.3}$$

and the input matrices $\mathbf{B}$ and $\mathbf{B}_v$ can be derived as

$$\mathbf{B} = \begin{bmatrix} \mathbf{0} \\ \mathbf{0} \\ \mathbf{M}^{-1}\mathbf{B}_q \end{bmatrix} \quad \text{and} \quad \mathbf{B}_v = \begin{bmatrix} \mathbf{B}_{va} \\ \mathbf{0} \\ \mathbf{M}^{-1}\mathbf{B}_{vs} \end{bmatrix} \tag{5.4}$$

Note that further inputs from the controller may be appended to the input vector $\mathbf{u}$, whereby the input matrix $\mathbf{B}$ is extended accordingly. The output vector $\mathbf{y}$ in Equation (5.2) depend on the signals needed for the controller. These signals are defined by the output matrix $\mathbf{C}$ from the system states, the feed-through matrix $\mathbf{D}$ from control inputs, and the feed-through matrix $\mathbf{D}_v$ from wind inputs. Examples of the setup of these matrices are given in the following section.

The controller equations can be written on first order form as

$$\dot{\mathbf{x}}_c = \mathbf{A}_c\mathbf{x}_c + \mathbf{B}_c\mathbf{y} \tag{5.5a}$$

$$\mathbf{u} = \mathbf{C}_c\mathbf{x}_c + \mathbf{D}_c\mathbf{y} \tag{5.5b}$$

where the state vector $\mathbf{x}_c$ and the system matrix $\mathbf{A}_c$ describe the controller system driven by the output of the aeroelastic system $\mathbf{y}$ through the controller input matrix $\mathbf{B}_c$. The output of the controller $\mathbf{u}$ (the controller input to the aeroelastic system) is defined by the output matrix $\mathbf{C}_c$ from controller states and the feed-through matrix $\mathbf{D}_c$ from the aeroelastic system output. Examples of the setup of these matrices are also given for the pitch controllers considered in the following section.

The closed-loop aero-servo-elastic equations are obtained by first inserting Equation (5.5b) into Equation (5.2b) and solving for the output $\mathbf{y}$. The resulting output $\mathbf{y}$ is then inserted into Equation (5.5b) for the controller input $\mathbf{u}$, whereby these vectors are given by the aeroelastic and controller state variables and the wind input. Insertion into the system Equations (5.2a) and (5.5a) yields the closed-loop aero-servo-elastic equations:

$$\dot{\mathbf{x}}_{\text{ase}} = \mathbf{A}_{\text{ase}}\mathbf{x}_{\text{ase}} + \mathbf{B}_{v,\text{ase}}\mathbf{v} \tag{5.6a}$$

$$\mathbf{y}_{\text{ase}} = \mathbf{C}_{\text{ase}}\mathbf{x}_{\text{ase}} + \mathbf{D}_{v,\text{ase}}\mathbf{v} \tag{5.6b}$$

where the aero-servo-elastic state and output vectors are $\mathbf{x}_{\text{ase}} = \{\mathbf{x}\ \mathbf{x}_c\}^T$ and $\mathbf{y}_{\text{ase}} = \{\mathbf{y}\ \mathbf{u}\}^T$,

respectively. The aero-servo-elastic system and input matrices are

$$\mathbf{A}_{\text{ase}} = \begin{bmatrix} \mathbf{A}+\mathbf{B}\mathbf{D}_c(\mathbf{I}-\mathbf{D}\mathbf{D}_c)^{-1}\mathbf{C} & \mathbf{B}\mathbf{C}_c+\mathbf{B}\mathbf{D}_c(\mathbf{I}-\mathbf{D}\mathbf{D}_c)^{-1}\mathbf{D}\mathbf{C}_c \\ \mathbf{B}_c(\mathbf{I}-\mathbf{D}\mathbf{D}_c)^{-1}\mathbf{C} & \mathbf{A}_c+\mathbf{B}_c(\mathbf{I}-\mathbf{D}\mathbf{D}_c)^{-1}\mathbf{D}\mathbf{C}_c \end{bmatrix} \tag{5.7a}$$

$$\mathbf{B}_{v,\text{ase}} = \begin{bmatrix} \mathbf{B}_v+\mathbf{B}\mathbf{D}_c(\mathbf{I}-\mathbf{D}\mathbf{D}_c)^{-1}\mathbf{D}_v \\ \mathbf{B}_c(\mathbf{I}-\mathbf{D}\mathbf{D}_c)^{-1}\mathbf{D}_v \end{bmatrix} \tag{5.7b}$$

and the output and feed-through matrices are

$$\mathbf{C}_{\text{ase}} = \begin{bmatrix} (\mathbf{I}-\mathbf{D}\mathbf{D}_c)^{-1}\mathbf{C} & (\mathbf{I}-\mathbf{D}\mathbf{D}_c)^{-1}\mathbf{D}\mathbf{C}_c \\ \mathbf{D}_c(\mathbf{I}-\mathbf{D}\mathbf{D}_c)^{-1}\mathbf{C} & \mathbf{C}_c+\mathbf{D}_c(\mathbf{I}-\mathbf{D}\mathbf{D}_c)^{-1}\mathbf{D}\mathbf{C}_c \end{bmatrix} \tag{5.8a}$$

$$\mathbf{D}_{v,\text{ase}} = \begin{bmatrix} (\mathbf{I}-\mathbf{D}\mathbf{D}_c)^{-1}\mathbf{D}_v \\ \mathbf{D}_c(\mathbf{I}-\mathbf{D}\mathbf{D}_c)^{-1}\mathbf{D}_v \end{bmatrix} \tag{5.8b}$$

Note that the isolation of the output vector $\mathbf{y}$ using Equations (5.2b) and (5.5b) involves the inversion of the matrix subtraction $\mathbf{I}-\mathbf{D}\mathbf{D}_c$, which may cause the problem of an algebraic loop, e.g. by a proportional feedback of an acceleration signal. Such problem can be solved by inserting a filter on the acceleration signal before the feedback, whereby it is moved from the feed-through matrix $\mathbf{D}_c$ to the controller output matrix $\mathbf{C}_c$.

Pitch servo model

The pitch actuator can either be modelled by a physical model of for example a hydraulic pitch system yielding a torque to a free bearing at the blade root flange [6], or by a generic PID controller giving such pitch bearing torque based on an error between the actual pitch angle of the free bearing and the pitch demand angle.

A much simpler model is often used in load simulations with the multi-body code HAWC2, where a constraint is set up to prescribe the angle of the bearing between hub and blade. This prescribed angle is then set to be the second order low-pass filtered value of the pitch demand angle for the particular blade:

$$\ddot{\Theta}_k + 2\xi_\theta\omega_\theta\dot{\Theta}_k + \omega_\theta^2\Theta_k = \omega_\theta^2\Theta_{k,\text{ref}} \tag{5.9}$$

where $\dot{(\cdot)} = d/dt$ denotes time-derivation, and the parameters ω_θ and ξ_θ are the frequency and damping ratio of the low-pass filter between the actual absolute pitch angle Θ_k and the absolute demand/reference pitch $\Theta_{k,\text{ref}}$ for blade number k.

To implement this second order pitch servo model in the HAWCStab2 model (5.1a) for the multi-blade coordinates of the pitch bearing rotations (θ_{col}, $\theta_{\cos}$, and $\theta_{\sin}$), the mean steady state pitch angle of the operational point (Θ_0) must be subtracted from the absolute value ($\theta_k = \Theta_k - \Theta_0$) in Equation (5.9), and the resulting equations for $k = 1,2,3$ must then be Coleman transformed yielding three governing equations for the pitch variations described in multi-blade coordinates

$$\begin{Bmatrix} \ddot{\theta}_{\text{col}} \\ \ddot{\theta}_{\cos} \\ \ddot{\theta}_{\sin} \end{Bmatrix} + \begin{bmatrix} 2\xi_\theta & 0 & 0 \\ 0 & 2\xi_\theta & 2\Omega \\ 0 & -2\Omega & 2\xi_\theta \end{bmatrix} \begin{Bmatrix} \dot{\theta}_{\text{col}} \\ \dot{\theta}_{\cos} \\ \dot{\theta}_{\sin} \end{Bmatrix} + \begin{bmatrix} \omega_\theta^2 & 0 & 0 \\ 0 & \omega_\theta^2-\Omega^2 & 2\xi_\theta\Omega \\ 0 & -2\xi_\theta\Omega & \omega_\theta^2-\Omega^2 \end{bmatrix} \begin{Bmatrix} \theta_{\text{col}} \\ \theta_{\cos} \\ \theta_{\sin} \end{Bmatrix} = \begin{Bmatrix} \theta_{0,\text{ref}} \\ \theta_{\cos,\text{ref}} \\ \theta_{\sin,\text{ref}} \end{Bmatrix} \tag{5.10}$$

Note that the filter frequencies of the cyclic components decrease as the rotor speed Ω increases, which reflects the fact that a stationary input on a cyclic pitch demand will correspond to a 1P harmonic input to the actuator on the blade. The implementation of Equation (5.10) in the closed-loop equations (5.6) follows from their replacement of the three equations in (5.1a) that govern the pitch bearing rotations of the blades, whereby the input vector $\mathbf{u}$ contains pitch reference/demand signals instead of torque values.

5.2 Collective and cyclic pitch controllers

To show the new possibilities of closed-loop analysis, a combined collective and cyclic pitch controller is tuned for above rated wind speed operation, and the aero-servo-elastic frequency response of the NREL 5MW reference turbine ($\Omega_r = 12.1$ rpm = 0.2 Hz) is analysed using HAWCStab2. First, the equations of the two Proportional-Integral (PI) pitch controllers are written in the form described above. Then, the collective pitch controller is tuned using the pole placement method suggested by Øye [7], and the placement of the speed regulator mode is checked with full state eigenvalue analysis in HAWCStab2. Then, the cyclic pitch controller is tuned using the open-loop frequency response functions (FRFs) from cyclic pitch inputs to rotor moment outputs, and the Ziegler-Nichols method based on full state eigenvalue analysis. The calculation of closed-loop FRFs using HAWCStab2 show large reductions of the low frequency rotor moment loads due to the cyclic pitch controller, which finally are confirmed by HAWC2 time domain simulations showing 25 – 30 % reductions in equivalent fatigue loads of the flapwise blade root blade moments. In all computations and simulations, the frequency of the second order pitch servo model described above is set to 100 Hz to remove its effect, however, the model is needed to use pitch demand angles as input the aeroelastic system equations instead of pitch torques.

Controller equations

Figure 5.1 shows a schematics of the two combined collective and cyclic PI pitch controllers that are operative above rated wind speed, which are similar to the controllers suggested by Larsen [8]. The right side of the schematics shows the collective pitch controller that regulates the rotor speed Ω to maintain the rated speed of Ω_r. The rotor speed Ω is measured at the generator end of the drivetrain (there is no gearbox model included and the rotational inertia on the HSS are related to the LSS by multiplication with the squared of the gear ratio). It's fed through a second order low-pass filter with frequency $\omega_{lp,\Omega}$ and damping ratio $\zeta_{lp,\Omega}$, and the rated speed Ω_r is subtracted from the filtered rotor speed Ω before it enters the PI controller with the gains k_P and k_I. The output of the PI controller is multiplied by a gain scheduling factor η_K to give the collective pitch demand angle θ_{col}. The power is controlled by the generator torque either as ideal constant power control $Q_g = -P_r/\Omega$, or constant torque control $Q_g = -P_r/\Omega_r$.

The left side of Figure 5.1 shows the schematics of the cyclic pitch controller that give cyclic pitch inputs based on the azimuthal rotor position and the flapwise blade root moments assumed to be measurable by strain gauges, or similar sensors. The flapwise blade root moments m_1^x, m_2^x, and m_3^x are first inverse Coleman transformed using the azimuthal angle ψ_1 of blade 1 (blades are here numbered in the direction of the rotation, opposite the tower passage order). The resulting tilt and yaw rotor moments, m_{tilt} and m_{yaw}, are fed through two individual second order filters both with the same frequency $\omega_{lp,c}$ and damping ratio $\zeta_{lp,c}$. The filtered rotor moments $\bar{m}_{\text{tilt}}$ and $\bar{m}_{\text{yaw}}$ are fed to two individual PI controllers with the same gains k_P^c and k_I^c. The controller outputs are the two cyclic pitch demand angles, θ_{tilt} and θ_{yaw}, that would be required to cancel out the combination of rotor tilt and yaw moments if the blade were rigid. However, the flapping motion of the blades due to their flapwise flexibility will change the phase between the cyclic pitch angle variation and the resulting tilt and yaw rotor moments [9]. To correct for this phase lag, the two cyclic pitch demand angles, θ_{tilt} and θ_{yaw}, are azimuthally rotated by a *lead angle* denoted ψ_0 (see the later Figure 5.6) to give these signals the correct lead that compensates the lag:

$$\begin{Bmatrix} \theta_{\cos} \\ \theta_{\sin} \end{Bmatrix} = \begin{bmatrix} \cos\psi_0 & \sin\psi_0 \\ -\sin\psi_0 & \cos\psi_0 \end{bmatrix} \begin{Bmatrix} \theta_{\text{tilt}} \\ \theta_{\text{yaw}} \end{Bmatrix} \tag{5.11}$$

The two new cyclic pitch demand angles, $\theta_{\cos}$ and $\theta_{\sin}$, correspond to the two cyclic multi-blade components of the pitch demand angle for each blade k, which by using the Coleman transformation can be computed as

$$\theta_k = \theta_{\text{col}} + \theta_{\cos}\cos\psi_k + \theta_{\sin}\sin\psi_k \tag{5.12}$$

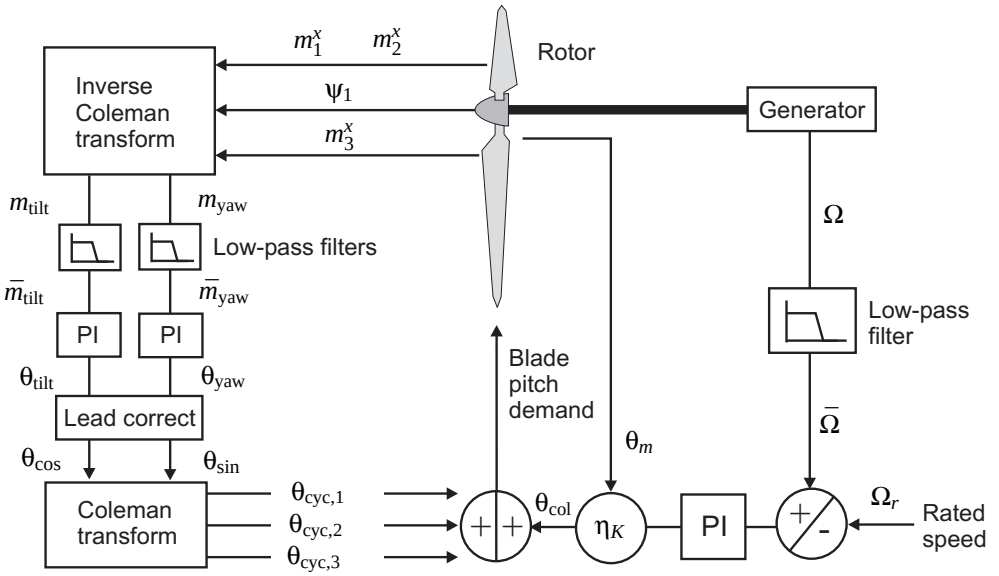

Figure 5.1. Schematics of the two combined collective and cyclic PI pitch controllers operative above rated. The gain-scheduling factor $\eta_K = 1/(1+\theta_m/K_K)$ reduces the collective pitch feedback for increasing wind speed measured by a mean pitch angle θ_m.

where ψ_k is the azimuth angle to blade k. Note that here the subscript "ref" has been omitted from these pitch demand angles.

From the above description of the aero-servo-elastic system, the output vector of the aeroelastic system can be defined as

$$\mathbf{y} = \{\omega \;\; m_{\text{tilt}} \;\; m_{\text{yaw}}\}^T \tag{5.13}$$

where $\omega = \Omega - \Omega_r$ is the speed error, which corresponds to the velocity state variable of the generator bearing degree of freedom in the HAWCStab2 model. The rotor moments m_{tilt} and m_{yaw} (which have zero mean due to the assumption of uniform inflow and zero gravity) are obtained from the inverse Coleman transformation of the three flapwise blade root moments. However, due to the multi-blade description of the rotor deformation in the HAWCStab2 model, these moments can be computed directly from the cosine and sine components of the cyclic deformation of the first element at the blade root. Noting that the state vector is divided into aerodynamic states, structural deflection states and velocity states ($\mathbf{x} = \{\mathbf{z}_a \; \mathbf{z}_s \; \dot{\mathbf{z}}_s\}^T$), the output matrix can be written on the form

$$\mathbf{C} = \left[\begin{array}{c|c|c} \mathbf{0} & \multicolumn{3}{c|}{\mathbf{0}} & \multicolumn{3}{c}{} \\ \mathbf{0} & 0 \ldots\ldots 0 \;\; \mathbf{k}_{\text{flap}} \;\; 0 \ldots & \ldots\ldots\ldots 0 & \multicolumn{3}{c}{} \\ \mathbf{0} & 0 \ldots\ldots\ldots\ldots\ldots & \ldots 0 \;\; \mathbf{k}_{\text{flap}} \;\; 0 \ldots 0 & \multicolumn{3}{c}{} \end{array}\right.\left|\begin{array}{ccc} 0 \ldots 0 & 1 & 0 \ldots 0 \\ & \mathbf{0} & \\ & \mathbf{0} & \end{array}\right] \tag{5.14}$$

where $\mathbf{k}_{\text{flap}}$ is a 1×6 matrix that is extracted from the elastic stiffness matrix describing the flapwise moment due to the deflection of the second blade node away from its steady state deflection. Note that this matrix is the same for both the tilt and yaw moments; the difference is the placement of the matrix in the output matrix $\mathbf{C}$: to obtain the tilt moment it is multiplied on the cosine component of the blade root element deflection, and the yaw moment is obtained from the sine component, noting that the azimuth angle is measured from the blade down position. The output vector (5.13) is given by the states, i.e., there are no feed-through terms thus $\mathbf{D} = \mathbf{D}_v = \mathbf{0}$.

The combined collective and cyclic pitch controllers has the state vector

$$\mathbf{x}_c = \left\{\bar{\omega} \;\; \dot{\bar{\omega}} \;\; \phi \;\; \bar{m}_{\text{tilt}} \;\; \dot{\bar{m}}_{\text{tilt}} \;\; M_{\text{tilt}} \;\; \bar{m}_{\text{yaw}} \;\; \dot{\bar{m}}_{\text{yaw}} \;\; M_{\text{yaw}}\right\}^T \tag{5.15}$$

where $\bar{\omega}$ and $\dot{\bar{\omega}}$ are the filtered rotor speed variation and its time derivative, and ϕ is the integral of the filtered rotor speed variation $\dot{\phi} = \bar{\omega}$. Similar, for $\bar{m}_{\text{tilt}}$, $\dot{\bar{m}}_{\text{tilt}}$, and M_{tilt} and for $\bar{m}_{\text{yaw}}$, $\dot{\bar{m}}_{\text{yaw}}$,

and M_{yaw}, which are the filtered rotor moment, its time derivative, and its time integral, respectively, for each the tilt and yaw moments. The 9×9 controller system matrix $\mathbf{A}_c$ can be setup as

$$\mathbf{A}_c = \begin{bmatrix} \mathbf{A}_{c,\Omega} & \mathbf{0} & \mathbf{0} \\ \mathbf{0} & \mathbf{A}_{c,\text{cyc}} & \mathbf{0} \\ \mathbf{0} & \mathbf{0} & \mathbf{A}_{c,\text{cyc}} \end{bmatrix} \tag{5.16}$$

where $\mathbf{A}_{c,\Omega}$ and $\mathbf{A}_{c,\text{cyc}}$ are 3×3 system matrices for the three pairs of a second order filter and an integrator which are given as

$$\mathbf{A}_{c,\Omega} = \begin{bmatrix} 0 & 1 & 0 \\ -\omega_{lp,\Omega}^2 & 2\zeta_{lp,\Omega}\omega_{lp,\Omega} & 0 \\ 1 & 0 & 0 \end{bmatrix} \text{ and } \mathbf{A}_{c,\text{cyc}} = \begin{bmatrix} 0 & 1 & 0 \\ -\omega_{lp,c}^2 & 2\zeta_{lp,c}\omega_{lp,c} & 0 \\ 1 & 0 & 0 \end{bmatrix} \tag{5.17}$$

The 9×3 input matrix $\mathbf{B}_c$ to the controller system states can be written as

$$\mathbf{B}_c^T = \begin{bmatrix} 0 & \omega_{lp,\Omega}^2 & 0 & 0 \ldots\ldots\ldots\ldots\ldots 0 \\ 0 \ldots\ldots 0 & 0 & \omega_{lp,c}^2 & 0 & 0 \ldots\ldots 0 \\ 0 \ldots\ldots\ldots\ldots\ldots 0 & & 0 & \omega_{lp,c}^2 & 0 \end{bmatrix} \tag{5.18}$$

The output vector from the controller (the input to the aeroelastic system) is

$$\mathbf{u} = \{q_g \;\; \theta_{\text{col,ref}} \;\; \theta_{\text{cos,ref}} \;\; \theta_{\text{sin,ref}}\}^T \tag{5.19}$$

where q_g is the generator torque variation about the steady state value P_r/Ω_r, $\theta_{\text{col,ref}}$ is the collective pitch demand, and $\theta_{\text{cos,ref}}$ and $\theta_{\text{sin,ref}}$ are the two cyclic pitch demand angles from the cyclic pitch controller. The pitch demand angles are obtained from the controller states by the 4×9 output matrix

$$\mathbf{C}_c = \begin{bmatrix} 0 & 0 & 0 & 0 & 0 & 0 & 0 & 0 & 0 \\ k_P & 0 & k_I & 0 & 0 & 0 & 0 & 0 & 0 \\ 0 & 0 & 0 & k_P^c\cos\psi_0 & 0 & k_I^c\cos\psi_0 & k_P^c\sin\psi_0 & 0 & k_I^c\sin\psi_0 \\ 0 & 0 & 0 & -k_P^c\sin\psi_0 & 0 & -k_I^c\sin\psi_0 & k_P^c\cos\psi_0 & 0 & k_I^c\cos\psi_0 \end{bmatrix} \tag{5.20}$$

that contains the gains of the PI controllers and the lead angle. The power controller is modeled as either ideal constant power control with $Q_g = -P_r/\Omega$, or constant torque control with $Q_g = -P_r/\Omega_r$. Linearization about the steady state value $\Omega = \Omega_r + \omega$ yields $q_g = \frac{\partial Q_g}{\partial \Omega}\,\omega$, whereby the 4×3 feed-through matrix becomes

$$\mathbf{D}_c = \begin{bmatrix} \frac{\partial Q_g}{\partial \Omega} & 0 & 0 \\ & \mathbf{0} & \end{bmatrix}, \text{ where } \frac{\partial Q_g}{\partial \Omega} = \begin{cases} 0 & \text{constanst torque} \\ \frac{P_r}{\Omega_r^2} & \text{constant power} \end{cases} \tag{5.21}$$

Note that ideal constant power control leads to negative damping through the term $\mathbf{B}\mathbf{D}_c\mathbf{C}$ in the upper left part of the closed-loop aero-servo-elastic system matrix (5.7a).

Tuning of collective pitch controller

The PI gains of the collective pitch controller are tuned using pole placement of the rigid body drivetrain mode as suggested by Øye [7]. The frequency of this speed regulator mode must be sufficiently below the tower frequency to avoid excitation of the longitudinal tower mode, and sufficiently high to avoid large rotor speed excursions.

Assuming rigid turbine and neglecting the pitch actuator dynamics, leaving the drivetrain rotation variation as the only free degree of freedom (ϕ), and assuming quasi-steady aerodynamics ($\dot{\mathbf{z}}_a = \mathbf{0}$), the closed-loop aero-servo-elastic system equations (5.6) can be written on second order form as

$$\left(I_r + n_g^2 I_g\right)\ddot{\phi} + \left(\frac{\partial Q_g}{\partial \Omega} - \frac{\partial Q}{\partial \Omega} - \frac{\partial Q}{\partial \theta}k_P\right)\dot{\phi} - \frac{\partial Q}{\partial \theta}k_I\phi = 0 \tag{5.22}$$

where I_r and I_g are the rotational inertia of the rotor and generator, respectively, n_g is the gear ratio, $\partial Q/\partial\Omega$ is the gradient of the aerodynamic rotor torque Q with respect to rotor

speed variation (aerodynamic damping of the drivetrain), and $\partial Q/\partial\theta$ is the gradient of the aerodynamic rotor torque with respect to the collective pitch angle (aerodynamic gain). Øye has suggested that the PI gains are set to obtain particular natural frequency ω_Ω and damping ratio ζ_Ω of the speed regulator mode described by the differential eigenvalue problem (5.22), whereby the PI gains can be derived as

$$k_P = \frac{2\,\zeta_\Omega\omega_\Omega\,(I_r + {n_g}^2 I_g) - \frac{\partial Q_g}{\partial\Omega} + \frac{\partial Q}{\partial\Omega}}{-\frac{\partial Q}{\partial\theta}} \quad \text{and} \quad k_I = \frac{\omega_\Omega^2\,\left(I_r + n_g^2 I_g\right)}{-\frac{\partial Q}{\partial\theta}} \tag{5.23}$$

Based on experiments with the old 2 MW turbine sited in Tjæreborg, Øye has suggested that the natural frequency and damping ratio should be 0.1 Hz and 0.6 – 0.7, respectively. Note that the aerodynamic damping $\partial Q/\partial\Omega$ and gain $\partial Q/\partial\theta$ must be evaluated for operation at the steady state values of pitch angle and rotor speed for each wind speed. These aerodynamic gains will therefore change with wind speed and it is beneficial to gain schedule of PI gains accordingly.

Figure 5.2 shows the aerodynamic gain $\partial Q/\partial\theta$ for the NREL turbine assuming constant induced velocities (frozen wake) as function of steady state collective pitch angle. The gains are computed using HAWCStab2 for different wind speeds (red circles), but they are plotted as function of the pitch angle, because the mean pitch angle of the blades denoted θ_m will be used as the gain scheduling parameter. A linear fit (green line) shows that the aerodynamic gain can be approximated by the expression

$$\frac{\partial Q}{\partial\theta} = \left.\frac{\partial Q}{\partial\theta}\right|_0 \left(1 + \frac{\theta_m}{K_K}\right) \tag{5.24}$$

where $\left.\frac{\partial Q}{\partial\theta}\right|_0 \approx -334$ kNm/deg is the aerodynamic gain at zero pitch angle $\theta_m = 0$, and $K_K \approx 5.5$ deg is the pitch angle at which the gain is doubled.

Figure 5.3 shows the aerodynamic drivetrain damping $\partial Q/\partial\Omega$ assuming frozen wake, which shows a clear quadratic dependency on the steady state pitch angle. The aerodynamic damping increases as the blades pitch due to the resulting increased flapwise blade motion in the drivetrain rotation mode. Note that close to zero pitch around the rated wind speed, the aerodynamic damping is small and Øye suggest that it's completely neglected in the pole placement; the effect of this assumption is shown later. Insertion of (5.24) and $\partial Q/\partial\Omega = 0$ into Equation (5.23)

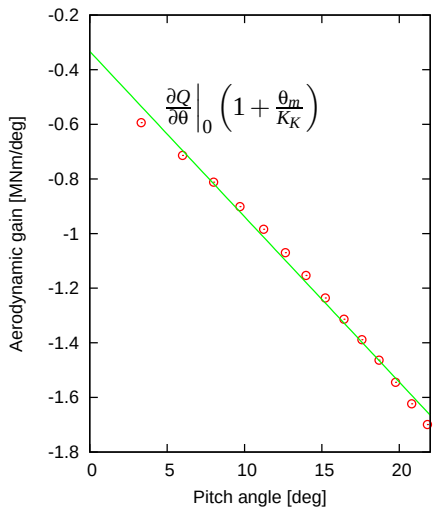

Figure 5.2. Gradient of aerodynamic torque due to change of pitch angle $\partial Q/\partial\theta$ assuming constant induced velocities (frozen wake). Circles: HAWCStab2 computations and line: Linear fit.

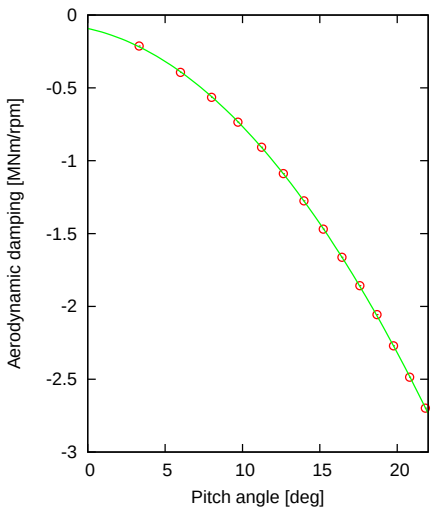

Figure 5.3. Gradient of aerodynamic torque due to change of rotor speed $\partial Q/\partial\Omega$ assuming constant induced velocities. Circles: HAWCStab2 computations and curve: Second order polynomial fit.

yields the PI gains

$$k_P = \eta_K \frac{2\,\zeta_\Omega \omega_\Omega \left(I_r + {n_g}^2 I_g\right) - \frac{\partial Q_g}{\partial \Omega}}{-\left.\frac{\partial Q}{\partial \theta}\right|_0} \quad \text{and} \quad k_I = \eta_K \frac{\omega_\Omega^2 \left(I_r + n_g^2 I_g\right)}{-\left.\frac{\partial Q}{\partial \theta}\right|_0} \tag{5.25}$$

where $\eta_K = 1/(1+\theta_m/K_K)$ is the gain scheduling factor that depend on the mean pitch angle of the three blades. For the NREL turbine, the total rotor and drivetrain inertia is $I_r + n_g I_g \approx 39 \cdot 10^8$ kgm^2 and the constant torque control has been selected $\frac{\partial Q_g}{\partial \Omega} = 0$. With these parameters and the desired natural frequency $\omega_\Omega = 0.1$ Hz and damping ratio $\zeta_\Omega = 0.7$ of the speed regulator mode, the PI gains are set to

$$k_P = \eta_K \cdot 2.2 \text{ rad/(rad/s)} \quad \text{and} \quad k_I = \eta_K \cdot 0.91 \text{ rad/rad} \tag{5.26}$$

The natural frequency $\omega_{lp,\Omega}$ and damping ratio $\zeta_{lp,\Omega}$ of the low-pass filter on the rotor speed are also part of the tuning. The purpose of the filter is to reduce the response of the free-free drivetrain mode, otherwise the collective pitch controller will excite this mode due to the counter phase between the rotor speed measured at the generator side of the drivetrain and the aerodynamic actuation torque from the rotor. The free-free drivetrain frequency of the NREL turbine is approximately 1.7 Hz and the filter frequency is initial set to 0.7 Hz. The damping ratio of the filter is set to 0.8.

To check if the PI gains (5.26) and the low-pass filter parameters give the desired closed-loop behavior of the NREL turbine, the aero-servo-elastic eigenvalues and mode shapes have been computed with HAWCStab2 for the above rated wind speeds. Figure 5.4 shows closed-loop aero-servo-elastic frequencies of the first 13 turbine modes as function of wind speed (green curves), where BW and FW in the mode names refers to backward and forward whirling. The red curve is the frequency of the drivetrain speed regulator mode when the turbine is made stiff, which corresponds to the tuning system in Equation (5.22), except that the second order filter on the rotor speed variation and the unsteady aerodynamic model are active. Hence, the red curve should theoretically be around the tuned frequency of the speed regulator mode $\omega_\Omega \sqrt{1-\zeta_\Omega^2} \approx 0.07$ Hz, however, it is seen to lie above this value with the lowest value being

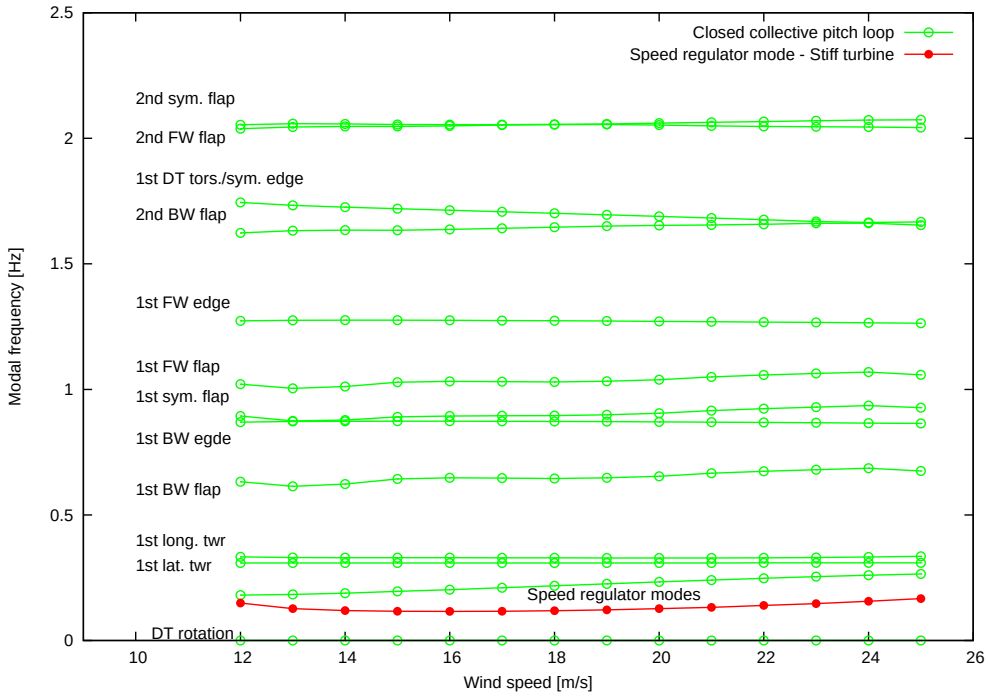

Figure 5.4. Aero-servo-elastic frequencies of the first 13 turbine modes of the 5 MW NREL reference turbine with the collective pitch loop closed. The red curve is the frequency of the drivetrain speed regulator mode when the turbine is made stiff.

0.11 Hz around 16 m/s. This increase is mainly caused by a coupling of the speed regulator mode to the the second order filter at 0.7 Hz. At lower and higher wind speeds, the speed regulator frequency of the the stiff turbine is further increased because the actual aerodynamic gains are larger than those values used in the gain scheduling (5.24), which can be seen in Figure 5.2, where the actual gains (red points) are numerically larger than the gains of the linear fit (green line) used in the gain scheduling for low and high pitch angles.

When the turbine is flexible the frequency of the speed regulator mode is seen to increase further and almost linearly with the wind speed. This increase is mainly caused by the flexibility of the blades that deflect as the aerodynamic loading changes due to the blade pitching which is part of the speed regulator mode shape. The rotor and drivetrain are no longer performing a rigid body rotation with corresponding high inertia, hence the frequency increases due to the lower effective inertia involved in the mode. The linear increase with the wind speed is caused by the pitching of the blades whereby more of the dominating flapwise blade motion couples with the speed regulator mode.

The closed-loop frequencies of the remaining modes in Figure 5.4 are similar to the open-loop aeroelastic frequencies, except that the frequency of the first free-free drivetrain torsion mode decreases with wind speed instead of remaining almost constant. This wind speed dependency can also be explained by the increased coupling with the flapwise blade motion due to the pitch action in this mode. Note that there is a rigid drivetrain rotation mode with zero frequency (and zero damping) expressing that aerodynamic forces and generator torque are independent of azimuthal rotor position.

Figure 5.5 shows the corresponding closed-loop aero-servo-elastic damping ratios of the first 12 turbine modes (the drivetrain rotation mode with zero damping is not shown) as function of wind speed (green curves). The red curve is the damping ratio of the drivetrain speed regulator mode when the turbine is made stiff, which should correspond to the tuning value of 0.7. The increasing damping with wind speed is mainly due to the increasing aerodynamic damping of

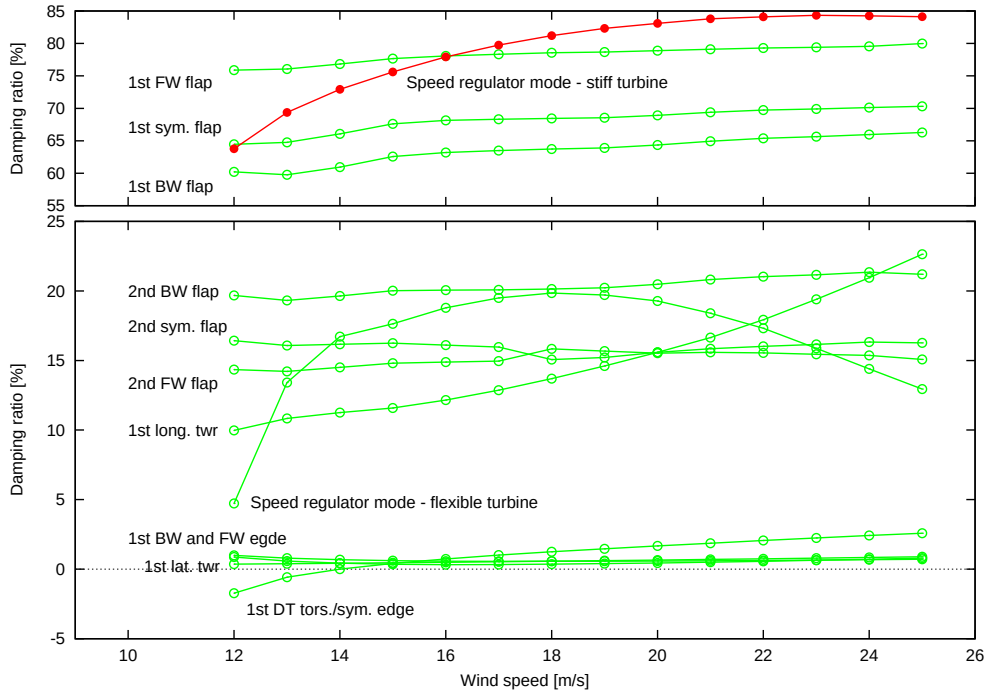

Figure 5.5. Aero-servo-elastic damping ratios of the first 12 turbine modes (rigid body drive-train rotation mode is removed) of the 5 MW NREL reference turbine with the collective pitch loop closed. The red curve is the damping of the drivetrain speed regulator mode when the turbine is made stiff.

the drivetrain (cf. Figure 5.3) which is not included in the gain scheduling.

The closed-loop damping of the speed regulator mode is dramatically decreased by the flexibility of the turbine. Similar to risk of controller induced vibrations of the free-free drivetrain torsion mode, the flexibility of the blades will cause a phase difference between the rotor speed measured at the generator and the aerodynamic rotor torque obtained by the pitch action, which is not included in the tuning model. Furthermore, the longitudinal motion of the flexible tower due to the pitch action will cause a phase difference between the pitch action and the obtained aerodynamic torque that is also not included in the tuning model. These effects of the turbine flexibility are amplified by the second order rotor speed filter; if the filter frequency is decreased from 0.7 Hz to 0.5 Hz, the closed-loop damping of the speed regulator mode even becomes negative at operation at 12 m/s (results not shown), where the aerodynamic damping of the drivetrain is lowest (cf. Figure 5.3). For this wind speed, the closed-loop damping of the first free-free drivetrain torsion mode. This controller induced instability, due to insufficient filtering of the response of this mode, can be avoided by lowering the filter frequency; however, noting that a too low frequency will cause negative closed-loop damping of the speed regulator mode. The highest minimum damping of the two modes at 12 m/s is obtained by a filter frequency of 0.55 Hz.

The closed-loop damping ratios of the remaining modes in Figure 5.5 are similar to the open-loop aeroelastic damping ratios, except that the damping of the first longitudinal tower bending mode is slightly higher due to the collective pitch controller.

Tuning of cyclic pitch controller

The lead angle, gains, and low-pass filter of the cyclic pitch controller are now tuned for operation at 17 m/s. A gain scheduling similar to the scheduling of the collective pitch controller gains will probably improve the cyclic pitch controller performance; however, it has not been investigated in the current implementation. The tuning is performed by first selecting a lead angle, and then determining the PI gains by the Ziegler-Nichols method for three different frequencies of the low-pass filter.

The lead angle must compensate the azimuthal lag of the rotor moment obtained from a cyclic pitch action, which is mainly caused by the flapwise motion of the blades that couples through the angle of attack to the aerodynamic forces. Figure 5.6 illustrates a typical lag angle to the azimuthal position of maximum combined tilt and yaw rotor moment due to a 1P cyclic cosine pitch signal. It can be estimated from the open-loop frequency response functions (FRFs) from cosine pitch demand signal $\theta_{\cos}$ to rotor tilt and yaw moments m_{tilt} and m_{yaw}. These FRFs are plotted for the NREL turbine in the top of Figure 5.7. The bottom plot shows the lag angle computed from the magnitudes of the moments as $\arctan(|m_{\text{yaw}}|/|m_{\text{tilt}}|)$. A stationary input (zero frequency) on the cosine pitch signal, corresponding to a 1P input, yields a lag angle of approximately 30 deg, and it remains between 10–40 deg up to 2 Hz. The main objectives of the cyclic pitch controller are the reductions of the 1P components of the blade root moments, corresponding to the stationary components of the rotor moments, and the lead angle is therefore set to $\psi_0 = 30$ deg.

The purpose of the identical low-pass filters on the tilt and yaw rotor moments is to limit the pitch action to an appropriate frequency band. For pitch action beyond the frequency of the first torsional blade mode, the blade torsion will be in counter phase with the pitch torque. Although, the pitch actuator dynamics is expected to add some mechanical low-pass filtering of the pitch demand signal, there is a theoretical risk of exciting the torsional whirling modes [1] by the cyclic pitch controller without these low-pass filters. The main purpose of the cyclic pitch controller is to reduce the 1P blade and shaft bending loads, however, there has been a discussion of the use of cyclic pitch to reduce loads at higher harmonics than 1P by letting the cyclic controller operate in a wider frequency band. To investigate the effect of the filter frequency, the PI gains are now tuned by the Zielger-Nichols method for $\omega_{lp,c} = 0.4$ Hz (2P),

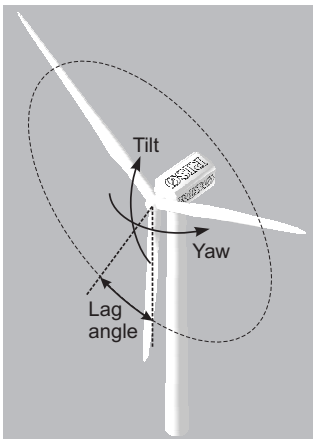

Figure 5.6. Lag angle to azimuthal position of maximum combined rotor moment due to cyclic cosine pitch for the NREL turbine at 17 m/s.

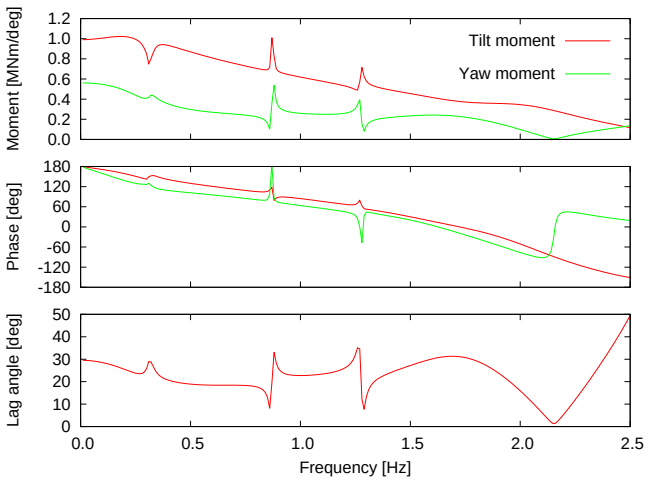

Figure 5.7. Magnitude and phase of open-loop frequency response functions (top two plots) from cosine pitch demand signal $\theta_{\cos}$ to rotor tilt and yaw moments m_{tilt} and m_{yaw} for the NREL turbine at 17 m/s. Bottom plot: The lag angle computed from the magnitudes of the moments as $\arctan(|m_{yaw}|/|m_{tilt}|)$.

$\omega_{lp,c} = 0.8$ Hz (4P), and $\omega_{lp,c} = 5.0$ Hz (25P). The damping ratios of all filter are set to $\zeta_{lp,c} = 0.9$.

To determine the ultimate proportional gain, the integral gain is set to zero and then the aero-servo-elastic eigenvalues of the NREL turbine with both the collective and cyclic pitch loops closed are computed for increasing proportional gains. Figure 5.8 shows these closed-loop eigenvalues in a pole plot limited from -7 s^{-1} to 3 s^{-1} on the real (damping) axis and from 0 Hz to 5 Hz on the frequency axis.

The larger red circles present the open-cyclic-pitch-loop eigenvalues, where the tuned collective pitch loop is closed but the PI gains of the cyclic pitch controller are zeroed. Eigenvalues related to structural turbine modes have been identified and named in the plot from animations. Note that the named eigenvalues up to the second symmetric flap mode correspond to the modal frequencies and damping ratios seen in Figures 5.4 and 5.5 at the wind speed of 17 m/s. The many unidentified eigenvalues on the real axis and the line at 0.2 Hz (1P) are modes with dominating aerodynamic components not related to a structural mode.

As the proportional gain is increased with steps of 0.2 deg/MNm, the eigenvalues of modes that involve asymmetric rotor motion are affected and move either left (higher damping) or right (less damping), only small changes in the frequencies of these modes are observed. The ultimate gain k_u is the proportional gain when the lowest damped mode crosses into the right half plane and becomes negatively damped. Figure 5.9 shows a zoom on the closed-loop aero-servo-elastic eigenvalues in Figure 5.8, where it is seen that the second backward whirling edgewise mode is first to become negatively damped at a proportional gain of $k_P^c = 1.4$ deg/MNm. The next crossings occur the first and second forward whirling flapwise modes at around $k_P^c = 2.0$ deg/MNm. A crossing of these two flapwise whirling modes will be significantly more dominating in the turbine response than a crossing of second backward whirling mode due to their direct coupling between the flapwise vibrations to the rotor moments, which can be seen in Figure 5.10 showing the FRF of the rotor moments for $k_P^c = 2.0$ deg/MNm (and $k_I^c = 0.0$) due to a harmonic variation in vertical wind shear, where zero frequency corresponds to a stationary shear. The ultimate gain is therefore set to $k_u = 1.9$ deg/MNm and the ultimate period $T_u = 1/1.3 \approx 0.77$ s is obtained from the frequency of the second forward whirling flap mode as it crosses into the right half-plane. Using the Ziegler-Nichols method, the PI gains of

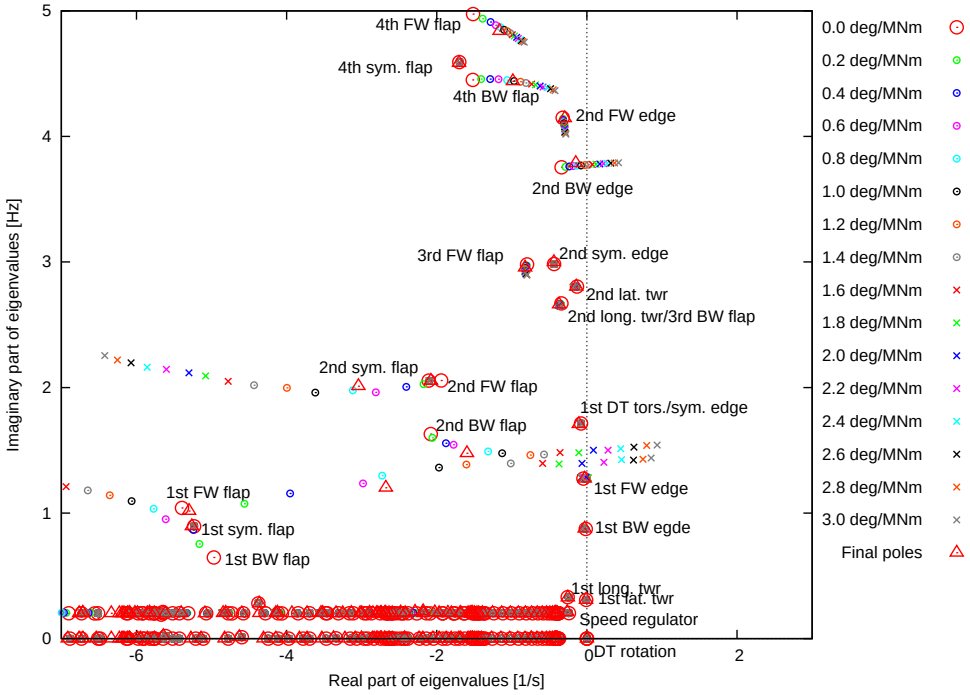

Figure 5.8. Pole plot of closed-loop aero-servo-elastic eigenvalues for the NREL turbine at 17 m/s with zero integral and different proportional cyclic feedback gains and with 25P (5 Hz) low-pass filtering on rotor moments. The pole plot is limited from -7 s^{-1} to 3 s^{-1} on the real (damping) axis and from 0 Hz to 5 Hz on the frequency axis.

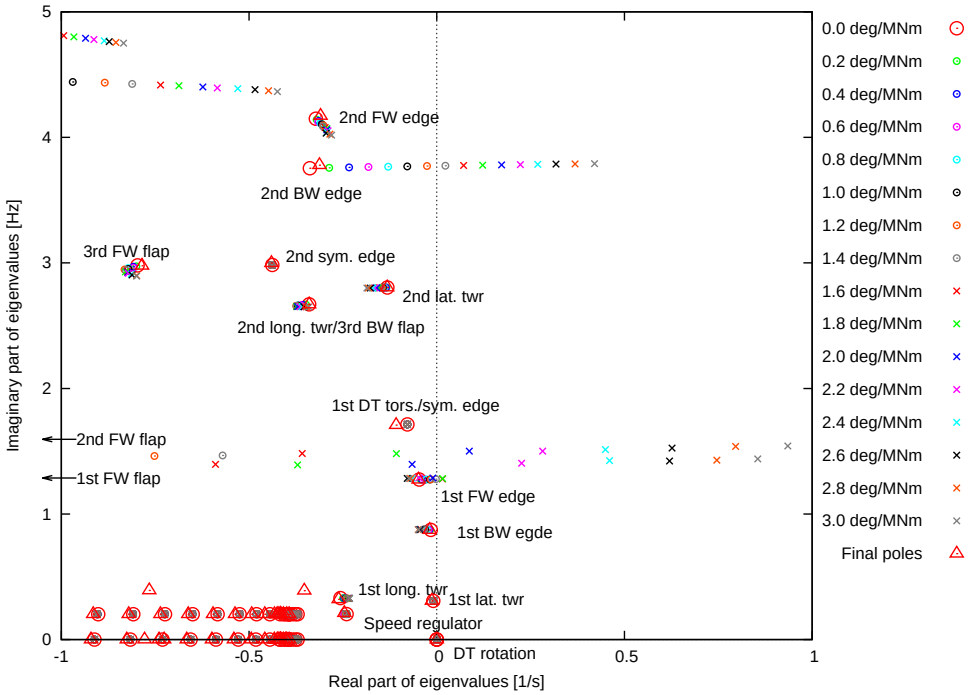

Figure 5.9. Zoom on the closed-loop aero-servo-elastic eigenvalues in Figure 5.8 ranging from -1 s^{-1} to 1 s^{-1} on the real (damping) axis and from 0 Hz to 5 Hz on the frequency axis.

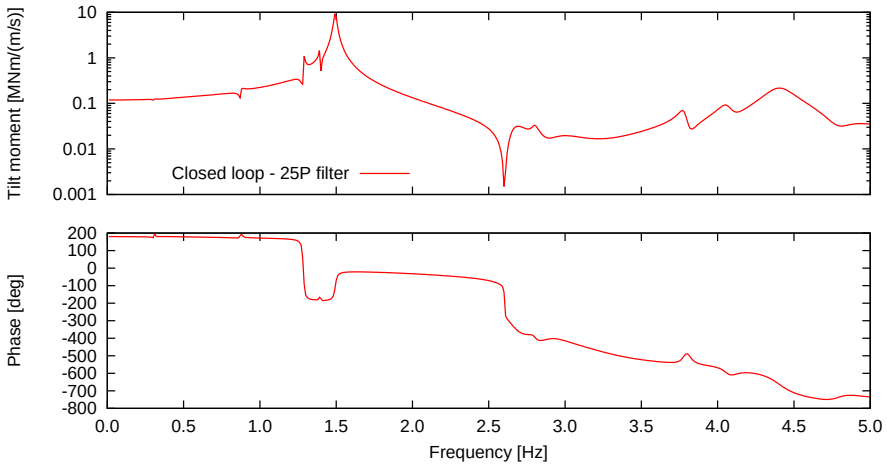

Figure 5.10. Frequency response function of the rotor tilt moment due to harmonic variation in vertical wind shear for the NREL turbine at 17 m/s with the cyclic pitch controller gains $k_P^c = 2.0$ *deg/MNm and* $k_I^c = 0.0$.

the cyclic controller with low-pass filters at 25P are therefore set to

$$k_P^c = 0.4k_u = 0.76 \text{ deg/MNm} \quad \text{and} \quad k_I^c = \frac{1.2k_P^c}{T_u} \approx 1.2 \text{ deg/s/MNm} \tag{5.27}$$

The PI gains are tuned similarly when the filter frequency is 2P and 4P, except that the critical modes determining the ultimate gains and ultimate periods are different.

Figures 5.11 and 5.12 show the closed-loop eigenvalues for the 4P low-pass filtering of the rotor moments, where the first backward whirling edgewise mode is the first to become negative damped at the proportional gain of 1.2 deg/MNm, which is used as the ultimate gain. The modal frequency is approximately 0.88 Hz giving an ultimate period of 1.1 s, whereby the PI gains of the cyclic controller with 4P filters are set to

$$k_P^c = 0.4k_u = 0.48 \text{ deg/MNm} \quad \text{and} \quad k_I^c = \frac{1.2k_P^c}{T_u} \approx 0.51 \text{ deg/s/MNm} \tag{5.28}$$

Note in Figure 5.12 that the eigenvalues related to the filters, denoted “filter poles”, cross into the right half plane at slightly higher proportional gains. This controller induced instability is caused by the shift in the phase between measured rotor moments and the feedback to the cyclic pitch action due to the filters.

Figures 5.13 and 5.14 show the closed-loop eigenvalues for the 2P low-pass filtering of the rotor moments, where the eigenvalues related to the filters are the first to cross into right half plane at the proportional gain of 2.6 deg/MNm, which is used as the ultimate gain. The frequency is approximately 0.6 Hz giving an ultimate period of 1.7 s, whereby the PI gains of the cyclic controller with 2P filters are set to

$$k_P^c = 0.4k_u = 1.04 \text{ deg/MNm} \quad \text{and} \quad k_I^c = \frac{1.2k_P^c}{T_u} \approx 0.75 \text{ deg/s/MNm} \tag{5.29}$$

Comparing the gains for the three different filter frequencies, it is seen that the gains do not increase with the decreasing filter frequency, as one may have excepted due to feedback reduction effect of a lower filter frequency. The gains for the 4P filter (5.28) are lower than the gains for the 2P filter (5.29), which can be explained by the proximity of the 4P (0.8 Hz) and the 0.88 Hz frequency of the first backward whirling mode that is the critical mode determining the ultimate gain for this filter.

The effects of the cyclic pitch controllers with different filter frequencies on the rotor moments are illustrated in Figure 5.15, showing Bode plots of the open- and closed-loop FRFs of the rotor tilt moment due to a harmonic variation in vertical linear wind shear computed with HAWCStab2, where a stationary wind shear corresponds to zero frequency. A similar plot can

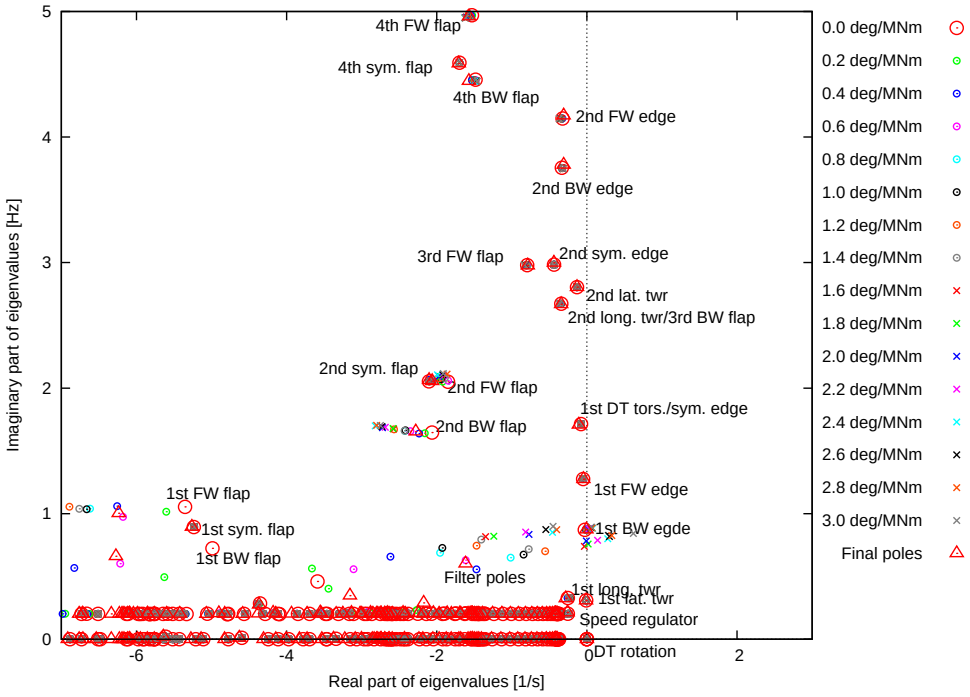

Figure 5.11. Pole plot of closed-loop aero-servo-elastic eigenvalues for the NREL turbine at 17 m/s with zero integral and different proportional cyclic feedback gains and with 4P (0.8 Hz) low-pass filtering on rotor moments. The pole plot is limited from -7 s^{-1} to 3 s^{-1} on the real (damping) axis and from 0 Hz to 5 Hz on the frequency axis.

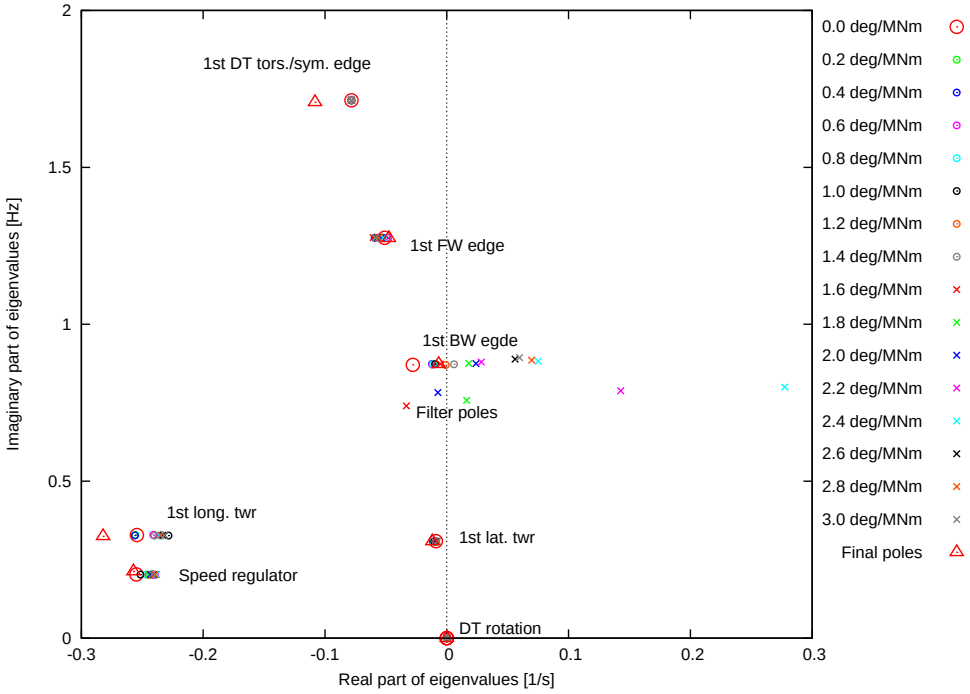

Figure 5.12. Zoom on the closed-loop aero-servo-elastic eigenvalues in Figure 5.11 ranging from -0.3 s^{-1} to 0.3 s^{-1} on the real (damping) axis and from 0 Hz to 2 Hz on the frequency axis.

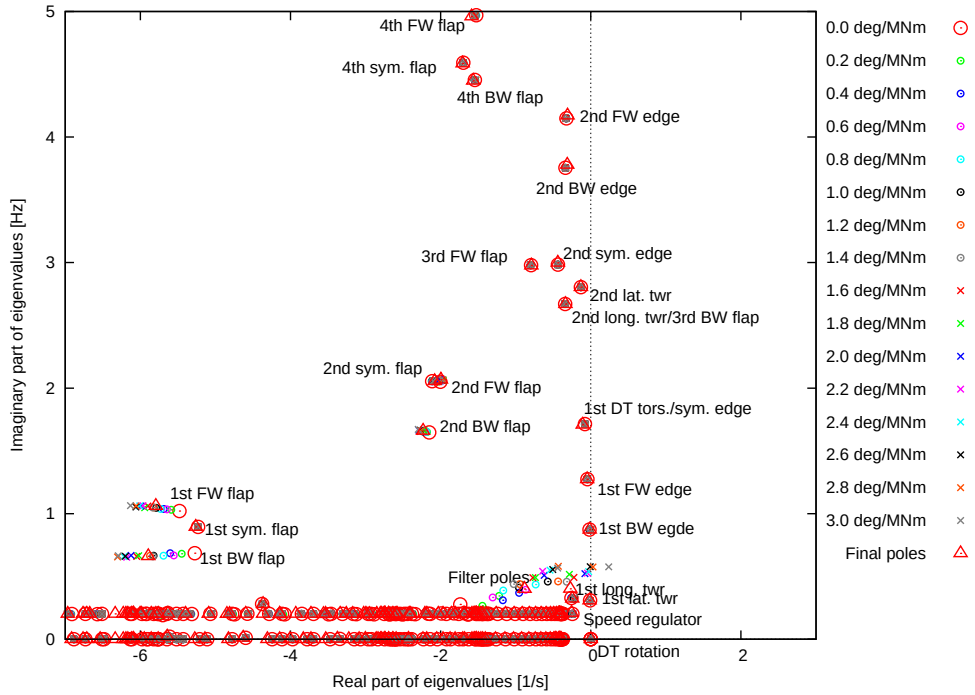

Figure 5.13. Pole plot of closed-loop aero-servo-elastic eigenvalues for the NREL turbine at 17 m/s with zero integral and different proportional cyclic feedback gains and with 2P (0.4 Hz) low-pass filtering on rotor moments. The pole plot is limited from -7 s^{-1} to 3 s^{-1} on the real (damping) axis and from 0 Hz to 5 Hz on the frequency axis.

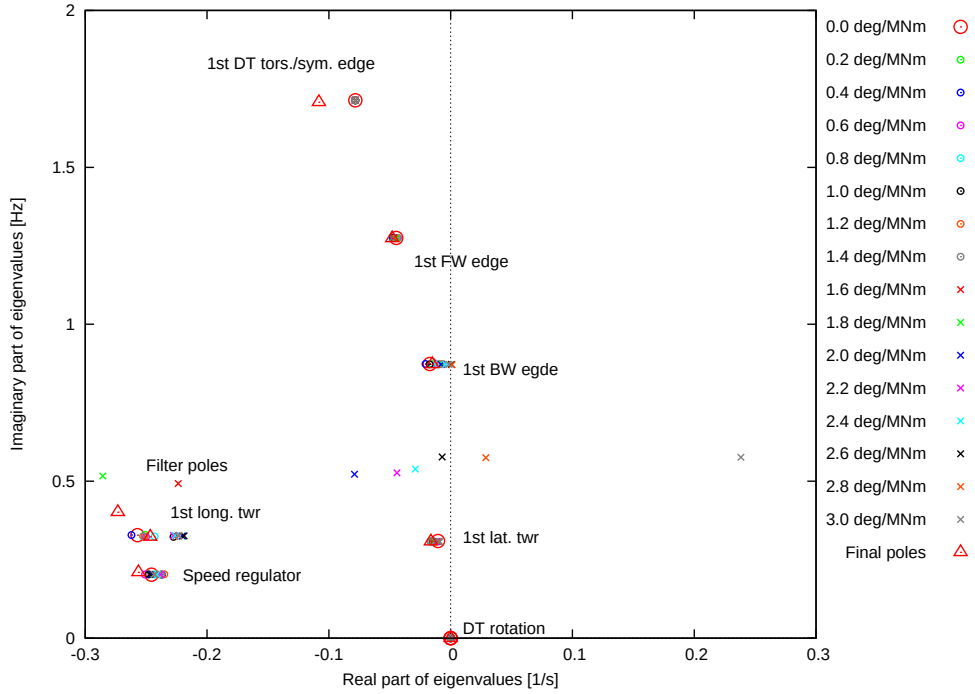

Figure 5.14. Zoom on the closed-loop aero-servo-elastic eigenvalues in Figure 5.13 ranging from -0.3 s^{-1} to 0.3 s^{-1} on the real (damping) axis and from 0 Hz to 2 Hz on the frequency axis.

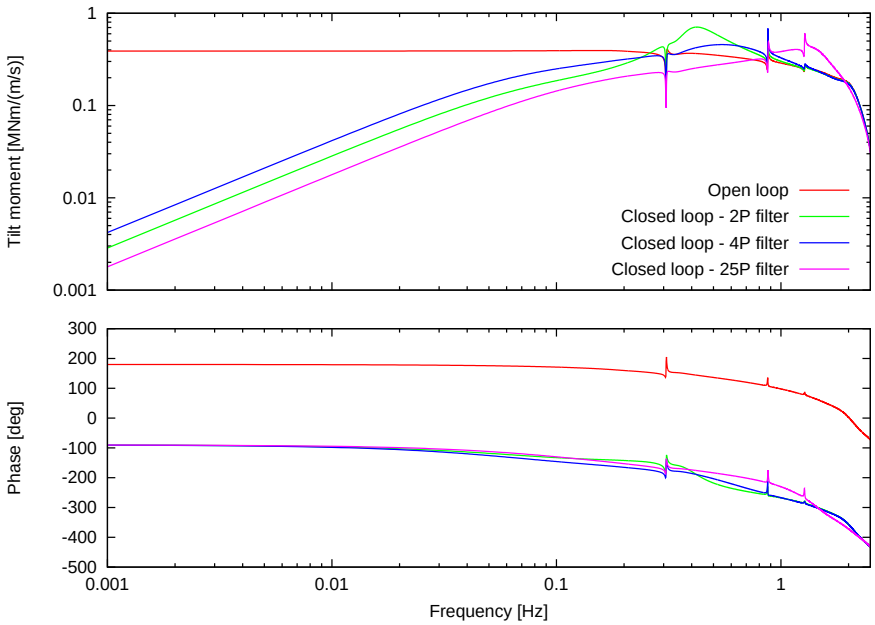

Figure 5.15. Frequency response functions of the rotor tilt moment due to harmonic variation in vertical wind shear for the NREL turbine at 17 m/s in open- and closed-cyclic-pitch-loop using three different filter frequencies.

be made for the rotor yaw moment due to a vertical linear wind shear. Note that the tilt and yaw rotor moments exhibit symmetric properties by being interchanged for harmonic variations in horizontal linear wind shear.

The low frequency response is significantly reduced by the cyclic pitch controller. The steady state tilt rotor moment become zero for all filters in the limit of zero frequency, corresponding to zero 1P flapwise blade loads due to a stationary linear vertical wind shear. Turbulence can be Fourier transformed spatially in the azimuthal direction (due to periodicity). The first harmonics are the vertical and horizontal linear shears, which will capture the largest structures of the turbulence with the highest energy and they will vary slowly in time [10]. From Figure 5.15, it is predicted that the closed-loop flapwise blade root moment due to these components will be lowest for the controller with the 25P filter, second lowest with the 2P filter, and highest with the 4P filter.

The closed-loop response of the controller with the 2P filter shows a significant but damped response peak at 2P (0.4 Hz). It is caused by the phase shift of the measured rotor moments by the filter, whereby the cyclic controller is increasing the response at around the filter frequency. A similar but more damped peak is seen for the 4P filter slightly below 4P (0.8 Hz). This small shift in resonance frequency of the filter is probably caused by its coupling with the first backward whirling edgewise mode with a sharp resonance peak at approximately 0.88 Hz.

Simulations in HAWC2

To check the tuning of the controller and evaluate the efficiency of the cyclic pitch controller, the response of the NREL turbine has been simulated with HAWC2 at 17 m/s in Class B normal turbulence and wind shear exponent of 0.2 without and with the cyclic pitch controller using different filter frequencies. The collective pitch controller is active in all simulations using constant torque control and the same turbulence box. Simulations are run for 700 s and the first 100 s are discarded as transients.

Figure 5.16 shows the wind speed at hub height, rotor speed at the generator, pitch angle and flapwise blade root moment of blade 1, and moment at the yaw bearing from the HAWC2 sim-

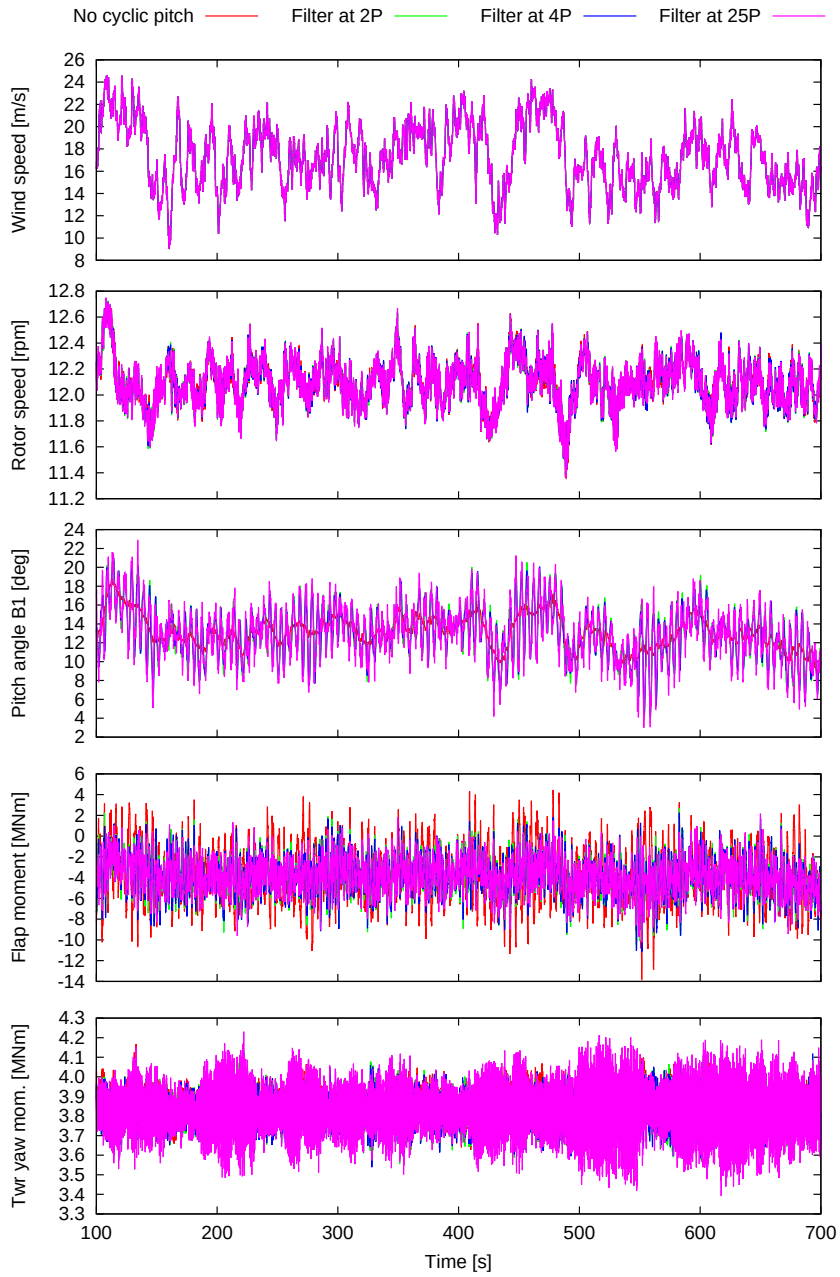

Figure 5.16. Time series from simulations of the NREL turbine at 17 m/s in Class B normal turbulence and wind shear exponent of 0.2 without cyclic pitch and with cyclic pitch using different filter frequencies.

ulations. There are significantly larger pitch actions and indications of lower flapwise moments when the cyclic pitch loop is closed. These observations are more clear in Figure 5.17 showing a 20 s section of the same time series from 370 s and onwards. Nearly periodic closed-loop pitch variations with a period of 5 s corresponding to 1P (0.2 Hz) are seen in the first part of this 20 s section, where also the closed-loop responses of the flapwise blade moment are reduced. The wind speed at hub height drops significantly towards the end of this 20 s section of the simulation, which indicates a larger turbulence structure that dominates the deterministic wind shear and thereby reduces the effectiveness of the cyclic controller. The variations yaw moment seem to be higher for the closed-loop responses. Note that the pitch actions have a larger frequency content for the cyclic controller with the 25P filter, as expected.

Figure 5.18 shows the Power Spectral Densities (PSDs) of the flapwise blade root moment

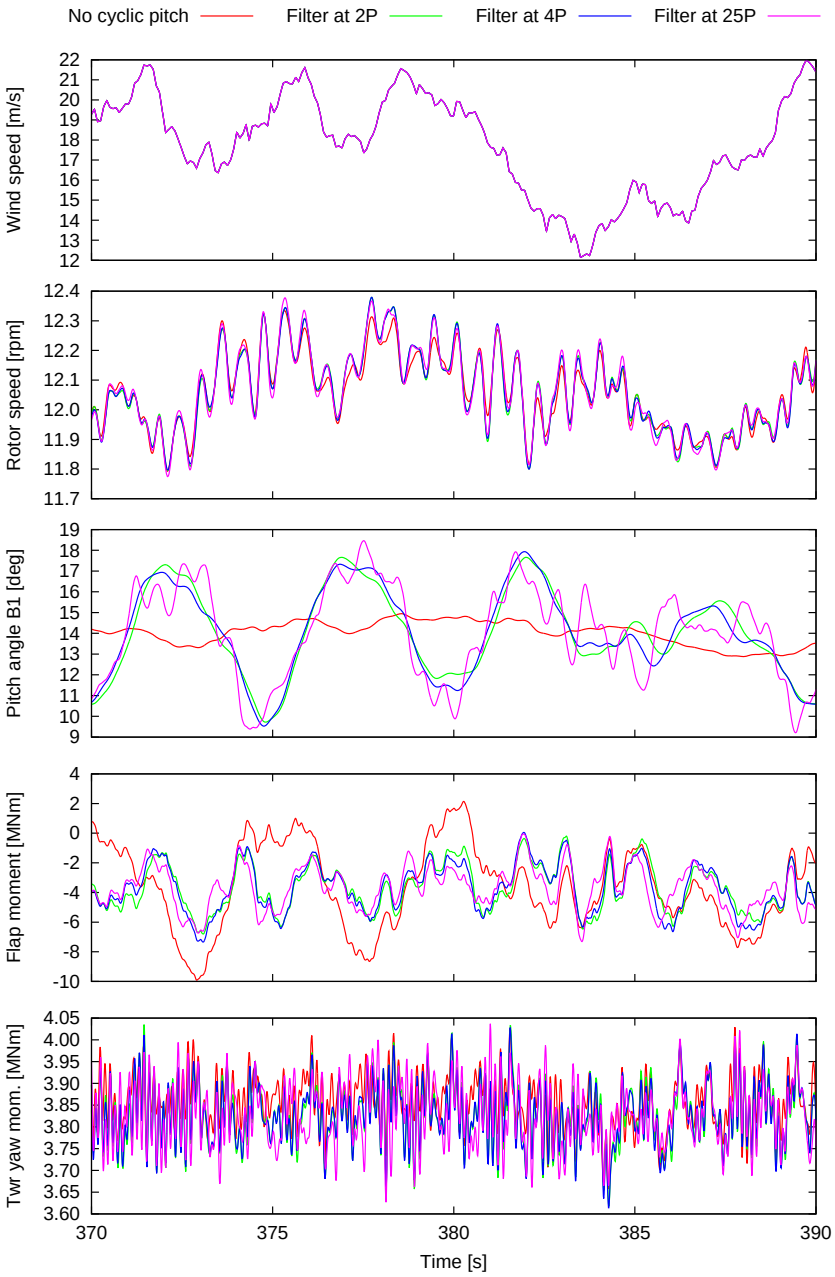

Figure 5.17. Zoom of the time series in Figure 5.16.

and pitch angle of blade 1, and the tower yaw moment. Here, the 1P blade load variations due to wind shear are reduced by a factor of 20 – 100 depending on the filter frequency used in the cyclic pitch controller. The 2P peak is slightly increased for the two controllers with low frequency filters. The pitch action is mainly on 1P but the level of pitch variations is consistently higher when the cyclic pitch controller loop is closed, especially with the 25P filter. Below 1P, the yaw moment is reduced similar to the flapwise moment but it is increased at 3P for the low filter frequencies and at 6P for the high filter frequency. Note that there is a response at 2P for the filter with this frequency.

Table 5.1 shows the 1 Hz equivalent fatigue loads of the flapwise blade root moment (material exponent of 10), yaw moment at tower top/nacelle connection (material exponent of 4), and the mean pitch actuation power computed from the HAWC2 simulations shown in Figure 5.16. The mean pitch actuation power is approximated by integration of the blade root torsional moment

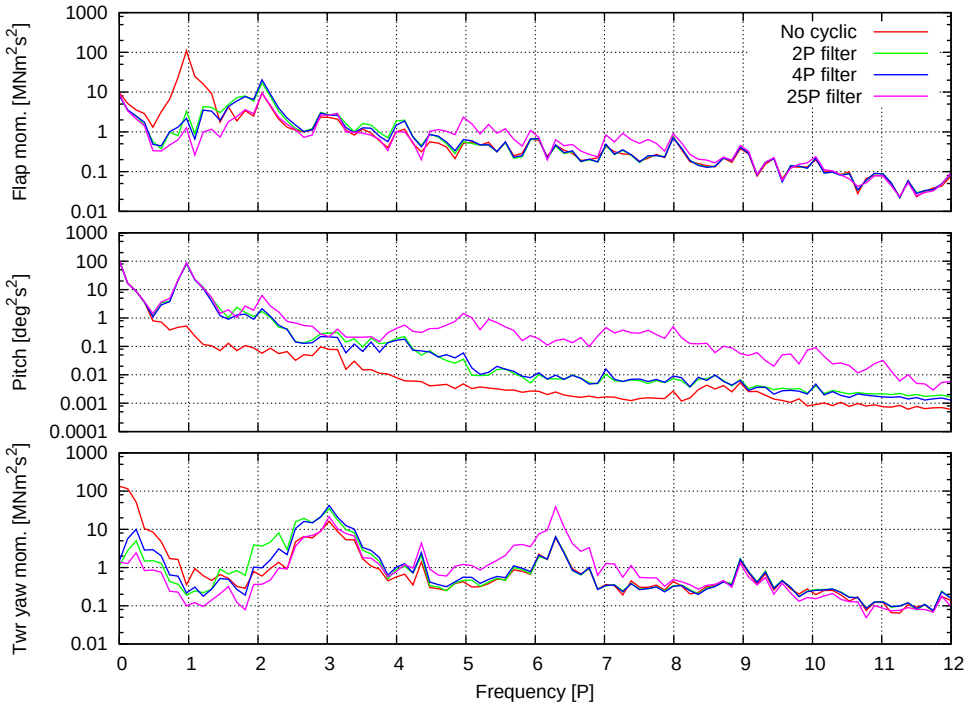

Figure 5.18. Power Spectral Densities (PSDs) of flapwise blade root moment, tower top yaw moment, and pitch angle on blade 1 based on the time series in Figure 5.16.

Sensor	No cyclic	2P filter	4P filter	25P filter
Fatigue flap moment [MNm/index]	10.3/100	7.65/75	7.77/75	7.07/69
Fatigue tower yaw moment [MNm/index]	6.64/100	7.42/112	7.49/113	8.01/121
Mean pitch act. power [kW/index]	0.17/100	1.02/591	1.03/597	2.02/1174

Table 5.1. Comparison of 1 Hz equivalent fatigue loads for the flapwise blade root (exponent of 10) and tower top yaw (exponent of 4) moments, and mean pitch actuator power computed from the 10 min simulations shown in Figure 5.16.

times the pitch velocity divided by 600 s. It is only intended for comparison, because there is no model of bearing friction included in the simulations, which may significantly increase the actual required actuation power.

The indices for the closed-loop responses show that the flapwise fatigue loads are reduced by 25 % with the low filter frequencies and by 31 % for the high filter frequency. The expenses of these load reductions are significant increases in yaw moment at the tower top/nacelle connection of about 12 % for the low filter frequencies and 21 % for the high filter frequency. The pitch actuator power (and pitch travel which is not shown) are significantly increased; six times higher mean actuator power for the low filter frequencies, and even twelve times higher for the high filter frequency.

5.3 Conclusion

New possibilities of closed-loop aero-servo-elastic eigenvalue and frequency-domain analyses of wind turbines based on the recent code HAWCStab2 have been described. Linear models of actuators and controllers have been added to the linear aeroelastic models, which has enabled closed-loop aero-servo-elastic eigenvalue and frequency-domain analysis useful for controller tuning and for aero-servo-elastic stability analysis. These capabilities have been illustrated by tuning and analyzing the closed-loop response of the NREL 5 MW turbine with two combined collective and cyclic pitch controllers for above rated wind speed operation. The collective pitch

controller is tuned by pole placement of a low order model, and the aero-servo-elastic full state eigenvalue analysis showed that the turbine flexibility has a large impact on the closed-loop response. The cyclic pitch controller is tuned by first computing the lead angle from the open-loop frequency response, and then tuning the cyclic feedback gains from blade root moments using the Ziegler-Nichols method based on aero-servo-elastic full state eigenvalue analysis. Time simulations with HAWC2 shows that the tuned controllers are able to reduce the fatigue flapwise blade root moments by up to 25 %, however, at the expense of six times higher pitch actuation and up to 21 % higher fatigue yaw moment at the tower top. HAWCStab2 is currently being extended to facilitate the derivation of linear first-principle reduced order models for model-based controllers, which for instance will enable optimal control that lowers the flapwise blade moment without increasing the yaw moment on the tower.

References

[1] M. H. Hansen. Aeroelastic instability problems for wind turbines. *Wind Energy*, 10:551–577, 2007.

[2] M. A. Crisfield. *Non-linear Finite Element Analysis of Solids and Structures*, volume 2. Wiley, New York, 1997.

[3] L. Meirovitch. *Methods of Analytical Dynamics*. McGraw-Hill, New York, 1970.

[4] P. F. Skjoldan and M. H. Hansen. On the similarity of the coleman and lyapunov-floquet transformations for modal analysis of bladed rotor structures. *Journal of Sound and Vibration*, 327:424–439, 2009.

[5] R. W. Clough and J. Penzien. *Dynamics of Structures*. McGraw-Hill, Inc., 2nd edition, 1993.

[6] M.H. Hansen and B. S. Kallese. Servo-elastic dynamics of a hydraulic actuator pitching a blade with large deflections. In *Proceedings of The Science of Making Torque from Wind*, Lyngby, 2007.

[7] M. H. Hansen, A. Hansen, T. J. Larsen, S. Øye, P. Sørensen, and P. Fuglsang. Control design for a pitch-regulated, variable speed wind turbine. Technical Report Risø–R–1500(EN), Risø National Laboratory, Denmark, January 2005. (Available from www.vindenergi.dtu.dk).

[8] T. J. Larsen, H. Aa. Madsen, and K. Thomsen. Active load reduction using individual pitch based on local blade flow measurement. *Wind Energy*, 8:67–80, 2005.

[9] W. Johnson. *Helicopter Theory*. Princeton University Press, New Jersey, 1980.

[10] J. Mann. Wind Field Simulation. *Prob. Engng. Mech., Elsevier Science*, vol. 13(no. 4):pp. 269–283, 1998.

6 Lateral tower vibrations on offshore turbines

Author: Bjarne S. Kallesøe, Niels Troldborg, Niels N. Sørensen, and Anders Yde

6.1 Introduction

This chapter deals with different aspects of lateral tower vibration. Offshore turbines can experience situations where the wave direction is orthogonal to the wind direction and thereby adding energy to the lateral tower mode. The first tower resonance frequency is often included in the wave frequency band with the implication that the wave loading can lead to resonance excitation of the very low aerodynamically damped lateral tower mode, resulting in a high fatigue contribution on the tower and foundation.

This chapter looks into three aspects of this problem: First, an analysis of the aerodynamic damping contribution to the first lateral tower mode; then, a study of using active generator control to reduce the lateral tower fatigue; and finally, a study of the feasibility of using a passive yaw slip to limit excessive lateral tower vibrations.

6.2 Aerodynamic Damping of Lateral Rotor Oscillations

Aeroelastic stability and simulations tools based on the Blade Element Momentum (BEM) method shows very low aerodynamic damping for the first lateral tower mode. BEM is derived on basis of a balance of momentum and kinetic energy in a streamtube enclosing the rotor. Lateral rotor motion affects the BEM model through changes in angle of attack, changes in relative wind speeds and, if present, yaw correction models. It has been questioned if BEM yields the correct aerodynamic forces for these lateral motions of the rotor. In this work, the aerodynamic work on lateral harmonic rotor motion is computed by both BEM and from computational fluid dynamics (CFD) using respectively a fully resolved rotor geometry and an actuator line (AL) representation of the turbine. The computations from BEM, AL and the fully resolved rotor CFD shows a reasonable agreement. The aerodynamic work is converted into equivalent damping for the first lateral tower mode, and the difference in damping contributions from the different models were found to be negligible. Finally, the pure lateral rotor motion is compared to the true first lateral tower mode motions, and the aerodynamic damping of this tower mode is described.

6.2.1 Fully resolved rotor CFD computations

The in-house flow solver EllipSys3D is used for the three resolved CFD computations presented in this work. The code is developed in co-operation between the Department of Mechanical Engineering at the Technical University of Denmark and the Wind Energy Division at Risø-DTU, see [1, 2] and [3].

The EllipSys code is second order accurate in time, using a second order backward differencing time discretization and sub-iteration within each time step. In the present computations, the diffusive terms are discretized with a second order central differencing scheme. The convective fluxes are computed using the third order accurate QUICK scheme of Leonard [4].

In the present work the turbulence in the boundary layer is modeled by the k-ω Shear Stress Transport (SST) eddy viscosity model [5] in its standard RANS form.

To account for the rotation and translation of the rotor, a deforming mesh (DM) formulation is used in a fixed frame of reference. In the present study the whole mesh is moved as a solid body to enforce the rotor rotation and axial translation, even though the DM option is implemented in a generalized way allowing arbitrary deformation of the computational mesh. To assure that

no artificial mass sources are generated by the mesh deformation, the mesh velocities needed for the convective terms are computed enforcing the space conservation law, as described by [6]. The following inflow parameters are used for the fully resolved CFD: The inflow velocity is specified according to the free wind conditions 6, 12, and 22 m/s, a density of 1.225 kg/m^3 and the viscosity was 1.78×10^{-5} kg/m/s. A standard low turbulent laminar inflow is obtained by using a specific dissipation rate $\omega = 1 \times 10^6$ s^{-1} and a turbulent kinetic energy $k = 1.0 \times 10^{-2}$ m^2/s.

For grid generation, the full three bladed rotor is modeled to allow the cross stream movement of the rotor, emulating the tower vibrations. The mesh uses an O-O-topology, where the individual blades are meshed with 256 cells around the blade chord, 128 cells in the spanwise direction and a 64×64 block at the blade tip. In the normal direction, 128 cells are used. The height of the cells at the wall is $\sim 5 \times 10^{-6}$ m to resolve the boundary layers and keep y^+ around 1. The outer boundary of the domain is located $\sim$ 1100 meters from the rotor center or approximately 10 rotor diameters away. The grid generation is performed with the 3D enhanced hyperbolic grid generation program HypGrid3D which is a 3D version of the 2D hyperbolic grid generator described in [7]. The total number of cells used is 14 million.

Inlet conditions corresponding to the described cases are specified at the upstream part of the outer boundary, while outlet conditions corresponding to a fully developed flow are used at the downstream part of the outer domain boundary. No-slip conditions are applied at the rotor surface. The edgewise vibration computations are performed as transient simulations, using a time step of 1.267×10^{-3} s along with six sub-iterations within each time step.

6.2.2 Actuator line computations

The actuator line (AL) model, developed by Sørensen and Shen [8], combines three-dimensional Navier-Stokes simulations of the flow field with a technique in which body forces are distributed radially along lines representing the blades of the wind turbine using a suitable smearing function. The body forces acting on the blades are determined using a blade element approach combined with tabulated two-dimensional airfoil data. The main advantage of representing the blades by airfoil data is that the geometry of the blades does not need to be meshed and that it is not required to resolve the boundary layer around the blades, which result in a considerable reduction in computer resource requirements.

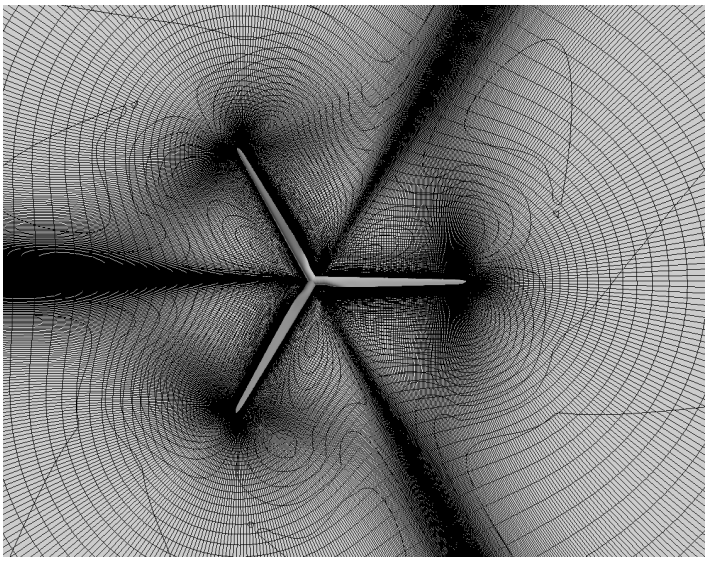

Figure 6.1. Detail of the mesh for the resolved rotor computations, showing the rotor geometry and a slice through the rotor plane.

In the present AL simulations, the flow field is computed using EllipSys3D, as for the full rotor CFD. The convective terms are discretized using a hybrid scheme combining the third order accurate QUICK (10%) scheme and the fourth order CDS scheme (90%). All AL computations are furthermore conducted as Large Eddy Simulations (LES) employing the mixed sub-grid scale (SGS) model [9]. The mixed SGS viscosity model depends on a filter function and some empirically determined constants, which are chosen in accordance with previous work [10].

The time step in the AL simulations is $\Delta t = 3.5 \times 10^{-3} R/U_0$ where R is the radius of the turbine and U_0 the free-stream velocity. The Reynolds number based on rotor radius is $Re = 10^{-5}$.

The AL computations are conducted in a cubic computational domain with side length $L_x = L_y = L_z = 24R$ and the turbine is placed with its point of rotation in the domain center. A high concentration of grid points is distributed equidistantly in a cubic region around the turbine. The side length of the equidistant region is $2.6R$ and the resolution here corresponds to 30 grid points per rotor radius, which in [10] was shown to fulfill the basic demands for a well resolved LES. The total number of grid points in the grid used for the AL simulation is 2.1×10^6.

The boundary conditions are as follows: The velocity is specified according to the free stream velocity at the inlet, unsteady convective conditions at the outlet, symmetry conditions at the bottom and top boundaries and periodic conditions on the sides.

6.2.3 BEM computations

The in-house aeroelastic code HAWC2 [15–17] is used to conduct the BEM aerodynamic computations. The aerodynamic part of the HAWC2 code is based on the BEM method, but extended from the classical approach to handle dynamic inflow, dynamic stall, skew inflow, shear effects on the induction and effects from large deflections. One example is the effect of large flapwise blade deflections causing a change in the effective rotor diameter and that the blade forces are no longer perpendicular to the rotor plane. This reduces the thrust on the rotor and thereby changing the induced velocities and vice versa. Dynamic stall is modeled by a modified Beddoes-Leishmann model that includes the effects of shed vorticity from the trailing edge (Theodorsen Theory), as well as the effects of stall separation lag caused by an unsteady trailing edge separation point. The time scale of the dynamic inflow model is so slow that it is not active during the tower oscillations; however, the dynamic stall model will affect the results.

To mimic the rigid CFD model, all structural members in the model are made very stiff by increasing the Young's and shear modulus. The tower bottom is placed on a bearing, such that the turbine can be moved side-to-side like an inverted pendulum whereby the rotor center will perform an almost pure lateral motion.

6.2.4 Computational setup

The turbine used as an example in this study is the NREL 5 MW reference turbine [14]. The rotor is undergoing prescribed sinusoidal oscillations in the cross flow direction according to:

$$r(t) = A \sin\left(\frac{2\pi}{T} t\right) ,$$

where $A = 1$ m is the amplitude and $T = 3.3333$ s is the period of the cross stream vibrations. Thus the hub of the rotor is oscillating at a frequency of 0.3 Hz, corresponding to the first tower mode frequency of this particular turbine.

The inflow velocities in the simulations are set to respectively, 6 m/s, 12 m/s and 22 m/s. The three cases is chosen to cover: below rated power at a low rotational speed, around rated power with a high loading, and above rated power with pitched blades.

6.2.5 CFD, AL and BEM results

Figure 6.2 shows the lateral aerodynamic forces as function of lateral hub position during the harmonic oscillations. Table 6.1 shows the lateral aerodynamic work per oscillation cycle. A negative aerodynamic work indicates that the flow extracts energy from the oscillations, i.e., adding damping to the mode of motion.

For the 6 m/s case (cf. Figure 6.2a), there are significant differences between the results from full rotor CFD, AL, and BEM. The slope of the principal axis of the loop predicted by BEM points in another direction than in the CFD results. These qualitative differences in the loops can be explained by the added mass of the rotor. The added mass effect is inherent in the CFD formulation while it is neglected in the BEM formulation. The added mass is estimated by assuming that the added mass of the blade is the same as for a circle with the same diameter as the projected height of the airfoil in the direction of motion

$$m_{add} = \int_0^R \rho \frac{a(r)^2}{4} \pi \cos(\psi) dr \tag{6.1}$$

where R is the rotor radius, ρ is the air density, ψ is the azimuth angle of the particular blade

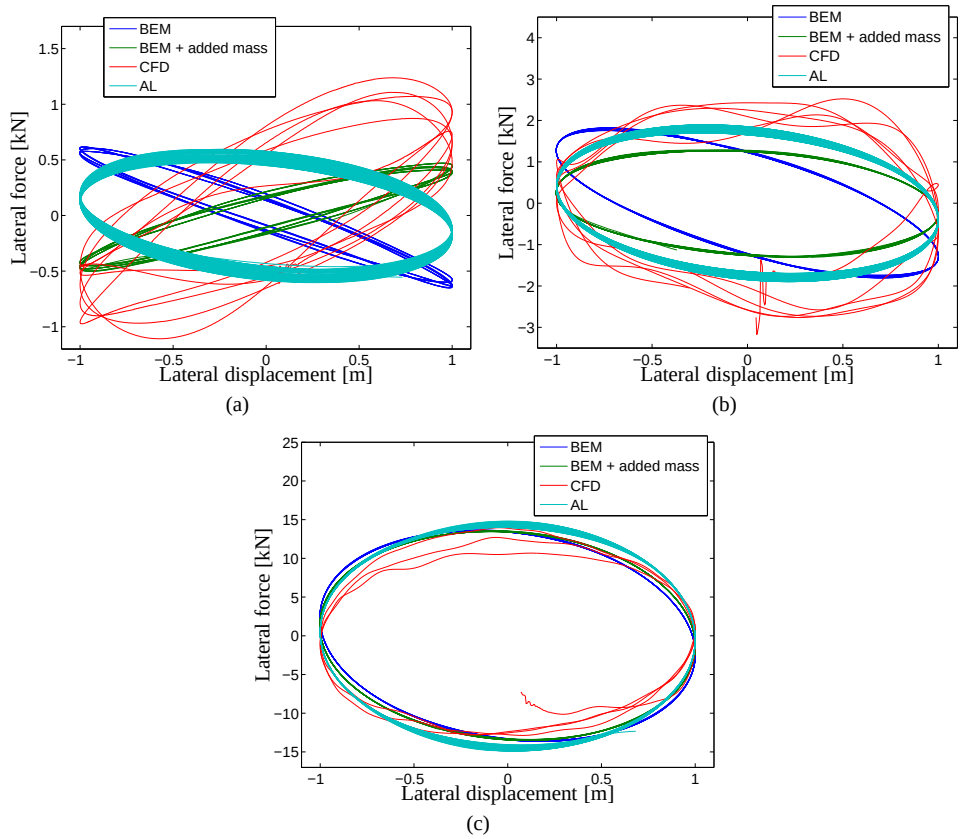

Figure 6.2. Lateral aerodynamic forces for lateral harmonic oscillations of the rotor at 0.3 Hz and 1 m amplitude. All loops runs in a counter clockwise direction. a) 6 m/s, b) 12 m/s and c) 22 m/s.

Table 6.1. Aerodynamic work per cycle.

	HAWC2	HAWC2 + added mass	CFD	AL
6 m/s	-0.4 kJ	-0.5 kJ	-1.7 kJ	-1.6 kJ
12 m/s	-3.9 kJ	-3.9 kJ	-7.3 kJ	-5.5 kJ
22 m/s	-42.1 kJ	-42.2 kJ	-39.0 kJ	-45.3 kJ

and $a(r)$ is the width of the airfoil projected onto the lateral direction of motion. Summing up for all three blades yields the total added mass to the rotor

$$M_{add} = \sum_{i=1}^{3} m_{add}\left(\psi = \frac{i-1}{3}2\pi\right) = 2m_{add} \tag{6.2}$$

Figure 6.2a shows that including this added mass in the post-processing of the HAWC2 results explains the qualitative difference between BEM and CFD. Regarding the slope of the loops, the AL results lie in between the BEM and the BEM including added mass. The size of the loops also vary quit a lot, but it should be noticed that the forces are very small, such that it is only small differences in absolute numbers.

Table 6.1 shows the lateral work done in one oscillation. The difference in work between the BEM and CFD is also seen to be relatively large, as expected by the difference in the shape of the loops. It will later be shown that even though as the differences are relatively large, the effect on damping is negligible for all practical applications. It should be noted that the added mass effects do not affect the aerodynamic work (Table 6.1) and neither the damping. The extra forces from the added mass are very small and can only be seen because the level of the lateral aerodynamic forces is very low in the 6 m/s case. The added mass is *not* important for the aeroelastic results, it is merely included here to explain the small qualitative difference between CFD and BEM in the 6 m/s case.

For the 12 m/s case (cf. Figure 6.2b), there is a much better agreement between all the results. The effect of added mass is much less pronounced because the absolute force level is higher. The CFD results still show a larger aerodynamic work than the BEM and AL results, but the differences are much smaller than for the 6 m/s case. For the 22 m/s case (cf. Figure 6.2c), all results are seen to agree very well. Also the aerodynamic work is very similar (Table 6.1).

To compare the aerodynamic work to the damping contribution a first order dynamic system is considered

$$m\ddot{x} + c\dot{x} + kx = 0 \tag{6.3}$$

where m is the modal mass of the first tower mode and k is the modal stiffness. The term $c\dot{x}$ is then the damping force. The work carried out by the damping force term for one oscillation is given by

$$W = \int_{x}^{x+x_T} c\dot{x}\mathrm{d}x \tag{6.4}$$

where x_T is the trajectory of one oscillation. Assuming harmonic oscillations $x = A\sin(\omega t)$ Equation (6.4) becomes

$$W = \int_{t}^{t+2\pi/\omega} cA^2\omega^2\cos^2(\omega t)\mathrm{d}t = cA^2\omega\pi \tag{6.5}$$

The damping ratio is given by $\beta = \frac{c}{\sqrt{km}} = \frac{c}{4\pi f m}$, where $f = \frac{\omega}{2\pi} = \frac{1}{2\pi}\sqrt{\frac{k}{m}}$ is the natural frequency of the first tower mode. Using this definition of the damping ratio, the relation between aerodynamic work and damping can be established as

$$\beta = \frac{W}{8A^2 f^2 m\pi^3} \tag{6.6}$$

Hence, the aerodynamic work is related to the damping ratio by a constant $(8Af^2m\pi^3)^{-1}$ determined by the modal frequency f and modal mass m, and the oscillation amplitude A.

To measure the damping, the 5 MW turbine is modeled in HAWC2 with the lateral tower direction as the only flexible component. The tower is excited by an external force at the tower top with the first lateral tower frequency until the tower top has an amplitude of 1 m. The damping is then estimated by measuring the decay of the tower top oscillations. Figure 6.3 shows the lateral tower top deflection for the 22 m/s simulation.

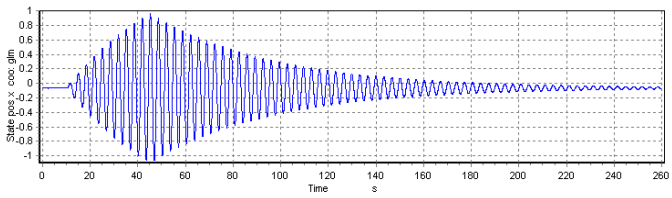

Figure 6.3. Lateral tower top deflection for the 22 m/s simulation. The excitation of the tower top starts at 10 seconds and stops at 41 seconds, where the amplitude has reached 1 m.

To compare the aerodynamic work and aerodynamic damping, all aerodynamic work has to be taken into account, and the internal work done by the generator has to be subtracted

$$W_{tot} = \int_t^{t+2\pi/\omega} \mathbf{f} \cdot \mathbf{v} dt + \int_t^{t+2\pi/\omega} \mathbf{T} \cdot \Omega dt - \int_t^{t+2\pi/\omega} T_{gen} \Omega_{gen} dt \tag{6.7}$$

where $\mathbf{f}$ is the aerodynamic forces in the three translations directions, $\mathbf{v}$ is the corresponding velocities of the rotor center, $\mathbf{T}$ is the aerodynamic moment around the three axis, Ω is the corresponding rotation speeds of the rotor center, T_{gen} is the generator torque and Ω_{gen} is the generator speed.

Figure 6.4a shows the measured aerodynamic work and the aerodynamic damping for the example turbine with the lateral tower mode as the only flexible component. The aerodynamic damping is given in logarithmic decrement ($\eta = 2\pi\beta$). The aerodynamic work is scaled by the square of the oscillation amplitude, as suggested by Equation (6.6).

The aerodynamic work and damping is seen to be similar except for a constant, as expected from Equation (6.6). Using this relation between aerodynamic work and damping the results from the full rotor CFD, AL and BEM comparison (cf. Table 6.1) can be converted into tower damping and the importance of the differences can be evaluated. Figure 6.4b shows the computed aerodynamic damping for the lateral aerodynamic work from Table 6.1. It is seen that even though there are relatively large differences between the aerodynamic work for the 6 m/s case, the damping is so low that it do not have any practical importance whether the damping is 0.05 or 0.15 % logarithmic decrement.

The reason for the difference in damping and aerodynamic work in Figure 6.4a and 6.4b is that in Figure 6.4b the tower top is moved in a pure lateral motion of the rotor center whereas in Figure 6.4a the tower mode motion also include some vertical motion and a rotation of the tower top. Especially the aerodynamic work related to the rotation of the tower top extract some extra energy work from the system.

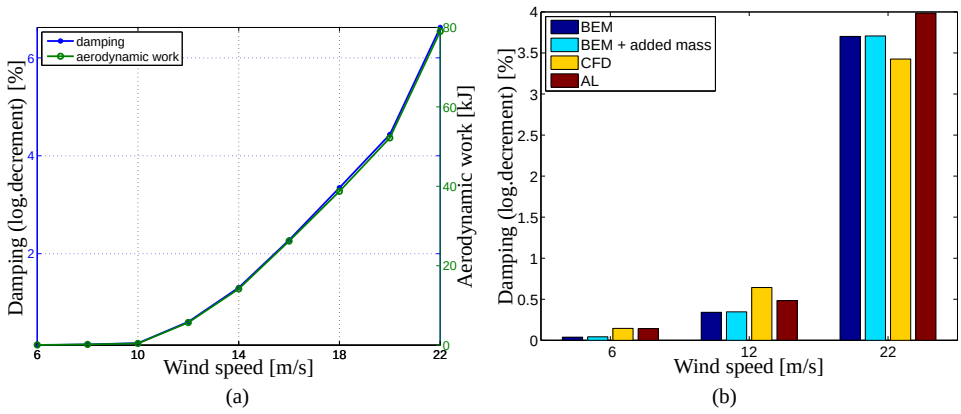

Figure 6.4. a) Aerodynamic work and damping for simulations with only tower lateral flexibility. b) Damping computed on basis of Table 6.1.

6.2.6 Comparison pure lateral oscillations and true tower mode

The first lateral tower mode of a true turbine differers from the pure lateral tower mode investigated in the previous section. Figure 6.5 shows the tower top motion for three different wind speeds for the full flexible turbine. It is seen that the tower mode includes a considerably amount of longitudinal tower motion, and that the mode changes for the different wind speeds.

Figure 6.6 shows the aerodynamic damping of first lateral tower mode for different wind speeds. The damping is estimated, as above, by exciting the tower top until an amplitude of 1 m and than measure the decay. The individual aerodynamic work contributions from the three translations and three rotations of the rotor center is also shown. The damping is seen to stay between 1 and 2 % logarithmic decrement and peaking around 10 m/s, where the turbine is heaviest loaded. It is seen that the damping contribution for the lateral motion (x) is increasing for increasing wind speeds, in agreement with the analysis above (Figure 6.4), but especially the rotation around the y axis contribute negatively to the damping (positive aerodynamic work).

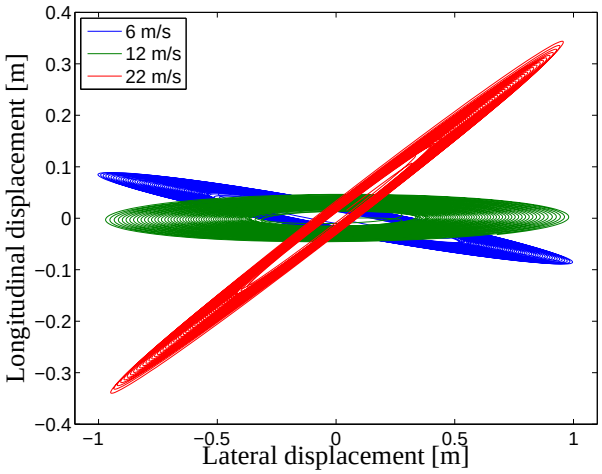

Figure 6.5. Tower top displacement for first lateral tower modes. Top-down look with y-axis pointing down wind.

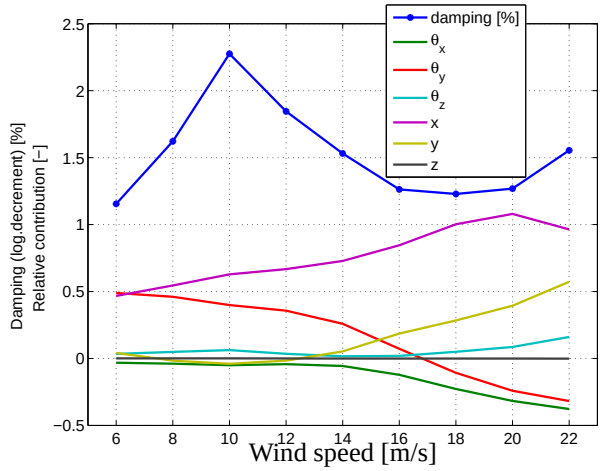

Figure 6.6. Aerodynamic damping of the first lateral tower mode for different wind speeds together with the individual aerodynamic work contributions from the three translations and three rotations of the rotor center. The directions is denoted as y pointing downwind, z pointing downwards and x is given by a right hand coordinate system. The rotations is denoted around these axis. The work done by the generator is subtract from the aerodynamic work related to the rotation θ_y around the y axis (which is pointing downwind).

6.2.7 Summary

The analysis of lateral tower damping computations shows that the BEM corresponds well to fully resolved rotor CFD and AL CFD results for any practical applications. There are some disagreements, but they are related to small damping values and are considered unimportant.

6.3 Lateral Tower Load Mitigation by Generator Torque Control

This section analysis the potentials of using the generator torque to reduce lateral tower vibrations, and thereby reduce the tower and foundation fatigue. The tower motion can be reduced by active damping systems. One actuator option is yaw: Ekelund [12] shows that the tower motion can be reduced by an active yaw control, this will however require continuous yaw actuation, which normal yaw systems are not designed for. Another actuator option is the generator torque, which affects the lateral tower mode through the reaction torque on the tower top. Wright and Stol [18] implemented a lateral tower mode load reducing controller using generator torque as an actuator, achieving a tower load reduction of 79 %. Such an additional generator torque controller will also affect both the power quality and the drive train loads, but does not need any new actuator systems.

In this work, a low order system describing the essential dynamics involved in the lateral tower motion is used to evaluate and design a lateral tower load reducing generator torque controller. The low order model contains a tower mode, a drive train mode and generator speed. The controller is tested in nonlinear aeroelastic simulations using the NREL 5 MW reference turbine as example. The results shows that there is a potential for reducing the tower load without increasing the drive train load too much, the example shows a 40 % reduction of tower fatigue load with a 10 % increase in drive train load.

6.3.1 The turbine model

Figure 6.7a shows the tower model seen from the upwind side. The tower height is denoted L , tower stiffness and mass $EI(z)$ and $m(z)$, respectively, tower top mass and inertia M and I_t, respectively, with applied generator torque $T_g(t)$ and wave loading $f(t)$ at mean sea level d. The lateral tower deflection is denoted $u(z,t)$.

The tower motion is approximated by its first mode shape. The mode shape is computed by a finite difference discretization of the conical tower with top mass. Using this modal description the tower deflection is given by

$$u(z,t) \equiv \phi(z)q(t) \tag{6.8}$$

where $\phi(z)$ is the first mode shape of the tower with tower top mass and $q(t)$ is the time changes

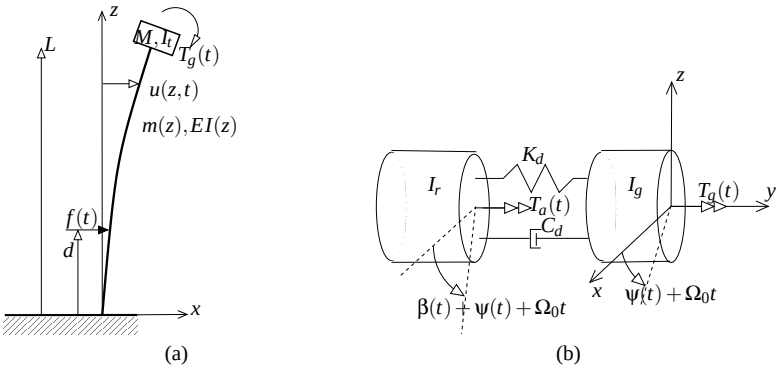

Figure 6.7. a) Tower model. b) drive train model .

of tower position. Figure 6.7b shows the drive train model, which reference frame follows the tower top rotations $u'(L,t)$. All the drive train component are related to the low speed shaft. The generator inertia I_g, related to the low speed shaft, located to the right and the rotor inertia I_r to the left connected by a torsional stiffness K_d and damping C_d. The azimuth angle of the generator is given by the windup of the reference rotor speed $\Omega_0 t$ and the disturbance of the generator azimuth angle $\psi(t)$, hence the resulting generator speed is $\Omega_g = \Omega_0 + \dot{\psi}$. The azimuth angle of the rotor is achieved by adding the deflection of the drive train $\beta(t)$ to the azimuth angle of the generator, hence the resulting rotor speed is $\Omega_r = \Omega_0 + \dot{\psi} + \dot{\beta}$.

With the one mode beam description of the tower (Equation (6.8)) and the drive train model (Figure 6.7b) the kinetic energy of this system is given by

$$T = \int_0^L \frac{1}{2} m(z)\phi(z)^2 \dot{q}(t)^2 \mathrm{d}z + \frac{1}{2} M\phi(L)^2 \dot{q}(t)^2 + \frac{1}{2} I_t \phi'(L)^2 \dot{q}(t)^2 + \frac{1}{2} I_r \left(\dot{\psi}(t) + \dot{\beta}(t) + \Omega_0 + \phi'(L)\dot{q}(t)\right)^2 + \frac{1}{2} I_g \left(\dot{\psi}(t) + \Omega_0 + \phi'(L)\dot{q}(t)\right)^2 \quad (6.9)$$

and the potential energy is given by

$$V = \int_0^L \frac{1}{2} EI\phi''(z)^2 q(t)^2 \mathrm{d}z + \frac{1}{2} K_d \beta(t)^2 - T_g(t)\left(\psi(t) + \Omega_0 t\right) - T_a(t)\left(\psi(t) + \Omega_0 t + \beta(t) + \phi'(L)q(t)\right) - f(t)\phi(d)q(t) \quad (6.10)$$

Where $T_a(t)$ is the aerodynamic torque which can be described by the aerodynamic model

$$T_a = \frac{1}{\Omega_r} P(U, \Omega_r, \theta) \approx \frac{P_0}{\Omega_0} - P_0 \frac{\dot{\psi}(t) + \dot{\beta}(t)}{\Omega_0^2} + \frac{1}{\Omega_0}\left(\frac{\partial P}{\partial \theta}\Big|_{\theta_0} \theta_1 + \frac{\partial P}{\partial U}\Big|_{U_0} U_1\right) \quad (6.11)$$

where P is the aerodynamic power, which is a function of wind speed U, rotor speed Ω_r and pitch angle θ. The aerodynamic power function is linearized and the subscript 0 denote the steady state value and the subscript 1 denote the linear variations around this steady state value.

Using Lagrange's equation [13] the equations of motion for tower, drive-train and generator degrees of freedom can be derived

$$\mathbf{M}\ddot{\mathbf{z}} + \mathbf{D}\dot{\mathbf{z}} + \mathbf{K}\mathbf{z} = \mathbf{f}_0 + \mathbf{F}\mathbf{f} \quad (6.12)$$

where $\mathbf{z} = [q(t), \beta(t), \psi(t)]^T$ is a vector with the time dependent deflections and

$$\mathbf{M} = \begin{bmatrix} \int_0^L m(z)\phi(z)^2 \mathrm{d}z + M\phi(L) + (I_t + I_g + I_r)\phi'(L)^2 & I_r\phi'(L) & (I_g + I_r)\phi'(L) \\ I_r\phi'(L) & I_r & I_r \\ (I_g + I_r)\phi'(L) & I_r & I_r + I_g \end{bmatrix} \quad (6.13)$$

$$\mathbf{D} = \begin{bmatrix} C_t + \left(\frac{P_0}{\Omega^2} - \frac{1}{\Omega}\frac{\partial P}{\partial \Omega}\big|_\Omega\right)\phi'(L)^2 & \left(\frac{P_0}{\Omega^2} - \frac{1}{\Omega}\frac{\partial P}{\partial \Omega}\big|_\Omega\right)\phi'(L) & \left(\frac{P_0}{\Omega^2} - \frac{1}{\Omega}\frac{\partial P}{\partial \Omega}\big|_\Omega\right)\phi'(L) \\ \left(\frac{P_0}{\Omega^2} - \frac{1}{\Omega}\frac{\partial P}{\partial \Omega}\big|_\Omega\right)\phi'(L) & C_d + \frac{P_0}{\Omega^2} - \frac{1}{\Omega}\frac{\partial P}{\partial \Omega}\big|_\Omega & \frac{P_0}{\Omega^2} - \frac{1}{\Omega}\frac{\partial P}{\partial \Omega}\big|_\Omega \\ \left(\frac{P_0}{\Omega^2} - \frac{1}{\Omega}\frac{\partial P}{\partial \Omega}\big|_\Omega\right)\phi'(L) & \frac{P_0}{\Omega^2} - \frac{1}{\Omega}\frac{\partial P}{\partial \Omega}\big|_\Omega & \frac{P_0}{\Omega^2} - \frac{1}{\Omega}\frac{\partial P}{\partial \Omega}\big|_\Omega \end{bmatrix} \quad (6.14)$$

where C_t and C_d are structural tower and drive-train damping, and

$$\mathbf{K} = \begin{bmatrix} \int_0^L EI(z)\phi''(z)^2 \mathrm{d}z & 0 & 0 \\ 0 & K_d & 0 \\ 0 & 0 & 0 \end{bmatrix} \quad (6.15)$$

where it is noted that the generator speed degree of freedom does not have any stiffness term. The steady state forces on the system are given by $\mathbf{f}_0 = [\phi'(L)T_{g,0}, T_{a,0}, T_{a,0}]^T$, where the steady state generator torque $T_{g,0}$ is equal to the steady state aerodynamic torque $T_{a,0} = \frac{P_0}{\Omega_0}$. The linear gains on the time varying generator torque, wave forces, wind speed and pitch changes are given by

$$\mathbf{F} = \begin{bmatrix} 0 & \phi(d) & \frac{1}{\Omega_0}\frac{\partial P}{\partial U}\big|_{U_0}\phi'(L) & \frac{1}{\Omega_0}\frac{\partial P}{\partial \theta}\big|_{\theta_0}\phi'(L) \\ 0 & 0 & \frac{1}{\Omega_0}\frac{\partial P}{\partial U}\big|_{U_0} & \frac{1}{\Omega_0}\frac{\partial P}{\partial \theta}\big|_{\theta_0} \\ 1 & 0 & \frac{1}{\Omega_0}\frac{\partial P}{\partial U}\big|_{U_0} & \frac{1}{\Omega_0}\frac{\partial P}{\partial \theta}\big|_{\theta_0} \end{bmatrix} \quad (6.16)$$

and the time varying loading $\mathbf{f} = [T_{g,1}(t), f(t), U_1(t), \theta_1(t)]^T$. The steady state solution of the tower and drive train state is given by

$$\begin{bmatrix} q_0 \\ \beta_0 \end{bmatrix} = \mathbf{K}_{(1:2,1:2)} \mathbf{f}_{0,(1:2)} \tag{6.17}$$

where the subscript $(1:2, 1:2)$ denote the sub-matrix consisting of the first to second columns of the first to second rows and the subscript $(1:2)$ denote the first two elements of the vector. Extracting this steady state solution from Equation (6.12) and rewriting the equations of motion to first order form gives

$$\dot{\mathbf{x}} = \mathbf{A}\mathbf{x} + \mathbf{B}\mathbf{u} \tag{6.18}$$

where

$$\mathbf{x} = \begin{bmatrix} q_1 \\ \beta_1 \\ \dot{q}_1 \\ \dot{\beta}_1 \\ \dot{\psi} \end{bmatrix}, \quad \mathbf{A} = \begin{bmatrix} \mathbf{I}_{2\times 2} & \mathbf{0}_{2\times 3} \\ -\mathbf{M}^{-1}\mathbf{K}_{(1:2,1:2)} & -\mathbf{M}^{-1}\mathbf{D} \end{bmatrix}, \quad \mathbf{B} = \begin{bmatrix} \mathbf{0}_{2\times 4} \\ \mathbf{M}^{-1}\mathbf{F} \end{bmatrix}, \quad \mathbf{u} = \mathbf{f} \tag{6.19}$$

and subscript 1 denotes the time varying linear part. It is noted that the two structural degrees of freedom results in two states each while the generator speed only results in one state, since it don't have any stiffness.

6.3.2 Power control

The aerodynamic damping of lateral tower mode of a pitch regulated turbine is lowest at low wind speeds [11], so the main problems with lateral tower vibrations will predominantly appear in the control region below rated wind speed. In this region, the turbine controller adjust the rotor speed to optimize power extraction from the wind and the blade pitch is kept constant.

The power control below rated wind speed can be handled by prescribing a given power at any generator speed. This can be done by a third order polynomial

$$P = K\Omega^3 \;\Rightarrow\; T_g = -\frac{P}{\Omega} = -K\Omega^2 \approx -K\Omega_0^2 - 2K\Omega_0\dot{\psi} \;\Rightarrow\; \begin{cases} T_{g,0} &= -K\Omega^2 \\ T_{g,1} &= -2K\Omega_0\dot{\psi} \end{cases} \tag{6.20}$$

where $K = P_0/\Omega_0^3$ when the operational conditions are known. Implementing this controller $u_{(1)} = -2K\Omega_0[0,0,0,0,1]\mathbf{x}$ (the subscript (1) denote first element in the control vector $\mathbf{u}$) in Equation (6.18) leads to the following extra terms in the $\mathbf{A}$ matrix

$$\mathbf{A}_b = \begin{bmatrix} & & \mathbf{0}_{2\times 6} & & \\ 0 & 0 & 0 & 0 & 2K\Omega_0 \frac{\phi'(L)}{M_{towet}} \\ 0 & 0 & 0 & 0 & 2K\Omega_0 \frac{1}{I_g} \\ 0 & 0 & 0 & 0 & -2K\Omega_0 \left(\frac{1}{I_g} + \frac{\phi'(L)^2}{M_{towet}} \right) \end{bmatrix} \tag{6.21}$$

where $M_{tower} = \int_0^L m(z)\phi(z)^2 \mathrm{d}z + M\phi(L)^2 + I_t\phi'(L)^2$ is the modal tower mass. Equation (6.21) shows that the power controller damps the generator motion ($\dot{\psi}$) and the action on the generator results in reactions on the drive train and tower.

6.3.3 Load reducing control

The load reducing control strategy is to superpose a generator torque to the power controllers generator torque (Equation (6.20)). The reaction moment from the generator on the tower top gives a force on the lateral tower motions, as seen in Equation (6.21), so the generator torque can be used as actuator for a tower load reducing controller. The superposed generator torque is computed by a PI controller based on a measurement of tower top accelerations, which in

this model framework will is denoted $\ddot{q}$. The PI controller's integral gain K_i acts on the tower speed $\dot{q}$ and a proportional gain K_p on the acceleration. If instead the tower bottom strain was measured the K_i would be a differential gain in a PID controller. Implementing the integral gain controller $u_{(1)} = K_i[0,0,1,0,0]\mathbf{x}$ adds the below extra terms to the $\mathbf{A}$ matrix

$$\mathbf{A}_i = \begin{bmatrix} & & \mathbf{0}_{2\times 6} & & \\ 0 & 0 & -K_i\frac{\phi'(L)}{M_{tower}} & 0 & 0 \\ 0 & 0 & -K_i\frac{1}{I_g} & 0 & 0 \\ 0 & 0 & K_i\left(\frac{1}{I_g}+\frac{\phi'(L)^2}{M_{towet}}\right) & 0 & 0 \end{bmatrix} \tag{6.22}$$

so a positive K_i gain will add a tower damping term, but this will also excite the drive train and generator states, adding fatigue to drive train and reducing the power quality. The frequency of the drive train is higher than the tower frequency, so there will not be any resonance amplification but the drive train load will follow the superposed generator torque.

The proportional gain on the tower acceleration gives the control input $u_{(1)} = K_p[0,0,1,0,0]\dot{\mathbf{x}}$ which implemented in Equation (6.18) together with the power and integral control terms become

$$\begin{aligned} \dot{\mathbf{x}} &= (A + A_b + A_i)\mathbf{x} + K_p\mathbf{B}_{(:,1)}[0,0,1,0,0]\dot{\mathbf{x}} \Rightarrow \\ \dot{\mathbf{x}} &= \underbrace{\left(\mathbf{I}_{3\times 3} - K_p\mathbf{B}_{(:,1)}[0,0,1,0,0]\right)^{-1}}_{\mathbf{F}_{A_p}}(A + A_b + A_i)\mathbf{x} \end{aligned} \tag{6.23}$$

where the subscript $(:,1)$ denote the first column in the $\mathbf{B}$ matrix and

$$\mathbf{F}_{A_p} = \begin{bmatrix} & & \mathbf{I}_{2\times 2} & & \mathbf{0}_{2\times 3} \\ 0 & 0 & \frac{1}{1+\frac{K_p\phi'(L)}{M_{tower}}} & 0 & 0 \\ 0 & 0 & -\frac{K_p}{I_g\left(1+\frac{K_p\phi'(L)}{M_{tower}}\right)} & 1 & 0 \\ 0 & 0 & \frac{K_p\phi'(L)}{M_{tower}\left(1+\frac{K_p\phi'(L)}{M_{tower}}\right)} + \frac{K_p}{I_g\left(1+\frac{K_p\phi'(L)}{M_{tower}}\right)} & 0 & 1 \end{bmatrix} \tag{6.24}$$

is multiplied onto the $\mathbf{A}$ matrix of the system (Equation (6.18)) including the controller elements (Equation (6.21) and (6.22)). It is seen that the main effect of the proportional gain is a multiplication factor on the tower stiffness. The multiplication factor is less than one for positive K_p decreasing the effective stiffness of the tower and thereby decreasing the tower frequency. The integral gain K_i on the other hand directly adds damping to the tower, which will reduce the tower loads, but with the cost on drive train action and power quality. So the choice of gain will be a trade off between wanted tower load reduction and the acceptable drive train load and power quality.

6.3.4 Integral gain tuning

The integral gain K_i can be chosen to give a prescribed tower damping. Disregarding proportional gain $K_p = 0$, the tower damping ratio is approximated by

$$\zeta = \frac{-A_{c,(3,3)}}{2\sqrt{-A_{c,(3,1)}}} \tag{6.25}$$

where $\mathbf{A}_c = \mathbf{A} + \mathbf{A}_b + \mathbf{A}_i$ and the subscript numbers denote the row and column number of the matrix element. Rearranging Equation (6.25) the gain is given by

$$K_i = 2\zeta\frac{\sqrt{\int_0^L EI(z)\phi''(z)^2 \mathrm{d}z M_{tower}}}{\phi'(L)} - C_t\frac{M_{tower}}{\phi'(L)} \tag{6.26}$$

where ζ is the wanted damping ratio.

6.3.5 Example

The 5 MW NREL reference wind turbine [14] (RWT) is used as an example. The operational conditions are 6 m/s with 20.2 % turbulence (according to IEC 61400-1 for a class C1 turbine). The turbine is located at 20 m water depth, the wave conditions corresponds to north sea conditions with a significant wave height on 1.63 m and a period on 4.53 s. An irregular wave field described by a Pierson-Moskowitz spectrum is used and the wave direction is 90 deg on the wind direction. The turbine is modeled in the nonlinear aeroelastic code HAWC2 [15–17], which includes wave loading using Morisons formula. Figure 6.8 shows the results from nonlinear aeroelastic simulations of the turbine at the given operational conditions.

The equivalent wind speed extracted from aerodynamic power will be explained below. The spectrum of the wave loading is seen to be cutoff at 0.8 Hz, where the energy anyway is very low. This cutoff is an results of the wave modeling in HAWC2. The lateral tower bottom bending moment shows clear sign of resonance excitation of a low damped mode with the high narrow peak in the power spectrum. The drive train spectrum shows coupling to the longitudinal tower motion, but the main energy is at the free-free drive train frequency on around 1.8 Hz. This simulation shows the need of a lateral tower damping devise. The structural tower damping in this simulation is 1.3 % log. decrement, which may be low for a tower with passive a tower damper.

External loading on low order model With a given free wind speed, turbulence level and spectrum the response of the model depend on how the wind speed is sampled. The wind speeds used in this analysis is generated and sampled by the aeroelastic code HAWC2 using a rigid turbine, such that structural dynamic effects on the sampled wind speeds are removed.

The response of the rotor to the incoming wind field is an integrated response of the three blades to the different regions of turbulent wind speeds they each meet. The free wind parameters are given at one point at hub height, but on the one hand, the rotor covers a large area, which will smoothen some of the turbulence and on the other hand the blades rotate through different regions of wind speed increasing the effective turbulence on the blade. Figure 6.9 shows the time series and spectrum of the one point hub height wind, a mean of four fixed points in the rotor plane, the mean of one point at 3/4 radius of each of the three rotating blade and finally a

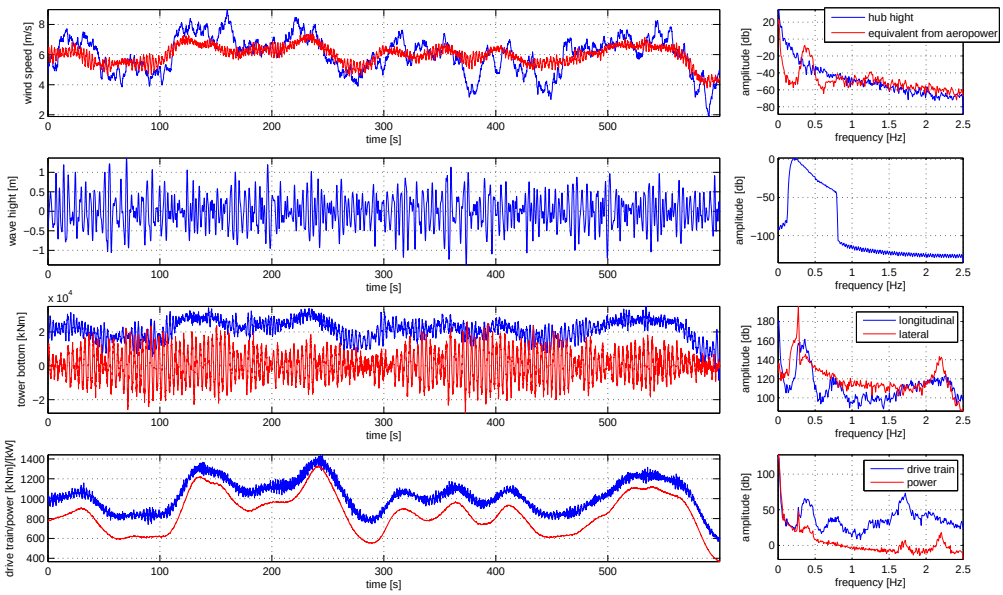

Figure 6.8. Results from aeroelastic simulations of the 5 MW RWT with power control but without load reducing tower controller. From the top the figures shows the wind speed, wave height, tower bottom bending moments, and drive train moment and generator power.

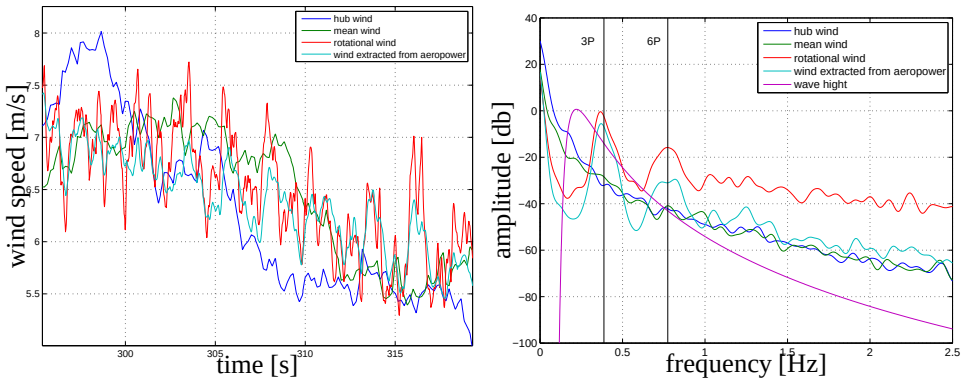

Figure 6.9. Wind and wave loading on structure. a) time series of wind sampled at hub height, as a mean of 4 points at the rotor plane, as one point on each rotating blade and computed from the aerodynamic power, respectively. b) Power spectrum of wind and wave loading.

equivalent wind speed extracted from the aerodynamic rotor power

$$P = \frac{1}{2}\rho A_r C_p U^3 \;\Rightarrow\quad U = \left(\frac{2P}{\rho A_r C_p}\right)^{1/3} \tag{6.27}$$

where A_r is the rotor area, ρ is the air density and C_p is the power coefficient.

The one point hub wind speed is the spectrum given by the standard. The four point rotor plan mean have a slightly lower energy at very low frequencies because some of the large scale low frequency turbulence structures are smoothed. At the higher frequencies there is no correlation between the points and the energy level is the same as for the one point sampling. The three point rotational sampling has a lower energy level at low frequencies because the rotational sampling chops up the large scale turbulence structures and thereby moves the energy to higher frequencies, especial to 3P corresponding to the three blades rotating through the same turbulence structure. There is also a peak at the first 3P harmonic. The equitant wind speed extracted for aerodynamic power have the same characteristic as the rotational sampled wind speed at low frequencies, but at the higher frequencies the energy follows the single hub point level. The equivalent wind integrates the response form all of the three blades and not just one point on each, therefor the highest frequency contributions are smoothed compared to the rotational sampled wind speed giving less energy on these frequencies.

The wave height used in the low order model is given by its spectrum and the transfer function from wave height to wave forces is extracted from the HAWC2 simulations.

Response to external loading The power spectrums of the external wind and wave loadings are applied to the model (Equation (6.18)) and the frequency response is shown on figure 6.10. The response is shown both for the case with single point hub height sampled wind speed and for the equivalent wind speed.

The responses is seen to be quite different for the drive train and generator states at low frequencies, as expected, since the loading spectrums differs in that region (Figure 6.9). For the further analysis the equivalent wind speed extracted from the aerodynamic power will be used, since it is this integrated rotor power that the drive train actually will feel.

Table 6.2 shows the resonance frequencies and damping for tower and drive train mode and the time constant for the generator state for different configurations of the model. The drive train frequency is seen to shift from the first version with fixed generator speed (clamped-free drive train frequency) to the other versions with generator control (free-free drive train frequency).

Figure 6.11 shows the response of the system with the power controller, and the power controller together with the integral and proportional tower load reducing controllers, respectively.

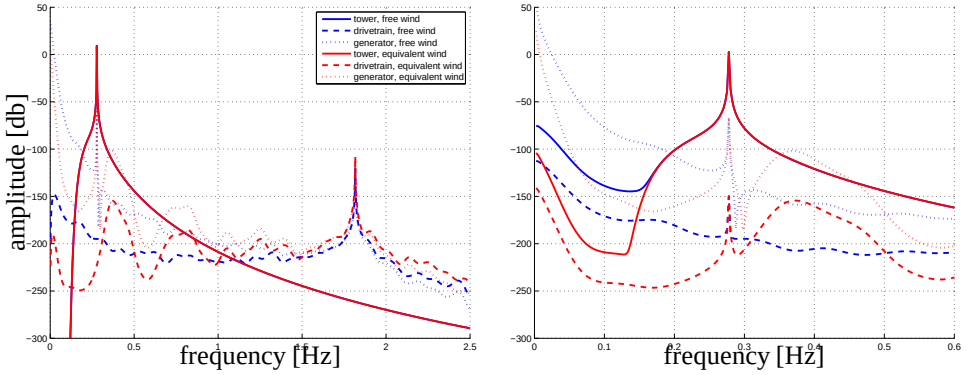

(a) (b)

Figure 6.10. a) Power spectrum for combined wave and wind loading with two different wind spectrum; blue=single point hub wind speed, red=equvilant wind speed extracted from aerodynamic power. b) Zoom of a).

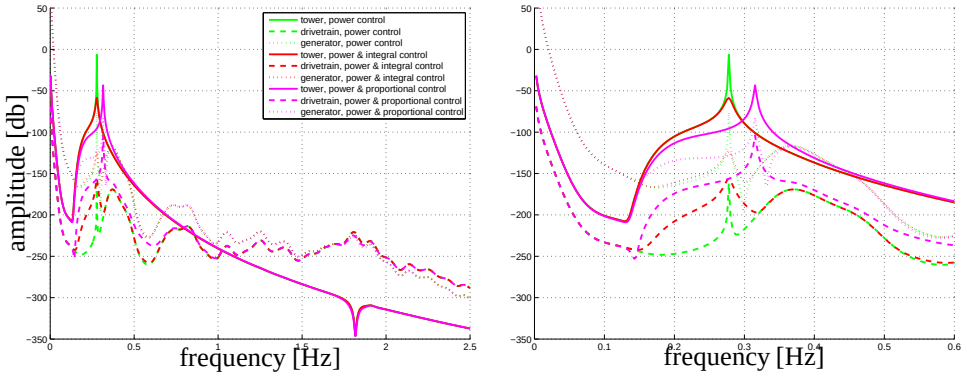

(a) (b)

Figure 6.11. a) Frequency response for combined wave and wind loading with the different controllers; blue=no control ($K = K_i = K_p = 0$), green=power control only ($K \neq 0, K_i = K_p = 0$), red=integral and power control ($K \neq 0, K_i \neq 0, K_p = 0$), megenta=proportional and power control ($K \neq 0, K_i = 0, K_p \neq 0$). Solid line=tower mode (q), dashed line=drive train (β) and dotted line=generator (ψ) b) Zoom.

The power controller changes the tower response at low frequencies because the power controller couples the tower motion to the drive train and generator speed through the applied generator torque (Equation (6.21)). Comparing Figure 6.10 and 6.11 it is seen that the drive train damping provided by the power controller (Equation (6.21)) suppresses the drive train resonance peak at the free-free drive train frequency (1.8 Hz). The integral control gain $K_i = 1.3 \cdot 10^6$is chosen to give 10 % log.decrement tower damping using Equation (6.26). This inte-

Table 6.2. Frequencies and damping for the tower and drive train mode, and the time constant for the generator state for different configurations of the model.

	control gains			tower		drive train		generator
	K	K_i 10^6	K_p 10^6	freq. [Hz]	damp. ratio [%]	freq. [Hz]	damp. ratio [%]	time con. [s]
Fixed generator speed; $\psi = \dot{\psi} = 0$	0	0	0	0.27	-0.1	0.63	-0.8	-
Without control	0	0	0	0.28	0	1.82	0	18.2
Power control	P_0/Ω_0^3	0	0	0.28	0.1	1.82	2.1	-151
Power and integral control	P_0/Ω_0^3	1.3	0	0.28	1.7	1.82	2.1	-151
Power and proportional control	P_0/Ω_0^3	0	-5	0.32	0.4	1.82	2.7	-151

gral gain is seen to suppress the tower resonance peak, so, this controller will reduce the tower fatigue considerably. The drive train response in the wave frequency range (0.15 Hz to 0.3 Hz) increases considerably because of the increased generator torque control action. The generator state is only increased right at the tower frequency peak. So, the integral tower load controller will increase the drive train load considerably and to some extent decrease the power quality.

The proportional tower load gain K_p is chosen to be $-5 \cdot 10^6$. The negative gain will increase the tower resonance frequency (Equation (6.24)) and thereby move the resonance frequency towards lower wave excitation energy (Figure 6.9b). Figure 6.11 shows that the tower resonance peak has moved to a higher frequency and that the over all tower response is decreased, indicating less fatigue load. However, the wave loading is stochastic and broad banded so the strategy to move the resonance frequency is connected with a large uncertainty.

To evaluate the performance of the controllers the system is simulated in the time domain.

$$\dot{\mathbf{x}} = (\mathbf{A} + \mathbf{A}_b + \mathbf{A}_i)\,\mathbf{x} + \mathbf{B}_{:,2:3}[F_{wave}, U_1] \tag{6.28}$$

where the subscript $(:, 2:3)$ denote the second and third column of the **B** matrix. The wave forces are extracted from HAWC2 simulations and the wind speed U_1 is equivalent wind speed extracted form the aerodynamic power (Equation (6.27)). The system is simulated for 600 s at 6 m/s with 20.2 % turbulence, as described above. The control performance is evaluated by computing the equivalent fatigue load for the tower and drive train (m equal to 3 and 6 respectively) and the standard deviation of the power. Figure 6.12 shows the results from simulations with integral and proportional gain, respectively, normalized with the results for the power control only case.

For the integral gain it is seen that the tower fatigue load drops off around a gain of $K_i = 10^5$ and that the cost on the drive train start to increase around a gain of $K_i = 10^7$. The results indicate that is should be possible to reduce the tower load considerably without increasing the drive train load and reduce the power quality too much. The power spectrum proportional gain controller (Figure 6.11) indicates that there could be some load reduction potentials. However the time simulations shows that the result is very varying. This variation is caused by the resonance peak not being moved out of the wave spectrum, so it depends on the individual realization of the wave field how much the tower is excited. The large uncertainty in load reduction makes the proportional control strategy unfavorable.

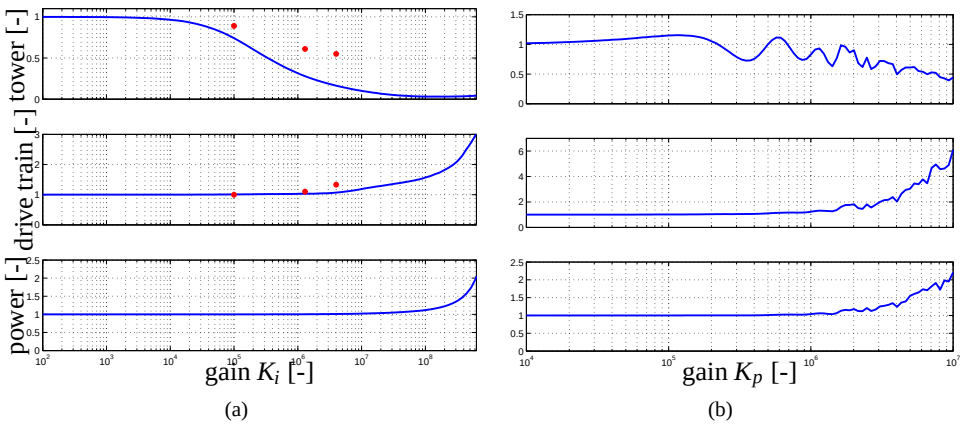

Figure 6.12. Normalized equivalent tower and drive train load (m equal to 3 and 6 respectively) and the standard deviation of the power for different integral control gains. The results are normalized with respect to the case with power control only. The red dots show the same results from nonlinear aeroelastic simulations with HAWC2. a) integral gain only and b) proportional gain only.

Nonlinear aeroelastic simulations To test the controller under more realistic conditions the integral gain controller is implemented in the nonlinear aeroelastic code HAWC2. The controller input is the tower top speed (the integral of the tower top acceleration) which is feed through a second order low pass filter with a cutoff frequency on 1 Hz. The filtered signal is multiplied by the K_i gain and superposed on the power controller's reference torque and send to the generator model. Figure 6.13 to 6.15 shows the lateral tower bottom bending moment, the shaft torque and the power output, respectively, for simulations with $K_i = 0$ and $K_i = 1.3 \cdot 10^6$. Table 6.3 shows the fatigue and power quality for different gains. The results in this table are also plotted on Figure 6.12. The results shows that tower oscillations are reduced considerably (40 %) without increasing the drive train activity too much (10 %). The tower load reduction for this full turbine system is less than predicted by the low order model. This is because many of the extra modes that exist in the full turbine model contributes to fatigue on the tower, but it is only the first tower mode that is included in the low order model and in the controller. The main conclusion is anyhow the same, that is is possible to reduce the tower loads considerably without increasing the drive train load compared to when the gain is kept below a given threshold.

6.3.6 Summary

A low order model of tower, drive train and generator speed is derived, the model capture the essential dynamic involved in lateral tower vibration and generator torque control of these. The

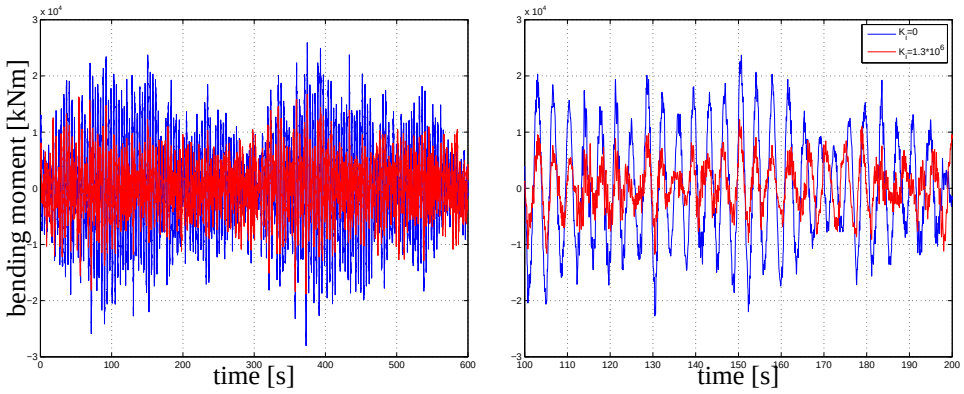

(a) (b)

Figure 6.13. Lateral tower bottom bending moment from nonlinear aeroelastic simulations. a) whole time series, b) zoom.

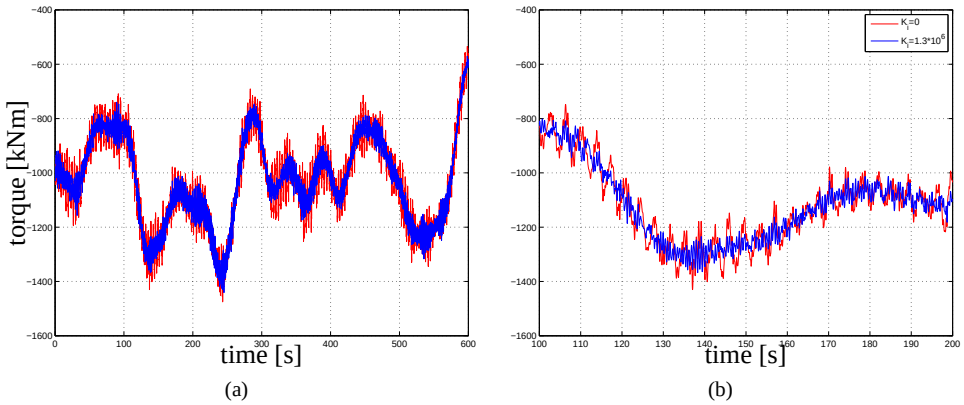

(a) (b)

Figure 6.14. Shaft torque from nonlinear aeroelastic simulations. a) whole time series, b) zoom.

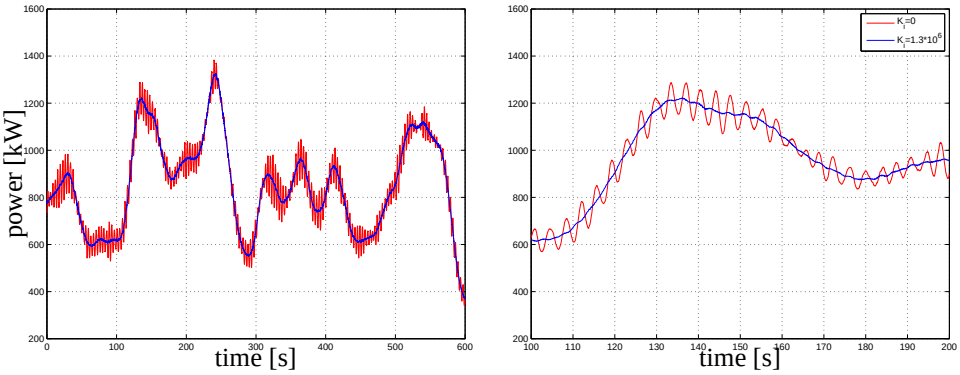

Figure 6.15. Power production from nonlinear aeroelastic simulations. a) whole time series, b) zoom.

Table 6.3. Tower and drive train equivalent fatigue load (m=3 and m=6 respectively) and standard deviation of power output. The results are normalized with respect to the results for the case without tower load controller ($K_i = 0$).

	$K_i = 1 \cdot 10^5$	$K_i = 1.3 \cdot 10^6$	$K_i = 4 \cdot 10^6$
Equivalent lateral bending moment	0.89	0.61	0.55
Equivalent haft torque	1.00	1.10	1.33
Standard deviation of power	1.00	1.02	1.07

model is used to analyze and explain the use of a PI-controller based on tower top acceleration to reduce lateral tower loads. The proportional term adds stiffness to the tower, increasing or decreasing the resonance frequency, but it is hard to move the resonance frequency out of wave excitation frequency band, so this control strategy is unreliable for load reduction. The integral control strategy adds a damping term to the tower and is very efficient for reducing the tower loads. When using a superimposed generator torque as actuator the controller also affects the drive train and power quality. An integral controller is implemented in the nonlinear aeroelastic code HAWC2 and the control strategy is tested in more realistic time simulations. The results shows that the tower fatigue load can be reduced by 40 % with the cost of an increased drive train fatigue load of only 10 %.

6.4 Lateral Tower Load Mitigation by Passive Yaw Slip

It has been suggested to use a passive yaw slip mechanism to ”kill” extensive lateral tower vibrations. The idea is, that lateral tower oscillations will create a yaw moment if the nacelle-rotor assembly center of gravity is not directly above the yaw axis. When the vibration reaches a critical amplitude this yaw moment should be so large that the yaw bearing slides in the breaks, extracting a large amount of energy and killing the vibrations. In this sections the feasibility of such a system is evaluated by some simple estimations.

The tower top motion caused by harmonic tower mode vibrations can be described by

$$x = A\sin(t\omega) \tag{6.29}$$

where A is the tower top deflection amplitude, t is time and ω is the tower mode frequency. The yaw moment caused by these the oscillations is then given by

$$M_{yaw} = -l_{cg} m A \omega^2 \sin(t\omega) \tag{6.30}$$

where l_{cg} is the distance from yaw axis to center of gravity of the nacelle-rotor assembly and m is the total mass of the nacelle-rotor assembly.

To compare this to yaw moments during normal operation the NREL 5 MW reference turbine is used as an example. Figure 6.16a shows the statistics for yaw moments at normal operation computed by the aeroelastic simulations tool HAWC2 and Figure 6.16b shows the time series of the 24 m/s case which has the highest yaw moments.

The maximum yaw moments is seen to be around ± 15 MNm and a common reach value is around ± 10 MNm. From a maintenance and power production point of view it is desirable that such a yaw system is not active during normal operation conditions. For a yaw slip mechanisms not to be active during normal operation, it has to have a slip force higher than at least the 10 MNm. Inserting this yaw moment and parameters from the 5 MW RWT into Equation (6.30) gives a tower top amplitude of

$$A = \frac{|M_{yaw}|}{l_{cg} m \omega^2} = 26.2m \tag{6.31}$$

where $|M_{yaw}| = 10$ MNm is the absolute value of the oscillating yaw moment, $l_{cg} = 1$ m, $m = 350 \cdot 10^3$ kg and $\omega = 2.01$ rad/s. Equation (6.31) shows that for this particular turbine configuration it is unrealistic to have lateral tower mode induced yaw moments that exceed the normal operation yaw moments. The only parameter that can be changes is the location of center of gravity of the rotor-nacelle assembly, which can be alternated by another nacelle design. Rearranging Equation (6.30) and assume the an $A = 1$ m tower top amplitude is critical gives a desired location of center of gravity

$$l_{cg} = \frac{|M_{yaw}|}{A m \omega^2} = 7.07m \tag{6.32}$$

which is seen to be an unrealistic location of center of gravity since the nacelle on this turbine only has an overhang of 5 m.

References

[1] J. A. Michelsen. Basis3D - a Platform for Development of Multiblock PDE Solvers. Technical Report AFM 92-05, Technical University of Denmark, 1992.

[2] J. A. Michelsen. Block structured Multigrid solution of 2D and 3D elliptic PDE's. Technical Report AFM 94-06, Technical University of Denmark, 1994.

[3] N. N. Sørensen. General Purpose Flow Solver Applied to Flow over Hills. Risø-R- 827-(EN), Risø National Laboratory, Roskilde, Denmark, June 1995.

[4] B. P. Leonard. A stable and accurate convective modelling procedure based on quadratic upstream interpolation. *Comput. Meths. Appl. Mech. Eng.*, 19:59–98, 1979.

[5] F. R. Menter. Zonal Two Equation k-ω Turbulence Models for Aerodynamic Flows. AIAA-paper-932906, 1993.

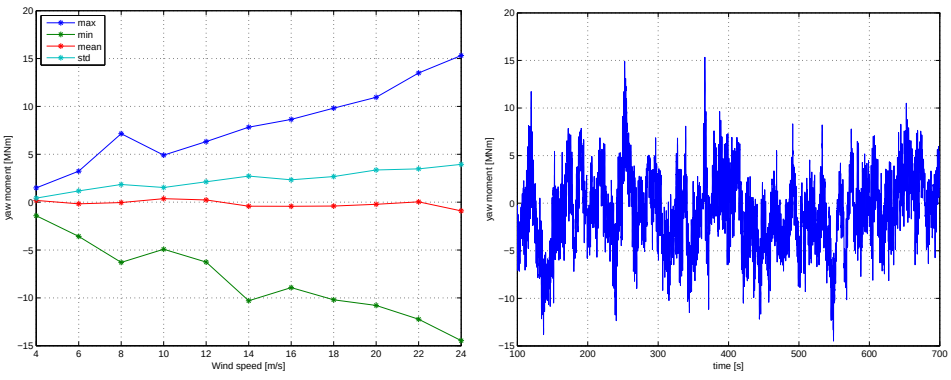

(a) (b)

Figure 6.16. a) Statistics for yaw moment for the NREL 5 MW reference turbine for normal production cases. b) Time series for of yaw moment for the 24 m/s case.

[6] J. H. Ferziger and M. Peric. *Computational Methods for Fluid Dynamics*. Springer-Verlag, 1996.

[7] N. N. Sørensen. HypGrid2D a 2-D Mesh Generator. Risø-R- 1035-(EN), Risø National Laboratory, Roskilde, Denmark, Feb 1998.

[8] J. N. Sørensen, W. Z. Shen Numerical modelling of Wind Turbine Wakes. Fluids Engineering, Vol. 124, Issue 2, 2002.

[9] L. Ta Phuoc, R. Lardat, M. Coutanceau, Pineau G. Rechereche et analyse de modeles de turbulence de sous maille adaptes aux ecoulments instationaires decolles. LIMSI Report 93074, LIMSI, France, 1994.

[10] N. Troldborg, J. N. Sørensen, R. Mikkelsen, Numerical simulations of wake characteristics of a wind turbine in uniform inflow. Wind Energy, 13:86-99. doi:10.1002/we.3452009.

[11] Tarp-Johansen, N., Andersen, L., Christensen, E., Mrch, C., Kallese, B., and Frandsen, S., Comparing Sources of Damping of Cross-Wind Motion, *Proceedings of the European Offshore Wind 2009, Stockholm*, September 2009.

[12] Ekelund, T., Yaw control for reduction of structural dynamic loads in wind turbines, *Journal of Wind Engineering and Industrial Aerodynamics*, Vol. 85, No. 3, 2000, pp. 241–262.

[13] Thomsen, J. J., *Vibrations and Stability: Advanced Theory, Analysis, and Tools*, Springer-Verlag: Berlin - Heidelberg - New York, 2003.

[14] Jonkman, J., NREL 5 MW Baseline Wind Turbine, Tech. rep., NREL/NWTC, 1617 Cole Boulevard; Golden, CO 80401-3393, USA, 2005.

[15] Larsen, T., Hansen, A., and Buhl, T., Aeroelastic effects of large blade deflections for wind turbines, *Proceedings of the special topic conference "The Science of making Torque from Wind"*, 2004, pp. 238–246.

[16] Larsen, T., Madsen, H., Hansen, A., and Thomsen, K., Investigations of stability effects of an offshore wind turbine using the new aeroelastic code HAWC2, *Proceedings of the conference "Copenhagen Offshore Wind 2005"*, 2005.

[17] (Editor), T. Larsen., How 2 HAWC2, the user's manual, Risø-r-1597(ver. 3-7)(en), RisøNational Laboratory, 2009.

[18] Wright, A. and Stol, K., Designing and Testing Controls to Mitigate Dynamic Loads in the Control Advanced Research Turbine, *Proceedings of the 46th AIAA Aerospace Sciences Meeting and Exhibit*, Reno, Nevada, Jan. 7-10, 2008.

7 Development of next generation aerodynamic design tools

Author: Jens N. Sørensen, Valery L. Okulov and Nstor R. Garca

This chapter describes the development of design tools for optimum design of wind turbine rotors using vortex modelling and viscous-inviscid interactive approaches. It comprises two main parts:

1. The development of a viscous-inviscid interactive boundary layer code for design of airfoils including rotational effects.
2. An inverse method for optimum design of wind turbine rotors based on an analytical model of helical vortices.

In the following we give a summary of the achievements of the work and present some of the most important results obtained during the project.

7.1 Viscous-Inviscid Interactive (VII) Boundary Layer Code

A computational model for predicting the aerodynamic behavior of airfoils of wind turbines subject to steady and unsteady motions has been developed [1]. The model is based on a viscous-inviscid interaction technique using strong coupling between the viscous and inviscid parts. The inviscid part is modeled using a panel method and the viscous part is modeled by using a integral form of the laminar and turbulent boundary layer equations, including a quasi-3D approach in order to include rotational effects. The code is capable of predicting laminar to turbulent transition either by using a numerical trip wire (fixed transition) or by using a modified e^n transition model (free transition). Validation of the steady two dimensional version of the code has been carried out against experiments for different airfoil geometries and Reynolds numbers. The unsteady version of the code has been benchmarked against experiments for different airfoil geometries at various reduced frequencies and oscillation amplitudes. In all cases, excellent agreement has generally been obtained between computed and measured lift and drag coefficients. The capability of the code to simulate a trailing edge flap under steady or unsteady flow conditions has also been proven. A parametric study on rotational effects induced by Coriolis and centrifugal forces in the boundary layer equations shows that the effect of rotation is to decrease the growth of the boundary layer, delay the onset of separation, and increase the lift coefficient and decrease the drag slightly.

A special inviscid version of the code has been developed to cope with massive separation. This special model demands knowledge of the position of the separation point. However, with a known position of the separation point, computed pressure distributions are in excellent agreement with experimental results.

Finally, the model has the possibility of taking into account wind tunnel blockage using an additional source distribution modeling the influence of wind tunnel walls. This is important when comparing results from the model with wind tunnel experiments.

In the following we will show some representative results obtained from the model.

7.1.1 Two-dimensional Steady VII Computations

This section presents a detailed comparison of lift and drag coefficients as function of angle of attack between measurements, the 2D Navier-Stokes flow solver EllipSys2D and viscous-inviscid interactive simulations. Xfoil and EllipSys2D computations used for benchmarking in

the present report where published by Bertagnolio et al. in 2001 in the Ris wind turbine airfoil catalogue [3], with exception of the Navier-Stokes computations on the NACA 65415 airfoil which have been carried out with the current EllipSys2D version. This airfoil is designed to attain its minimum pressure at 0.5c, defined by the 2nd digit, a design lift coefficient at zero angle of attack of 0.4, indicated by the 3rd digit, and with a 15% maximum thickness, given by the last two digits. Measurements were performed at the NASA low-turbulence pressure tunnel, reported by Abbott and von Doenhoff [2]. The Reynolds number in the experiments as well as in the computations was $3.0 \cdot 10^6$. In the following, viscous-inviscid interactive computations are referred to as Q^3UIC in the figures. In Figure 7.1 (a), lift comparisons are presented for angles of attack from 0 to 20 degrees. Both the VII solver and EllipSys2D are seen to over-predict the lift coefficient in the whole range of angles of attack if compared with experimental data. Drag curves are presented in Figure 7.1 (b). The VII predictions of drag at low angles of attack are in good agreement with experiments although it seems to under-predict the drag at angles of attack between 8° and 11°. In this region EllipSys computations are in better agreement with measured data.

Figure 7.2 compares computed pressure distributions with results from the EllipSys code (in the figure VII computations are referred to as *eNRG*). A good agreement between VII computations and EllipSys2D predictions of the surface pressure distributions is obtained at low angles of attack, although small discrepancies appear on the suction side of the trailing edge, Figures 7.2 (a) and (b). With increasing angle of attack, a progressive increase of the pressure peak near the airfoil leading edge is predicted. A recovery of the pressure from the pressure peak downstream is computed until $\alpha = 9°$, where the turbulent flow undergoes trailing edge separation and hence a region of nearly constant pressure is formed in the trailing edge vicinity. Laminar boundary layers undergo easier separation while turbulent boundary layers offer more resistance against the adverse pressure gradient. The viscous-inviscid computations predict a faster movement upstream of the turbulent separation point, as compared with EllipSys2D predictions. At the same time, the constant pressure region created by the reversal flow is also predicted at a lower absolute value by the VII computations, Figures 7.2 (c) and (d). When the separated region increases, the airfoil enters stalled conditions and the differences between the two simulations are reduced , Figures 7.2 (e) and (f).

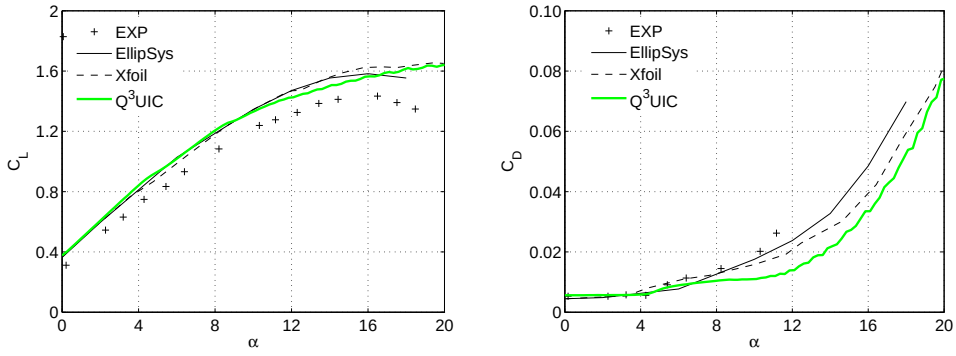

(a) (b)

Figure 7.1. Lift and drag coefficient as function of angle of attack of the NACA 65415 at Re = $3.0 \cdot 10^6$.

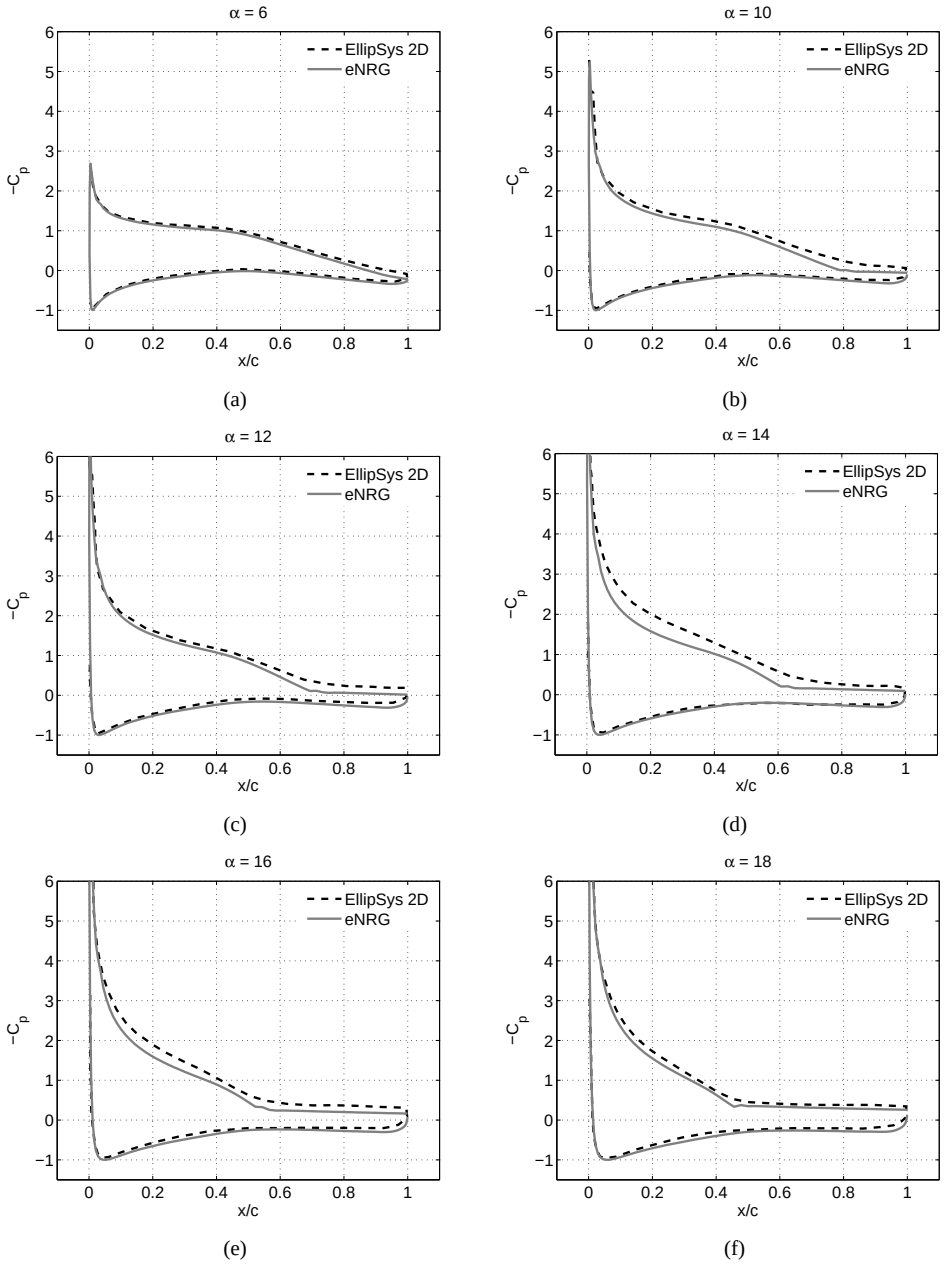

Figure 7.2. Surface pressure coefficients of the NACA 65415 Airfoil at Re $= 3.0 \cdot 10^6$.

To check the ability of the codes to compute wind turbine airfoils, Figure 7.3 compares VII computations of the FFA W3-241 airfoil [4] with experiments and computations using EllipSys and XFOIL.

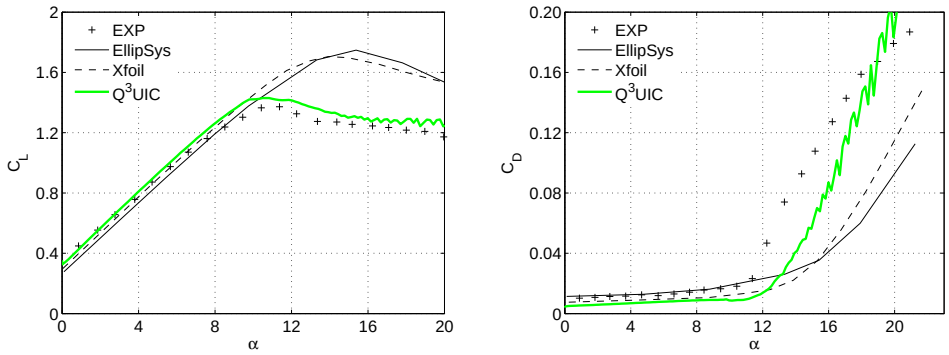

Figure 7.3. Lift and drag coefficient as a function of the angle of attack of the FFA W3-241 at $Re = 1.5 \cdot 10^6$.

From the figures the VII code is seen to perform very well with respect to both lift and drag predictions. Another wind turbine airfoil used for validating the code is the S814 airfoil. The results from computations of this airfoil, shown in Figure 7.4, exhibit similarly good results.

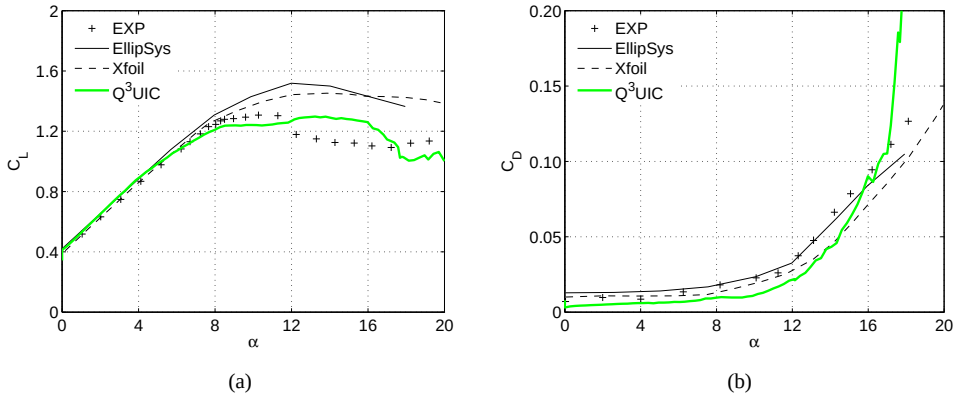

Figure 7.4. Lift and drag coefficient as a function of the angle of attack of the S814 at $Re = 1.0 \cdot 10^6$.

Finally, in order to verify the ability of the code to compute thick airfoils, computations were carried out for the 30% thick FFA W3-301 airfoil [4]. The results from these computations are shown in Figure 7.5. It appears clear that all computing codes have problems in determining the correct behavior in the stalled region. This could be related with the high turbulence level of the VELUX wind tunnel, which has an open section. The new VII code, however, seems to be capable of predicting the maximum lift value closer to experiments. It should be emphasized, however, that as the thickness of the airfoil increases, the results sensitivity to turbulence intensity may also increase. A higher turbulent intensity will trigger the laminar to turbulent transition earlier, consequently the trailing edge separation will appear at lower angles of attack, moving upstream and obtaining hence a lower maximum lift value. Here free transition computations have been compared. It is important to note that EllipSys2D computations running in fully turbulent mode are in much better agreement with experiments.

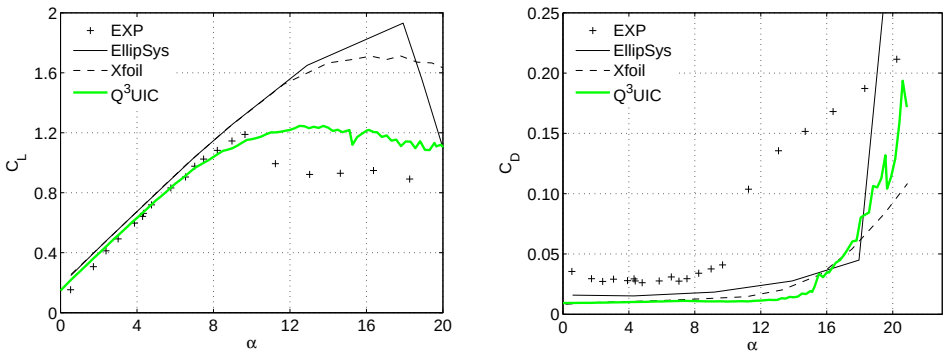

(a) (b)

Figure 7.5. Lift and drag coefficient as a function of the angle of attack of the FFA W3-301 at $Re = 1.5 \cdot 10^6$

7.1.2 Two-dimensional Unsteady VII Computations

Dynamic stall conditions are common on wind turbine rotors and affect their aerodynamic performance. Pitch regulated machines will on the upper part of the rotors operate under stall depending on the wind conditions while stall regulated and active stall machines will always operate under dynamic stall conditions at high wind speeds. Dynamic stall on a wind turbine blade can be induced by rotor yaw, blade control dynamics, flow control devices or changes in inflow conditions due to the turbulent nature of the atmospheric boundary layer. Most of these unsteady variations in flow characteristics are seen from the blade as a temporal change of angle of attack. Hence accurate predictions of the blade dynamic loads are of great importance in order to design new wind turbines blades with lower cost and better performance.

To validate the ability of the unsteady version of the viscous inviscid interactive model to simulate dynamic stall, comparisons of predicted aerodynamic coefficients C_L and C_D, are carried out and compared to wind tunnel experiments. Simulations are performed by keeping the airfoil at a fixed position, obtaining the change of the angle of attack according to variations of the free stream flow direction as a function of time. Different values of the mean angle of attack around which the airfoil oscillates, α_m, various amplitudes of oscillation, A, as well as reduced frequencies, k_A, are chosen in order to cover dynamic airfoil performance under a wide span of inflow conditions. Computations are run until a stable solution is reached, usually within no more than a couple of complete loops. In order to force an early turbulent boundary layer, in all cases the laminar to turbulent transition is forced at a position of 0.05c from the leading edge. A modified e^n method is used when the transition point moves upstream the boundary layer trip position. The viscous-inviscid interactive single wake model is used in all the computations.

As a first validation case is chosen a NACA 0012 profile subject to a harmonic pitch oscillation around $\alpha_m = 4^\circ$ with an amplitude $A = 6^\circ$, and a reduced frequency, $k_A = 0.021$. The reduced frequency is defined as:

$$k_A = \frac{\pi f_A c}{U_\infty} \tag{7.1}$$

where f_A is the oscillatory frequency, c is the chord length, and U_∞ is the free stream velocity.

In Figure 7.6 experimental lift coefficients for static and oscillating airfoil characteristics, carried out by Krzysiak and Narkiewicz [5], are compared against predictions of the VII code and static measurements carried out at the Sandia National Laboratories [6]. A counterclockwise loop is formed due to the attached nature of the boundary layer; unsteady terms on the boundary layer equations together with the influence of the unsteady vortex wake induce the hysteresis

effects. These effects grow with the frequency of the oscillating movement, i.e. at higher k_A, differences in lift between upstroke and down stroke motion are larger. The static experiments of Krzysiak and Narkiewicz present a lower lift in the vicinity of $\alpha = 10^\circ$, as compared to the Sandia Labs measurements. The same difference is observed when comparing the dynamic lift measurements of Krzysiak against the dynamic lift predictions of the VII code.

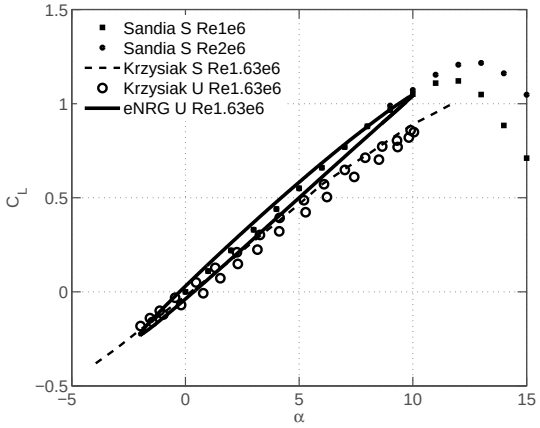

Figure 7.6. Comparison between computed and measured dynamic/static lift data of the NACA 0012 airfoil with: $\alpha_m = 4^\circ$ *,* $A = 6^\circ$*,* $k_A = 0.021$*, and Re* $= 1.63 \cdot 10^6$

As a second study case, the NACA 0015 airfoil was chosen. Experiments reported by Galbraith et al. [7] performed at the University of Glasgow are used for validation of the unsteady version of the VII code. In this case the NACA 0015 profile follows a harmonic pitch motion with a mean angle of attack, $\alpha_m = 11.37^\circ$, an amplitude of oscillation, $A = 4^\circ$, and a reduced frequency, $k_A = 0.102$. Computed values of normal and tangential force coefficients are compared against measurements in Figure 7.7. From Figure 7.7, predictions of dynamic forces around the airfoil are seen to be in good agreement with measurements. Both computations and experiments show how the flow fully reattaches to the airfoil surface around $\alpha = 3^\circ$ during the down stroke movement, creating a counter clockwise hysteresis lift loop.

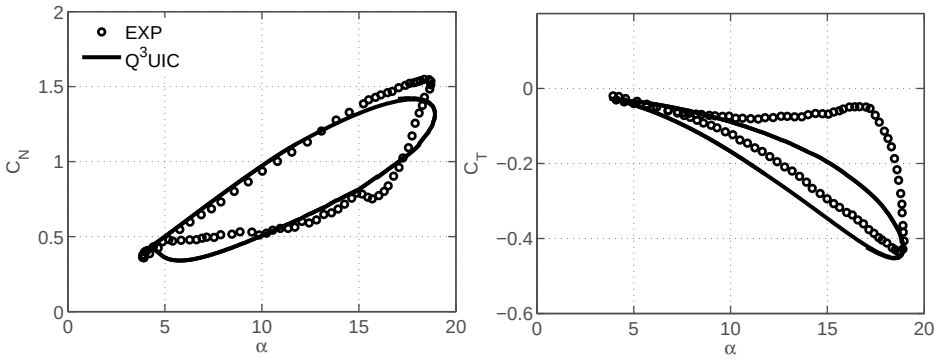

Figure 7.7. Comparison between computed and measured dynamic forces coefficients of the NACA 0015 airfoil with: $\alpha_m = 11.37^\circ$ *,* $A = 7.55^\circ$ *and* $k_A = 0.102$*, and Re* $= 1.5 \cdot 10^6$.

7.1.3 Two-dimensional Inviscid Double-Wake Computations

Because of poor performance of the single wake model at deep stall, a new approach for computing airfoil performance at high angles of attack has been developed. Knowing that the low performance is due to the lack of accuracy of solving the integral boundary layer equations

for flows with massive separation, in the new model the boundary layer is neglected and the flow is considered purely inviscid. Instead the pressure in the separated region is modeled by introducing an extended inviscid panel method. This model is referred to as the double wake model, due to the dual treatment of the separated region in two shear layers leaving the airfoil and converging downstream. Separation is one of the phenomena with the strongest influence on the aerodynamic design of wind turbine blades. Lift and drag forces are strongly affected when the flow undergoes separation, causing an exponential increment of drag at the same time as the lift curve stalls.

The bubble type of separation has been studied widely and the difficulties of modeling this kind of phenomena stems from the problem of predicting the pressure level in the separated region as well as determining the exact position where the attached boundary layer undergoes separation. The double wake model will allow us to compute with a high degree of accuracy the pressure distribution all over the airfoil, including the separated region. The double wake model will generate a vortex sheet that leaves the airfoil from the separation point at the same time as the trailing edge is releasing vorticity through another vortex sheet. The uniform vortex distribution around the two wakes will influence the tangential velocities at the airfoil surface, creating a region of reversed flow, which simulates the separation effect of the flow around an airfoil at high angles of attack. The region of fluid surrounding the airfoil and the separated wake is irrotational, and, assuming that the Mach number is low, compressibility is negligible. The area in between the two wakes does not contain any significant vorticity and has a more or less constant total pressure, and thus it is taken to be a potential flow region. The flow will then be assumed irrotational everywhere except in the two confined sheets of constant vorticity that forms the separated wake. The initial shape of the wake is obtained iteratively starting from an initial condition. As initial condition the wake sheets are represented by two straight lines in between the separation points and a common point downstream.

To validate the double wake model, the pressure distribution around the airfoil surface has been computed for different airfoils at different angles of attack in stalled conditions. Double wake model predictions are compared against experiments. The separation position at which the upper wake is shed is for all the considered cases obtained from the experimental pressure distribution. In Figure 7.8 inviscid double wake model pressure computations are compared against wind tunnel measured data at a Reynolds number $Re = 6.3 \cdot 10^6$. The simulated airfoil is a NACA 4412 at 17.6 and 22.1 degrees angle of attack. Experimental data used for validation was published in a NACA report by Robert M. Pinkerton [8]. For an angle of attack of 17.6°, the separation point is forced at 0.5331c in simulations. The position of separation is obtained from the experimental pressure distributions. At 22.1 degrees the separation position is forced at 0.1674c, obtained with similar procedure as in the first case. At $\alpha = 17.6^\circ$ a good agreement with measurements is achieved for both the upper and lower surface pressure distributions. The pressure peak is captured with high accuracy and also the rate at which the pressure recovers until separation is reached. In the case of $\alpha = 22.1^\circ$, a fairly good agreement is obtained for the suction surface, despite the fact that the absolute value of the pressure peak is slightly under predicted. In Figure 7.9, wind tunnel measurements of the surface pressure distribution around a GA(W)-1 airfoil are compared against the double wake model predictions. The experiments were carried out at the NASA Langley Wind Tunnel installation [9]. The Reynolds number in the experiments is $Re = 6.3 \cdot 10^6$ and a boundary layer trip was placed at 0.08c from the leading edge. Comparisons are presented for angles of attack of $\alpha = 20.05^\circ$ and $\alpha = 21.14^\circ$ respectively. In both cases, with the separation position determined from the experiments, nearly perfect agreement is achieved.

The drawback of the double wake model is of course that it demands a priori knowledge of the position of the separation point. In the present work we have only focused on comparing airfoils where we know the position of the separation point. However, in a further development of the code we intend to establish a data base on airfoil characteristics and employ this to parameterize the position of the separation point. Thus, knowing the point of separation as a

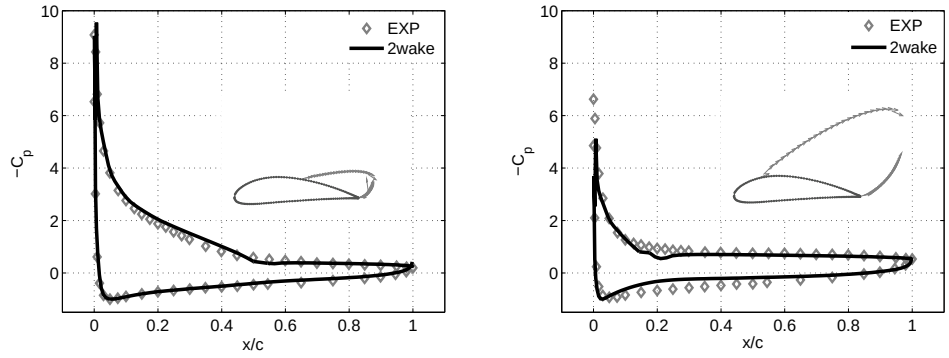

Figure 7.8. Surface pressure coefficients of the NACA 4412 airfoil at Re $= 6.3 \cdot 10^6$ *(a)* $\alpha = 17.6^\circ$*; (b)* $\alpha = 22.1^\circ$

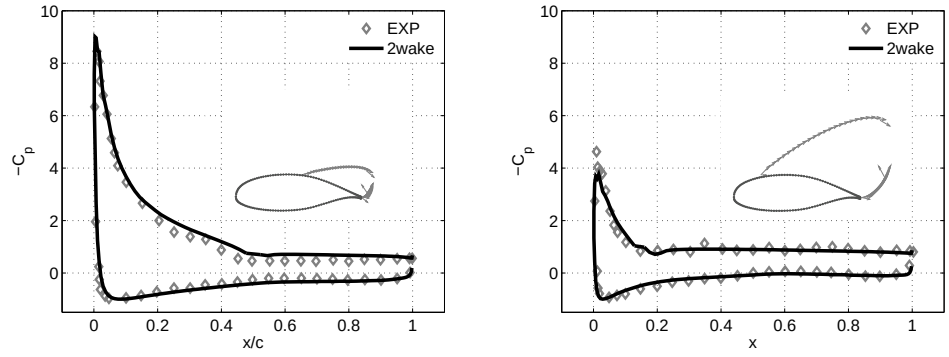

Figure 7.9. Surface pressure coefficients of the GA(W)-1 airfoil at Re $= 6.3 \cdot 10^6$*, (a)* $\alpha = 20.05^\circ$*; (b)* $\alpha = 21.14^\circ$

function of airfoil thickness, camber line, Reynolds number, type of airfoil, ambient turbulence, etc, we hope to come up with a simple code capable of giving the main characteristics of airfoils operating at high angles of attack.

7.1.4 Quasi Three-dimensional VII Computations

It is known that two dimensional measurements under predict the lift forces on rotor blades in stalled conditions. Centrifugal and Coriolis forces appearing in the rotational boundary layer are the most likely causes of the enhanced aerodynamic forces. The centrifugal force will produce a span wise outward velocity component which will give rise to Coriolis forces that will act as a favorable pressure gradient in the chord-wise direction. The centrifugal force also tends to reduce the thickness of the boundary layer by the outward movement of the fluid, more commonly known as the centrifugal pumping effect. It is known that rotational effects are stronger in regions close to the rotational axis and close to stall conditions, although a detailed study of the phenomenon has not yet been done. One of the objectives of the present study is to obtain a deeper understanding of the influence of rotation in the boundary layer. In the present work an interactive viscous-inviscid model has been developed with capability of solving the quasi-3D unsteady incompressible boundary layer equations. To reduce the 3D boundary layer equations to the quasi-3D ones, an assumption that simplifies the radial derivatives has been implemented. Hence the three dimensional boundary layer equations have been reduced to two dimensions and formulated in integral form with additional rotational terms that take into account the span-

wise velocity profile. The errors introduced by these assumptions are known to be small due to the small order of magnitude of the radial components of the boundary layer. With the present method we are capable of predicting the influence of rotation on lift and drag performance of a two-dimensional airfoil section of a rotating blade. Yawed flow, however, falls outside the capabilities of the code. Radial derivatives are simplified assuming a high local aspect ratio of the blade cross section.

To demonstrate the influence of the rotating effects in an airfoil section, a study of the aerodynamic performance of a S809 airfoil subjected to rotation has been carried out and is presented herein. The simulations are carried out at a Reynolds number of $1.0 \cdot 10^6$. The transition of the boundary layer from laminar to turbulent flow is forced at 0.05c from the leading edge. In Figures 7.10 lift variations as function of the chord-radius ratio, c/r, are shown for four values of the rotational number, $RO = \Omega\, r/U_{rel}$, where Ω is the rotational velocity of the rotor and U_{rel} is the local relative velocity. Generally as RO increases, maintaining a constant c/r ratio, the lift increases. As a consequence, an increase in RO results in an increase in maximum lift coefficient. In a similar way, as the ratio c/r increases, maintaining RO constant, $\alpha(C_L = C_{Lmax})$ increases, retarding stall in a similar way. After the maximum lift is reached the airfoil stalls, resulting in a negative lift slope for $\alpha > \alpha(C_L = C_{max})$, which increases for larger c/r ratios. Centrifugal and Coriolis forces create a favorable pressure gradient that thins the boundary layer and retards separation. At low angles of attack, i.e. attached flow, the rotational forces induce a thinner boundary layer. Since separation is not involved, the higher lift is created because of the lower obstruction exhibited by the thin boundary layer against the free stream flow. At higher angles of attack a delay in the separation location is predicted due to the favorable pressure gradient generated by rotation. A strong radial flow present in the bottom of a separated boundary layer modifies actively the lift characteristics of the airfoil sections. The later separation appears, the faster it moves towards the leading edge after stall is reached, this explains the drastic decrement in lift for $\alpha > \alpha(CL = CLmax)$. In the cases in which the influence of Coriolis and centrifugal forces are sufficiently large, the flow remains attached to the airfoil surface even at high angles of attack. In these cases the lift increases linearly with the angle of incidence.

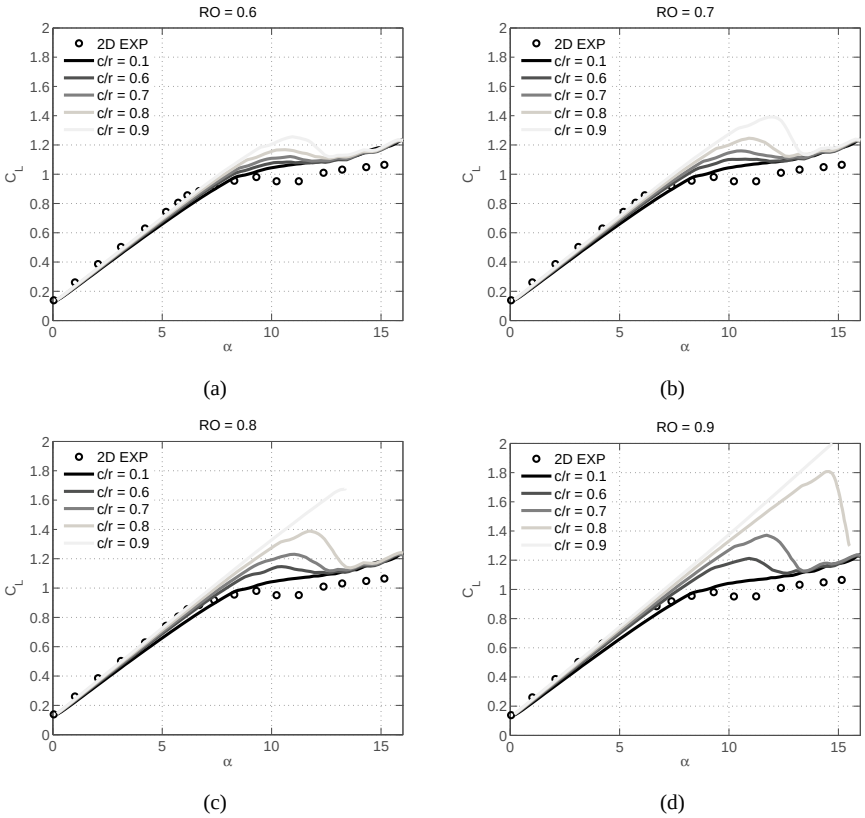

Figure 7.10. Influence of rotation on lift coefficient as function of angle of attack and rotational number, RO. S809 airfoil. c/r varies from 0.1 to 0.9; Re$= 1.0 \cdot 10^6$.

7.2 Vortex models for optimum inverse design of wind turbine blades

7.2.1 Analytical models

In the history of rotor aerodynamics two 'schools' have dominated the conceptual interpretation of the optimum rotor. In Russia, Joukowsky [10] defined the optimum rotor as one having constant circulation along the blades, such that the vortex system for an N_b bladed rotor consists of N_b helical tip vortices of strength Γ and an axial hub vortex of strength $-N_b\Gamma$. A simplified model of this vortex system can be obtained by representing it by a rotating horseshoe vortex (see Figure 7.11 a). The other school, which essentially was formed by Prandtl and Betz [11], assumed that optimum efficiency is obtained when the distribution of circulation along the blades generates a rigid helicoidal wake that moves in the direction of its axis with a constant velocity. Betz used a vortex model of the rotating blades based on the lifting-line technique of Prandtl in which the vortex strength varies along the wingspan (Figure 7.11 b). This distribution, usually referred to as the Goldstein circulation function, is rather complex and difficult to determine accurately [12]. In both cases only conceptual ideas were outlined for rotors with finite number of blades, whereas later theoretical works mainly concerned actuator disk theory. Hence, in practice, wind turbine blades are modeled using Blade-Element Momentum (BEM) theory, corrected by the tip correction of Prandtl.

It should be noted that none of the models fully simulates the actual vortex development behind a turbine. Typically a system of trailing vortices are formed on the rotor due to the radial distribution of circulation. This system further forms a set of helicoidal vortices, which, due the mutual interaction between the vortex lines, starts to roll up, eventually forming a flow field dominated by strong tip and root vortices. The roll-up process is initiated rather quickly and typically the tip vortices are formed after a half rotation of the vortex system. Further downstream, due to the inherent instability of the helical vortices, this system becomes unsteady

and breaks down into small-scale turbulence, forming the far wake [13], [14].

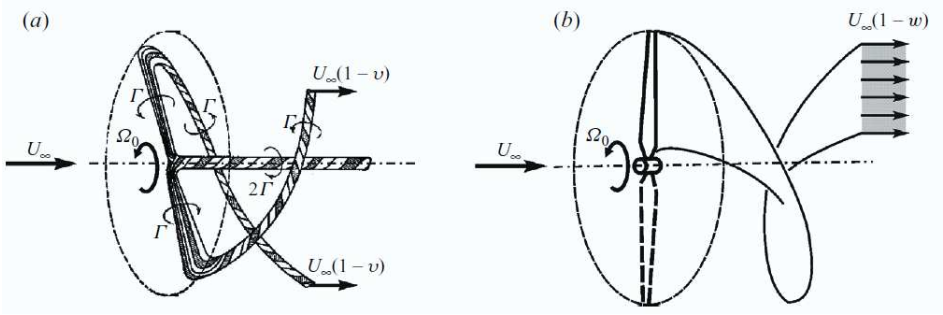

Figure 7.11. Sketch of the vortex system corresponding to lifting line theory of the ideal propeller of Joukowsky (a) and Betz (b)

Recently, we have derived an analytical solution for rotors with Goldstein distributions of circulation along the blade (Betz rotor) [15], [16] and [17] using a new analytical model of the velocity field induced by helical vortices. In the present work we exploit the analytical model further to develop a vortex theory of a rotor based on the concepts outlined by Joukowsky using constant circulation along the blades (Joukowsky rotor). Both solutions enable for the first time to compare the theoretical maximum efficiency of wind turbines with Betz and Joukowsky rotors.

In the vortex theory each of the blades is replaced by a lifting line on which the radial distribution of bound vorticity is represented by the circulation $\Gamma = \Gamma(r)$ which is a function of the radial distance along the rotor blade. This results in a free vortex system consisting of helical trailing vortices, as sketched in Figures 7.11. Using vortex theory, the bound vorticity serves to produce the local lift on the blades while the trailing vortices induce the velocity field in the rotor plane and in the wake. As illustrated in Figure 7.12 the velocity vector in the rotor plane is made up by the rotor angular velocity Ω_0, the undisturbed wind speed U_∞, the axial and circumferential velocity components u_{z_0} and u_{θ_0} , respectively, induced at a blade element in the rotor plane by the tip vortices, and v_{θ_0}, the circumferential velocity induced by the hub vortex. The fundamental expressions for the forces acting on a blade (Figure 7.12) is most conveniently expressed by the Kutta-Joukowsky theorem, which in vector form reads

$$d\overline{L} = \rho\overline{V_0} \times \overline{\Gamma}\, dr, \tag{7.2}$$

where $d\overline{L}$ is the lift force on a blade element of radial dimension dr, V_0 is the resultant relative velocity and ρ is the density of the air.

From the above equation, we can write the local torque dQ of a rotor blade as follows

$$dQ = \rho\Gamma\,(U_\infty - u_{z_0})\, r\, dr, \tag{7.3}$$

Integrating this equation along the blades and summing up, we get the following expression for the power output, $P = \Omega_0 Q$,

$$P = \rho N_b \Omega_0 \int_0^R \Gamma\,(U_\infty - u_{z_0})\, r\, dr, \tag{7.4}$$

where R is the radius of the rotor.

To determine the theoretical maximum efficiency of a rotor the power coefficient is introduced as follows,

$$C_P = P/\left(\frac{1}{2}\rho\pi R^2 U_\infty^3\right), \tag{7.5}$$

The maximum power that can be extracted from a stream of air contained in an area equivalent to that swept out by the rotor corresponds to the maximum value of the power coefficient.

The Joukowsky rotor

In the vortex theory of the Joukowsky rotor each of the blades is replaced by a lifting line about which the circulation associated with the bound vorticity is constant, resulting in a free vortex system consisting of helical vortices trailing from the tips of the blades and a rectilinear hub vortex. The vortex system may be interpreted as consisting of rotating horseshoe vortices with cores of finite size, as sketched in Figure 7.11 (a) which is reproduced from the original Joukowsky drawing's . The associated vortex system consists of a system of helical tip vortices of finite vortex cores ($\varepsilon << R$) with constant pitch h and circulation Γ. The vortices move downwind (in the case of a propeller) or upwind (in the case of a wind turbine) with a constant velocity $U_\infty(1\pm\nu)$ in the axial direction where ν denotes the difference between the wind speed and the axial translational velocity of the vortices. Denoting the angle between the axis of the tip vortex and the Trefftz plane as Φ (see Figure 7.12 a), the helical pitch of the multiplet is given as

$$h = 2\pi\, R\, tan\Phi, \;\; or \;\; l/R = h/2\pi R = tan\Phi \tag{7.6}$$

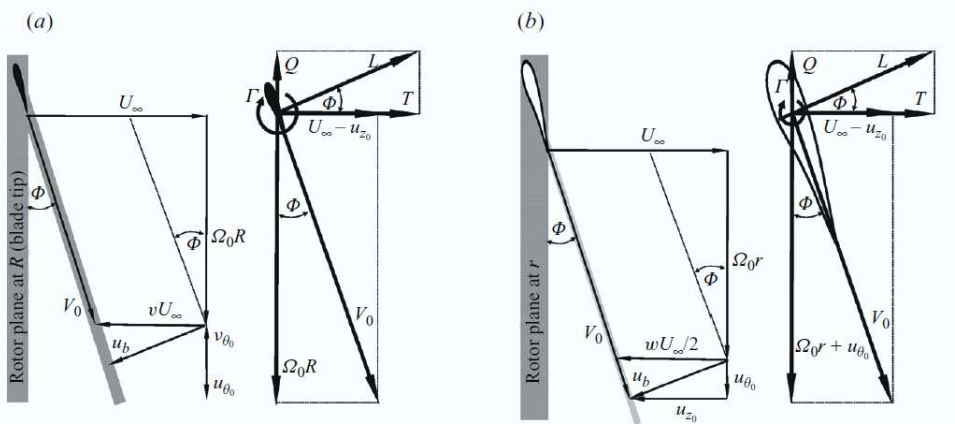

Figure 7.12. Velocity and power triangles in the rotor plane of (a) Joukowsky rotor and (b) Betz rotor.

The free vortex lines are made up by vortex cores of finite size in order to avoid singular behavior. The vortex cores are collinear to the axes of the helical lines and their vorticity is assumed to be uniform and densely distributed across the core cross-section. In cylindrical coordinates (r,θ,z), the components of fluid velocity induced by N_b helical vortices in the domain outside the vortex cores constitute an infinite series of Bessel functions. However, following the approach by Okulov [18], these equations can be put into a relatively simple closed form. Using the simplified equations derived by Okulov [18] it has for the first time been possible to determine the performance of the Joukowsky rotor with finite blades. We will not here go into the detail about these equations, but just show some relations resulting from the analysis. Introducing the azimuthally averaged induced axial velocity as

$$\langle u_z\rangle_\theta = \frac{1}{2\pi}\int_0^{2\pi} u_z d\theta \tag{7.7}$$

we get

$$\langle u_z \rangle_\theta = 0 \;\; for\, r > R \;\; and \, \langle u_z \rangle_\theta = \frac{N_b \Gamma}{2\pi l} \equiv \text{const} \;\; for\, r < R \tag{7.8}$$

It should be mentioned that the dimensionless averaged induced axial velocity in the wake $(0 < r < R)$, which is identical to the total axial wake interference factor a, takes the same constant value

$$aU_\infty \equiv \langle \langle u_z \rangle_\theta \rangle_{0<r<R} = \frac{N_b \Gamma}{2\pi l} \tag{7.9}$$

The vortex system also includes a rectilinear hub vortex of strength $-N_b\Gamma$, resulting in a simple formula for the additional induced velocity that only consists of the circumferential component,

$$v_\theta = -\frac{\Gamma N_b}{2\pi r}, \tag{7.10}$$

Defining the azimuthally averaged azimuthal velocity induced by the helical vortices as

$$\langle u_\theta \rangle_\theta = \frac{1}{2\pi} \int_0^{2\pi} u_\theta d\theta, \tag{7.11}$$

we get

$$v_\theta|_{r=R} = -\langle u_\theta \rangle_\theta |_{r=R} \tag{7.12}$$

To eliminate the singularity of the induced velocity field in the vicinity of the vortex filament the vortex system is represented by a set of helical vortices with finite core. For an unexpanded wake originating from a rotor with infinitely many blades, the convective velocity of the vortex system equals half the averaged induced axial velocity in the wake. This is sometimes referred to as the 'roller-bearing analogy'. Although this approximation cannot be rigorously justified for a vortex system consisting of a finite number of vortices, we employ the same analogy by assuming that the helical vortices are transported with a relative axial speed, ν, that corresponds to half the averaged induced velocity,

$$\nu = \frac{1}{2} a \frac{(R+\varepsilon)}{R}, \tag{7.13}$$

where a correction of small expansion of the cross-section of the wake is made in order to include the radius, ε, of the vortex cores. Introducing the non-dimensional pitch and radius of the vortex core, $\sigma = \varepsilon/R$, from simple geometric considerations in the rotor plane the angular pitch is given as

$$tan\Phi|_{r=R} = \frac{U_\infty - |u_{z_0}|_{r=R}}{\Omega_0 R + |u_{\theta_0}|_{r=R} - |v_{\theta_0}|_{r=R}} = \frac{U_\infty(1-\nu)}{\Omega_0 R} = \frac{U_\infty\left[1 - \frac{1}{2}a(1+\sigma)\right]}{\Omega_0 R} = \frac{l}{R} \tag{7.14}$$

Exploiting the various relations, the power can be determined from the following integral

$$P = \rho\pi R^2 U_\infty^3 a \left(1 - \frac{a}{2}(1+\sigma)\right)\left(1 - a\int_0^1 \widetilde{u}_z(x,0) x dx\right) \tag{7.15}$$

Performing the integration and introducing the dimensionless power coefficient, we get

$$C_P = 2a\left(1-\frac{1}{2}aJ_1\right)\left(1-\frac{1}{2}aJ_3\right) \tag{7.16}$$

where $J_1 = 1+\sigma$ and $J_3 = 2\int_0^1 \widetilde{u}_z(x,0)xdx$. For a given helicoidal wake structure, the power coefficient is seen to be uniquely determined, except for the parameter a. Differentiation of C_P with respect to a yields the maximum value of $C_{P_{max}}$, resulting in

$$a\,(C_P = C_{P_{max}}) = \frac{2}{3J_1J_3}\left(J_1+J_3-\sqrt{J_1^2-J_1J_3+J_3^2}\right) \tag{7.17}$$

The Betz rotor

To compare the efficiency of the Joukowsky rotor with the Betz rotor, we here outline the main points of the derivation of the aerodynamics of the Betz rotor (for more details we refer to [15] and [16]). In this model, which is based on Lanchester-Prandtl wing theory, the vortex strength of the lifting line varies along the blade span, following the so-called Goldstein distribution. This results in a vortex sheet that is continuously shed from the trailing edge (Figure 7.11 b). Betz showed that the ideal efficiency is obtained when the distribution of circulation along the blade produces a rigidly moving helicoidal vortex sheet with constant pitch, h, that moves downwind (in the case of a propeller) or upwind (in the case of a wind turbine) in the axial direction of its axis with a constant velocity $U_\infty(1\pm w)$. The associated vortex system to the wake consists of a regular helical sheet extended to infinity in both directions. Denoting the angle between the vortex sheet and the Trefftz plane as Φ (see Figure 7.12b), the pitch is given as

$$h = 2\pi r\, tan\Phi \;\; or, \;\; l/r = h/2\pi r = tan\Phi \tag{7.18}$$

where r is the radial distance along the sheet. Since the sheet is translated with constant relative axial speed, wU_∞, the induced velocity comprises only the component $wU_\infty cos\Phi$ that is 'pushed' normal to the screw surface (Figure 7.12b). The axial and circumferential velocity components u_z and u_θ induced by the infinite sheet at the sheet itself are therefore given as

$$u_\theta = wU_\infty cos\Phi sin\Phi \;\; and \;\; u_z = wU_\infty cos^2\Phi \tag{7.19}$$

From simple geometric considerations these equations are rewritten as

$$u_\theta = wU_\infty\frac{xl}{l^2+x^2}, \;\; and \;\; u_z = wU_\infty\frac{x^2}{l^2+x^2}, \tag{7.20}$$

where $x = r/R$ is the dimensionless radius.

Goldstein [19] was the first who found an analytical solution to the potential flow problem of the moving associated vortex system consisting of an infinite helical vortex sheet. In his model a dimensionless distribution $G(x,l)$ of circulation was introduced as follows

$$N_b\Gamma(x,l) = 2\pi l wU_\infty G(x,l) \tag{7.21}$$

Using an infinite series of Bessel functions, Goldstein [19] succeeded in obtaining an analytical solution to the problem, but for $N_b = 2$ and 4 only. We have recently computed the Goldstein

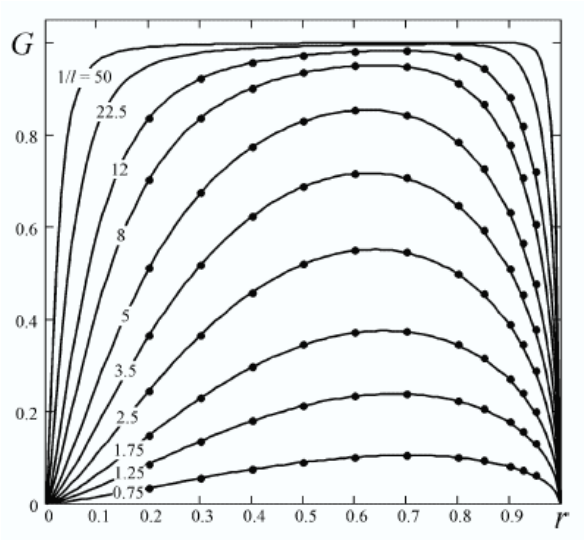

Figure 7.13. Computed Goldstein function for 3 blades and different values of helical pitch.

circulation function $G(x,l)$ for all relevant combinations of the wake pitch l and number of rotor blades N_b. In Figure 7.13 we sketch the Goldstein function for a 3-bladed rotor subject to various helical wake pitch values.

From geometric considerations in the rotor plane (Figure 7.12b), the angular pitch is given as

$$tan\Phi = \frac{U_\infty - \frac{1}{2}u_z}{\Omega_0 r + \frac{1}{2}u_\theta} = \frac{U_\infty(1-\frac{1}{2}w)}{\Omega_0 r} = \frac{l}{r} \tag{7.22}$$

This equation can be also written as

$$\Omega_0 l = U_\infty \left(1 - \frac{1}{2}w\right) \tag{7.23}$$

Combining the various equations, the power can be determined from the following integral

$$P = \rho\pi R^2 U_\infty^3 w \left(1 - \frac{w}{2}\right) \int_0^1 2G(x,l) \left(1 - \frac{w}{2}\frac{x^2}{x^2+l^2}\right) x dx \tag{7.24}$$

Performing the integration and introducing the dimensionless power coefficient, we get

$$C_P = 2w \left(1 - \frac{1}{2}w\right) \left(I_1 - \frac{1}{2}wI_3\right) \tag{7.25}$$

where

$$I_1 = 2\int_0^1 G(x,l)xdx \;\; and \;\; I_3 = 2\int_0^1 G(x,l)\frac{x^3 dx}{x^2+l^2} \tag{7.26}$$

The coefficients I_1 and I_3 are usually referred to as the mass coefficient and the axial energy factor, respectively.

For a given helicoidal wake structure, the power and thrust coefficients are seen to be uniquely determined, except for the parameter w. Differentiating of C_P with respect to w yields the maximum value of $C_{P_{max}}$, resulting in

$$w(C_P = C_{P_{max}}) = \frac{2}{3I_3}\left(I_1 + I_3 - \sqrt{I_1^2 - I_1 I_3 + I_3^2}\right) \tag{7.27}$$

7.2.2 Performance of the Joukowsky rotor and the Betz rotor

Figure 7.14 presents the optimum power coefficient of both models for different number of blades as function of tip speed ratio. From the plots it is evident that the optimum power coefficient of the Joukowsky rotor for all number of blades is larger than that for the Betz rotor. The difference, however, vanishes for $\lambda \to \infty$ or for $N_b \to \infty$, where both models tend towards the Betz limit.

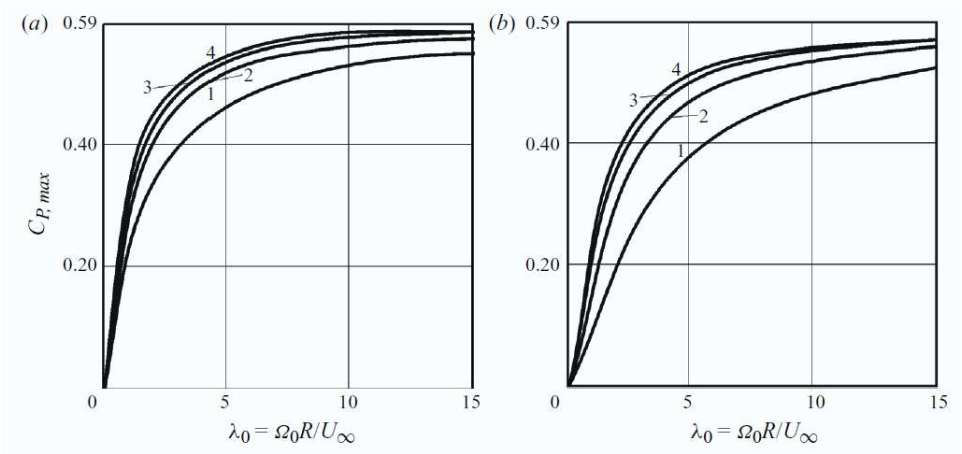

Figure 7.14. Power coefficients, C_P, of an optimum rotor as function of tip speed ratio and number of blades. Left: Joukowsky rotor; Right: Betz rotor.

In Figures 7.15 and 7.16 we show the resulting plan forms of the two optimized rotors at a tip speed ratio of 4 and 8, respectively. It is here seen that the optimum twist (local pitch) distribution is nearly the same for the two rotor designs. Furthermore, the two design tends toward the same distributions of both twist and chord when increasing the tip speed ratio. The main difference between the two designs are found at the root and the tip. This is easily explained by the difference in the load distribution, where there Goldstein distribution of circulation causes a more smooth gradual change in the chord distribution than the constant circulation in the Joukowsky model.

7.2.3 Numerical model

For more general design purposes, a design and optimization code based on a lifting line method coupled with a Lagrange multiplier approach has been developed [20]. In this model the circulation distribution minimizing the induced loss is determined, and the blade geometry is consequently derived using 2-D airfoil data. Airfoil viscous drag contribution can be included by adding it to the inviscid optimal solution. The code has been generalized to handle planar as well as non-planar blade geometries.

Two representative configurations were studied: a simple winglet, familiar from the aviation world, and a spiroid tip. The latter is a representative of what may be called highly nonplanar configurations.

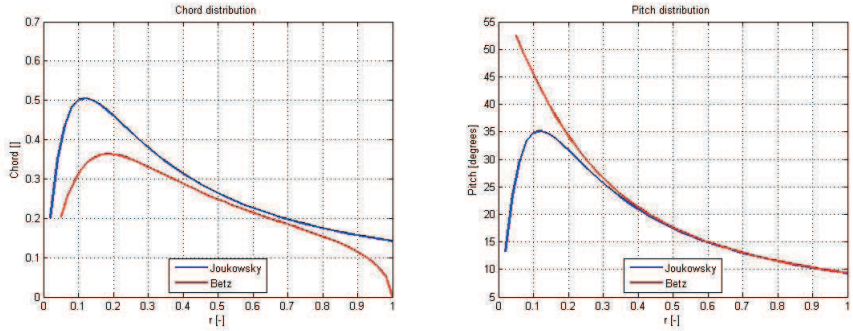

(a) (b)

Figure 7.15. Comparison of chord- and twist-distributions (referred as pitch in the figure) at tip speed ratio TSR=4. Left: Chord distribution rotor; Right: Twist distribution.

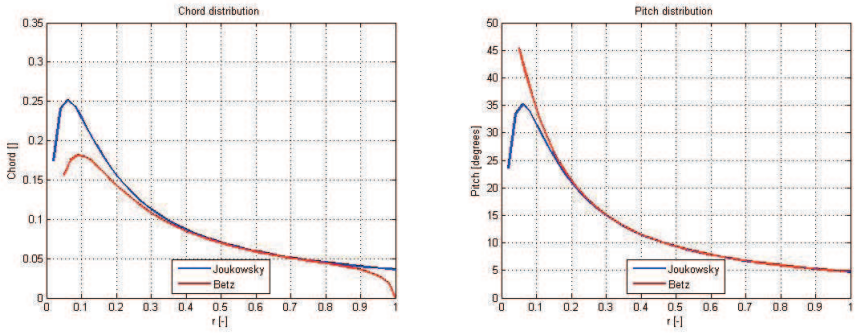

(a) (b)

Figure 7.16. Comparison of chord- and twist-distributions (referred as pitch in the figure) at tip speed ratio TSR=8. Left: Chord distribution rotor; Right: Twist distribution.

As wake model, a simple fixed pitch helical wake is used. In the case of non-planar blades, the wake helix is locally displaced as required, but it maintains the same pitch. In the planar blade case, it is completely consistent with the classical Goldstein solution. For non-planar blades, however, there is no rigorous justification for the validity of the helical approach, and therefore it must be considered as an approximation. An attempt to develop a more sophisticated wake model, a hybrid between a free wake and a fixed pitch wake, was not successful. It was found that, on one hand, the results obtained from this hybrid model are no more accurate than the results obtained from the fixed pitch model. On the other hand, the hybrid model is much more elaborate. Keeping in mind that for a preliminary design purposes a simple and robust code is desired, it is reckoned that the fixed pitch model is sufficient for this purpose. A time-stepping free wake code has been developed as a means of a further verification of the design code. In practice, the usage of this free wake code has been limited due to the prohibitive long run times. However, a few important insights were gained. It has been shown that, in the planar blade case, there is a good agreement with the design code. Additionally it has been shown that there is a fair agreement with some reference results in a case of blades with winglets. An important conclusion is that the design code is over-predicting the performance of tip devices due to the simplifications inherent to the simple fixed-pitch wake model. While still effective, the effect of these devices is actually confined to their immediate vicinity, as revealed by the free wake analysis.

7.3 Summary

A viscous-inviscid interactive (VII) boundary layer code for predicting airfoil performance has been developed and validated. The code is capable of computing flows with moderate stall. The model is extended with capabilities of simulating unsteady flow behavior (e.g. pitching airfoils), and it can take into consideration the influence of wind tunnel walls as well as rotational effects (Coriolis and centrifugal forces). Further, a special version of the code has been developed to cope with massive 'bubble-type' stall using a two-wake panel distribution. As compared to experiments and computed results using other codes, the code generally produces excellent results.

Both analytical and numerical inverse vortex codes have been developed and employed to predict aerodynamic optimized rotor plan forms following conceptual ideas outline by early aerodynamic theories. The analytical models can be employed to carry out initial rotor design. For more comprehensive design purposes, however, it is required to employ the numerical approach. In a continuation of the project the VII model will be coupled directly to the numerical design code, hence combining the design of airfoil sections with the plan form of the rotor.

References

[1] N. R. Garcia. *Unsteady Viscous-Inviscid Interaction Technique for Wind Turbine Airfoils*. PhD thesis, Danmarks Tekniske Universitet, 2011.

[2] I. H Abbott and A. E Doenhoff. Theory of wing sections. *Dover Publications, Inc., New York*, 1959.

[3] F. Bertagnolio, N. Sørensen, J. Johansen, and P. Fuglsang. Wind turbine airfoil catalogue. *Ris-R-1280(EN)*, 2001.

[4] A. Bjorck. Coordinates and calculations for the ffa-w1-xxx, ffa-w2-xxx and ffa-w3-xxx series of airfoils for horizontal axis wind turbines. (FFA TN 1990-15), 1990.

[5] A. Krzysiak and N. Narkiewicz. Aerodynamic loads on airfoil with trailing-edge flap pitching with different frequencies. *Journal of aircraft*, 43:407–418, 2006.

[6] R. E. Sheldahl and P. C. Klimas. Aerodynamic characteristics of seven symmetrical airfoil sections through 180 degree angle of attack for use in aerodynamic analysis of vertical axis wind turbines. 1981.

[7] R. A. McD Galbraith, M. W. Gracey, and E. Leich. Summary of pressure data for thirteen aerofoils on the university of glasgow's aerofoil database. *G.U Aero report 9221, University of Glasgow*, 1992.

[8] R. M. Pinkerton. The variation with reynolds number of pressure distribution over an airfoil section. *NACA Report No.613*.

[9] B. M. Maskew and F. A. Dvorak. The prediction of $c_{L_{MAX}}$ using a separated flow model. *Journal of the American Helicopter Society*, 23.

[10] N.E. Joukowsky. Vortex theory of skrew propeller, i. *Trudy Otdeleniya Fizicheskikh Nauk Obshchestva Lubitelei Estestvoznaniya 16(1), 1-31. French translation in*.

[11] A. Betz. *Schraubenpropeller mit Geringstem Energieverlust*. PhD thesis, Gttingen Nachrichten, Gttingen, 1919.

[12] H. Glauert. *Airplane propellers in Division L in Aerodynamic Theory, vol. IV, (ed. Durand W.F.). P. 169-360*. Springer: Berlin, 1935.

[13] V. L Okulov and J. N. Srensen. Stability of helical tip vortices in a rotor far wake. *Journal of Fluid Mechanics, vol. 576, pp. 1-25.*, 2007.

[14] J. N. Srensen. Instability of helical tip vortices in rotor wakes. *Journal of Fluid Mechanics, vol. 682, pp. 1-4*, 2011.

[15] V. L. Okulov and J. N. Srensen. Refined betz limit for rotors with a finite number of blades. *Wind Energy, 11(4), 415-426*, 2008.

[16] V. L. Okulov and J. N. Srensen. An ideal wind turbine with a finite number of blades. *Doklady Physics 53(6), 337-342*, 2008.

[17] V. L. Okulov and J. N. Srensen. Maximum efficiency of wind turbine rotors using joukowsky and betz approaches. *J. Fluid Mech. 649, 497-508*, 2010.

[18] V. L. Okulov. On the stability of multiple helical vortices. *J. Fluid Mech. 521, 319-342*, 2004.

[19] S. Goldstein. On the vortex theory of screw propellers. *Proc R Soc London A, 123, 440-465.*, 1929.

[20] R. Shankar. Design and optimization of planar and nonplanar wind turbine blades using vortex methods. *M.Sc. thesis, MEK-FM-EP-2010-08, DTU Mechanical Engineering*, 2010.

8 Flatback Airfoil Analysis

Author: Niels N. Sørensen

8.1 Introduction

The present study deals with so-called flatback airfoils, which are airfoils especially designed to have a relatively thick trailing edge. In contrast to truncated airfoils as discussed by Hoerner [1], as e.g. the FX77-W-343 , flatback airfoils can be designed with a desired camber distribution. Earlier studies [2],[3], have shown that flatback airfoils can obtain high lift at the cost of the glide ratio. The increase in drag will mainly be caused by base drag on the vertical trailing edge of the airfoil. In connection with the design of wind turbine rotors, flatback airfoils could be attractive from a structural point of view, while for inboard stations where the drag is mainly pointing in the thrust direction, the additional drag may be less important than the increase in lift.

The present study includes the following ingredients: a 2D steady and unsteady evaluation of the predictive capability of the RANS version of the EllipSys2D solver: a DDES study of a 3D blade section to investigate some of the features observed in the 2D study: and finally, a small example of a parametric study of possible ways to design a flatback airfoil.

8.2 Numerical study

8.2.1 Flow Solver

The in-house flow solver EllipSys in its 2D and 3D versions are used in all computations presented in this paper. The code is developed in co-operation between the Department of Mechanical Engineering at the Technical University of Denmark and The Department of Wind Energy at Risø National Laboratory, Risø-DTU, see [4, 5] and [6].

The EllipSys code is second order accurate in time, using a second order backward differencing time discretization and sub-iteration within each time step. In the present computation, the diffusive terms are discretized with a second order central differencing scheme. For the RANS simulations the convective fluxes are computed using the third order accurate QUICK scheme of Leonard [7]. For the DDES runs, the QUICK scheme is used for the RANS regions while a fourth order central scheme is used for the regions where the DDES model has switched to Large Eddy Simulation (LES) technique.

In the present work the turbulence in the boundary layer is modeled by the k-ω Shear Stress Transport (SST) eddy viscosity model [8] using it both in its standard RANS form but also as a DES model as proposed by Strelets [9] with the Delayed Detached Eddy Simulation (DDES) technique of Menter and Kuntz [10]. The effects of laminar/turbulent transition in the boundary layer on the blade is modeled with the $\gamma - \widetilde{\mathrm{Re}}_\theta$ correlation based transition model of Menter [11], for the present implementation see [12].

For the 2D cases, both steady state simulations and transient simulations are performed using the SIMPLE algorithm. For the unsteady simulations, a dimensionless time step of 1×10^{-2} is used along with four sub-iterations within each timestep. The dimensionless timestep is defined by Equation 8.1, where T is time s, U_∞ is the free stream velocity m/s, and C is the airfoil chord m. For the 3D DDES cases, transient simulations are performed with a time step of 1×10^{-2}, here using 6 sub-iteration.

$$T^* = \frac{TU_\infty}{C} \, . \tag{8.1}$$

The following inflow parameters are used. The inflow velocity is specified as 1 $\mathrm{m\,s^{-1}}$, a density of 1 $\mathrm{kg\,m^{-3}}$ and the viscosity was adjusted to obtain the correct Reynolds number based on an airfoil chord of 1 m. With a typical domain size of ~ 40 Chords, setting the specific dissipation rate $\omega = 1 \times 10^4$ $\mathrm{s^{-1}}$ a natural transition scenario with $Tu = 0.07\%$ requires a inlet value of the turbulent kinetic energy $k = 1.14 \times 10^{-2}$ $\mathrm{m^2\,s^{-1}}$. For the 3D computations including the tunnel walls, preventing the natural decay of turbulence taking place in the 2D simulations, $\omega = 1 \times 10^6$ $\mathrm{s^{-1}}$ and $k = 1.0 \times 10^{-2}$ $\mathrm{m^2\,s^{-1}}$ are used.

8.3 Grid generation

All meshes needed for the computations in the present work are generated with the 2D enhanced hyperbolic grid generation program HypGrid2D [13] as a 2D slice. The 3D grid is then generated by sweeping the grid in the span-wise direction, see Figure 8.1.

For the 2D airfoil computations, an O-mesh configuration with 320 cells around the chordwise direction, and 128 cells in the wall normal direction with a first cell height ($\frac{\Delta y}{C}$) of 1×10^{-6} assuring $y^+ < 2$ and the outer domain boundary placed approximately 40 chord lengths away from the surface. The surface of the airfoil is specified as no-slip, while outlet conditions assuming fully developed flow is specified for a region downstream of the airfoil covering form -20 degree below to 45 degrees above horizontal. Along the remaining part of the outer boundary inlet conditions are specified.

For the 3D DDES computations, a slightly more complex configuration is used to improve the resolution in the airfoil wake. Here a inner O-mesh of 320 chordwise and 160 normal cells is embedded in a outer stretched Cartesian grid, see Figure 8.2. Horizontally the mesh extends approximately 9 chords up- and downstream and vertically 4 chords above and below the airfoil. For the stretched Cartesian grid, 128 cells are used in vertical direction, with 32 above and below the O-mesh section. In the horizontal direction, 32 cells are used upstream of the O-mesh section, 96 cells along the O-mesh section and 96 cells downstream of the O-mesh section. In the span-wise direction 128 cells are used along the $1 \times C$ span, with stretching towards one side of the domain to allow resolution of the boundary layer developing on the tunnel wall. The spanwise cell size at the tunnel wall is ($\frac{\Delta y}{C}$) of 1×10^{-5} with expansion away from the wall to give a cell size of ($\frac{\Delta y}{C}$) of 1.26×10^{-2} over most of the spanwise length, see Figure 8.3. The grid has in total 9.4 million cells. The surface of the airfoil is modeled as a no-slip surface. The Cartesian upstream plane is specified as inlet while the Cartesian downstream plane is specified as outlet using an assumption about fully developed flow. At the top and bottom boundaries slip conditions are enforced, while the boundaries in the spanwise direction are specified as slip for the tunnel center plane and no-slip at the tunnel wall where the boundary layer is resolved. For some of the computations, the no-slip condition at the wind tunnel wall was changed to slip-conditions, to investigate the importance of the developing boundary layer on the tunnel wall.

8.4 Verification of the predictive capability of EllipSys2D for flatback airfoils

As the number of available flatback airfoils in the open literature is very limited, the FX77-W-343, FX77-W-400 and FX77-W-500 series of truncated airfoils are included in the evaluation. Even though these are designed in a different way, the problems associated with the numerical computations must be expected to be very similar to the problems of predicting a flatback airfoil. Afterwards, a series of real flatback airfoil, namely the FB-3500-0050, FB-3500-0400 and the FB-3500-1750 airfoils are examined.

The series of computations performed are listed in Table 8.1. As can be seen from the table, both steady state and transient computations are performed, as well as using both fully turbulent and transitional computations. One needs to be aware that the fully turbulent computations are

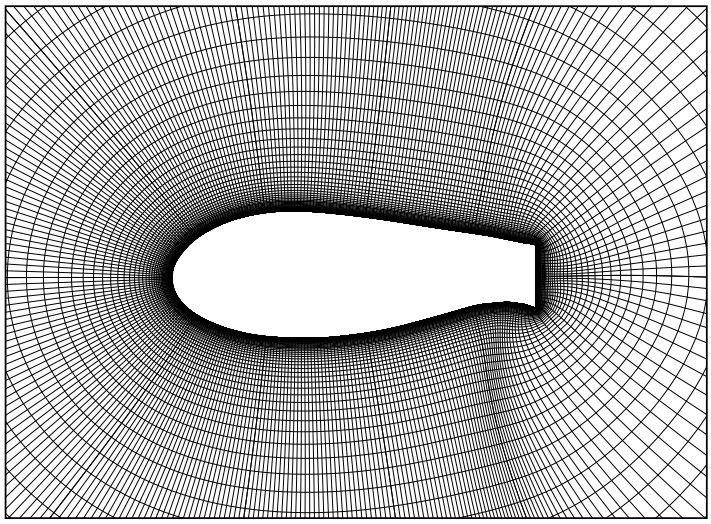

Figure 8.1. Grid detail around the fb-3500-1750 airfoil, showing the inner part of the 2D O-mesh topology.

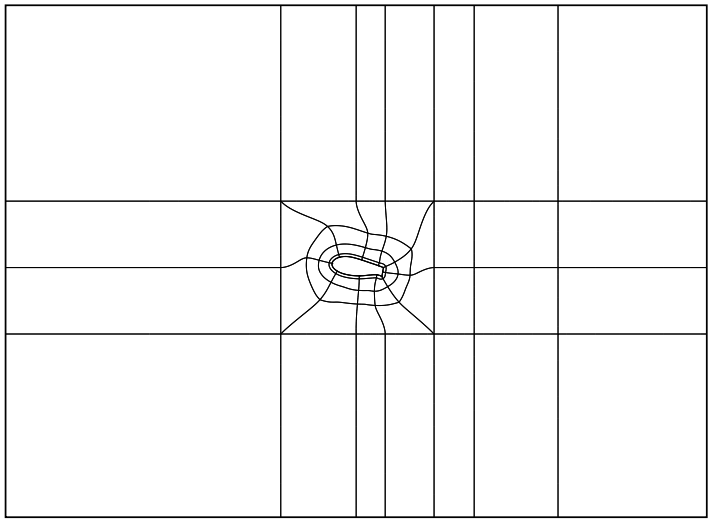

Figure 8.2. Grid topology in the chordwise plane for the 3D DDES computation, showing a sketch of the inner O-mesh embedded in the outer stretched Cartesian grid.

not necessarily equal to tripped experimental conditions, as the fully turbulent computations only allows the fully turbulent boundary layer to develop without modelling the actual physics of the tripping of the boundary layer. The modelling of the tripping could be attempted with the transition model, by specifying a trip point and a production factor in the trip region. This was not attempted here, as this requires parametric calibration to meet the experimental conditions of the physical tripping.

Typically, in all computations we strived to reduce the residuals four orders of magnitude to assure iterative convergence. Using steady state assumptions for thick airfoils, where separation often will take place eg. at the thick trailing edge, iterative convergence may not be obtained. In these cases the solution was continued until a periodic state was reached, and the averaged value was computed. For the transient simulations, the sub-iterations assures that the residuals stay approximately below the four order of magnitude criteria.

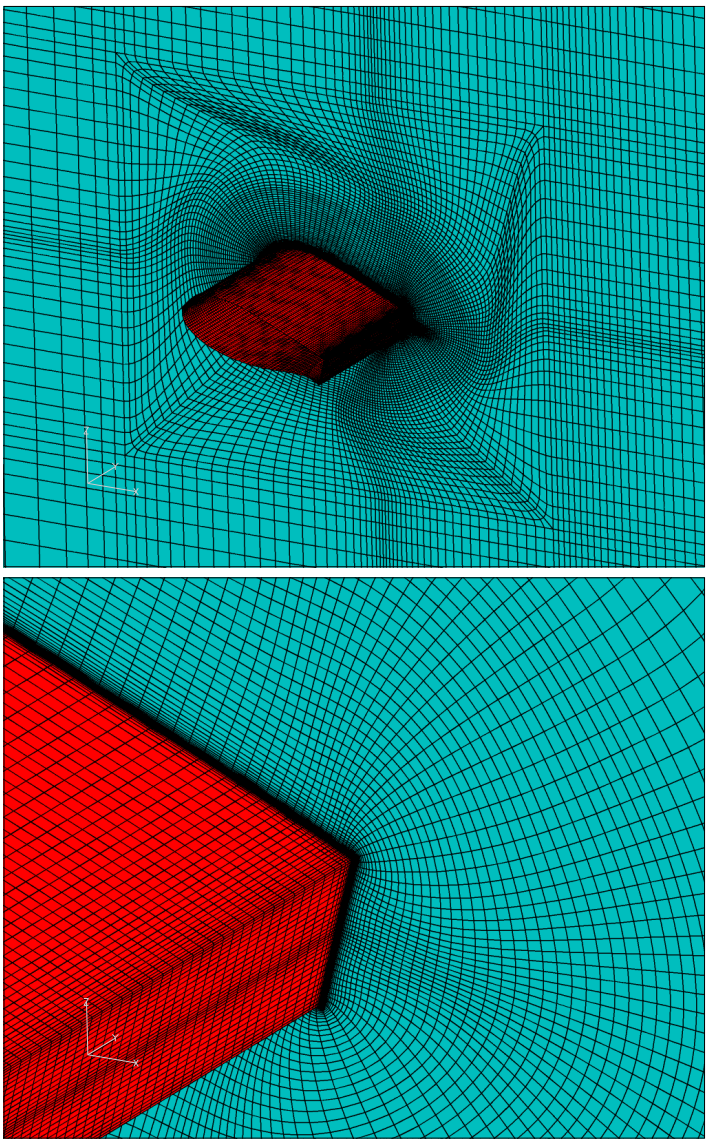

Figure 8.3. 3D grid details, showing in the upper frame a 3D view of the blade section and tunnel wall, and below the resolution normal to the wind tunnel wall.

8.4.1 FX77-w-XXX airfoils

The FX77-W-XXX geometries are constructed by truncating the original 34.3 percent thick FX77-W-343 to obtain a 40 percent thick airfoil, FX77-W-400, and the 50 percent thick airfoil FX77-W-500. As can be seen in Figure 8.4 the truncating process results in airfoils with much lower camber.

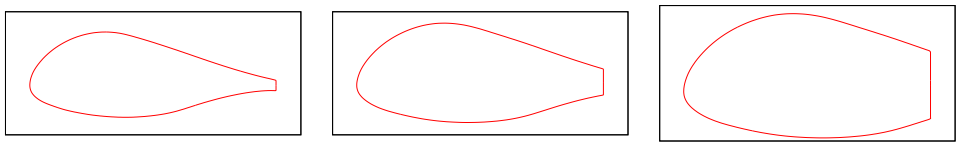

Figure 8.4. The three FX77-W-XXX airfoil geometries, from left to right FX77-W-343, FX77-W-400, FX77-W-500.

Table 8.1. Computational cases

Airfoil	Reynolds Number	Steady	Transient	Turb/Transitional
FX77-W-343	3 mill.	Steady	-	Transitional
FX77-W-343	3 mill.	-	1×10^{-2}	Transitional
FX77-W-400	4 mill.	Steady	-	Transitional
FX77-W-400	4 mill.	-	1×10^{-2}	Transitional
FX77-W-500	2.75 mill.	Steady	-	Transitional
FX77-W-500	2.75 mill.	-	1×10^{-2}	Transitional
FB-3500-0050	666.000	Steady	-	Turbulent
FB-3500-0050	666.000	Steady	-	Transitional
FB-3500-0050	666.000	-	1×10^{-2}	Turbulent
FB-3500-0050	666.000	-	1×10^{-2}	Transitional
FB-3500-0875	666.000	Steady	-	Turbulent
FB-3500-0875	666.000	Steady	-	Transitional
FB-3500-0875	666.000	-	1×10^{-2}	Turbulent
FB-3500-0875	666.000	-	1×10^{-2}	Transitional
FB-3500-1750	666.000	Steady	-	Turbulent
FB-3500-1750	666.000	Steady	-	Transitional
FB-3500-1750	666.000	-	1×10^{-2}	Turbulent
FB-3500-1750	666.000	-	1×10^{-2}	Transitional

The measurements for the FX77-W-XXX airfoils are taken from Althaus [14]. As all measurements are performed without tripping of the boundary layer in The Laminar Wind Tunnel of Stuttgart, a low turbulent scenario resulting in a natural transition scenario is used in the computations. The results are shown in Figure 8.5 to Figure 8.7.

The FX77-W-343 shown in Figure 8.5, is well predicted with respect to lift, drag and pitching moment. For this case, the steady state approximation and the transient computations predict nearly identical results. There is a tendency towards later separation for the transient simulations, but both the lift computed by the steady and transient methodology are embedded in the hysteresis of the measurements.

The FX77-W-400 airfoil is shown in Figure 8.6, is not quite as well predicted as the thinner FX77-W-343 airfoil. For the lift, the steady state simulations outperform the transient computations, by capturing both the linear region plus staying within the stall hysteresis loop of the measurements. In contrast the tendency of high lift predictions by the transient method here leads to over-prediction of Cl-max. For the drag, the results is opposite with superior agreement of the transient predictions, actually capturing the drag level of 0.03.

For the FX77-W-500 airfoil, which is very different from a normal airfoil shape, the steady state simulations give quite good results capturing the linear lift region well, along with the Cl-max, see Figure 8.7. In contrast to the FX77-W-400, where drag was predicted best with the transient method, the steady state simulations capture the drag of the FX77-W-500 quite well.

Concluding from all of the tree airfoils, the less physical 2D steady state simulations in general out-perform the more physical 2D transient simulations, by better capturing the Cl-max. Based on drag the study is less conclusive, but generally both the transient and steady state simulations capture the increasing drag trend when going from the thin 343 to the thick 500 airfoil.

8.4.2 FB-3500-XXXX airfoils

The FB series of airfoils was generated during the project 'Innovative Design Approaches for Large Wind turbine Blades' see [15]. The airfoil section is generated by combining the

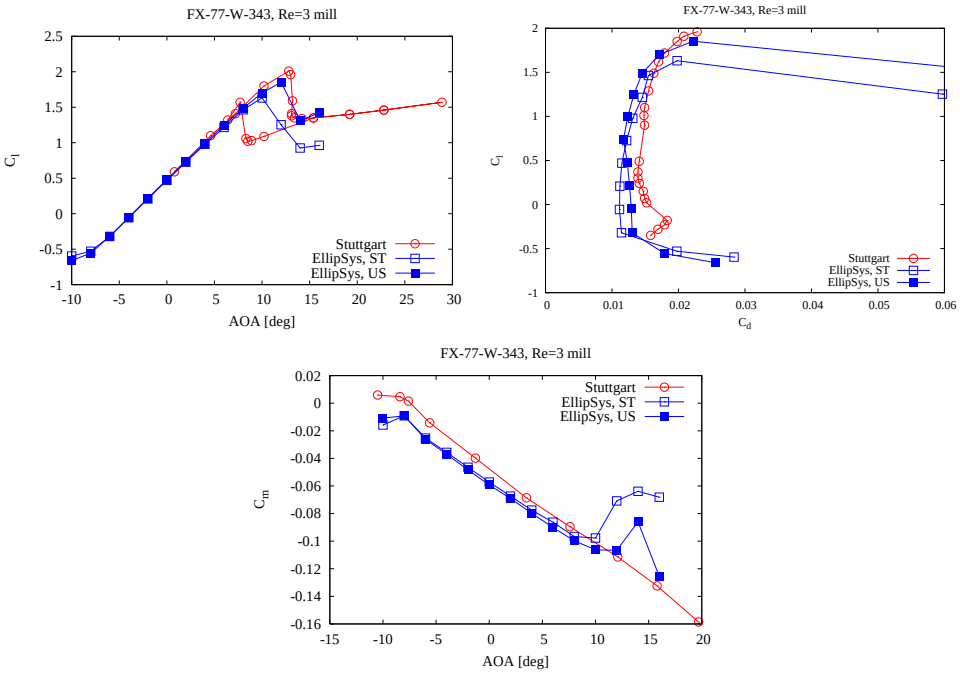

Figure 8.5. Comparison of measured and computed lift, drag and moment for the FX77-W-343 airfoil at a Reynolds number of 3 mill. Both steady and transient computations are shown.

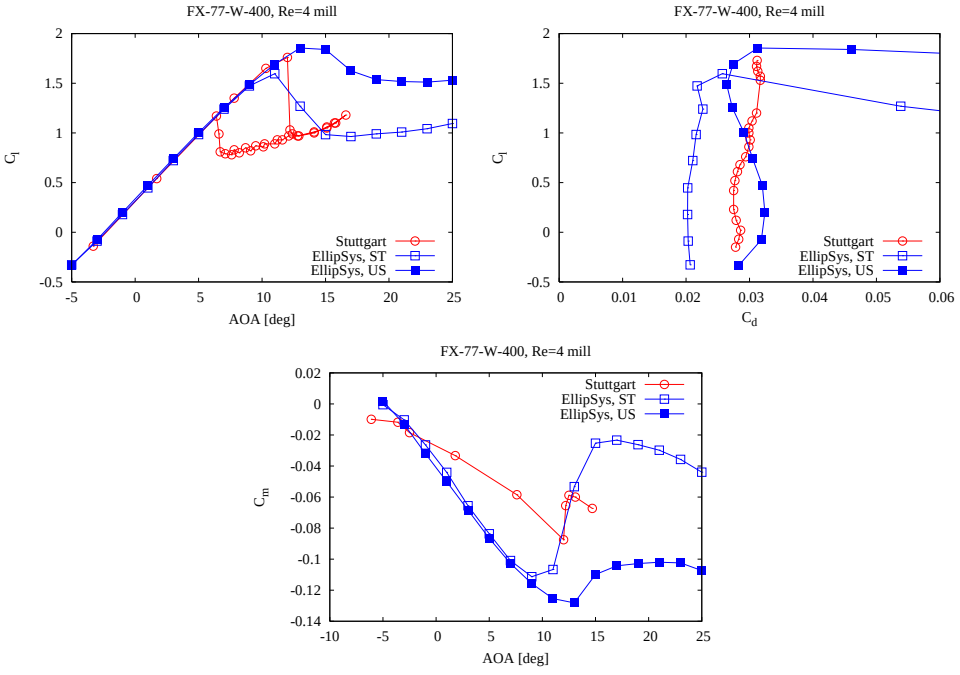

Figure 8.6. Comparison of measured and computed lift, drag and moment for the FX77-W-400 airfoil at a Reynolds number of 4 mill. Both steady and transient computations are shown.

suction side of a thick NREL airfoil section and the pressure side from a LS-1 series airfoil, see Figure 8.8. The FB-3500 airfoil series was chosen due to availability of measurements in the open literature, see [16]. The measured lift, drag and pitching moment published in [16] was not available in digital form and were digitized from the pdf documents. While the coordinates of the FB-4000-XXXX airfoil series are published, this is not the case of the FB-3500-XXXX

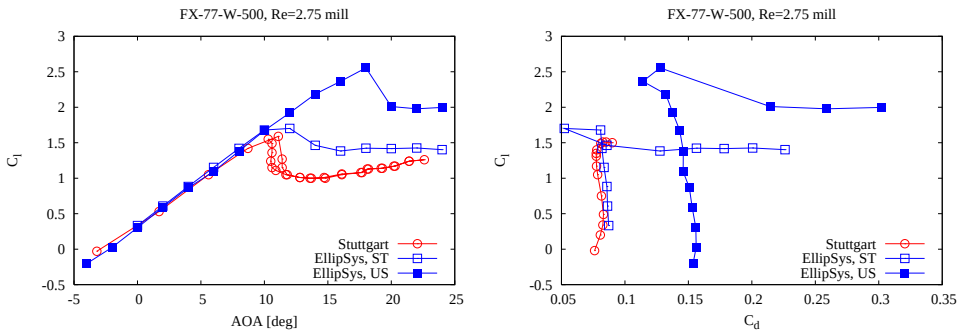

Figure 8.7. Comparison of measured and computed lift, drag and moment for the FX77-W-500 airfoil at a Reynolds number of 2.75 mill. Both steady and transient computations are shown.

airfoil series. To circumvent this problem, the airfoil shape were digitized from [16]. To verify that this procedure was sufficiently accurate the same procedure was first applied to the FB-4000-XXXX series where actual coordinates exist. Comparing computations based on actual coordinates with computations based on digitized coordinates showed negligible differences confirming that the digitized coordinates could be used.

The measurements for the FB-3500-XXXX airfoil sections were performed in the aeronautic wind tunnel at UC Davis, and with both free and tripped boundary layer. In the following, computations using the EllipSys2D will be performed using both steady and transient computations. Both fully turbulent and free transitional computations are compared with the measured values, see Figure 8.9 to Figure 8.14.

For the FB airfoil with the thinnest trailing edge, the FB-3500-0050 and free transition scenario the lift slope is approximately correct while the zero lift angle is offset to higher angles of attack, see Figure 8.9. Looking only at the lift for this case, the transient computations perform better than the steady state computations. For the drag, the agreement is quite good for both approaches, while the conclusion regarding the pitch moment may be less clear.

For the fixed transition case for the FB-3500-0050 airfoil, a linear lift region is nearly not present in the measurements, see Figure 8.10. In contrast to the prior example of free transition case, the steady state computations of the lift is superior to the transient computations for the fixed transition case. For the drag, the minimum drag is captured while the drag at higher AOA is over-predicted.

For the FB-3500-0875 and the FB-3500-1750, the general picture is that for both lift and drag the steady state results are superior to the transient results, see Figures 8.11 to 8.14. Generally, both types of simulations capture the linear region that may exist in the lift data quite well. The Cl-max prediction by the steady state method is superior to the transient simulations for both cases.

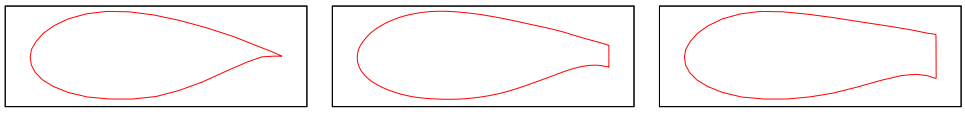

Figure 8.8. The three FB-3500-XXX airfoil geometries, from left to right FB-3500-0050, FB-3500-0875, FB-3500-1750.

Based on all three airfoils the following can be stated: The method is capable of predicting

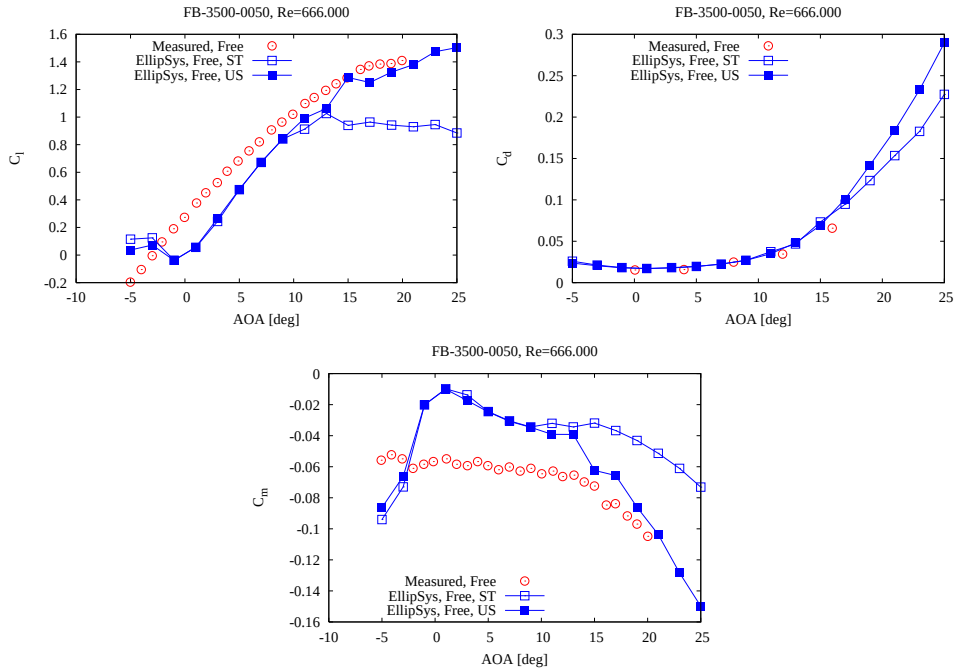

Figure 8.9. Comparison of measured and computed lift, drag and moment for the FB-3500-0050 airfoil at a Reynolds number of 666.000. Both steady and transient computations are shown for free transition conditions.

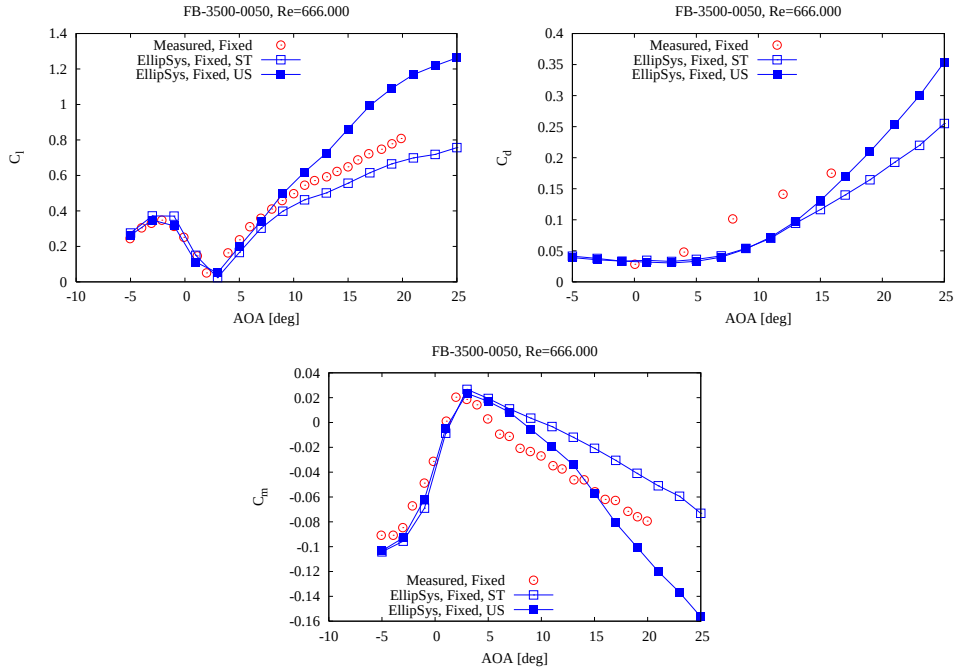

Figure 8.10. Comparison of measured and computed lift, drag and moment for the FB-3500-0050 airfoil at a Reynolds number of 666.000. Both steady and transient computations are shown for fully turbulent conditions.

the general trend caused by the switch from free to fixed transition both with respect to lift and drag. As an overall consideration, the steady state predictions are in better agreement with measurements. Additionally, the CFD predictions will be capable of predicting the relative

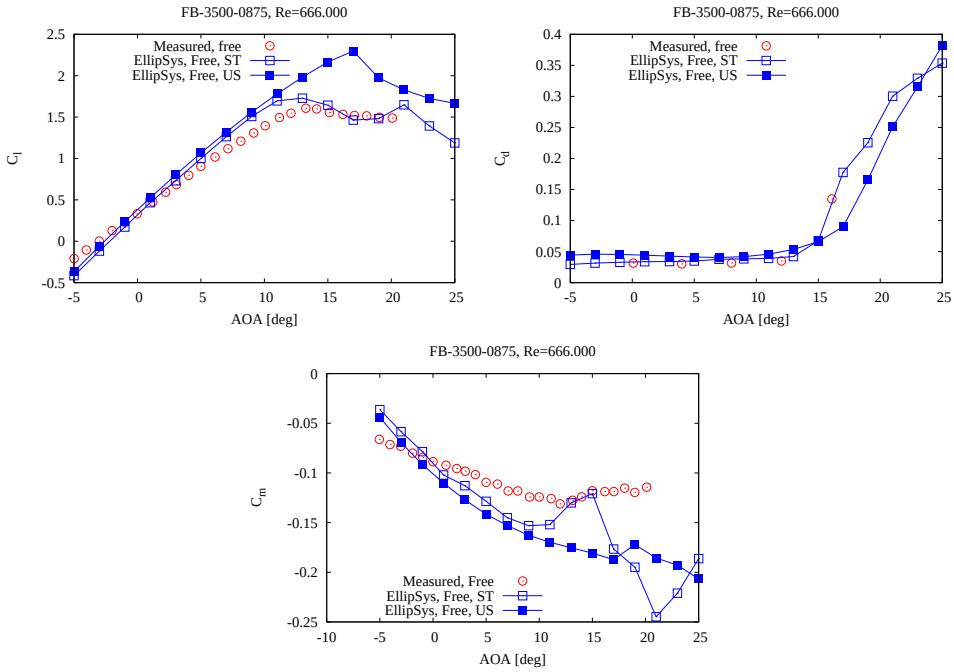

Figure 8.11. Comparison of measured and computed lift, drag and moment for the FB-3500-0875 airfoil at a Reynolds number of 666.000. Both steady and transient computations are shown for free transition conditions.

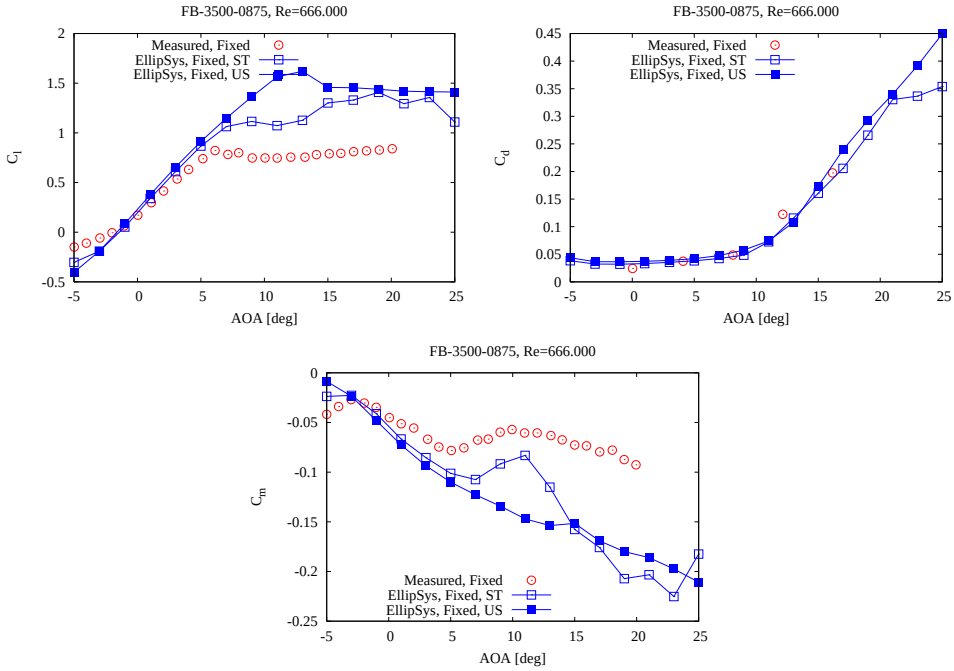

Figure 8.12. Comparison of measured and computed lift, drag and moment for the FB-3500-0875 airfoil at a Reynolds number of 666.000. Both steady and transient computations are shown for fully turbulent conditions.

performance of different flatback airfoils.

The conclusion that for many cases the steady state approximation out-performs the transient methodology is surprising at first. The tendency seems to be more pronounced for the thicker

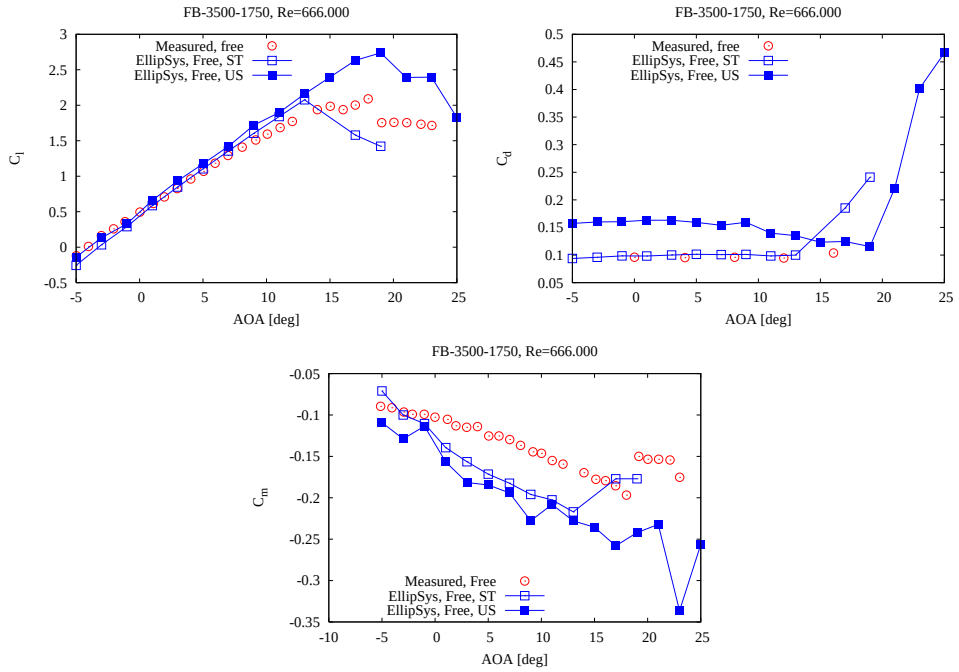

Figure 8.13. Comparison of measured and computed lift, drag and moment for the FB-3500-1750 airfoil at a Reynolds number of 666.000. Both steady and transient computations are shown for free transition conditions.

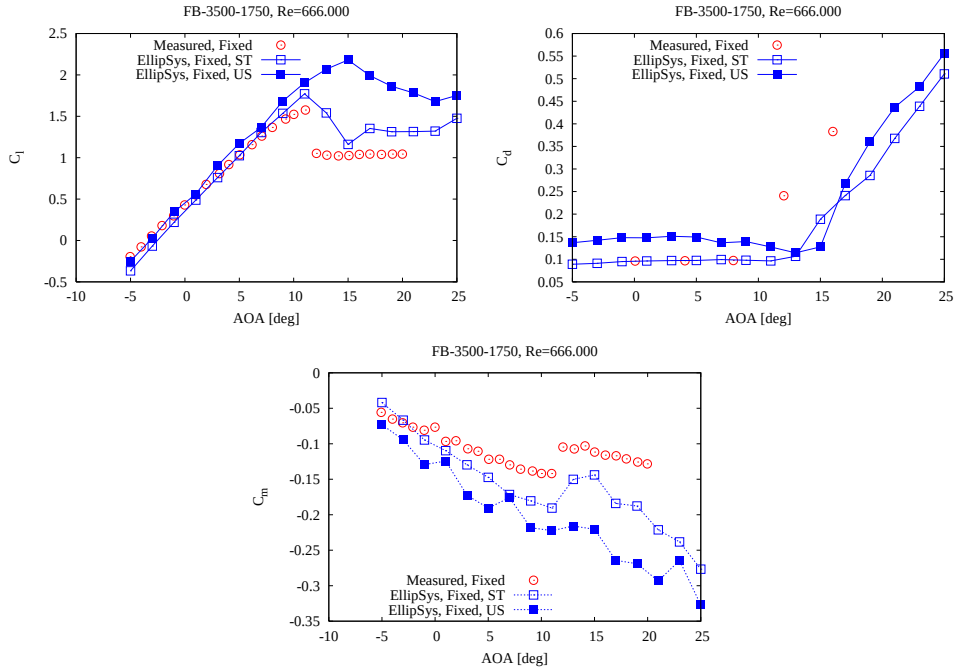

Figure 8.14. Comparison of measured and computed lift, drag and moment for the FB-3500-1750 airfoil at a Reynolds number of 666.000. Both steady and transient computations are shown for fully turbulent conditions.

airfoils where more unsteadiness is present in the form of separation and vortex shedding. To further investigate this issue, some full 3D DES studies were performed to help understand this paradox better.

8.5 3D airfoil computations

Based on the peculiar behavior that the steady state out-performs the transient computations for the 2D flatback airfoils, a 3D investigation of a flatback airfoil is performed.

It is well known, that 2D steady as well as 2D transient computations may produce bad results for flow cases where 3D structures exist. As an example the flow around a 2D cylinder or an airfoil at high AOA. Here we will use the 3D DDES method to try and gain more understanding of the problem observed in the 2D computations.

When an airfoil is mounted in a wind tunnel, as is the case of the UC Davis measurements, interference between the airfoil and the wind tunnel walls must be expected at the junction between those. Close to the wall, where the wind tunnel walls have decelerated the flow, the flow will have a larger tendency to stall and even form a horse shoe vortex upstream of the blade. Different techniques exist to remedy this problem, energizing the flow by blowing or use of vortex generators upstream of the blade, and eg. suction applied to the separated area behind the blade.

As we do not have the details about the actual flow in the UC Davis tunnel, we merely aim at illustrating a plausible explanation for the discrepancy between the computed and measured data. As described in the section about grid generation, the 3D model is set up having a spanwise extent of two chords between the wind tunnel walls. In the actual simulation only half of the domain is simulated using a symmetry plane at the tunnel center section and a no-slip wall at the location of the wind tunnel wall, see Figure 8.2.

The main part of the 3D simulations are computed with a no-slip wind tunnel wall, but a single simulation of a unconstrained situation is performed at 19 degrees angle of attack to illustrate the effect of the wind tunnel wall boundary layer on the blade flow. The flow conditions are similar to the 2D conditions using a Reynolds number of 666.000. To avoid an excessive build-up of the wall boundary layer on the tunnel wall, the inflow turbulence is set very low using $\omega = 1 \times 10^6\ \mathrm{s}^{-1}$ and $k = 1.0 \times 10^{-2}\ \mathrm{m}^2\,\mathrm{s}^{-1}$.

Visualization of the wall constrained situation for the five lowest angles of attack are shown in Figure 8.15, clearly indicating the development of the flow pattern over the airfoil suction side. In the range from 5 to 17 degrees, separation exists only at the blunt trailing edge, and the spanwise lift and drag distributions stay nearly two dimensional, see Figure 8.16. When increasing the angle of attack to 19 degree, the flow is suddenly separated and in contrast to the lower angles of attack a highly 3D flow pattern is observed, see Figure 8.15. For the 19 degree angle of attack case, the lift and drag also reveals a strong variation along the span, see Figure 8.16. The separation is triggered by the presence of the wall, as illustrated by the comparison with a 3D free flow where only a limited area of separated flow exists at the trailing edge of the airfoil, see Figure 8.17. The increased tendency towards separation of the wall bounded wind tunnel flow, is caused by the deceleration of the flow in the boundary layer on the wind tunnel wall.

In the previous 2D simulation, the wind tunnel walls are not represented, and the situation is very similar to the free situation studied in the 19 degrees case. It is well know from previous studies, that 2D simulations may heavily over predict the load in separated flows, e.g. drag prediction of a cylinder or a blade at high angle of attack, see [17]. This is normally explained by lack of 3D break-up of the flow structures. Comparing the lift and drag between the 2D simulations, the 3D wall constrained tunnel simulation and the 3D free configuration a very revealing picture is seen, see Figure 8.18. Below onset of stall, all simulations predicts the same lift irrespectively of them being 2D, 3D, steady or unsteady. At high angle of attack, the 3D unsteady simulations agree well with the 2D unsteady simulations as long as the separation is limited. When the flow starts to be massively separated, the 3D simulations whether of wall bounded or free, instead approach the 2D steady results. The effect of the wind tunnel wall boundary layer is clearly seen in the earlier separation of the wall bounded flow.

There is no good explanation why the 2D steady simulations should perform better than the 2D unsteady simulations, but similar results were seen in [17], where the 2D steady state prediction of a flat plat at 90 degrees also was closer to the full 3D unsteady simulations and measurements. One possible explanation why this happens could be the unphysical use of different time steps in different regions of the flow domain, which may help to break up large coherent structures sometime seen in 2D time true simulations, and produce results closer to 3D reality and the break up seen also in the 3D separated DDES computations.

Additionally, the difference between the two 3D simulations tunnel and free, highlights a problem that may also exist in measurements. When performing tunnel measurements, especially for thick airfoils or at high angle of attack the onset of stall may be heavily influenced by the wall boundary layers on the wind tunnel walls.

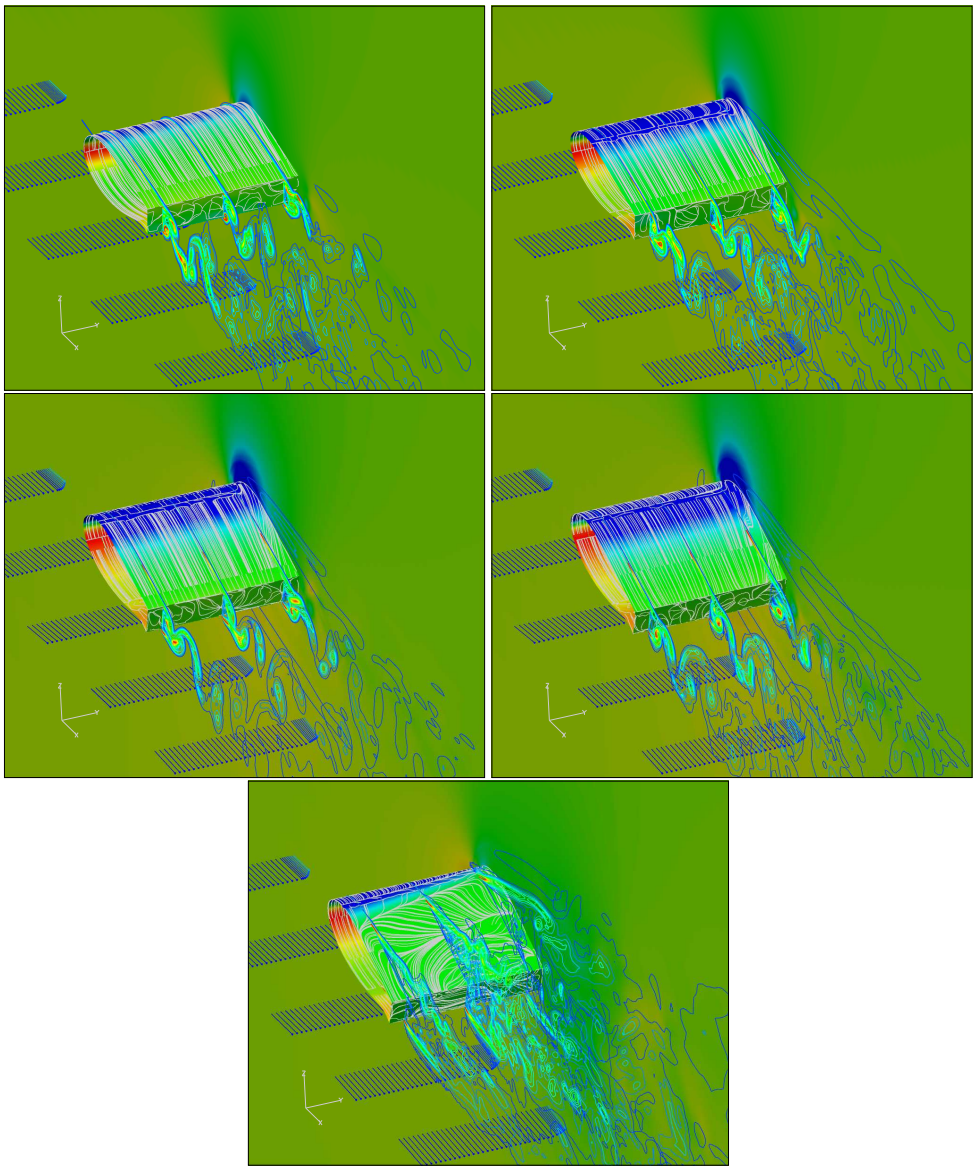

Figure 8.15. Flow field around the 3D FB-3500-1750 airfoil in the wind tunnel, at a Reynolds number of 666.000. The airfoil is attached to the tunnel wall on the left side with a symmetry condition at the right hand side of the span extent. The figure show the following angles of attack from the top left corner, (5, 10, 15, 17,19) degrees.

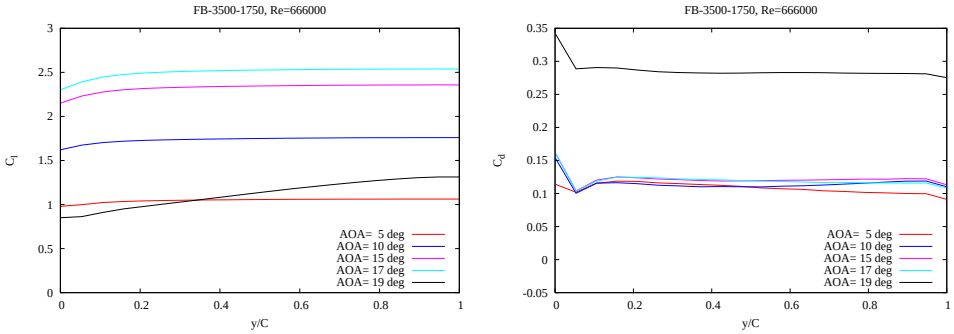

Figure 8.16. Spanwise variation of the lift and drag along the span from the 3D tunnel computation of the FB-3500-1750 airfoil.

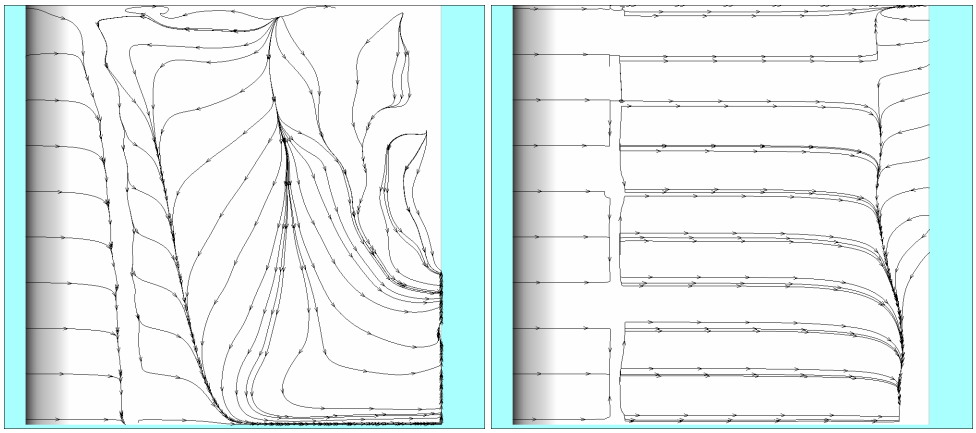

Figure 8.17. Comparison of the computed skin friction lines at the suction side of the wind tunnel configuration right and the free configuration left, at 19 degrees angle of attack and a Reynolds number of 666.000. The flow direction is right to left, and the airfoil section is seen in a top down view. The spanwise variation introduced by the wind tunnel wall clearly changes the flow situation compared to the free configuration.

8.6 Parametric Study, 2D

The examination of the applicability of EllipSys2D revealed that, for the present airfoils in 2D there is no advantages of applying unsteady simulations compared to a steady approach.

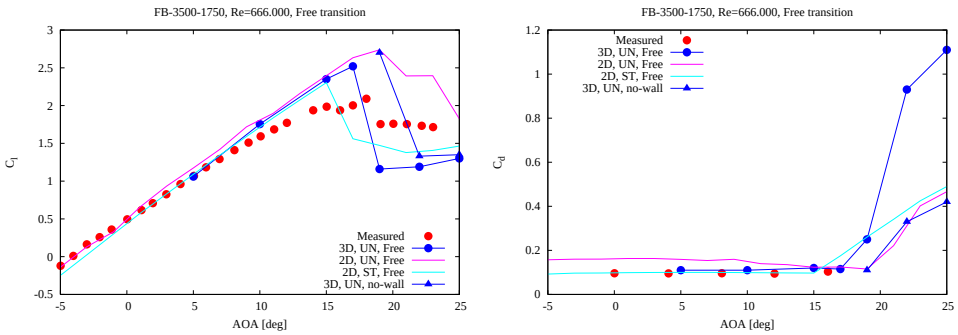

Figure 8.18. Comparison of the computed lift between the measurements, the steady and unsteady 2D simulations, the 3D tunnel simulations of the FB-3500-1750 airfoil. Additionally a 3D simulation at 19 degrees without tunnel wall is shown for comparison.

The preliminary simulations showed that both for the truncated as well as the flatback airfoils, the EllipSys code qualitatively is able to predict the change in lift and drag. Based on this we conclude that the code can be used for parametric investigations of the aerodynamic behavior of flatback airfoils.

As an example of a parametric study, the EllipSys2D code is used to study the effect of opening the trailing edge towards the pressure and suction sides of the airfoil, respectively. In the present investigation, the trailing edge is opened 15 percent of the airfoil chord. The geometrical changes made by opening the airfoil in the four different ways, is shown in Figure 8.19.

The original airfoil is a DU-97-W-300 airfoil of 30 percent thickness and we investigate a Reynolds number of 3.2 million using natural transition in a low turbulent environment.

The effect of the parametric variation of the trailing edge opening can be seen in Figure 8.20. Except for the case where the opening is done only towards the suction side (Suction-15, Pressure-00), all flatbacks exhibit improved max lift, see Figure 8.20. For all the parametric variations an increased minimum drag level is observed, which should be expected. Looking at the $C_l - C_d$ plot in Figure 8.20, the (Suction-00, Pressure-15) is clearly the most attractive with respect to the increase in obtainable lift.

Based on this simple study, we must conclude that changing the present airfoil into a flatback airfoil by simply opening the trailing edge, opening towards the pressure side should be preferred.

8.7 Conclusion

The EllipSys code is validated for airfoils with thick trailing edges as seen for truncated and flatback airfoils. The agreement with measurements is not perfect, neither using 2D steady or 2D unsteady simulations, but the solver is capable of predicting the correct qualitative behavior. There is a tendency that the 2D steady state simulations out-perform the 2D unsteady simulations for this type of airfoil, where a large region of separated flow may exist.

To further investigate the 2D steady/unsteady issue, a series of 3D DDES simulations of the FB3500-1750 airfoil in a wind tunnel configuration revealed that to predict the correct stalling behavior the inclusion of the tunnel walls may be important as these may also in the experiment play an important role in the actual aerodynamic behavior.

Finally, the 2D EllipSys code was applied to a parametric study of the most efficient way of opening an airfoil to obtain a flatback. This study clearly indicates that the present investigated airfoil should be opened toward the pressure side to obtain the highest Cl_{max}.

8.8 Acknowledgements

Computations were made possible by the use of the PC-cluster provided by DCSC and the Risø-DTU central computing facility.

References

[1] F.S. Hoerner and H.V. Borst. *Fluid-Dynamic Lift.* Mrs. Liselotte A. Hoerner, Brick Town, 1985.

[2] K.J. Standish and van. Aerodynamic analysis of blunt trailing edge airfoils. *Journal of Solar Energy Engineering*, 125:479–487, November 2003.

[3] T Winnemller and van. Design and numerical optimization of thick airfoils including blunt trailing edges. *JOURNAL OF AIRCRAFT*, 44(1):232–240, 2007.

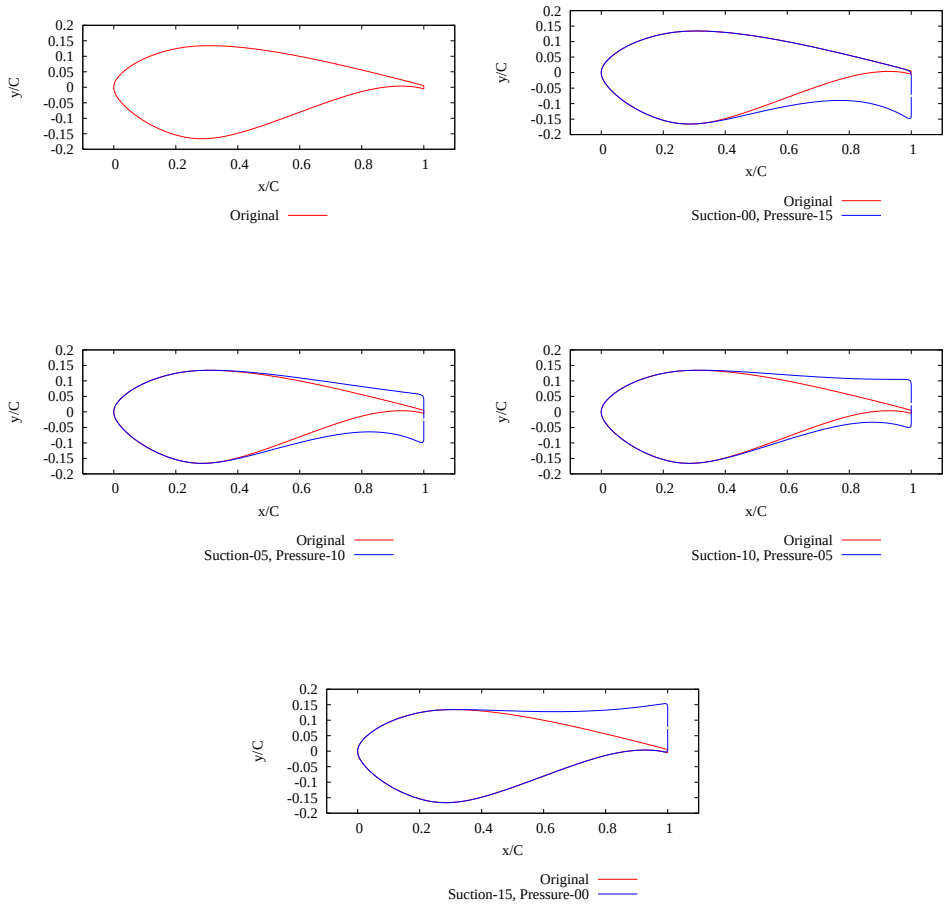

Figure 8.19. The parametric variation of the DU-97-W-300 airfoil shape. The top left plot show the original shape, while the remaining plots show parametric variation of the trailing edge opening corresponding to 15% chord

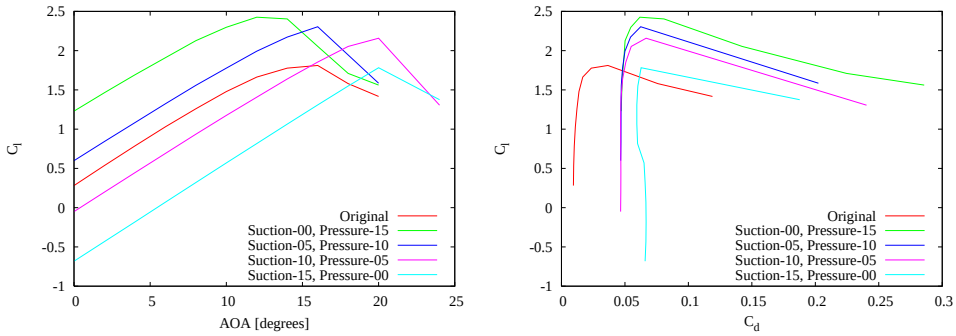

Figure 8.20. The lift and glide ratio for the DU-97-W-300 airfoil exposed to different ways of opening the trailing edge, at a Reynolds number of 3.2 million for natural transition.

[4] J. A. Michelsen. Basis3D - a Platform for Development of Multiblock PDE Solvers. Technical Report AFM 92-05, Technical University of Denmark, 1992.

[5] J. A. Michelsen. Block structured Multigrid solution of 2D and 3D elliptic PDE's. Technical Report AFM 94-06, Technical University of Denmark, 1994.

[6] N. N. Sørensen. General Purpose Flow Solver Applied to Flow over Hills. Risø-R- 827-(EN), Risø National Laboratory, Roskilde, Denmark, June 1995.

[7] B. P. Leonard. A stable and accurate convective modelling procedure based on quadratic upstream interpolation. *Comput. Meths. Appl. Mech. Eng.*, 19:59–98, 1979.

[8] F. R. Menter. Zonal Two Equation k-ω Turbulence Models for Aerodynamic Flows. AIAA-paper-932906, 1993.

[9] M. Strelets. Detached Eddy Simulation of Massively Separated Flows. AIAA Paper 2001-0879, Russian Scientific Center "Applied Chemistry" St. Petersburg, 2001.

[10] F.R. Menter and M. Kuntz. *The Aerodynamics of Heavy Vehicles: Trucks, Buses, and Trains*, volume 19 of *Lecture Notes in Applied and Computational Mechanics*, chapter Adaptation of Eddy-Viscosity Turbulence Models to Unsteady Separated Flow Behind Vehicles, pages 339–352. Springer, 2004.

[11] F. R. Menter, R. B. Langtry, S. R. Likki, Y. B. Suzen, P. G. Huang, and S. Völker. A Correlation-Based Transition Model Using Local Variables, Part I - Model Formulation. In *Proceedings of ASME Turbo Expo 2004, Power for Land, Sea, and Air*, Vienna, Austria, June 14-17 2004. ASME. GT2004-53452.

[12] Niels N. Sørensen. Cfd modelling of laminar-turbulent transition for airfoils and rotors using the $\gamma - \tilde{Re}_\theta$ model. *Wind Energy*, 12(8):715–733, 2009.

[13] N. N. Sørensen. HypGrid2D a 2-D Mesh Generator. Risø-R- 1035-(EN), Risø National Laboratory, Roskilde, Denmark, Feb 1998.

[14] D. Althaus. *Niedriggeschwindigkeitsprofile*. Number ISBN 3-528-03820-9. Friedr. Vieweg & Sohn Verlagsgesellschaft mbH, 1996.

[15] Inc. TPI Composits. Innovative design approaches for large wind turbine blades final report. Unknown SAND 2004-0074, Sandia National Laboratories, Albuquerque, New Mexico 87185 and Livermore, California 94550, May 2008. WindPACT Blade System Design Studies.

[16] P. Baker, C.P. Case van Dam, and B.L. Gilbert. Flatback airfoil wind tunnel experiment. SANDIA REPORT SAND2008-2008, Sandia National Laboratories,, Albuquerque, New Mexico 87185 and Livermore, California 94550, April 2008.

[17] N. N. Sørensen and J. A. Michelsen. Drag Prediction for Blades at High Angle of Attack Using CFD. AIAA Paper 2004-0831, 2004.

9 Design of a Thick, Flatback, Multi-Element High-Lift Airfoil

Author: Frederik Zahle, Mac Gaunaa, Niels N. Sørensen, and Christian Bak

9.1 Introduction

In recent work at Risø DTU [4], it was shown that a higher loading towards the root of the blade can yield a higher energy production of the rotor due to rotational effects normally ignored in Blade Element Momentum (BEM) design codes. Based on numerical simulations on the IEA 5MW Reference Wind Turbine (RWT), Johansen et al. [3] showed that it was possible to gain an increase of 8% in the power coefficient at the expense of a 12% increase in the thrust coefficient from a new design aiming at an optimal loading (a=1/3) along the entire blade. Increased loading can be achieved by simply increasing the chord towards the root, as done in the study by Johansen et al. [3]. However, limitations due to transport requirements of the blades and increases in extreme loads from an increased chord makes this choice undesirable. A more desirable option would be to have airfoils in the root section capable of operating at very high lift coefficients, thus reducing the chord length necessary to achieve the high loading. However, using conventional thick airfoils it is not possible to achieve very high lift coefficients. That is why recent studies have turned to multiple element airfoils [1, 14], which by Gaunaa and Sørensen [1] were shown to be able to achieve lift coefficients above 2.5 using a slat chord length of 30% of the main airfoil chord. In the work by Gaunaa and Sørensen [1], slat configurations were designed using a panel code capable of handling multiple elements. A parameter study was carried out to identify slat configurations that yielded a high performance, and based on this study key factors were identified that influence the performance of a thick multi-element airfoil.

The aim of the present work has been to design a thick flatback airfoil combined with a leading edge slat suitable for wind tunnel testing and benchmarking of numerical codes. In the present work, the tools developed in [1, 14] have been extended to include an efficient optimization method for designing the slat element, as well as a coupling of the optimization to the Navier-Stokes solver EllipSys2D, replacing the previously used panel method. In the following chapter, Chapter 10, the wind tunnel testing and detailed comparison to numerical results are presented.

9.1.1 Multi-Element Airfoil Aerodynamics

To design an efficient multi-element airfoil it is necessary to have a basic understanding of how and why such a configuration can generate much higher lift coefficients compared to conventional single element airfoils. An explanation of the aerodynamic mechanisms responsible for generating high lift on multi-element airfoils can be found by consulting the extensive work by Smith [12]. Although this has also been explained in previous work by Gaunaa and Sørensen [1] it will for completeness be summarised in this work as well. Smith [12] outlines five main mechanisms at play:

1. **Slat effect:** Due to the circulation on the forward element (the slat), the pressure peak on the main element is reduced, which effectively delays the stall on the main element. An unavoidable consequence of this is that the load on the main element is reduced.
2. **Circulation effect:** Positioning the trailing edge of the forward element in the accelerated flow over the main element gives rise to an increase in the mean angle of the flow leaving the trailing edge of the forward element, increasing the circulation over this element.
3. **Dumping effect:** The accelerated flow at the trailing edge of the forward element makes it possible to 'dump' the forward element boundary layer at a much higher velocity than

under free-stream conditions. This reduces the required pressure recovery, thus delaying stall and enabling high lift on the forward element.

4. **Off-the-surface pressure recovery:** Deceleration of the boundary layer from the forward element to free-stream velocity takes place in the wake of the forward element without contact with a wall, which is more efficient.
5. **Fresh boundary layer effect:** Breaking the flow into a number of independent boundary layers on each element helps delay separation since a thin and 'fresh' boundary layer is better capable of withstanding an adverse pressure gradient than a thick one.

The above conclusions can help narrowing down the design space when designing and positioning a slat relative to a main element. The forward element should thus be placed in close vicinity to the point of minimum pressure on the main airfoil to fulfil the first three items in the list. For thin airfoils this point would be quite far forward on the main element at approximately x/c=0.02, which is also reflected in the designs of slats for commercial aircraft. However, on a very thick airfoil this point is considerably further downstream at about x/c=0.1. Lastly, item 5 above suggests that the boundary layers on the elements should not mix, suggesting some minimum distance between the elements exists below which the boundary layer profiles will mix and ruin the 'fresh boundary layer effect'.

The angle of the slat relative to the main airfoil as well as its shape depend on a number of factors that all interact. However, an optimal configuration in terms of maximum lift would be one where both elements stall at approximately the same (highest possible) angle of attack. Due to the upwash upstream of the main element the slat angle needs to be quite high to ensure that the flow does not stall prematurely on the slat. Examples of optimal configurations obtained in the work of Gaunaa and Sørensen [1] are shown in Figure 9.1.

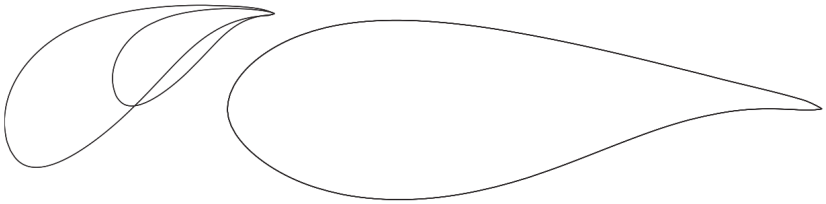

Figure 9.1. Optimal configurations found using the fast design code developed by Gaunaa and Sørensen [1] with c_{slat}/c_{main}=0.3 and c_{slat}/c_{main}=0.5.

9.2 2D Optimization of Slatted airfoils

9.2.1 Optimization Method

The optimization method developed for this work was programmed in Matlab, and uses the built-in optimization routine `fminsearch` which employs a simplex optimization method. This routine, however, is unbounded, and as such a community-developed wrapper routine named `fminsearchbnd` was used in combination with `fminsearch`, which allows for bounds on the optimization problem.

The overall goal of the optimization is to achieve a slat configuration which meets the target lift coefficients at an angle of attack which can be either specified or unspecified, while also providing a high maximum lift beyond the design point to provide enough lift reserve to tackle large changes in angle of attack.

The optimizer attempts to minimize a function which is composed of three factors: a penalty function which forces the optimizer towards achieving the desired lift coefficient, $C_{l,target}$, at

the specified target angle of attack, α_{target}; the function A_1 which evaluates the lift-to-drag ratio at the target angle of attack; and finally the function A_2, which seeks to maximize the lift coefficient at some angle of attack, which the optimizer is free to tune. The two functions A_1 and A_2 are normalized with a predefined reference lift-to-drag ratio and lift coefficient.

$$CostFun = -Penalty\,(A_1 + A_2) \tag{9.1}$$

with the *penalty* function defined as

$$Penalty = exp\left(-\frac{\left(C_l(\alpha_{target}) - C_{l,target}\right)\right)^2}{2\sigma_{penalty}}\right) \tag{9.2}$$

where the penalty variance σ=0.02, and the two functions A_1 and A_2 is defined as

$$A_1 = \frac{C_l(\alpha_{target})}{C_d(\alpha_{target})} \cdot \frac{1}{(C_l/C_d)_{target,ref}} \cdot K_{optim} \tag{9.3}$$

$$A_2 = \frac{C_l(\alpha)}{C_{l,maxref}} \cdot (1 - K_{optim}) \tag{9.4}$$

K_{optim} is a factor in the range [0:1] which biases the cost function towards obtaining the target lift coefficient or lift-to-drag ratio. Although the lift-to-drag ratio is typically not as important towards the root section of a blade as it is further out on the blade, it is needed in this optimization method in order to force the optimization towards slat configurations where the flow is attached.

For each optimization iteration two evaluations are thus needed: one at the target angle of attack, and another at a free angle of attack which seeks to maximize C_l. Besides the angle of attack, the optimization code was allowed to vary the following geometrical parameters of the slat:

- Position of slat trailing edge measured as:
  - Surface distance along main airfoil surface from leading edge,
  - Normal distance from main airfoil surface to slat trailing edge.
- Slat angle relative to main airfoil.
- Slat camber (parabolic curve).

Figure 9.2 shows a schematic drawing of an airfoil fitted with a slat with the optimization parameters indicated.

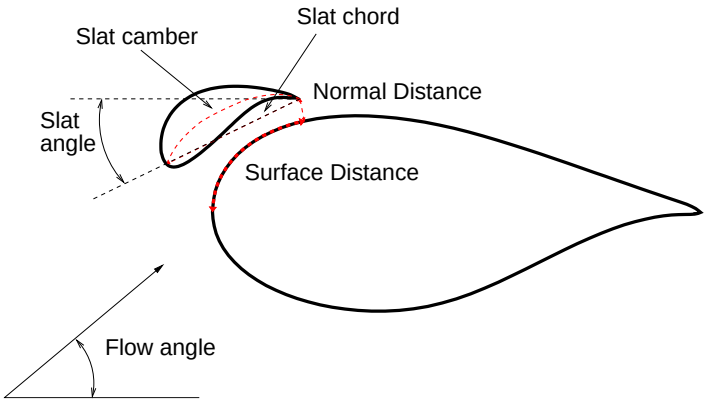

Figure 9.2. Geometrical parameters that the optimization code can adjust to meet the optimization targets.

9.2.2 Navier-Stokes Solver

The in-house flow solver EllipSys2D is used for all CFD computations presented in this report. The code is developed in co-operation between the Department of Mechanical Engineering at the Technical University of Denmark and The Department of Wind Energy at Risø National Laboratory, see [7, 8, 13]. The EllipSys code is a multiblock finite volume discretization of the incompressible Reynolds Averaged Navier-Stokes (RANS) equations in general curvilinear coordinates. The code uses a collocated variable arrangement, with Rhie/Chow interpolation [11] and either the SIMPLE algorithm of Patankar and Spalding [9, 10] or the PISO algorithm of Issa[2] to enforce the pressure/velocity coupling. The convective terms are discretized using a third order QUICK upwind scheme, implemented using the deferred correction approach first suggested by Khosla and Rubin CITE. Central differences are used for the viscous terms. In the present work the turbulence in the boundary layer is modeled by the $k-\omega$ Shear Stress Transport (SST) eddy viscosity model [6]. The laminar to turbulent transition process is modeled by the $\gamma - Re\theta$ correlation based transition model of Menter et al. [5], for the present implementation see [15]. The EllipSys code is parallelized with the Message-Passing Interface (MPI) for executions on distributed memory machines, using a non-overlapping domain decomposition technique.

The grids needed for the CFD computations are slightly more complicated than the ones used for standard single element airfoils. Here, a topology with an inner topology consisting of individual O-meshes around each of the elements were chosen, these being connected by an additional block in the channel between the elements, see Figure 9.3 for an example of this grid layout. The assembled inner grid topology is finally embedded in a O-mesh topology taking the grid to the farfield region. The O- meshes around the airfoil sections each has 320 cells in chordwise direction. The y+ of the normal cell at the walls are below 2, and the distance to the other boundary is approximately 60 chords using in total 96 cells in this direction. The total number of grid cells is $\sim$47000.

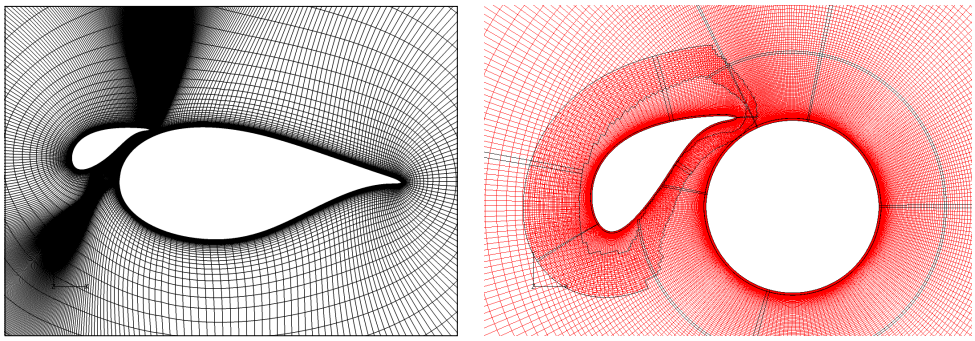

Figure 9.3. Typical meshes generated using the automated meshing scripts, left: standard patched grid, right: overset grid.

EllipSys2D is also capable of handling an overset grid topology [16]. Each group of patched blocks is solved using boundary conditions on the overlapping interfaces based on interpolated values of velocity from neighbouring grids using trilinear interpolation. An explicit correction of the conservation error is implemented, since a divergence free field is required to solve the pressure-correction equation. The correction is placed in internal cells along the overset boundaries and is distributed proportionally to the local mass flux. The solution of the pressure is obtained on the basis of the mass fluxes calculated from the momentum equations. The grid connectivity is handled using a procedure based on the inverse map method which allows very fast location of points. The hole-cutting is fully automated and uses criteria based on local cell volume and distance to the nearest wall to determine the hole topology. For the purposes of automation of the grid generation, this procedure is very simple and robust, since it requires very little user-intervention and rarely fails. Figure 9.3 shows an example of such a mesh.

9.2.3 Optimization Using CFD

The optimization code written in Matlab, described in Section 9.2, has been coupled to a multi-element panel code as well as the CFD code EllipSys2D. In the present work, all optimizations were carried out using the CFD code as flow solver.

The grid generation procedures described above were fully automated requiring only the geometry of the slat as input. The communication between Matlab and EllipSys2D was handled from a series of Bash scripts that read files written by each code. Matlab ran in the background, outputting for each optimization step a file containing the coordinates of the slat as well as the required angle of attack. EllipSys was executed in parallel for maximum speed, and subsequently returned values of C_l and C_d for the given configuration. Figure 9.4 shows a flowchart summarising the optimization process.

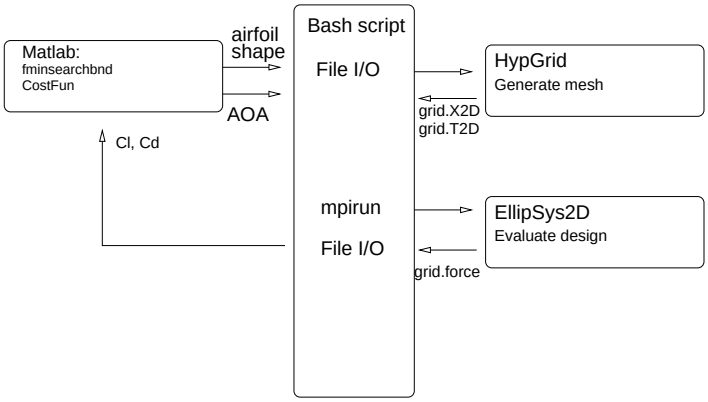

Figure 9.4. Flowchart illustrating the different components in the optimization process.

All optimizations were carried out using steady state computations assuming fully turbulent flow over the surface of the airfoil. The automated procedures were found to be very robust for the setups tested in this work. With a mesh of 19 blocks of 64^2 parallelized across 19 processors one CFD calculation completed in approximately 170 s yielding a total optimization time of 10 hours for 100 iterations (with two CFD calculations in each step) after which a converged result was typically obtained.

9.3 Results

9.3.1 Baseline Flatback airfoil

The present study is based on the FFA-W3-360 airfoil which was modified in the following manner:

- Increased thickness from 36% chord to 40% chord,
- Opening of trailing edge from 3.24% chord to 5.39% chord.

Figure 9.5 shows the original, the 40% thick airfoil and finally, the 40% thick flatback version of the airfoil.

Figure 9.6 shows the computed lift coefficient versus angle of attack as well as the drag coefficient versus lift coefficient for the original 36% airfoil and the two modified airfoils computed assuming fully turbulent flow on the surface of the airfoil. Looking firstly at the FFA-W3-340 airfoil, the increased thickness significantly lowers C_{l-max} from 1.4 to 1.0 accompanied by an increase in drag. Opening the trailing edge from 3.24% chord to 5.39% chord improves C_{l-max}

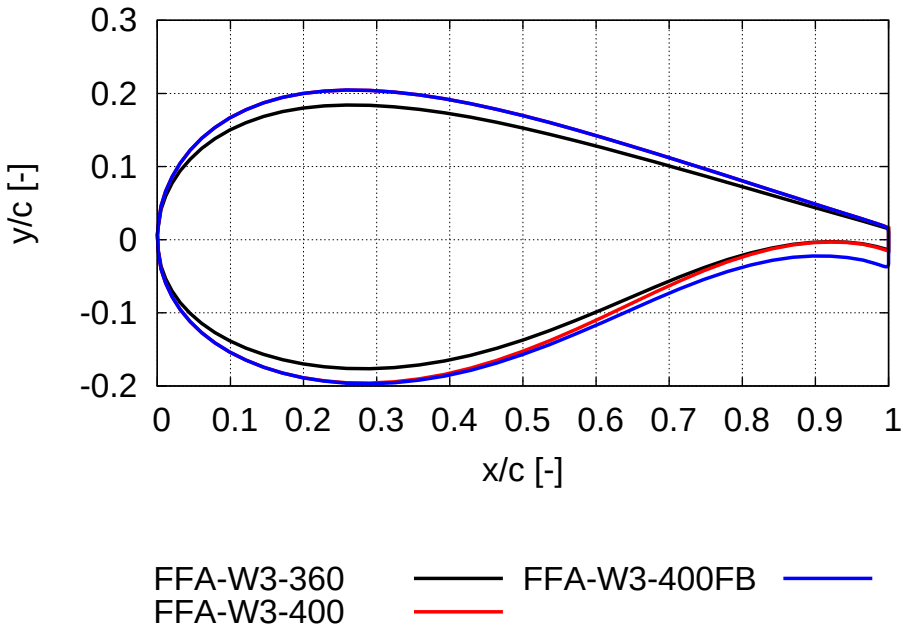

Figure 9.5. FFA-W3 original profile compared to modified profiles.

from 1.0 to 1.24 and due to the increased base drag on the blunt trailing edge also increases drag.

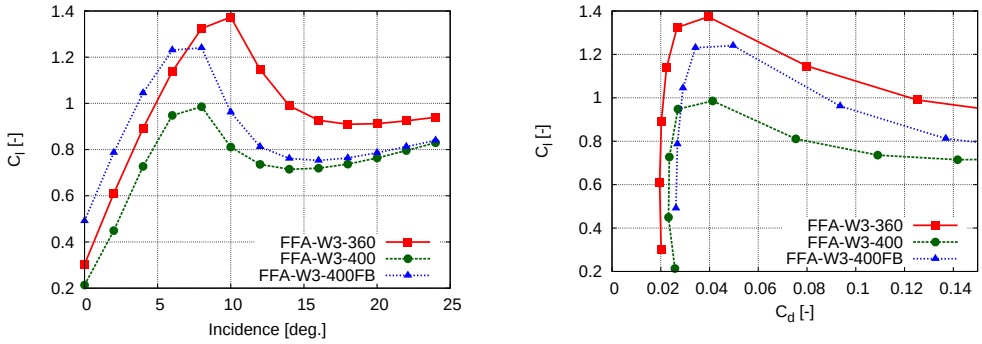

Figure 9.6. Comparison of the original FFA-W3-360 airfoil with the modified 40% flatback airfoil. Computations assumed fully turbulent flow on the surface of the profiles.

9.3.2 Slat Optimization

The parameter k_{optim} in the optimization algorithm (Eqns. 9.3, 9.4) controlled the weighing between emphasis on reaching the target lift or reaching the target lift-do-drag ratio, with k_{optim}=0 taking only the target lift into account and k_{optim}=1 only taking lift-to-drag into account. Four optimizations with different values of k_{optim} were carried out. The resulting configurations are shown in Figure 9.7 with corresponding lift coefficients and lift-to-drag ratios plotted in Figure 9.8. Note that the lift coefficient is normalized relative to the main airfoil chord length in all plots in this work unless stated otherwise.

All four optimizations produce configurations that yielded maximum lift coefficients over 2.5

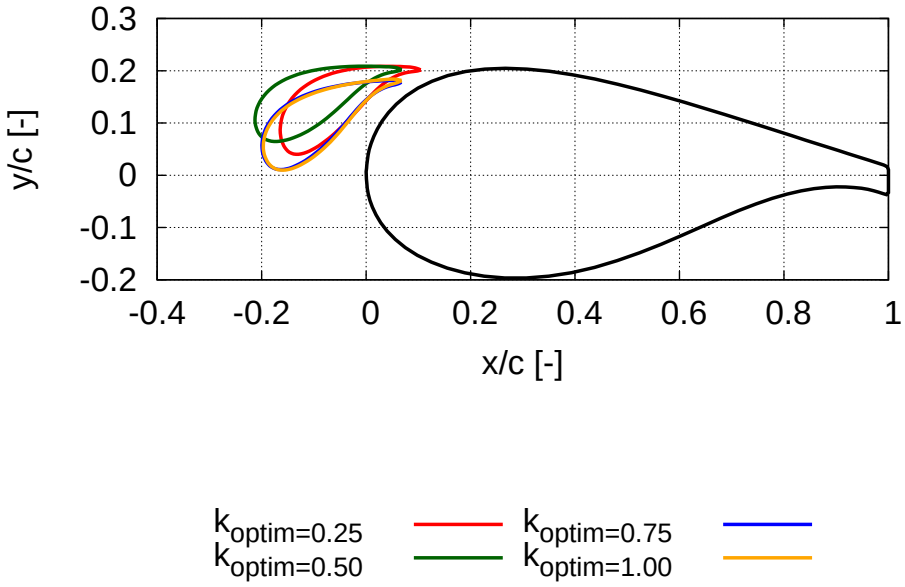

Figure 9.7. Slat configurations for different values of k_{optim}.

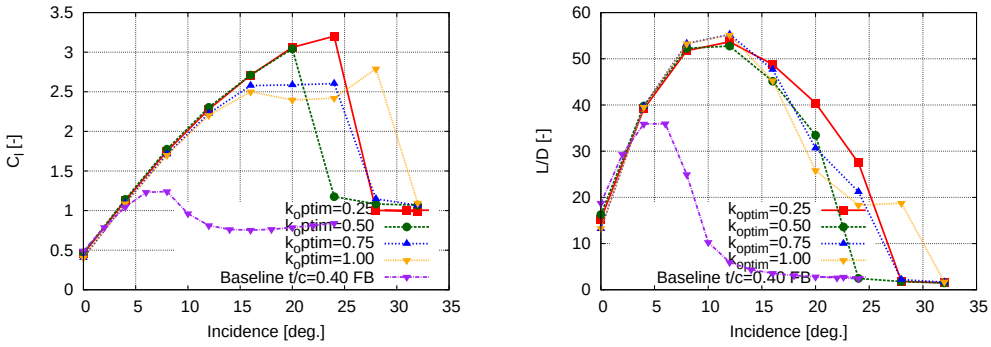

Figure 9.8. Slat performance dependence on k_{optim}. 2D lift coefficielt and lift to drag ratio as function of incidence compared to the baseline airfoil.

which is twice that of the baseline maximum lift coefficient. Likewise, all configurations resulted in a significant increase in the lift-to-drag ratio from 38 to values above 50. Looking at the lift coefficient of the slat and main element individually with the slat lift coefficient normalized with a chord of 0.3, it is seen in Figure 9.9 that the best performing slat has a maximum lift coefficient of 6, and consistently performs better than the other three configurations. The flow appears to stall earlier on the main element for increasing k_{optim}, which is linked to the fact that increasing k_{optim} results in the slat being placed further forward. For k=0.25 the two elements appear to stall at similar angles of attack, but due to lack of resolution of the lift curve the exact stall angles are not available. Of the four optimization results, it was concluded that k_{optim}=0.25 produced the best performing slat configuration with both the highest maximum lift and relatively good lift-to-drag performance across a wide range of angles of attack.

Figure 9.10 shows a comparison of the chosen slat configuration with the baseline flatback 40% airfoil for both fully turbulent and transitional computations. As is evident, the lift of the slatted

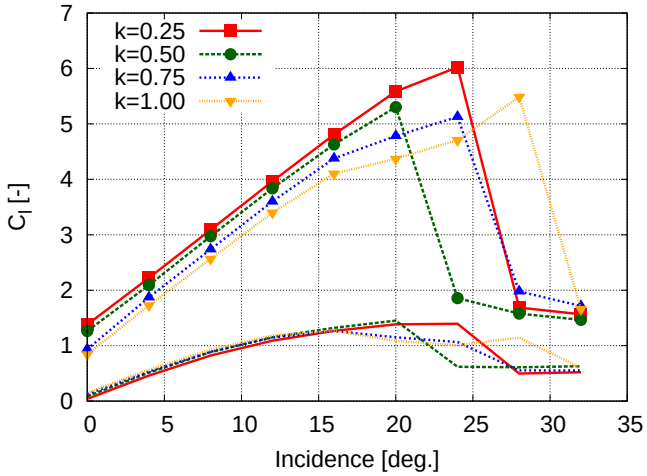

Figure 9.9. Slat performance dependence on k_{optim}. Lines with dots: 2D slat lift coefficielt as function of incidence normalized with the slat chord, lines only: 2D main airfoil lift coefficient normalized with the main airfoil chord.

airfoil is not as sensitive to transition as the baseline airfoil, whereas both airfoils exhibit significant increases in the lift-to-drag ratio in the transitional computations. The small difference between the predicted lift for the fully turbulent and transitional computations indicate that this slatted airfoil could exhibit low sensitivity to surface roughness, which is a very desirable characteristic for wind turbine airfoils. The larger dependence seen in the lift-to-drag ratio is not as important on airfoil sections located near the root, since the drag component on the airfoil does not play a significant role close to the root.

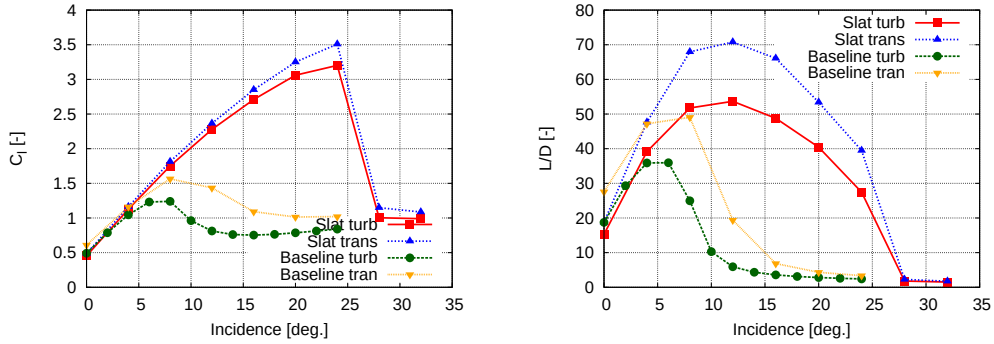

Figure 9.10. 2D lift coefficielt and lift to drag ratio as function of incidence for fully turbulent and transitional boundary layers (TI=0.1%).

With the geometry of the slat fixed, a sensitivity study was carried out where a number of positions of the slat were investigated given by the grid shown in Figure 9.11, allowing only the angle of the slat and the angle of attack to be optimized to reach the same goals as for the original optimization. These degrees of freedom corresponded to those in the wind tunnel tests described in Section 10, where the slat position and angle were adjustable. A total of 42 positions were computed with 60 CFD computations for each slat position optimization.

In order to reduce the computational cost of the study, all simulations were carried out using a coarser grid where every second grid cell was removed from the domain. Comparing a representative solution on a coarse grid with a solution on the finest grid used to optimize the shape of the slat, Figure 9.12, it is seen that there is good agreement on the lift in the linear region, whereas the coarse grid predicts stall at a lower AOA than the fine grid solution. The

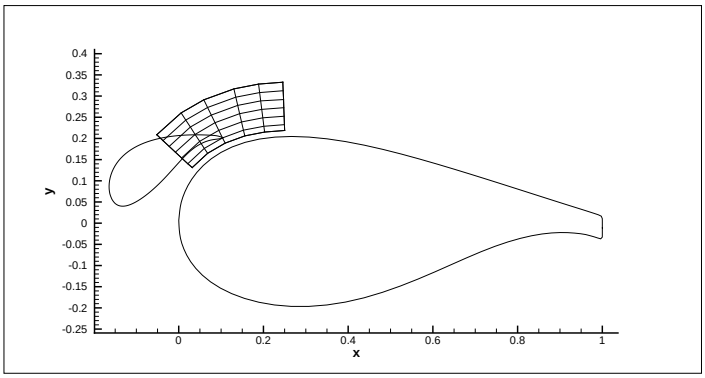

Figure 9.11. Positions of the slat trailing edge which were optimized for slat angle and optimum flow angle in the parameter study.

lift-to-drag ratio shows poorer agreement due to the higher drag on the coarser grid, with a 16% difference between the solutions at 14 deg. AOA. Assuming that the relative differences between the fine and the coarse grids are consistent for the different slat positions, the absolute difference between the two grid resolutions was not essential, since this parameter study was mainly carried out to find the general trends related to the variation of position of the slat.

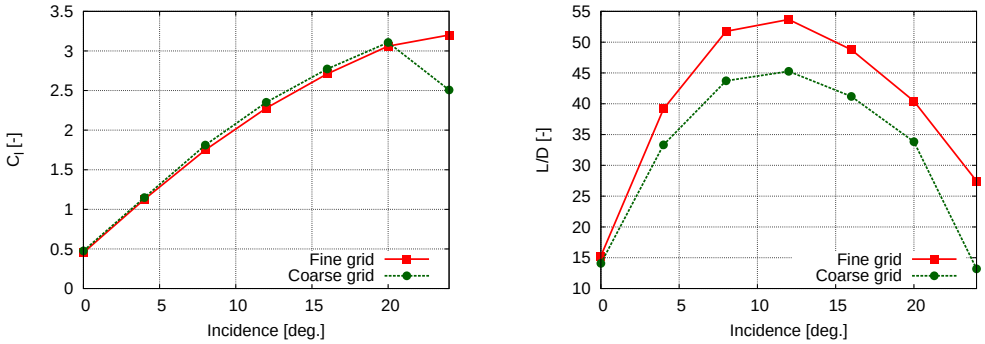

Figure 9.12. 2D lift coefficielt and lift to drag ratio as function of incidence predicted using a coarse grid compared to the fine grid otherwise used in this study.

Figure 9.13 shows contour plots of C_{l-max} and L/D_{max} for the 42 positions. Figure 9.14 show similar plots for an angle of attack 5 deg. lower than the optimized maximum lift angle of attack, which is more representative of the performance the slat would deliver under operational conditions. As is evident, high lift performance can be gained in a rather large but well-defined region around the position found by the optimization. The lift-to-drag ratio appears to have a maximum at the optimized position in Figure 9.13, which, however, for the lower angles of attack in Figure 9.14 is a more flat optimum. This corresponds well to the lift-to-drag ratios plotted in Figure 9.10, where the gradient in L/D generally is lower in ranges of angle of attack 8 deg. to 16 deg. than at angles close to stall.

9.4 Discussion

The results of the parameter study shown in Figures 9.13 and 9.14 revealed that a well-defined region exists on the suction side of the main airfoil where the slat produced good performance. This finding can be linked directly to the velocity magnitude of the flow (or suction) over the isolated main airfoil which reaches a maximum in exactly this region, as shown in Figure 9.15. For reference, the trailing edge positions used in the parameter study is overlaid on the plot.

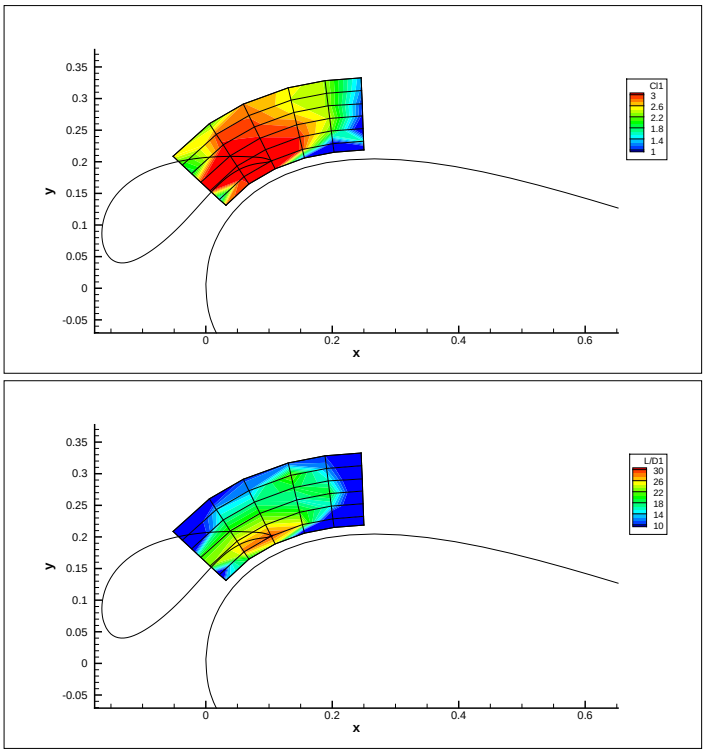

Figure 9.13. Parameter study of slat positioning showing contours of C_{l-max} and L/D at $\alpha_{C_{lmax}}$.

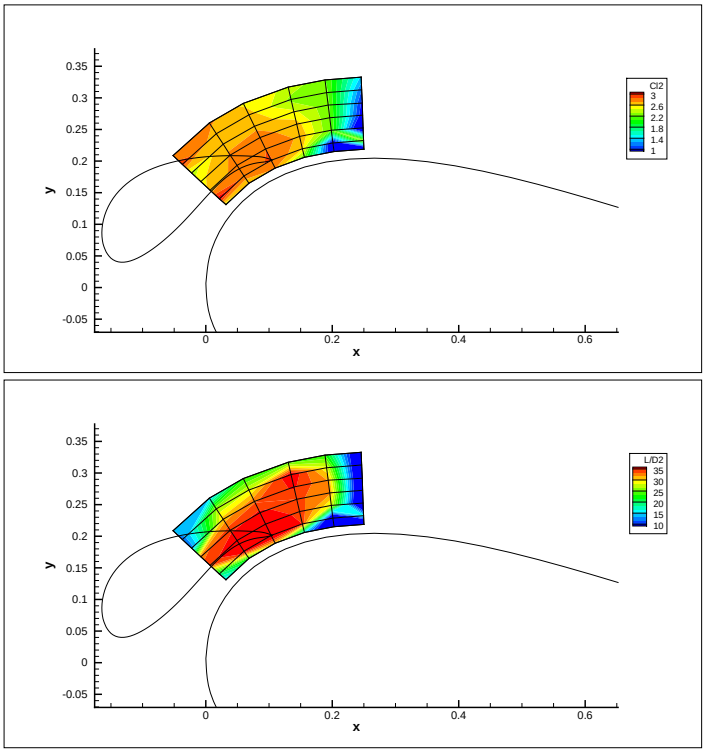

Figure 9.14. Parameter study of slat positioning showing contours of C_l and L/D at α=$\alpha_{C_{lmax}}$-5.

This finding is in excellent agreement with the general aerodynamic characteristics of a multi-element airfoil outlined in Section 9.1.1, which states that a forward element should indeed be placed in a region with highest possible velocity to reduce the requirements of the pressure

recovery, allowing very high suction peaks on the slat. When the slat element is placed too far away from the main airfoil, both the reduction of the suction peak on the main airfoil and the increase in circulation on the slat element diminish, reducing the performance of the slat. Likewise, if the slat is placed too far forward or backward, the same tendency of the slat to perform worse is observed.

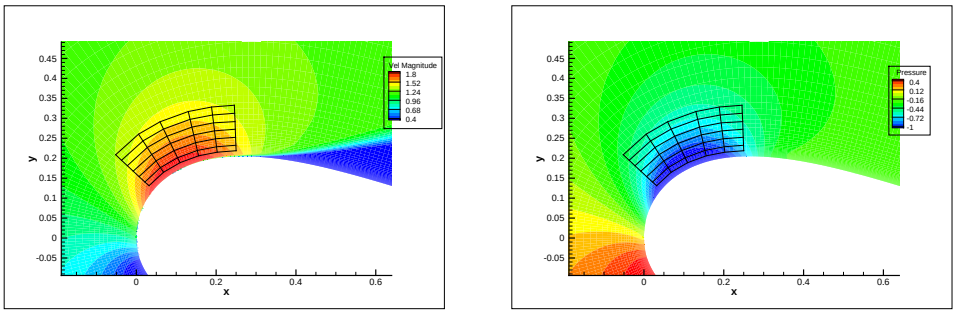

Figure 9.15. Contours of velocity magnitude (left) and pressure coefficient (right) for the baseline FFA-W3-3400FB profile at an incidence of 16 degrees.

Figure 9.16 shows the pressure distributions over the baseline airfoil compared to that of the slatted airfoil. The suction peak on the isolated airfoil moves forward with increasing angle of attack and is at 20 deg. angle of attack slightly forward of the location where the slat trailing edge was positioned in the slatted configurations. At 8 deg. angle of attack the so-called circulation effect is clearly visible with the suction peak of the main airfoil reduced significantly and moved further aft. Notice also that at high angles of attack the pressure at the trailing edge of the slat is equal to the pressure on the main airfoil, illustrating the 'dumping effect' discussed in Section 9.1.1. The flow thus leaves the slat trailing edge at a pressure coefficient equal to -3 at 24 deg. angle of attack, allowing the pressure coefficient on the slat to reach a minimum of -10, which far exceeds that on the isolated main airfoil which reaches a minimum of 3.2 at 8 deg. angle of attack.

9.5 Conclusions

A new tool for optimization of multi-element airfoils has been developed that couples a Matlab-based optimization algorithm with the 2D CFD solver EllipSys2D. The tool includes a fully automated meshing method that uses the in-house mesh generator HypGrid2D. A typical optimization required a total of 100 optimization steps each with 2 CFD computations. The FFA-W3-340 airfoil was modified to have a thickness of 40%c and a so-called 'flatback' trailing edge with a thickness of 5.3%. A leading edge slat with 30% chord length was designed for the modified airfoil, which achieved a maximum lift above 3.0 - a considerable improvement compared to the baseline airfoil which had a maximum lift in the range of 1.3 to 1.6 depending on transition properties. Also the lift-to-drag ratio was vastly improved from between 35 to 50 to between 50 to 70. A parameter study where the position of the slat was systematically changed with optimization of the slat angle showed that the slat performed well within a well-defined region corresponding to the region on the main airfoil where the flow speed was greatest. These findings are in good agreement with results in literature.

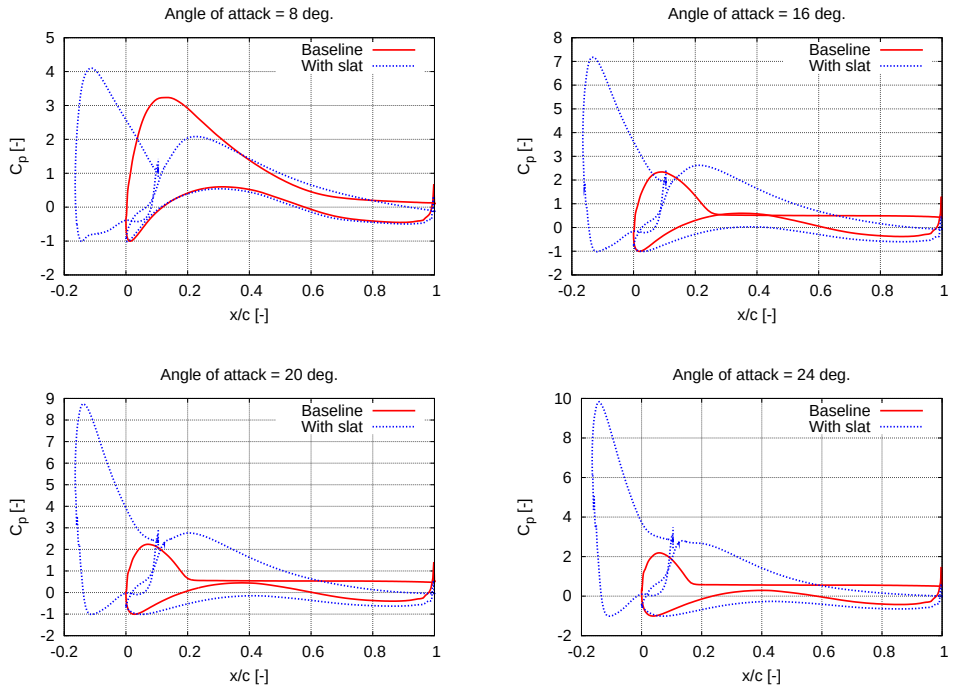

Figure 9.16. Pressure distributions for baseline and slatted airfoil at various angles of attack.

References

[1] M. Gaunaa and N. N. Sørensen. Thick multiple element airfoils for use on the inner part of wind turbine rotors. In *The Science of Making Torque from Wind*, Crete, Greece, June 2010.

[2] R. I. Issa. Solution of the implicitly discretised fluid flow equations by operator-splitting. *journal of Computational Physics*, 62:40–65, 1985.

[3] J. Johansen, H. A. Madsen, M. Gaunaa, and B. Christian. Design of a wind turbine rotor for maximum aerodynamic efficiency. *Wind Energy*, 12:261–273, 2009.

[4] H. A. Madsen. Two modifications of the BEM method based on validation with results of actuator disc results. Technical Report Risø-R-1611(EN), Risø National Laboratory for Sustainable Energy DTU, 2006.

[5] F. Menter, R. Langtry, S. Likki, Y. Suzen, P. Huang, , and S. Volker. A correlation-based transition model using local variables, part I - model formulation. In *Proceedings of ASME Turbo Expo 2004, Power for Land, Sea, and Air*, number ASME. GT2004-53452, Vienna, Austria, June 14-17 2004.

[6] F. R. Menter. Zonal two-equation $k-\omega$ models for aerodynamic flows. *AIAA paper 93-2906*, 1993.

[7] J. A. Michelsen. Basis3D—a platform for development of multiblock PDE solvers. Technical Report AFM 92-05, Technical University of Denmark, 1992.

[8] J. A. Michelsen. Block structured multigrid solution of 2D and 3D elliptic PDEs. Technical Report AFM 94-06, Technical University of Denmark, 1994.

[9] S. V. Patankar. *Numerical Heat Transfer and Fluid Flow*. Hemisphere Publishing Corporation, 1980.

[10] S. V. Patankar and D. B. Spalding. A calculation procedure for heat, mass and momentum transfer in three-dimensional parabolic flows. *International Journal of Heat and Mass Transfer*, 15:1787–1806, 1972.

[11] C. M. Rhie and W. L. Chow. Numerical study of the turbulent flow past an aerofoil with trailing edge separation. *AIAA journal*, 21:1525–1532, 1983.

[12] A. M. O. Smith. High-Lift Aerodynamics. *Journal of Aircraft*, 12(6):501–530, June 1975. ISSN 0021-8669. doi: 10.2514/3.59830.

[13] N. N. Sørensen. General purpose flow solver applied to flow over hills. Technical Report Risø-R-827(EN), Risoe National Laboratory, 1995.

[14] N. N. Sørensen. Prediction of multi-element airfoils with the EllipSys code. In T. Buhl, editor, *Research in Aeroelasticity EFP-2007-II*, number Risø-R-1698(EN), chapter 3. 2007.

[15] N. N. Sørensen. CFD modelling of laminar-turbulent transition for airfoils and rotors using the γ-Re_θ model. *Wind Energy*, DOI 10.1002/we.325, 2009.

[16] F. Zahle. *Wind Turbine Aerodynamics Using an Incompressible Overset Grid Method*. PhD thesis, Imperial College, London, 2006.

10 Wind Tunnel Testing of a Thick, Flatback, Multi-Element High-Lift Airfoil

Author: Frederik Zahle, Mac Gaunaa, Niels N. Sørensen, and Christian Bak

10.1 Introduction

This section describes the wind tunnel tests carried out in the LM Wind Power wind tunnel on the thick, flatback, multi-element high-lift airfoil designed within the present project, as described in Section 9. Additionally, detailed comparisons between experiment and 2D CFD predictions of pressure distributions, lift and drag are discussed. The purpose of the wind tunnel tests was to experimentally validate the designed airfoil as well as providing a dataset suitable for validation of numerical codes.

The most common use of multi-element airfoils is within the aviation industry, where airfoils with as many as five elements are used for high-lift landing configurations for commercial airliners. An extensive list of literature exists on this subject, and for an overview of the accuracy of state-of-the-art CFD tools in predicting flow over multi-element airfoils, the reader is referred to Rumsey and Ying [1]. The main conclusions from the paper are that 2D CFD methods are generally capable of predicting surface pressures, skin friction, lift, and drag quite accurately for angles of attack below stall; Velocity profiles with the exception of the slat wake are predicted well; Effects due to Reynolds number also seem to be predicted well. The main source of uncertainty in comparison to experimental results were concluded to be numerical errors and lack of geometric or modeling fidelity, i.e. lack of grid resolution in critical areas or simplification or inaccuracies of the modelled configuration. Rumsey et al. [2] discuss the possible sources of the discrepancies between 2D and 3D CFD and nominally 2D experiments. They firstly conclude that side-wall venting in the experiment is essential to avoid 3D flow effects due to wall interference. In comparison to experimental results, however, even when including side-walls and venting 3D CFD failed to accurately predict the flow around stall whereas both 2D and 3D CFD were quite accurate for angles of attack up to 16 degrees.

The key difference between multi-element airfoils used in the aviation industry and airfoils relevant to wind turbine applications is that aviation airfoils are generally quite thin, whereas the use of multi-element airfoils on wind turbines is most relevant on the inner part of the blade where the airfoil thickness is typically in excess of 40%. It is well-known that wind tunnel testing on thick, high-lift airfoils presents several challenges compared to tests on thin airfoils. Increased tunnel blockage, 3D tunnel effects due to thicker boundary layers, high lift coefficients at high angles of attack are all effects which adds considerable challenges to a normal wind tunnel setup. The LM wind tunnel is designed for thin airfoils with maximum lift coefficients in the range of 2-2.5 which made the present tests tread on unchartered territories. In this light, it was evident that a quantification of the accuracy of both the numerical tools as well as experimental wind tunnel testing of thick, high-lift, multiple element airfoils was needed.

10.2 Wind Tunnel Setup

The lift is measured using either the surface pressure taps on the airfoil, which is a sectional measurement, the load cell, which measures the total lift force on the entire airfoil, and finally the wall pressures, which although the pressure is measured along a line, can be expected to capture a somewhat three-dimensional lift coefficient based on the forces from the whole span length.

The drag is also measured three different ways: Using load cells, from integration of the surface

pressures from the pressure taps on the airfoil, or using a wake rake. The load cells give a three-dimensional drag coefficient based on the loading on the whole wing. In contrast to this, the drag as obtained from the integration of the pressure taps yield a local value. Since, however, forces for the fluid acting on the airfoil are the sum of pressure forces acting normal to the surface and viscous shear forces acting parallel to the surface, the pressure tab integration forces do not include the contribution from viscous shear forces. These forces are negligible in the lift direction, but can be significant in the drag direction below stall. Therefore, usually the drag as obtained from the pressure integration should be lower than the true value. The last method of obtaining drag, with the wake rake, essentially integrating the velocity deficit in the wake to obtain the drag via momentum considerations, include also the effects of the viscous shear forces. The assumptions under which the underlying theory is derived include stationary flow conditions, which effectively means that this method cannot be used under stalled conditions. Another detail that should be mentioned regarding the drag measurements is that uncertainties in defining effective flow direction/angle of attack arising from inductions from non-uniform span-wise loading and/or tunnel induced velocities, influence the drag as determined from surface pressure integration dramatically, whereas this has no bearing on the drag as determined using a wake rake, which essentially determines the 2D drag.

Figure 10.1 shows a perspective view of the test setup for the airfoil fitted with a leading edge slat. The drawing shows the slat (in darker green) and the way in which it is mounted on the side wall (in blue). The main airfoil (in light green) had a chord of 0.6 m and was fitted with 64 pressure taps, while the slat airfoil had a chord of 0.18 m and had 32 taps. The tunnel has a width of 1.3 m, resulting in an aspect ratio of the main airfoil of 2.17. By repositioning the leading edge within the grid on the side wall and adjusting the stepless bracket (in dark red) the slat position and angle could be adjusted with a short turn-around time. The slat angle was determined using two methods in parallel: One method used a custom made bracket that fitted onto the leading edge of the slat, which together with a digital spirit level was used to measure the angle. As a control method the normal distance from the main airfoil surface to the slat trailing edge was measured to match that in the CFD calculations.

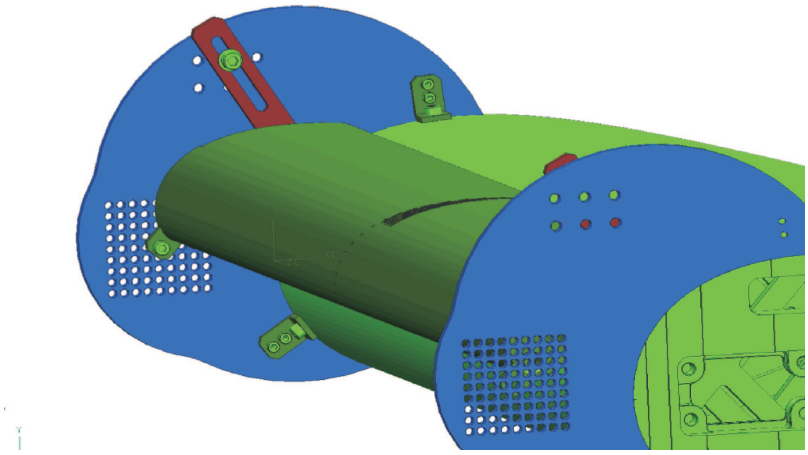

Figure 10.1. CAD drawing of the wind tunnel slat mounting designed by LM Wind Power.

10.3 Test Matrix

The wind tunnel tests were split into two campaigns, one on the isolated flatback airfoil, and another on the combined flatback and slat airfoil. A total of 56 lift polars were measured, 25 on the isolated airfoil and 31 on the multi-element airfoil.

On the isolated flatback airfoil the following tests were performed:

- Smooth surface, four Reynolds numbers based on the main airfoil of: 1, 2, 3 and 4×10^6,
- Roughness, Vortex generators, Gurney flaps.

On the airfoil fitted with a slat the test matrix was more extensive since it involved repositioning of the slat:

- Smooth surface, four Reynolds numbers based on the main airfoil of: 1, 2, 3 and 4×10^6,
- Seven slat positions,
- Slat angle variations at five positions,
- Roughness, Vortex generators, Gurney flaps at one position.
- Flow visualization using wool tufts.

To design the test matrix a parameter study similar to the one discussed in Section 9 was carried out where the slat angle was optimized for each position in the test setup grid. The resulting contour plot of the optimization object function (see Section 9.2) is shown in Figure 10.2. Marked with red filled circles are the five test positions discussed in this work. Position 5E is the reference position where the slat was predicted to perform near optimum. This position lies very close to the position found in the optimization study. The four off-design positions were chosen with the intent of obtaining results with significant variation in the performance of the airfoil compared to the reference position.

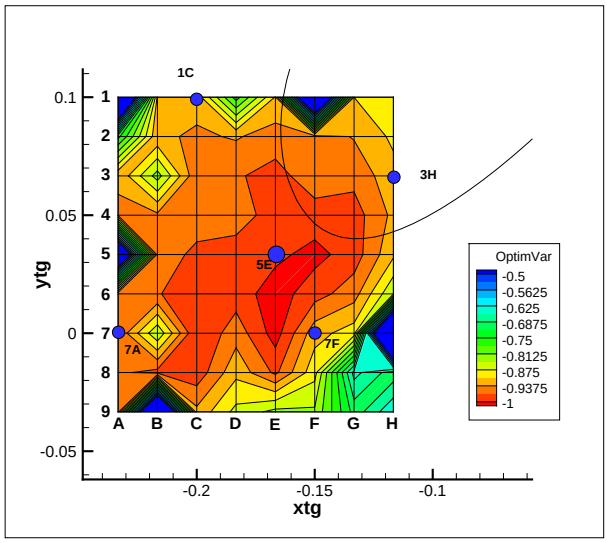

Figure 10.2. Contour plot of the objective function for the slat positioned within the test setup grid optimized for best performance with the slat angle as the only design variable. The curved line entering the picture from top right is the leading edge of the slat as mounted in the 5E position.

10.4 Flatback Airfoil Results

This section summarises the results obtained from the wind tunnel tests on the isolated flatback airfoil.

Measurement sources

Figure 10.3 shows the airfoil tested with smooth surface conditions at a Reynolds number of Re=2×10^6. The figure shows the three measurement sources available for both the lift and drag. For the lift measurement the surface airfoil pressure (AP) and load cell measurements (LC) agree very well between -10 degrees and 5 degrees angle of attack. At 5 degrees AOA the load cell lift quite distinctly changes slope with a linear increase in lift up to 24 degrees AOA. Except for a constant offset in C_l, the 3D lift measurement methods (wall pressure (WP) and load cell measuremens) are in close agreement with each other. Above 5 degrees angle of attack the load cell (3D) measurements predicts a lower C_l than the (2D) airfoil pressure measurement, indicating the onset of 3D flow situations in the tunnel at 5 degrees angle of attack for this configuration. The almost constant offset between the load cell and wall pressure lift is likely due to a single malfunctional pressure port in the wall pressures. Notice also that the load cell and wall pressure measurements do not display the same stall behaviour; in fact, no stall really takes place when looking at the wall pressure and load cell data, whereas the airfoil pressure indicates the onset of stall at approximately 14 degrees AOA.

Turning to the drag measurements, the airfoil pressure drag is at low angles of attack as expected lower than the wake rake drag. However, at 5 degrees AOA the airfoil pressure drag increases drastically to a drag of 0.08 at 10 degrees AOA, where the wake rake drag is 0.023. It is noted that the location where the drag obtained using the different methods starts differing is the same angle for which the lift measurements indicated a 3D flow situation in the tunnel. This reassures the suspicion that after 5 degrees angle of attack the flow in the tunnel is no longer two-dimensional, but is influenced by tunnel effects.

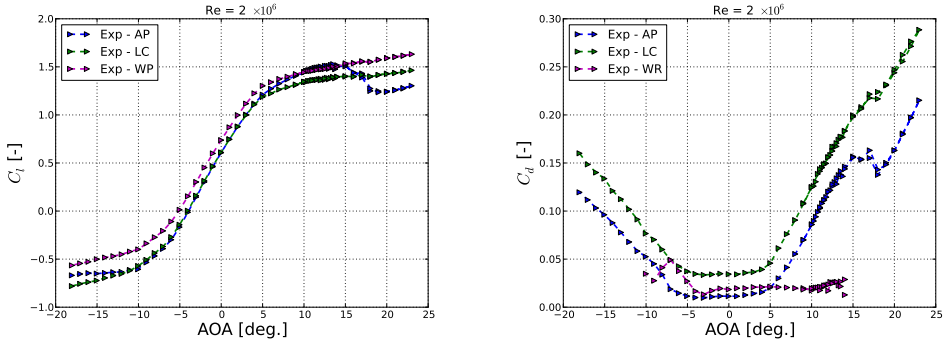

Figure 10.3. Lift and drag coefficients for the flatback airfoil tested at Re=2×10^6.

Figure 10.4 shows the lift and drag contributions at smooth conditions for Re=4×10^6. It is noted that generally the same behaviour as for Re=2×10^6 is seen. In the case, however, the onset of 3D flow conditions starts at a slightly lower angle of attack and the stall behaviour of the lift is changed to be more abrupt. It is also noted that maximum lift is also lower than for Re=2×10^6. This is speculated to be due to an increased turbulence level in the tunnel for increasing flow speed.

Dependence on turbulence intensity

The dependence on turbulence intensity (TI) in the CFD simulations was investigated with simulations with a turbulence intensity of 0.1%, 0.2%, 0.3%, and 0.4%, see Figure 10.5. The measured airfoil stalls considerably later than in the computed results, regardless of TI in the computations. The computations exhibit a very high dependence on TI with as much as 30% variation in the predicted C_{l-max}. The computations with low TI agree well for negative angles

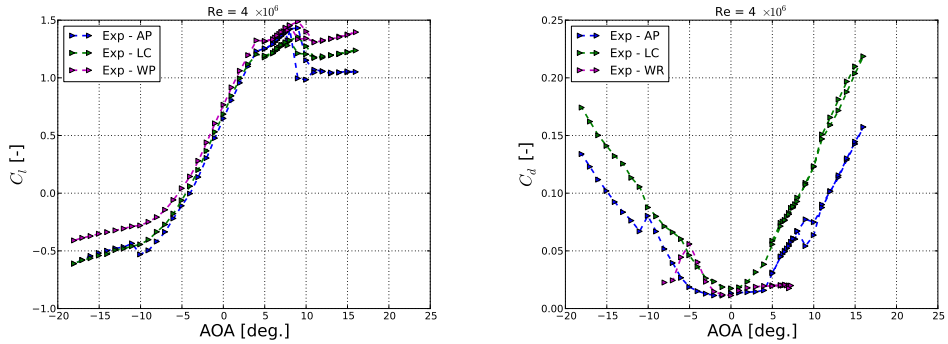

Figure 10.4. Lift and drag coefficients for the flatback airfoil tested at Re=4×10^6.

of attack, whereas at higher angles of attack the agreement is best with computations with higher TI. The same tendency is seen for the drag where the agreement is quite fair with low TI computations at low angles of attack, and likewise good with high TI computations at higher angles of attack. These results suggest that the wind tunnel tunnel turbulence intensity varies with angle of attack of the blade section. Work carried out internally at LM Wind Power in fact showed that at low angles of attack the measured turbulence intensity immediately upstream of the airfoil was 0.2% whereas close to stall it was 0.35%. Based on the LM measurements and the results shown in 10.5 it was decided that all computations in this study would be carried out using a TI=0.3%.

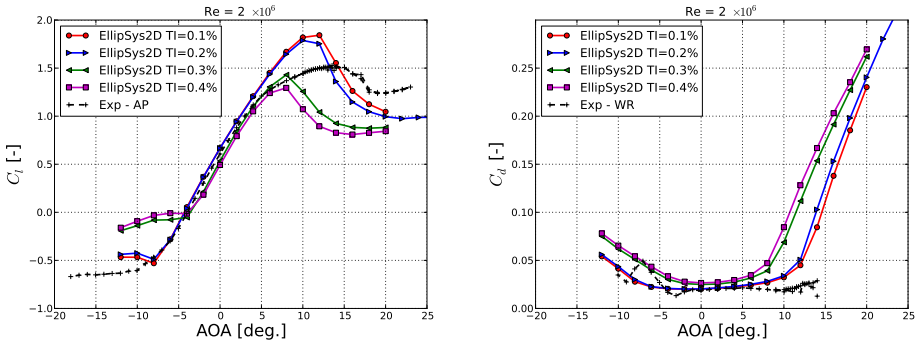

Figure 10.5. Lift and drag coefficients for the flatback airfoil at Re=2×10^6 computed with different inflow turbulence intensities.

Pressure distributions

Figure 10.6 shows the pressure distributions at four angles of attack at a Reynolds number of 2×10^6. The computed results shown are for a turbulence intensity of 0.3%. At low angles of attack the agreement is very good between EllipSys2D and the experiment, whereas at 12 degrees angles of attack, the computed flow is stalled which is not the case in the experiment.

Dependence on Reynolds number

The wind tunnel tests were carried out at four Reynolds numbers of 1,2, and 4 ×10^6. Figure 10.7 shows the experimental results for the flatback airfoil for these Reynolds numbers. The results show a quite large dependence on Reynolds number with a decreasing C_{l-max} for

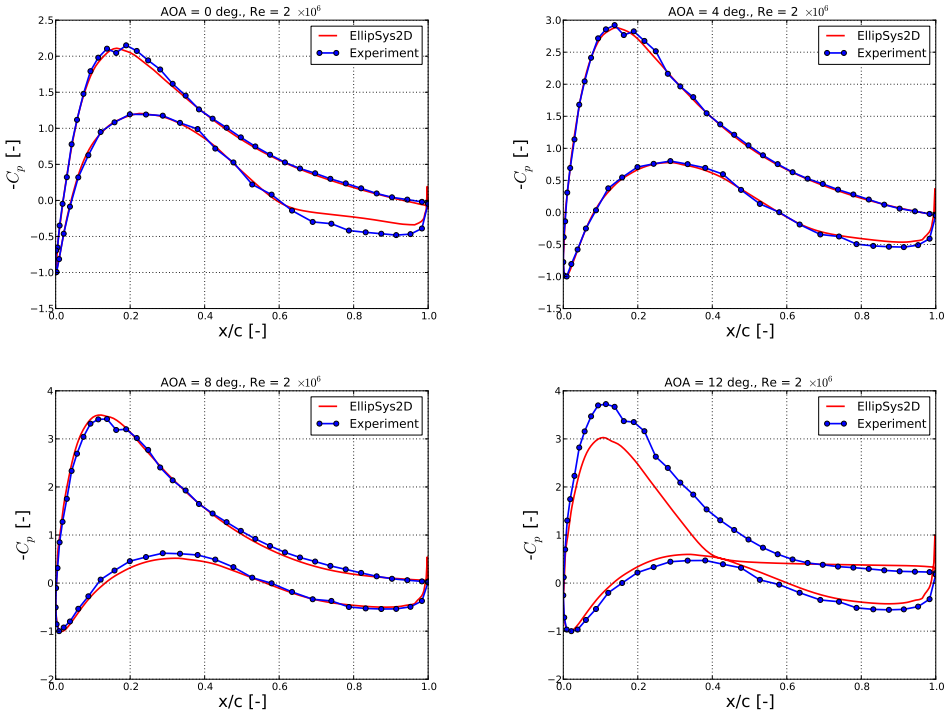

Figure 10.6. Pressure coefficients for the flatback airfoil tested at Re=2×10^6.

increasing Reynolds number.

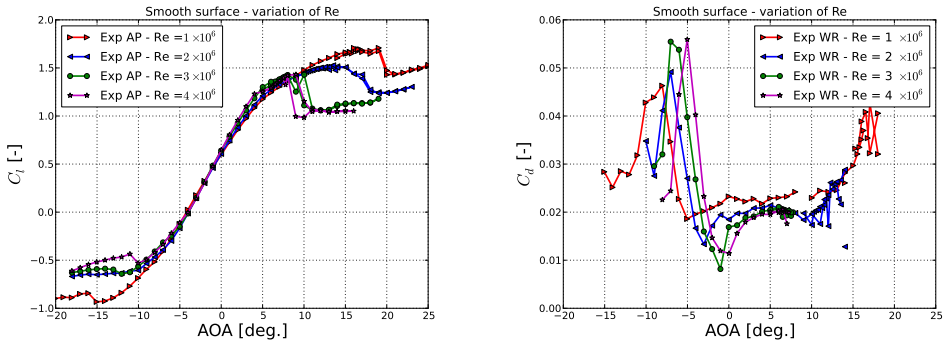

Figure 10.7. Lift and drag coefficients for the flatback airfoil tested at at various Reynolds numbers.

Dependence on surface roughness

Figure 10.8 shows the roughness sensitivity of the airfoil, and the ability of vortex generators to restore a large part of the lifting performance of the soiled airfoil.

Surface mounted devices

Figure 10.9 shows the effect of adding vortex generators, gurney flaps or both on the lifting capabilities of a smooth airfoil. It is seen that vortex generators located at x/c=0.2 increase the

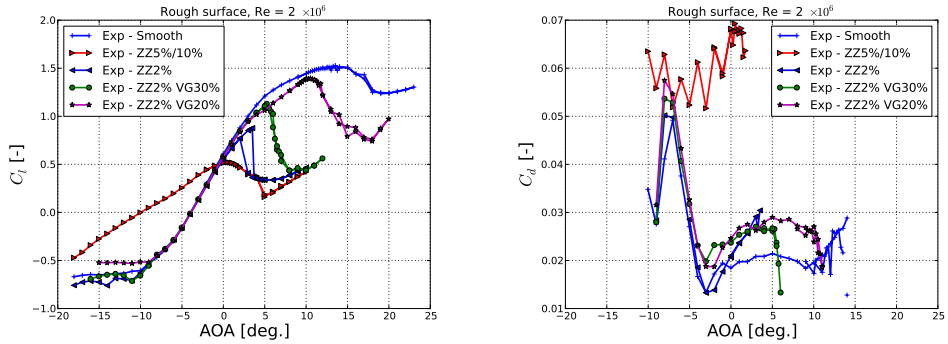

Figure 10.8. Lift and drag coefficients for the flatback airfoil with rough surface conditions tested at Re=2×10^6.

lift with a factor of approx. 2/3. The addition of gurney flaps to either case only increase the lift a small value compared to this.

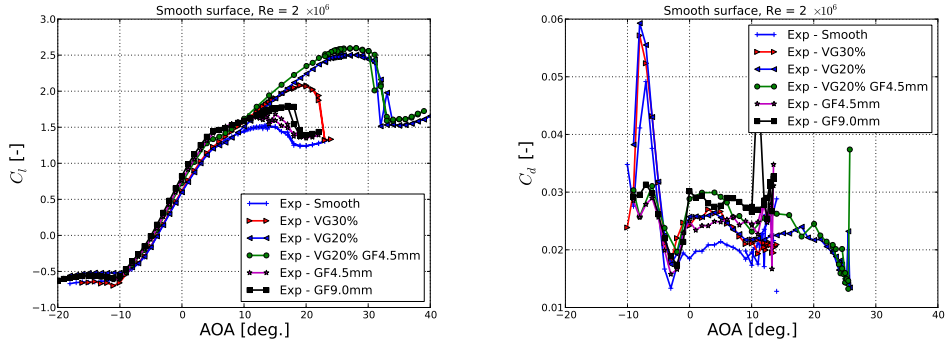

Figure 10.9. Lift and drag coefficients for the flatback airfoil fitted with various devices tested at Re=2×10^6.

10.5 Flatback Airfoil with Slat Results

In this section the main results from the wind tunnel tests on the flatback airfoil fitted with a slat is presented. As described in Section 10.3 seven different slat positions were investigated; here, five positions (5E, 7F, 7A, 1C and 3H) will be discussed. All wind tunnel results are not corrected for wind tunnel effects, and unless otherwise specified all lift coefficients are based on integration of the pressure distributions over each element and drag is based on the wake rake measurements. The lift shown from the CFD simulations is likewise based on on surface pressure only, and drag is likewise based on both skin friction and pressure contributions. The CFD simulations are all computed with free transition and an inflow turbulence intensity of 0.3% unless otherwise specified. For each position the integrated lift and drag coefficients are presented as well as pressure distributions for 12 degrees and 22 degrees angle of attack. Lift coefficients for the combined main and slat elements are normalized with the main element chord, whereas lift coefficients for each individual element are normalized with their respective chord lengths. Likewise for the drag coefficients.

Measurement sources

Figure 10.10 shows the lift and drag coefficients for the multi-element airfoil with the slat in position 5E showing the various measurement sources in the experiment. In contrast to the obser-

vations made on the isolated flatback airfoil, the load cell lift coefficient has an offset compared to the two other measurements where for the isolated flatback airfoil it was the wall pressure measurement that was offset relative to the two other sources. All measurement sources exhibit the same 'kink' in the lift curve at approximately 5 degrees angle of attack. The airfoil pressure and wall pressure lift coefficient curves have a different slope across all angles of attack with the largest differences appearing above 10 degrees angle of attack. The wall pressure and airfoil pressure maximum lift coefficient differ by 8%.

In the drag measurements the load cell drag is also offset compared to the two other sources, which is consistent with the isolated flatback measurements. The airfoil pressure drag and wall pressure drag are in good agreement for angles of attack below 4 degrees after which the airfoil pressure drag increases drastically reaching 0.3 at 20 degrees angle of attack. The drastic increase is consistent with the point at which the 'kink' occurs in the lift measurements, and likewise consistent with the observations made on the isolated flatback airfoil. The load cell drag behaves very similarly to the wall pressure drag with a similar increase at 4 degrees angle of attack.

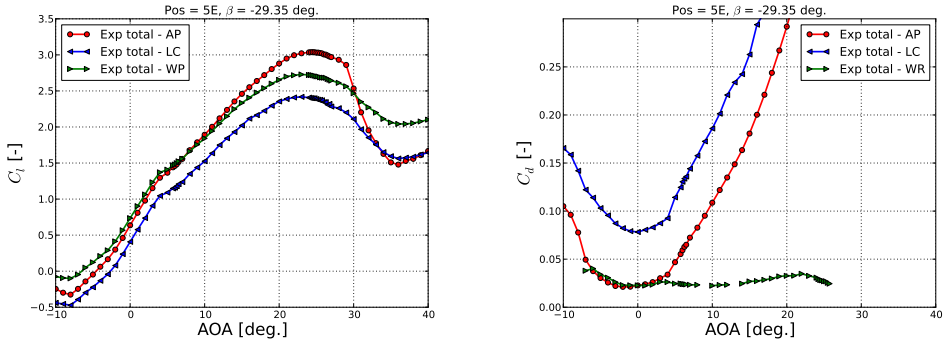

Figure 10.10. Total lift and drag coefficients for the slatted airfoil with the slat in position 5E tested at Re=2×10^6 showing measurements from three different sources for lift and drag (AP: Airfoil pressure, LC: Load cell, WP: Wall pressure, WR: Wake rake).

The most likely explanation for this large discrepancy in the measurement sources is that considerable 3D flow effects occur along the wind tunnel side walls affecting the flow along the entire span of the wind tunnel model. These effects will be discussed in more detail later in this chapter.

Wake rake measurements of drag on a thick airfoil are associated with some degree of uncertainty since the flow can be unsteady for a large range of angles of attack. However, this source was concluded to be the most reliable source of measurement compared to the load cell and airfoil pressure measurements and as such, results presented in the following sections will use only the wake rake measurement.

Dependence on turbulence intensity

Figure 10.11 shows the lift and drag coefficients for position 5E with a slat angle, β=-29.35 deg, where the experimental results are compared to EllipSys2D computations with different inflow turbulence intensities (TI). In line with the results for the isolated flatback airfoil, the computations showed a fairly large dependence on TI, with a decrease in C_{l-max} with increasing TI. While there is improvement in the agreement at C_{l-max} with computations of increasing TI, the difference in slope between computations and experimental data is still fairly large regardless of TI. The simulated and measured drag are in reasonably good agreement up to 14 degrees angle of attack, after which the measured drag is considerably lower than the simulated.

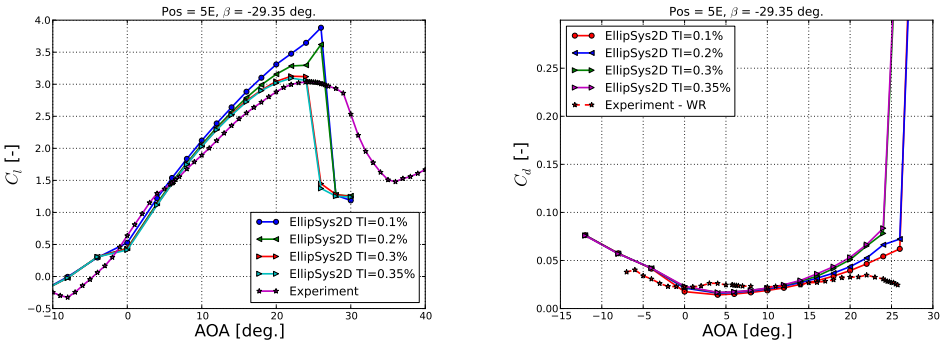

Figure 10.11. Lift and drag coefficients for the flatback airfoil tested at Re=2×10^6.

Position 5E

Figure 10.12 shows the multi-element airfoil with the slat in position 5E and a slat angle, β=-29.4 degrees which in the remainder of this report will be referred to as the reference position.

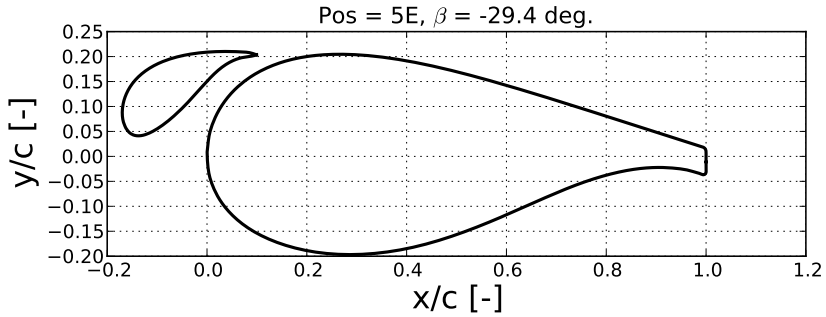

Figure 10.12. Configuration with the slat in position 5E.

Figure 10.13 shows integrated lift and drag coefficients for both experiment and computations. Consider first the curves for the total lift (sum of lift on the slat and main airfoil), where similarly to the experimental results for the isolated flatback airfoil, there is a distinct kink in the lift curve around 5 degrees angle of attack where the experimental data shifts from being above the CFD results to below. Likewise, the slope of the experimental lift curve decreases at this point, which is not consistent with the CFD computations. The stall in the experimental data is quite smooth and reaches a maximum at 24 degrees angle of attack, but is not fully stalled until beyond 30 degrees angle of attack. The CFD simulations around stall are not entirely consistent and exhibit an unnatural kink at 26 degrees angle of attack, at which point the airfoil stalls very abruptly. It is likely that the separation process on the airfoil is quite unsteady, and that a steady state simulation therefore does not capture this process entirely correctly.

Turning to the individual contributions to lift from the main and slat elements it is clear that the kink in the experimental lift data at 5 degrees angle of attack and subsequent discrepancy with simulations beyond this point stems primarily from the main element. The measured and predicted lift on the slat element, however, are in better agreement, although the experimental data has a lower lift curve slope than the predicted. The stall point on the two elements are not captured very accurately by the computations. The stall on the main element is in the measurements quite smooth, whereas the compuatations predict a more abrupt stall. On the slat element, the stall occurs at 29 degrees angle of attack in the experiment whereas it is predicted

at 26 deg angle of attack in the simulations.

The drag is in reasonably good agreement in the range -8 degrees to 14 degrees angle of attack, although the predicted drag is considerably smoother than the experimental data. This could be related to differences in the transition points in the computations and experiment, which in both cases were un-tripped. Beyond 14 degrees angle of attack the predicted drag is higher than the measured. This could be caused by unsteadiness in the flow or that the wake is too wide for the wake rake to capture completely.

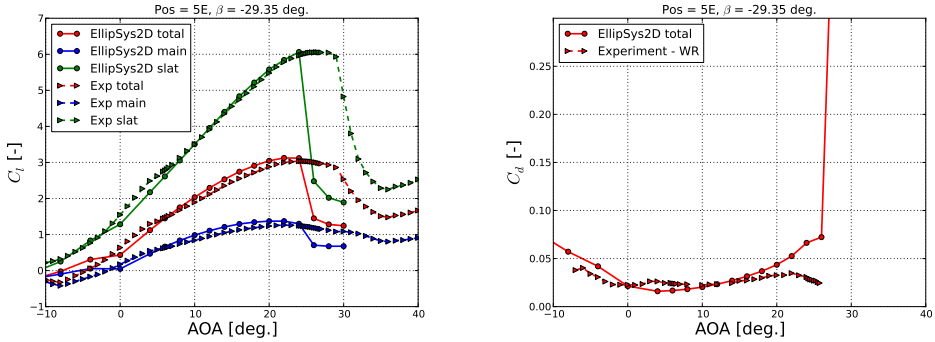

Figure 10.13. Lift and drag coefficients for the slatted airfoil with the slat in position 5E tested at Re=2×10^6.

Pressure coefficients for angles of attack of 12 degrees and 22 degrees are shown in Figure 10.14. Note that the pressure distributions are plotted with normalized relative chord lengths with the leading edges of both elements placed at x/c=0. For both angles of attack there is a fairly high discrepancy between the measurements and computations, although the same general features are similar with characteristic kinks in the pressure distributions on the two elements in the region where they are in close proximity. In this gap region region, the computations predict a higher suction than observed in the experiment. For both angles of attack the computations predict a higher suction peak on the slat than measured in the experiment, and likewise on the main element, the suction peak is stronger in the computations. At 22 degrees angle of attack, the computed pressure distribution is very flat at the trailing edge whereas the gradient is slightly higher in the measurements, indicating that the flow is partially stalled in the computations and not in the measurements.

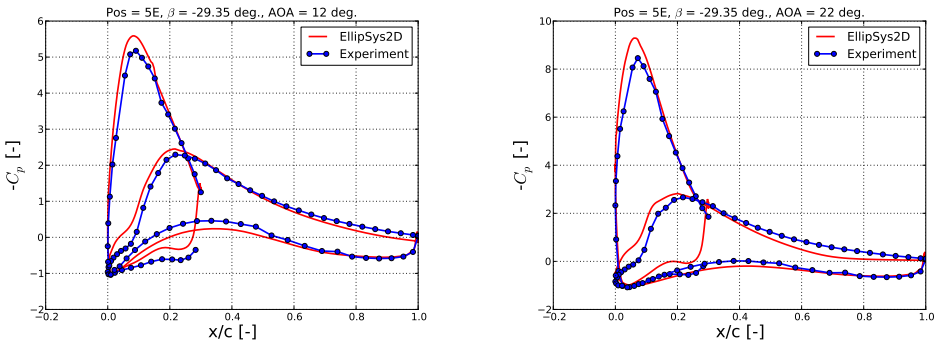

Figure 10.14. Pressure coefficients for the slatted airfoil with the slat in position 5E tested at Re=2×10^6.

Position 7F

Figure 10.15 shows the multi-element airfoil with the slat in position 7F and a slat angle, β=-34.2 degrees

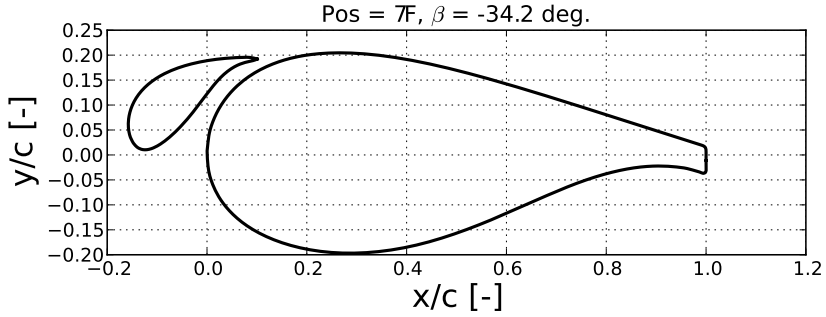

Figure 10.15. Configuration with the slat in position 7F.

Similarly to position 5E a kink also exists in the experimental lift curve at around 3-5 degrees angle of attack, where the measured lift shifts from being higher than to lower than the predicted lift. At position 7F the performance of the airfoil is predicted to be poorer than at the reference position 5E, see Figure 10.2. As shown in Figure 10.16 this is indeed also the case in the experiment, where the maximum lift is predicted to be 2.83, where position 5E had a maximum lift of 3.03. C_{l-max} in the experiment is at approximately 24 degrees and also for this case the stall is very gentle. In the computations the airfoil does not stall until 28 degrees angle of attack, although the lift curve exhibits the same tendency as in position 5E where the curve initially flattens out after which the lift increases again before dropping steeply.

The individual components of lift for each element exhibit in many respects the same features as for position 5E, with a significantly better agreement between measurements and computations on the slat, and quite poor agreement on the main element. The agreement for the slat is very good up until 22 degrees angle of attack where beyond this point the computations predict a continued increase in lift, which is not seen in the experiment. Notice that the main element stalls significantly earlier in both experiment and computations.

The measured and computed drag is for this slat position in very poor agreement. For the range 0 degrees to 20 degrees angle of attack the measured drag is largely unchanged whereas the computed drag is steadily increasing. As for position 5E, the measured wake rake drag appears to be unusable beyond 20 degrees angle of attack, since the drag here is measured to be decreasing.

The two pressure distributions shown in Figure 10.17 exhibit the same tendencies as for position 5E. The computations predict a slightly lower pressure on the pressure side of the slat than observed in the experiment, and likewise on the main element, the suction is slightly higher in the computations. The suction peak on the slat is at 12 degrees slightly higher than the measurements in agreement with position 5E. The opposite is the case at 22 degrees angle of attack. As for position 5E the pressure gradient on the main element is flatter at the trailing edge than observed in the experiment.

Position 7A

Figure 10.18 shows the multi-element airfoil with the slat in position 7A and a slat angle, β=-29.4 degrees.

General tendencies for the lift distributions are very similar for this case to the two previously

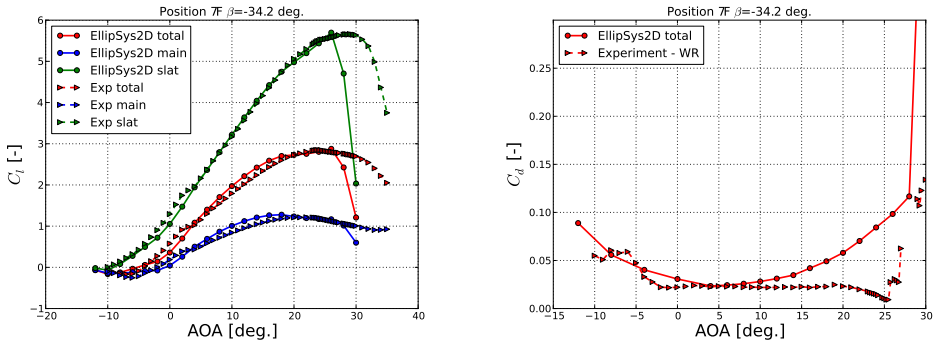

Figure 10.16. Lift and drag coefficients for the slatted airfoil with the slat in position 7F tested at Re=2×10^6.

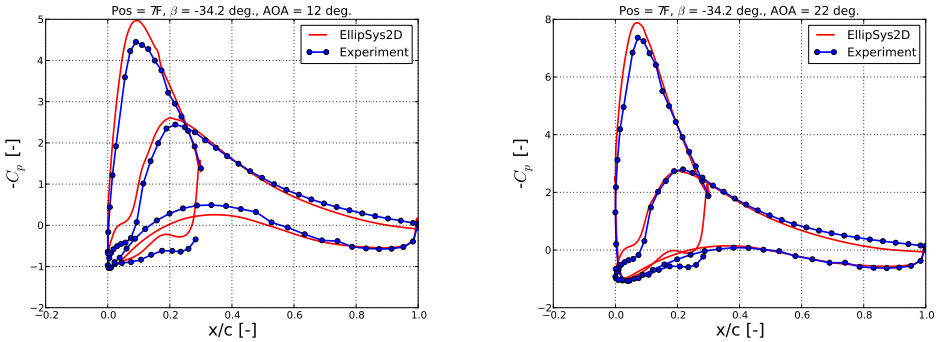

Figure 10.17. Pressure coefficients for the slatted airfoil with the slat in position 7F tested at Re=2×10^6.

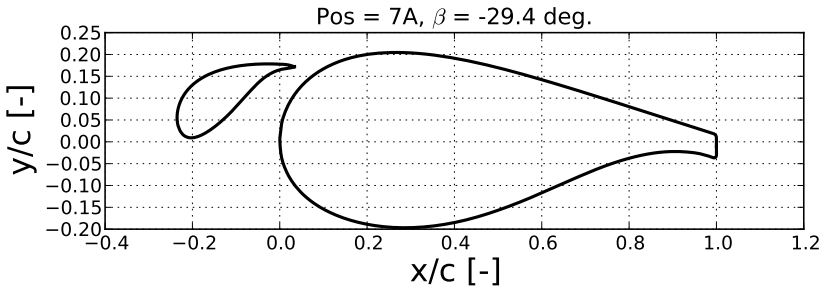

Figure 10.18. Configuration with the slat in position 7A.

discussed. The most notable difference between this case and the other two cases is that the computations predict a very early trailing edge separation on the main airfoil at approximately 16 degrees angle of attack, which is not seen in the experiment. This results in the slat lift also being in poor agreement beyond this angle of attack. The explanation for the early stall in the computations can be given by referring to [3] who explains this by the so-called 'circulation effect', also summarised in Section 9.1.1. With the slat in a very forward position, it is not very effective at limiting the suction peak on the main airfoil, which subsequently stalls earlier.

The predicted and measured drag for this case exhibit very similar trends for angles of attack of -2 degrees to 16 degrees except for a consistently higher drag level in the simulations. Above

16 degrees angle of attack the two diverge significantly with a considerably higher drag in the computations.

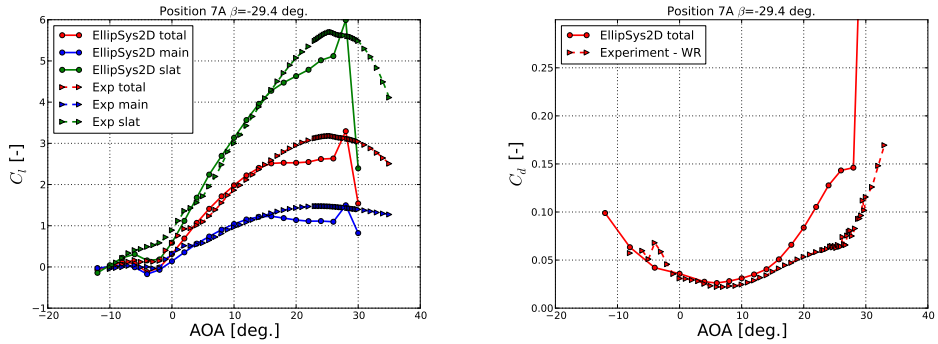

Figure 10.19. Lift and drag coefficients for the slatted airfoil with the slat in position 7A tested at Re=2×10^6.

The pressure distributions shown in Figure 10.20 are in good agreement at 12 degrees angle of attack on both the main and slat elements. In contrast to the previous positions discussed, the pressure on the slat and main airfoil in the region where they are in close proximity are in very good agreement. At 22 degrees angle of attack the trailing edge stall on the main element is clearly visible in the computations, whereas the flow is still completely attached in the experiment.

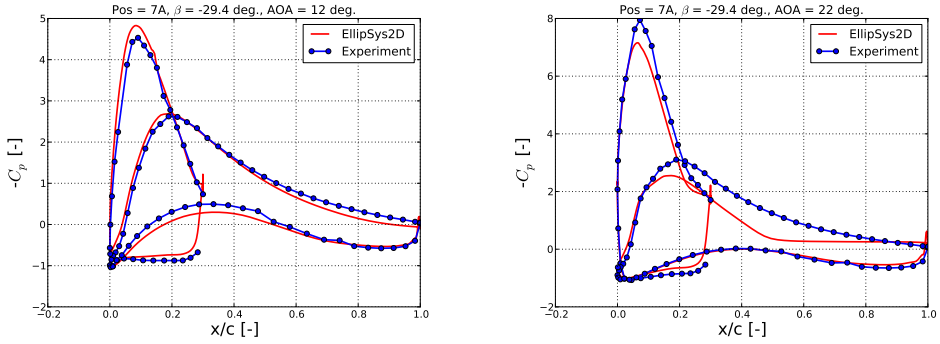

Figure 10.20. Pressure coefficients for the slatted airfoil with the slat in position 7A tested at Re=2×10^6.

Position 1C

Figure 10.21 shows the multi-element airfoil with the slat in position 1C and a slat angle, β=-23.7 degrees

At position 1C the characteristic kink in the measured lift at low angle of attack appears significantly later at approximately 8 degrees to 10. degrees angle of attack. The measured total lift coefficient reaches a maximum at approximately 20 degrees angle of attack and remains constant up to 26 degrees angle of attack after which it begins to drop. The computations predict a significantly higher maximum lift of 3.4 at 24 degrees angle of attack followed by a abrupt stall. The lift coefficient on the slat is in relatively poorer agreement at this position than at the previous with a change in slope in the experiment not observed in the computations. The slat stalls at 20 degrees angle of attack in the experiment where it continues to provide lift up to 24 degrees angle of attack in the computations.

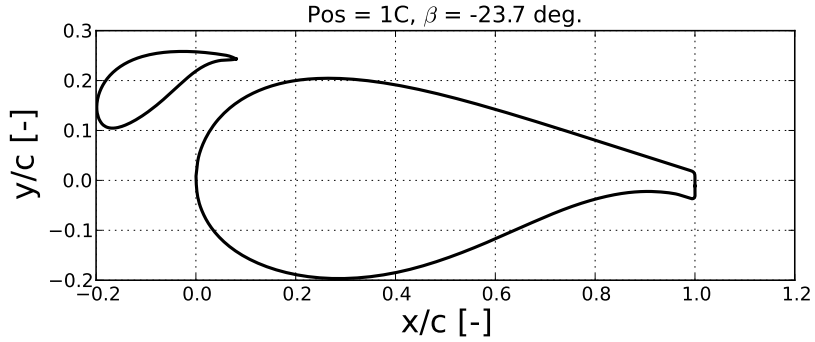

Figure 10.21. Configuration with the slat in position 1C.

The predicted and measured drag are in reasonably good agreement over the full range of incidences exhibiting the same tendencies. There is, however, still a difference in the overall level, which for this case is higher in the measurements, which is opposite to positions 7A.

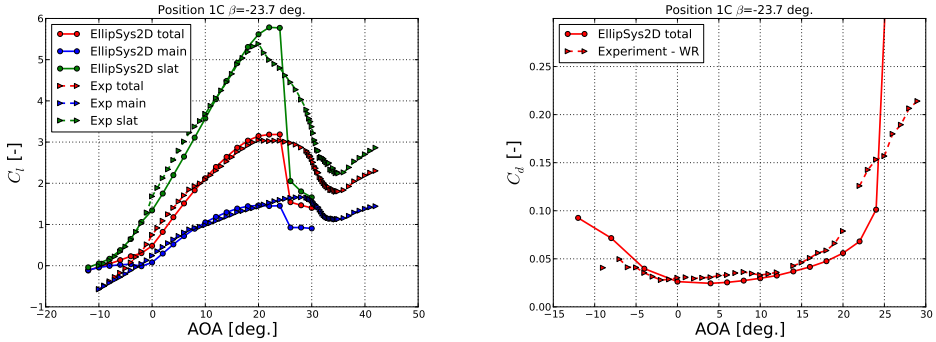

Figure 10.22. Lift and drag coefficients for the slatted airfoil with the slat in position 1C tested at Re=2×10^6.

As for position 7A the pressure distributions are in reasonably good agreement at 12 degrees angle of attack except for a lower suction peak on the slat in the computations. At 22 degrees angle of attack the flow is clearly completely stalled on the slat in the experimental data, which causes the pressure distribution on the main element to also be in poor agreement to the computations. On the pressure side, however, the agreement is quite good.

Position 3H

Figure 10.24 shows the multi-element airfoil with the slat in position 3H and a slat angle, β=-25.6 degrees

The final position discussed in this report, position 3H was expected to be the poorest of all configurations tested. In this respect the computations and measurements are in good agreement predicting a maximum lift of approximately 2.85. The measured stall angle is, however, considerably higher than the computed, since the flow on both the slat and main airfoil stalls later than predicted, see Figure 10.25.

Similarly to a few of the other cases the measured drag does not increase noticeably with increasing angle of attack, which is consistently the case in the computations. In the range 0 degrees to 10 degrees angle of attack, however, the agreement is fair, see Figure 10.25.

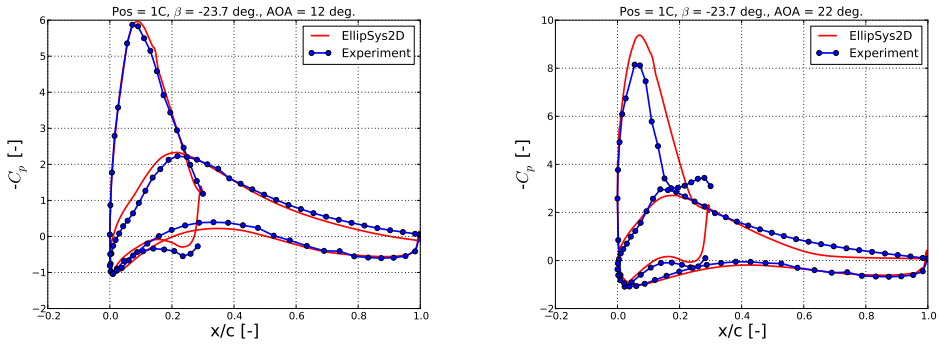

Figure 10.23. Pressure coefficients for the slatted airfoil with the slat in position 1C tested at $Re=2\times10^6$.

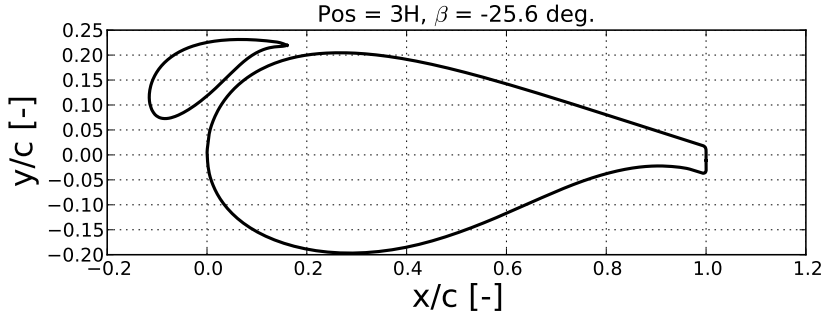

Figure 10.24. Configuration with the slat in position 3H.

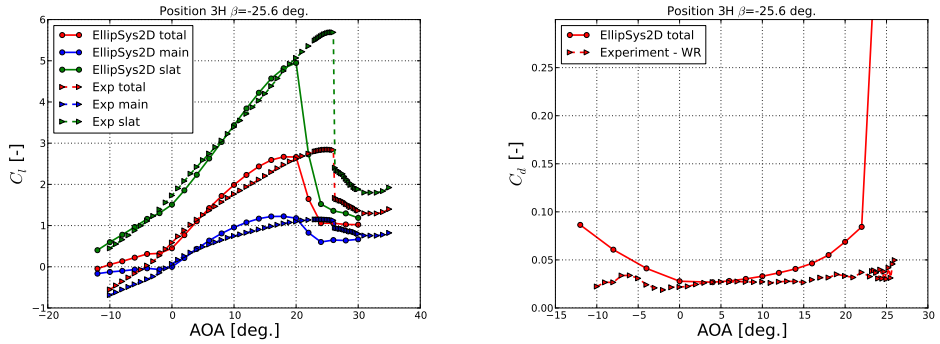

Figure 10.25. Lift and drag coefficients for the slatted airfoil with the slat in position 3H tested at $Re=2\times10^6$.

Similar to other cases where the slat and main airfoil are in very close proximity, the computations predict a considerably higher suction on both slat and main element in the region where they are in close proximity, see Figure 10.26. At 12 degrees angle of attack, however, the agreement is quite good except in the above mentioned region. At 24 degrees angle of attack the same tendency of the flow stalling earlier on the main element in the computations than in the measurements is observed.

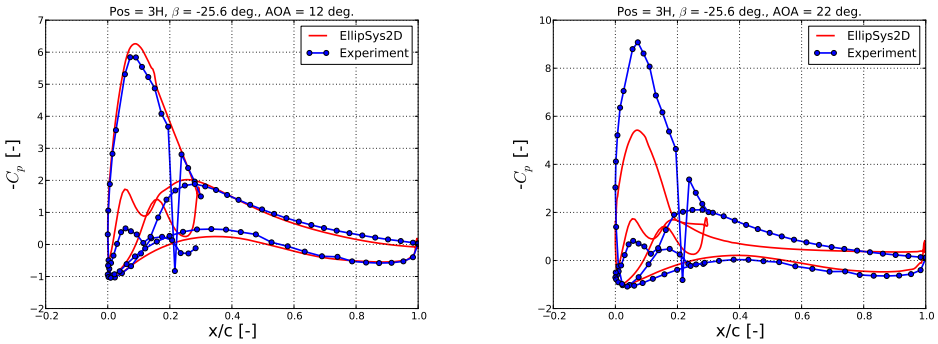

Figure 10.26. Pressure coefficients for the slatted airfoil with the slat in position 3H tested at $Re=2\times10^6$.

Position 5E - Variation of slat angle β

At position 5E, three β angles in addition to the reference angle were investigated. Figure 10.27 shows the airfoil configuration with the four different slat angles.

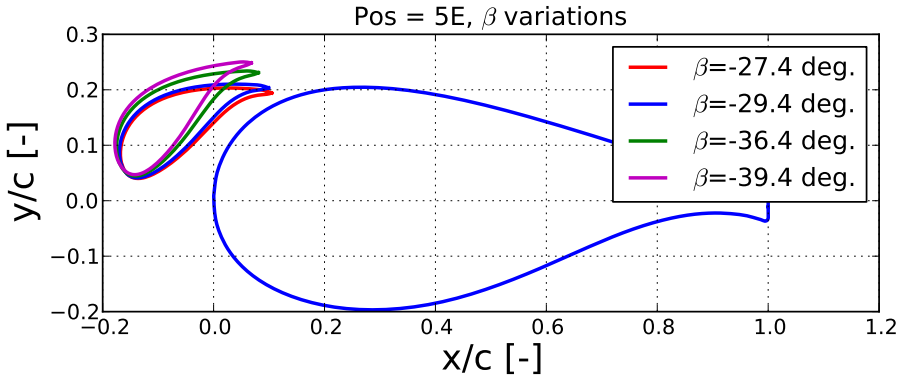

Figure 10.27. Configuration with the slat in position 5E for various β *angles.*

Figure 10.28 shows the computed and measured lift coefficients for the five slat angles. EllipSys2D predicts the reference position with β=-29.35 degrees to be the best, closely followed by β=-27.35 degrees, whereas the two configurations with higher slat inclinations perform very poorly. In the experiment, however, the trend is completely different, with the configurations with high slat inclination out-performing the two others quite significantly. The explanation for the large discrepancy is explained when looking closer at the lift curves for each element individually.

Figure 10.29 shows the lift and drag coefficients for the slat in position 5E with β=-35.35 degrees. The flow stalls at around 17 degrees angle of attack on the main element in the computations, whereas the flow does not appear to stall until beyond 30 degrees in the experiment. The lack of stall observed here corresponds well to the observations made for all other configurations, where the flow over the main airfoil consistently stalled later in the experiment than in the computations. It is likely that wind tunnel effects stemming both from side wall interference as well as blockage effects at high angles of attack severely influenced the experimental results.

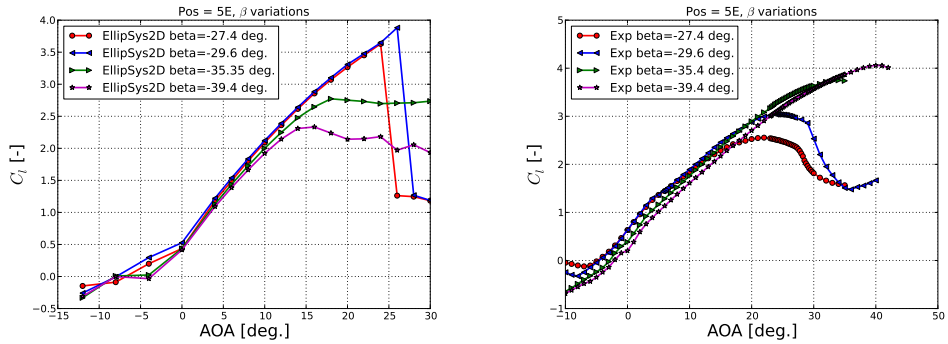

Figure 10.28. Lift coefficients for the flatback airfoil with the slat in position 5E for various β *angles tested at Re=2*$\times 10^6$.

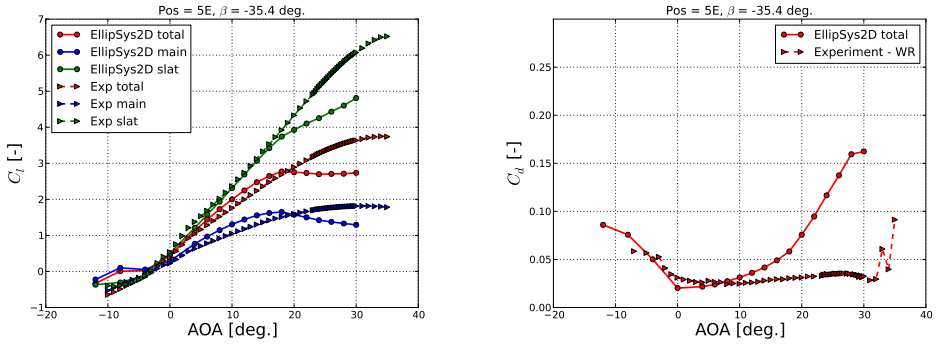

Figure 10.29. Lift and drag coefficients for the flatback airfoil with the slat in position 5E with β*=-35.35 degrees tested at Re=2*$\times 10^6$.

'2D' wind tunnel effects

To investigate to what degree the top and bottom wall of the wind tunnel had influence on the measurements, 2D CFD computations were carried out in a domain with top and bottom walls specified as symmetry conditions. The mesh used for this investigation was different from that used in the rest of this work and is therefore described below.

To carry out the simulations an overset grid was used with a Cartesian mesh discretizing the tunnel domain and two individual curvilinear meshes for the main airfoil and slat, respectively. This mesh had a considerably finer mesh resolution than the previously used meshes and contained 164000 cells. Figure 10.30 shows the tunnel mesh and details around the slat element. Another mesh was created with identical cell distribution around each element and in the Cartesian mesh close to the geometry, but with the outer boundaries extended 40 chord lengths away from the surface.

Figure 10.31 shows the lift and drag coefficients computed using a fully patched mesh which has no tunnel walls, and two overset grid simulations with and without tunnel walls compared to the wind tunnel measurement. Firstly, notice that there is a fairly large difference between the 'Std' fully pathced grid computations and the overset grid computations for angles of attack above 20 degrees with a significantly higher C_{l-max} in the overset simulations. Including the tunnel walls clearly has a significant influence on the lift coefficient, with an increase of 5% in C_{l-max}.

The computations with increased mesh resolution as well as tunnel walls, are not, however, in better agreement with the measurements than the patched grid computations. On the contrary, the discrepancy around C_{l-max} is even larger. However, at angles of attack below 5 degrees the

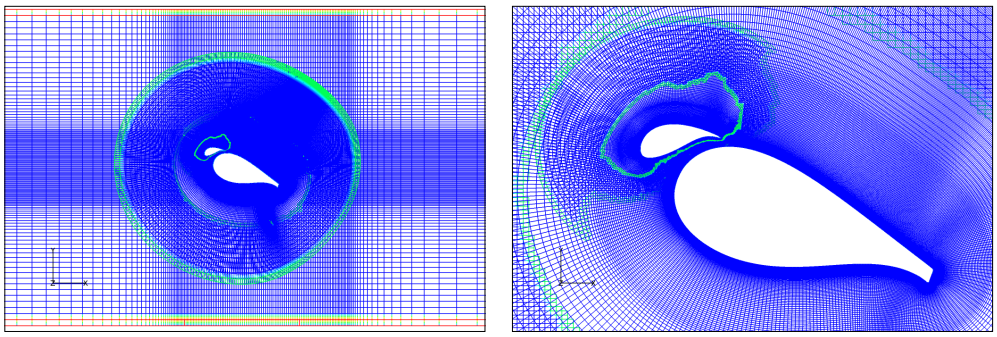

Figure 10.30. Overset grid for the multi-element airfoil with the slat in posiition 5E with upper and lower tunnel walls included as symmetry boundaries.

measurements and tunnel grid simulations are in very good agreement.

Turning to the drag coefficient, including the tunnel appears to reduce the drag coefficient slightly, but not to the extent that the agreement with the experimental data becomes noticeably better.

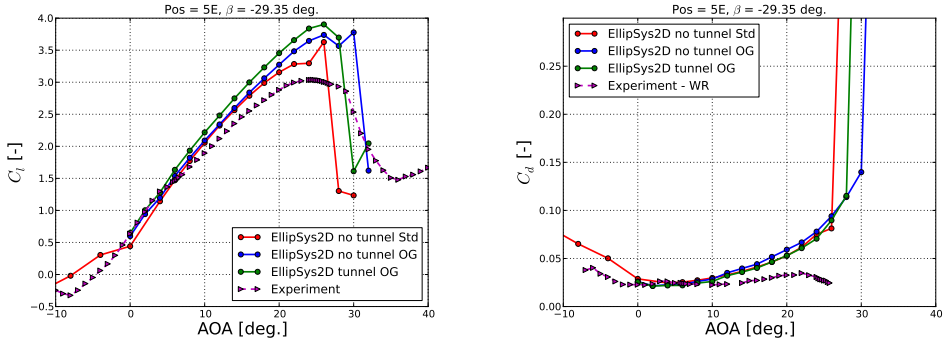

Figure 10.31. Lift and drag coefficients for the multi-element airfoil with the slat in position 5E tested at Re=2$\times 10^6$ in a 2D tunnel configuration.

3D flow effects due to wall interference

As discussed in Section 10.5 the three measurement sources for the lift and drag were not in very good agreement. Particularly the drag measurements were in very poor agreement with both the load cell drag and airfoil pressure drag increasing drastically for angles of attack over 5 degrees. Something not observed in the wake rake measurements or in the 2D CFD simulations. The sudden increase in drag was as discussed accompanied by a change in slope of the lift curve, something that was observed both for the isolated flatback airfoil and when fitted with the slat. It was hypothesised that this behaviour was caused by an onset of 3D flow caused by the side walls.

Flow visualizations were carried out using wool tufts mounted on the airfoil surfaces. These visualizations confirmed the hypothesis, which is clearly visible in Figure 10.33 which shows the airfoil operating at three different angles of attack. The picture is overlaid with lines highlighting the 3D flow structures showing two large flow structures emanating from the side walls, growing in extent with increasing angle of attack. To remedy this very undesirable flow feature it was attempted to mount vortex generators upstream of the point where the 3D flow structures occurred, both on the side walls and on the main airfoil. Although slight improvements were observed on the lift coefficient around the onset of its occurrence at 5 degrees angle of attack,

no improvement was observed in the drag coefficient.

To further investigate to what extent the flow was three-dimensional over the airfoil surface, measurements were carried out where the wake rake was traversed laterally along the span of the airfoil model. Two angles of attack were investigated, with two measurements at each angle of attack. Figure 10.32 shows the drag coefficient as function of lateral position for 0 degrees and 15 degrees angle of attack. At 0 degrees angle of attack there is a fairly high variation along the span and also some difference between the two measurements suggesting that the flow may be unsteady even at low angles of attack. At 15 degrees angle of attack the drag also varies quite significantly along the span. At $\pm$ 250 mm spanwise position the Series 34 measurement measured a very high drag of 0.54, which is not seen to the same extent in Series 36. This suggests that the flow near the sides of the tunnel is highly unsteady.

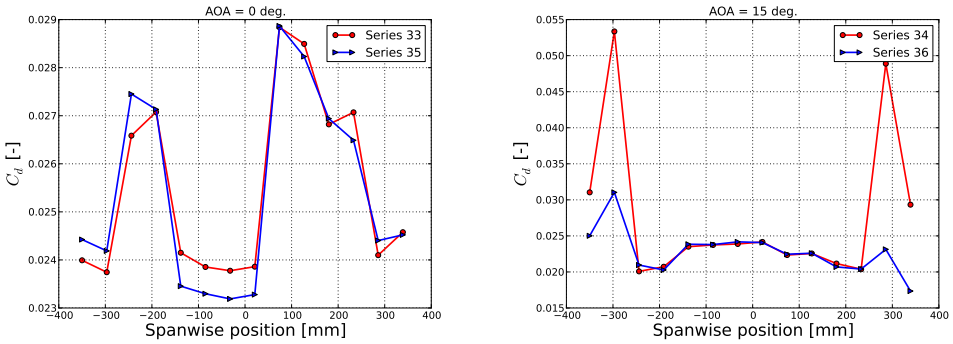

Figure 10.32. Drag coefficient as function of lateral measurement position for the multi-element airfoil with the slat in posiition 5E tested at Re=2$\times 10^6$. 0 mm is the center of the tunnel. The total tunnel width is 1400 mm.

The flow visualizations and wake rake traversals thus clearly demonstrated that the flow was not nominally 2D above 5 degrees angle of attack. The consequence of this was that flow measurements, whether sectional measurements as in the case of the airfoil pressure or integral as for the load cell, were fundamentally not 2D, making comparison of the experimental data to 2D CFD simulations very difficult. This finding supports the hypothesis that the change in lift curve slope at 5 degrees angle of attack was due to wall interference effects. As discussed by Rumsey et al. [2] it is very difficult to retain 2D flow characteristics near stall in wind tunnel measurements on high lift configurations. Side wall venting improved the flow quality considerable, but did not entirely remove the side wall effects.

Beyond stall, a peculiar flow phenomenon was observed, where seemingly the flow was not stalled on the main airfoil shown for 50 degrees angle of attack in Figure 10.34. As is evident from the picture the flow is fully stalled on the slat with the tufts pointing upstream, yet, the tufts on the main element indicate that the flow is attached. Note also that the two separated regions near the side walls of the tunnel are no longer present.

A particle tracking simulation was carried out using EllipSys2D where the same flow phenomenon could be observed. Figure 10.35 shows a snapshot of the flowfield with the slat in position 5E at 40 degrees angle of attack with particles seeded upstream of the airfoil. Particles that pass in between the slat airfoil and main airfoil appear to remain attached to the surface although the flow above the surface is fully stalled. Immediately above the surface of the main airfoil a small secondary vortex is formed below the main vortex which periodically is shed along with the main vortex emanating from the main airfoil trailing edge. This periodic shedding was believed also to have been observed in the experiment where very short bursts occurred where the tufts on the main airfoil would reverse direction and subsequently reattach to the surface.

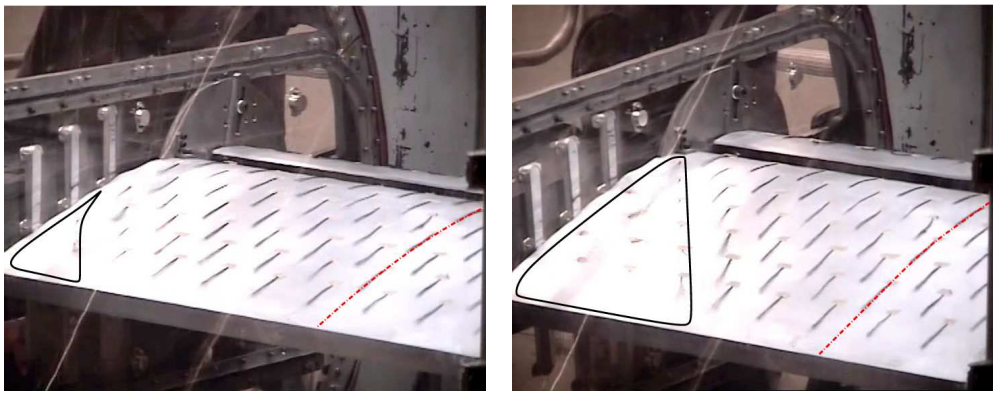

AOA=0 degrees AOA=5 degrees

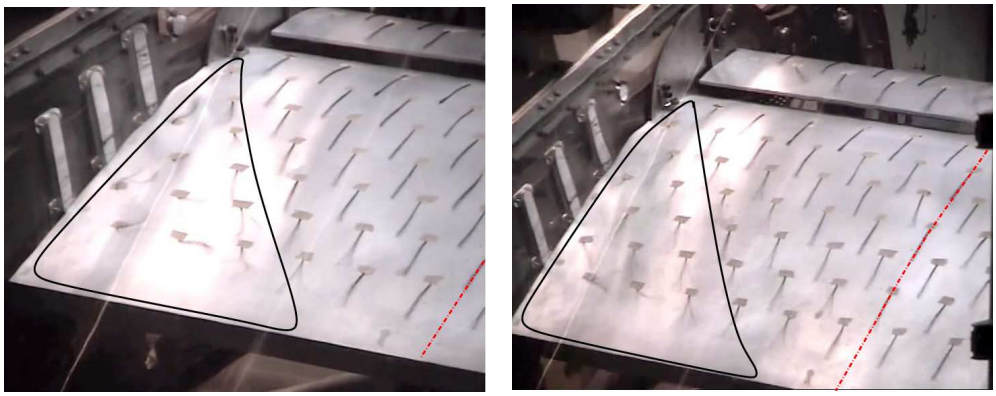

AOA=15 degrees AOA=24 degrees

Figure 10.33. Wool tufts flow visualization of the slatted airfoil at various angles of attack.

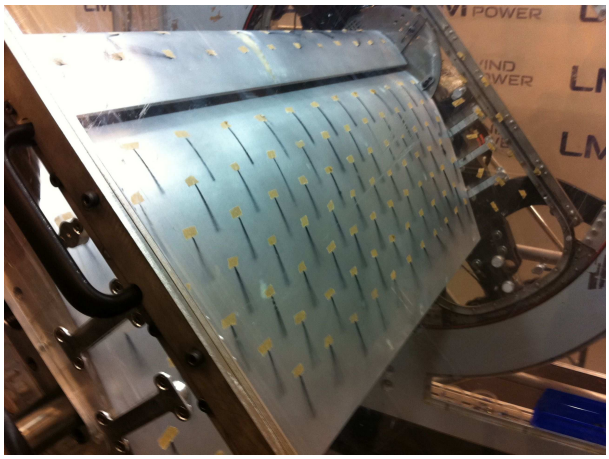

Figure 10.34. Wool tufts flow visualization of the slatted airfoil operating at 50 degrees angle of attack.

10.6 Summary and Conclusions

A wind tunnel measurement campaign was carried out on a newly designed thick, flatback, high-lift airfoil which consisted of a 40% thick main airfoil and a forward slat airfoil of 30% length relative to the main airfoil. The resulting data was used in an extensive validation study with comparisons between experimental data and computations performed using the incompressible Navier-Stokes solver EllipSys2D. Based on the results, a number of general tenden-

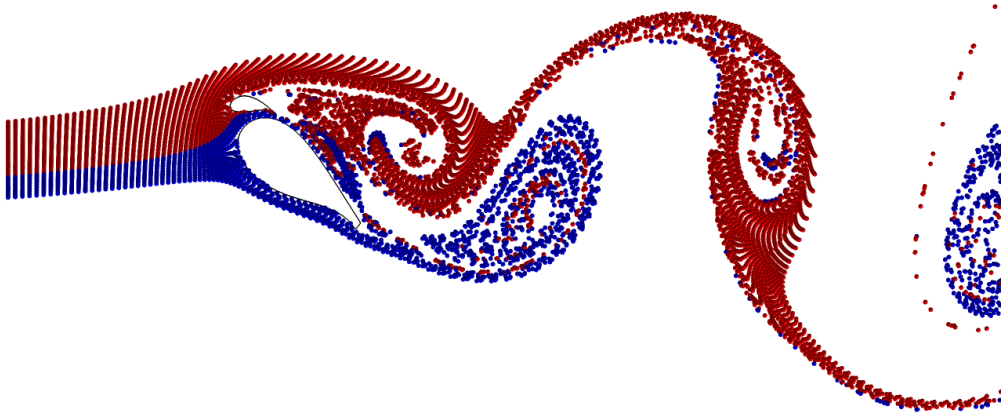

Figure 10.35. Snapshot of the flowfield of the configuration with the slat in position 5E operating at 40 degrees angle of attack.

cies observed in the measurements and computations were identified. Below, a summary of the main conclusions will be attempted.

Summary of the main observations made from the experiment:

- The measured airfoil pressure and wall pressure C_{l-max} differed by 8%. The three sources of measurement for both lift and drag were quite inconsistent, indicating the presence of 3D flow structures on the airfoil.
- The measurement data exhibited a 'kink' in the main element lift curve and subsequent change in slope around 5 degrees angle of attack for all configurations which was caused by the onset of 3D flow structures emanating from the side walls.
- The wake rake drag measurement was generally associated with uncertainty as well as inconsistency for some slat positions.

Summary of the main observations made in the CFD study:

- The computed lift on the slat airfoil was consistently in better agreement with the experiment than on the main airfoil.
- Trends due to changes in slat position and angle were not predicted consistently by CFD.
- The flow had a tendency to stall earlier on the main airfoil in the computations than in the experiment.
- The stall behaviour in the computations was generally more abrupt than in the experiment.
- Steady state simulations appear to be inadequate for predicting the correct stall behaviour with unnatural increases in lift at the point of stall.
- For configurations where the two elements were in close proximity, the computations predicted higher suction in the gap region between the two elements.
- Including top and bottom tunnel walls resulted in an increase in C_{l-max} of 5% in 2D simulations.

Acknowledgements

The authors wish to express their gratitude towards the technical staff and engineers at LM Wind Power who carried out the wind tunnel tests. In particular the efforts and patience of Rolf Hansen made the successful completion of the measurement campaign possible.

References

[1] C. L. Rumsey and S. X. Ying. Prediction of high lift: review of present CFD capability. *Progress in Aerospace Sciences*, 38(2):145–180, Feb. 2002. ISSN 03760421. doi: 10.1016/S0376-0421(02)00003-9.

[2] C. L. Rumsey, E. M. Lee-rausch, and R. D. Watson. Three-dimensional effects in multi-element high lift computations. *Computers & Fluids*, 32:631–657, 2003.

[3] A. M. O. Smith. High-Lift Aerodynamics. *Journal of Aircraft*, 12(6):501–530, June 1975. ISSN 0021-8669. doi: 10.2514/3.59830.

Risø DTU is the National Laboratory for Sustainable Energy. Our research focuses on development of energy technologies and systems with minimal effect on climate, and contributes to innovation, education and policy. Risø has large experimental facilities and interdisciplinary research environments, and includes the national centre for nuclear technologies.

Risø DTU
National Laboratory for Sustainable Energy
Technical University of Denmark

Frederiksborgvej 399
PO Box 49
DK-4000 Roskilde
Denmark
Phone +45 4677 4677
Fax +45 4677 5688

www.risoe.dtu.dk